Supporting Information

Room Temperature Acceptorless Alkane Dehydrogenation from Molecular σ-Alkane Complexes

Alasdair I. McKay,[1] Alexander J. Bukvic,[1] Bengt E. Tegner,[2] Arron L. Burnage,[2] Antonio J. Martinez-Martinez,[1] Nicholas H. Rees,[1] Stuart A. Macgregor,[2]* Andrew S. Weller.[1]*

[1] *Department of Chemistry, Chemistry Research Laboratories, University of Oxford, OX1 3TA, U.K. Email: andrew.weller@chem.ox.ac.uk*

[2] *Institute of Chemical Sciences, Heriot-Watt University, Edinburgh, EH14 4AS, UK. Email: S.A.Macgregor@hw.ac.uk*

TABLE OF CONTENTS

S.1. Experimental details

S.1.1. General Methods

All manipulations (unless otherwise stated) were performed under an atmosphere of argon, using standard Schlenk techniques on a dual vacuum/inlet manifold or by employment of an MBraun glovebox. Glassware was dried in an oven at 130°C overnight prior to use. Pentane, benzene and dichloromethane (abbreviated as CH_2Cl_2) were dried using an MBraun SPS-800 solvent purification system and degassed by three freeze-pump-thaw cycles. 1,2-$F_2C_6H_4$ (abbreviated as $F_2C_6H_4$) was stirred over Al_2O_3 for two hours then over CaH_2 overnight before being vacuum distilled and subsequently degassed by three freeze- pump-thaw cycles. d_2-dichloromethane (abbreviated to CD_2Cl_2) and d_3-acetonitrile (abbreviated to d_3-MeCN) was dried by stirring over CaH_2 overnight before being vacuum distilled onto 3 Å molecular sieves and subsequently degassed by three freeze-pump-thaw cycles. d_6-Benzene (abbreviated as C_6D_6) was stirred over Na pieces overnight before being vacuum distilled onto 3 Å molecular sieves and subsequently degassed by three freeze-pump-thaw cycles. Isobutene and Isobutane was purchased from CK Gases and used as received. All other chemicals were purchased from commercial vendors and used as received.

$[Rh(Cy_2PCH_2CH_2PCy_2)(C_6H_4F_2)][BAr^F{}_4]$[S1] **$[1\text{-}C_6H_4F_2][BAr^F{}_4]$**, $[Rh(Cy_2PCH_2CH_2PCy_2)(NBD)][BAr^F{}_4]$[S2] (NBD = norbornadiene) **$[1\text{-}NBD][[BAr^F{}_4]$** and $[Rh(Cy_2PCH_2CH_2PCy_2)(NBA)][BAr^F{}_4]$[S2] (NBA = norborane) **$[1\text{-}NBA][BAr^F{}_4]$** were prepared by the literature procedures.

Solution NMR data were collected on either a Bruker AVD 500 MHz or a Bruker Ascend 400 MHz spectrometer at room temperature unless otherwise started. Non-deuterated solvents were locked to standard external CD_2Cl_2 solutions. Residual protio solvent resonances were used as a reference for ^1H NMR spectra. ^2H NMR spectra were referenced to CD_2Cl_2 (δ 5.32). $^{31}P\{^1H\}$ NMR spectra were referenced externally to 85 % H_3PO_4 (D_2O). All chemical shifts (δ) are quoted in ppm and coupling constants in Hz.

Solid state NMR (SSNMR) samples were prepared packing powdered microcrystalline sample into either a 3.2 mm or 4 mm zirconia solid state rotor inside an argon filled glove box. SSNMR spectra were obtained on a Bruker Avance III HD spectrometer equipped with a 9.4 Tesla magnet, operating at 100.6 MHz for ^{13}C and 162 MHz for ^{31}P, respectively, and a MAS rate of 10 kHz. Relaxation time for ^{1}H and contact time for ^{31}P{^{1}H} CP/MAS, ^{13}C{^{1}H} CP/MAS, ^{13}C{^{1}H} NQS and FSLG-HETCOR NMR experiments were optimized for each compound as appropriate. All ^{13}C{^{1}H} CP/MAS spectra were referenced to adamantane (up field methine resonance, δ 29.5)[S3] on a scale where δ (TMS) = 0 as a secondary reference. The temperature for Variable Temperature (VT) NMR experiments at low temperatures was externally calibrated using lead nitrate ($PbNO_3$). The ^{1}H chemical shifts obtained from ^{1}H/^{13}C Frequency Switched Lee-Goldburg HETCOR SSNMR spectra were referenced internally to the *p*-ArH resonance of the $[BAr^F_4]^-$ (δ = 7.12).[S4]

Gas phase ^{1}H NMR spectroscopy was carried out using a Bruker Ascend 400 MHz spectrometer. The spectrometer was pre-locked and shimmed to a separate CD_2Cl_2 sample in a similar bore tube. The T1 delay was set to 1 s, and this has been previously shown to allow for the accurate comparison of integrals.[S5]

Electrospray ionization mass spectrometry (ESI-MS) was carried out using a Bruker MicrOTOF instrument directly connected to a modified Innovative Technology glovebox. [S6] Typical acquisition parameters were used (sample flow rate: 4 μL min^{-1}, nebulizer gas pressure: 0.4 bar, drying gas: Argon at 333 K flowing at 4 L min^{-1}, capillary voltage: 4.5 kV, exit voltage: 60 V). The spectrometer was calibrated using a mixture of tetraalkyl ammonium bromides $[N(C_nH_{2n+1})_4]Br$ (n = 2-8, 12, 16 and 18). Samples were diluted to a concentration of 1×10^{-6} M in the appropriate solvent before sampling by ESI-MS.

Gas Chromatography Electron Ionization-Mass Spectrometry (GC EI-MS) analyses were performed on an Agilent 7200 quadrupole time of flight (Q-ToF) instrument equipped with a 7890B gas chromatograph and a PAL auto-sampler fitted with a 2.5 mL headspaces syringe. Instrument control and data processing were performed using Agilent MassHunter software. The system was calibrated within 1 hour prior to the analysis and its mass accuracy with external calibration (as used for these experiments) is better than 5 ppm for 2 hours following calibration. Samples were prepared in 20 mL headspace vials. Vials were incubated at 35 °C for 30 seconds before a 2.5 mL sample of the headspace was taken and injected into the GC inlet (headspace syringe was held at 40°C). The GC-inlet was operated in split mode held at 300 °C with a 2:1 split. The column was a Restek RT Q-Bond 30 m x 320 µm with at 10 µm film thickness. The oven was held at 40 °C for 4 min then ramped at 20 °C/min to 300 and held for 3 min. Column flow rate was 1 mL/min. Mass spectrometer was operated in EI mode and with the ionization energy set to 20 eV.

Elemental analyses were conducted by Mr. Stephan Boyer at London Metropolitan University.

S.2. Synthetic procedures

S.2.1. [Rh($Cy_2PCH_2CH_2PCy_2$)(C_4H_8)][BAr^F_4], [1-C_4H_8][BAr^F_4]

S.2.1.1. Synthesis of [1-C_4H_8][BAr^F_4]

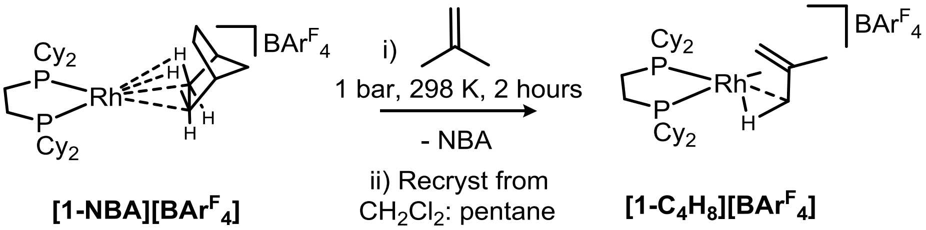

[1-NBA][BAr^F_4] **[1-C_4H_8][BAr^F_4]**

To an orange sample of crystalline **[1-NBA][BAr^F_4]** (200 mg, 135 μmol) in an evacuated (< 3 × 10^{-2} mbar) J Young flask (~ 50 mL) isobutene gas (1 bar, 298 K) was added and left to stand for 2 hours, to form [Rh($Cy_2PCH_2CH_2PCy_2$)(C_4H_8)][BAr^F_4], **[1-C_4H_8][BAr^F_4]**. After this time, working under an atmosphere of isobutene (1 bar) and at -78 °C in an acetone/dry ice bath, the sample was dissolved in CH_2Cl_2 (3 mL), filtered *via* cannula and layered with pentane (25 mL) at the same temperature. The solution was warmed to ambient temperature and after 3 days yielded orange block like crystals suitable for single crystal x-ray diffraction. Yield: 169 mg (86 %). The crystalline material is stored in a glove box in a freezer operating at -25 °C.

Note: CH_2Cl_2 and pentane used in this preparation were freeze-pump-thawed degassed three times and then saturated and stored with isobutene gas (1 bar) prior to use. When solvents were left under an argon atmosphere, ~ 50 % decomposition of **[1-C_4H_8][BAr^F_4]** to **[1-BAr^F_4]**[S2] occurs in 2 hours.

S.2.1.2. Characterization data for [1-C_4H_8][BAr^F_4]

^{1}H NMR (CD_2Cl_2, 298 K, 400 MHz): δ 7.72 (s, 8H, ortho-ArH), 7.55 (s, 4H, para-ArH), 2.09-1.64 (br m, 28H, overlapping aliphatic CH), 1.61-1.42 (br s, 8H, aliphatic CH), 1.40-1.0.96 (br m, 20H, overlapping aliphatic CH).

^{1}H NMR (CD_2Cl_2, 183 K, 400 MHz): δ 7.75 (s, 8H, ortho-ArH), 7.56 (s, 4H, para-ArH), 3.75 (br s, ~ 2H, alkene CH), 2.09-1.64 (br m, ~ 30H, overlapping aliphatic CH), 1.40-1.09 (br m, ~ 20H, overlapping aliphatic CH), -0.15 (br, CH_3).

Note: The low temperature limit was not reached at 183K in the ^{1}H NMR spectrum' so integrated values are approximate. NMR samples prepared under argon and immediately run after preparation.

^{31}P{^{1}H} NMR (CD_2Cl_2, 298 K, 162 MHz): δ 95.3 (d, J_{RhP} 179 Hz).

^{31}P{^{1}H} NMR (CD_2Cl_2, 183 K, 162 MHz): δ 97.6 (dd., J_{RhP} 201 Hz, J_{PP} 26 Hz *trans to agostic interaction*), 93.6 (d. of d., J_{RhP} 158 Hz, J_{PP} 26 Hz *trans to alkene*).

^{19}F{^{1}H} NMR (CD_2Cl_2, 298 K, 377 MHz): δ -62.9 (s).

^{13}C{^{1}H} NMR (CD_2Cl_2, 298 K, 126 MHz): δ 161.1 (1:1:1:1 q, J_{CB} 50 Hz, ipso-ArC), 134.6 (s, ortho-ArC), 128.8 (q, J_{CF} 32 Hz, meta-ArC), 124.8 (q, J_{CF} 272 Hz, CF_3), 117.3 (s, para-ArC), 53.8 (qu. CD_2Cl_2), 37.3 (s, cyclohexyl-CH), 30.9 (s, cyclohexyl-CH_2), 29.9 (s, cyclohexyl-CH_2), 29.6 (s, cyclohexyl-CH_2), 29.2 (s, cyclohexyl-CH_2), 26.5 (cyclohexyl-CH_2), 25.7 (cyclohexyl-CH_2), 25.3 (cyclohexyl-CH2), 22.1 (s, cyclohexyl-CH_2).

^{13}C{^{1}H} NMR (CD_2Cl_2, 183 K, 126 MHz): δ 161.1 (1:1:1:1 q, J_{CB} 50 Hz, ipso-ArC), 134.6 (s, ortho-ArC), 128.8 (q, J_{CF} 32 Hz, meta-ArC), 124.8 (q, J_{CF} 272 Hz, CF_3), 117.3 (s, para-ArC), 111.5 (br s, alkene-CH), 72.6 (br s, alkene-CH), 53.8 (qu. CD_2Cl_2), 36.7 (br s.), 35.2 (br s.), 31.1 (s, cyclohexyl-CH_2), 29.4 (m, cyclohexyl-CH_2), 25.6 (s, cyclohexyl-CH_2), 24.9 (s, cyclohexyl-CH_2), 24.3 (s, cyclohexyl-CH_2), 22.2 (s, cyclohexyl-CH_2), 19.4 (br. s).

^{31}P{^{1}H} SSNMR (162 MHz, 158 K, 10 kHz spin rate): δ 94.8 (br m, *coincident environments*).

$^{13}C\{^1H\}$ SSNMR (101 MHz, 158K, 10 kHz spin rate): δ 161.1 (ipso-ArC), 131.2 (ortho-ArC), 127.4 (meta-ArC), 122.9 (br, CF_3), 115.6 (para-ArC), 113.1 (para-ArC), 108.6 (**C**=CH_2), 70.6 (C=**C**H_2), 35.7, 34.3, 31.2, 29.8, 27.5, 24.1, 22.7, 21.9, 15.7.

Note: Signals at 108.6 and 70.6 disappeared upon addition of H_2, to form **[1-C_4H_{10}][$BAr^F{}_4$]**. The agostic –CH_3 could not be unambiguously identified, see section S.2.2.

ESI-MS: Not stable under mass spectrometric conditions (20eV, 333K). Species with appropriate isotopic distributions at m/z found = 581.240, calculated to $[(Cy_2PCH_2CH_2PCy_2)Rh(N_2)_2]^+$ (581.242). There is no evidence for the nitrogen compound in bulk samples so it is assumed to form via an in-situ ESI-MS process.

Elemental analysis found (calc. for $C_{62}H_{68}BF_{24}P_2Rh$): C 52.39 (51.54), H 4.87 (4.74).

S.2.1.3. NMR spectra of $[1\text{-}C_4H_8][BAr^F_4]$

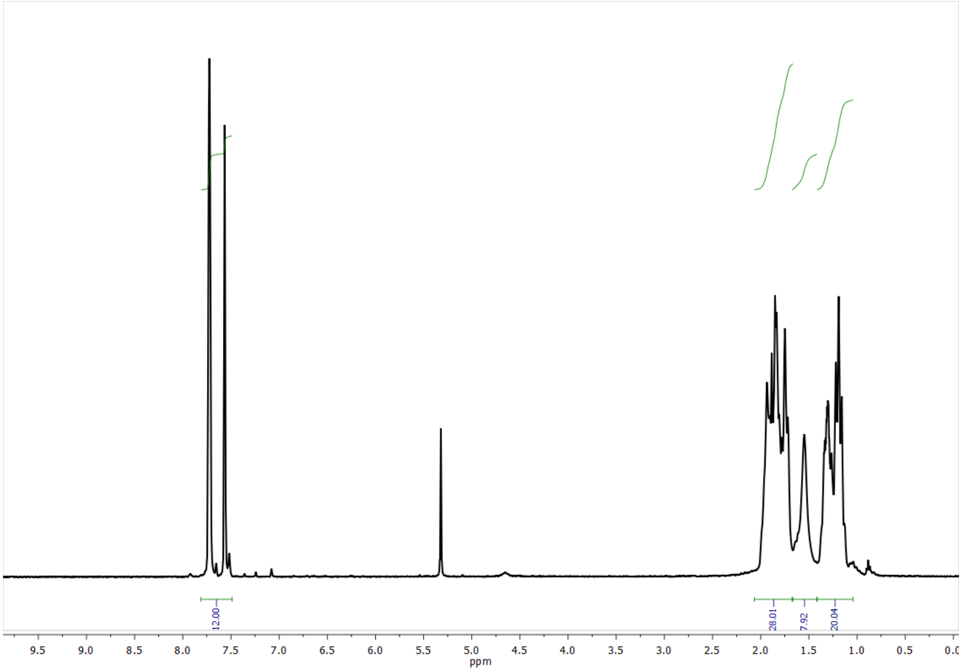

Figure S1: The solution ^{1}H NMR (CD_2Cl_2, 298 K, 400 MHz) spectrum of **$[1\text{-}C_4H_8][BAr^F_4]$**.

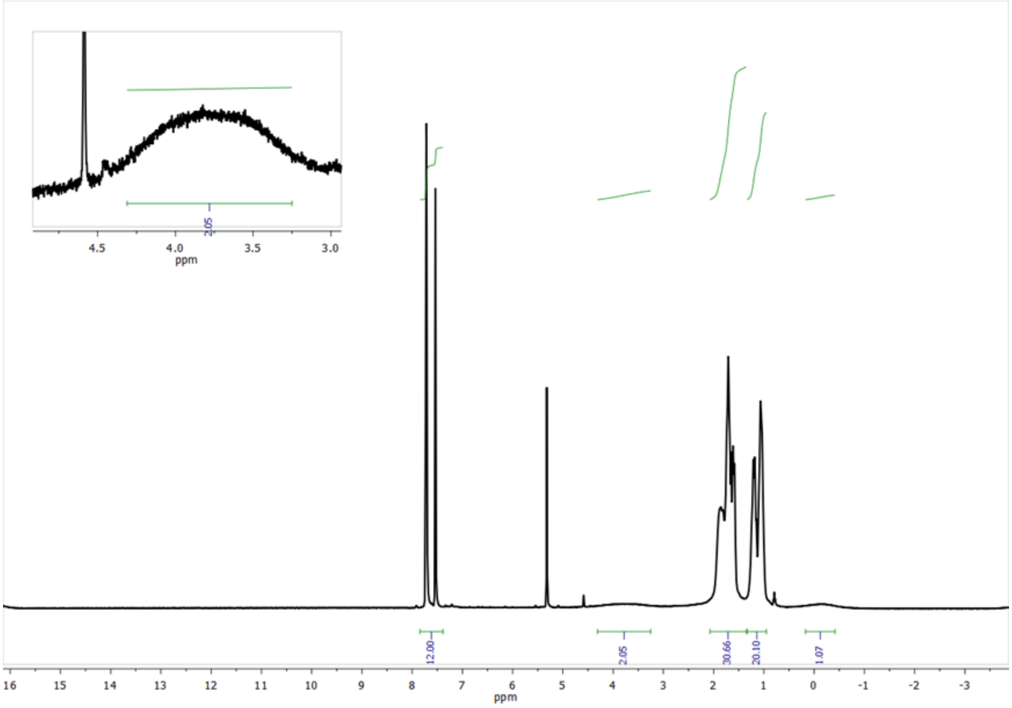

Figure S2: The solution ^{1}H NMR (CD_2Cl_2, 183 K, 400 MHz) spectrum of **$[1\text{-}C_4H_8][BAr^F_4]$**. The low temperature limit was not reached at 183K, so integrated values are approximate.

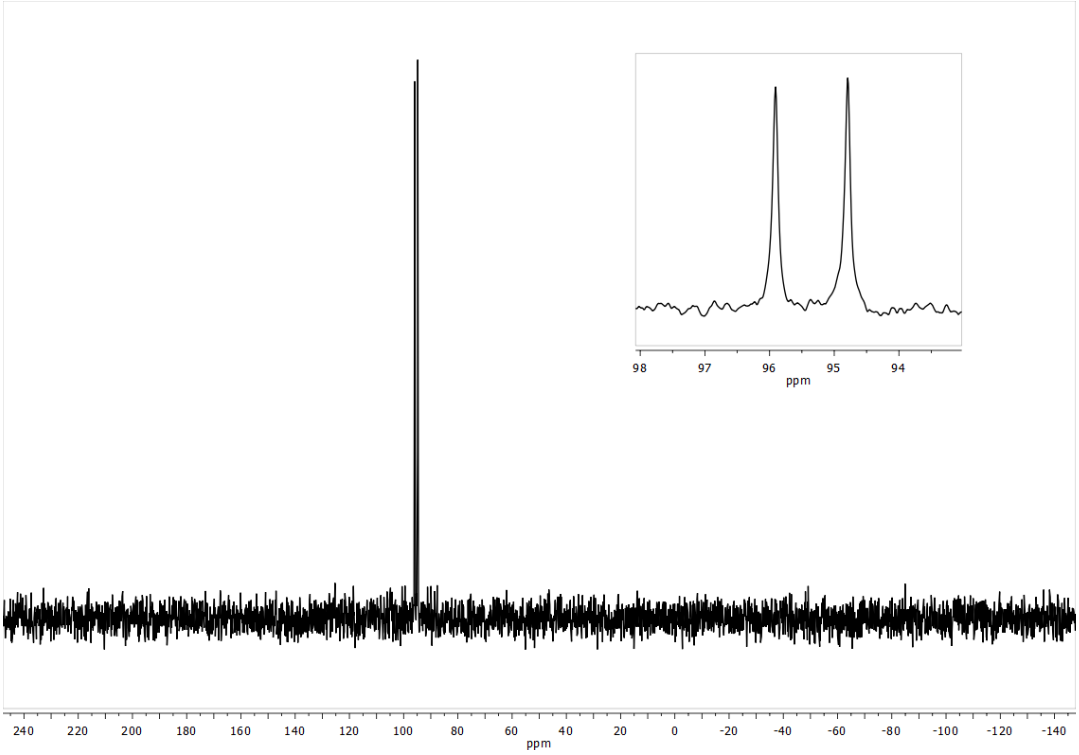

Figure S3: The solution $^{31}P\{^1H\}$ NMR (CD_2Cl_2, 298 K, 162 MHz) spectrum of **[1-C_4H_8][$BAr^F{}_4$]**.

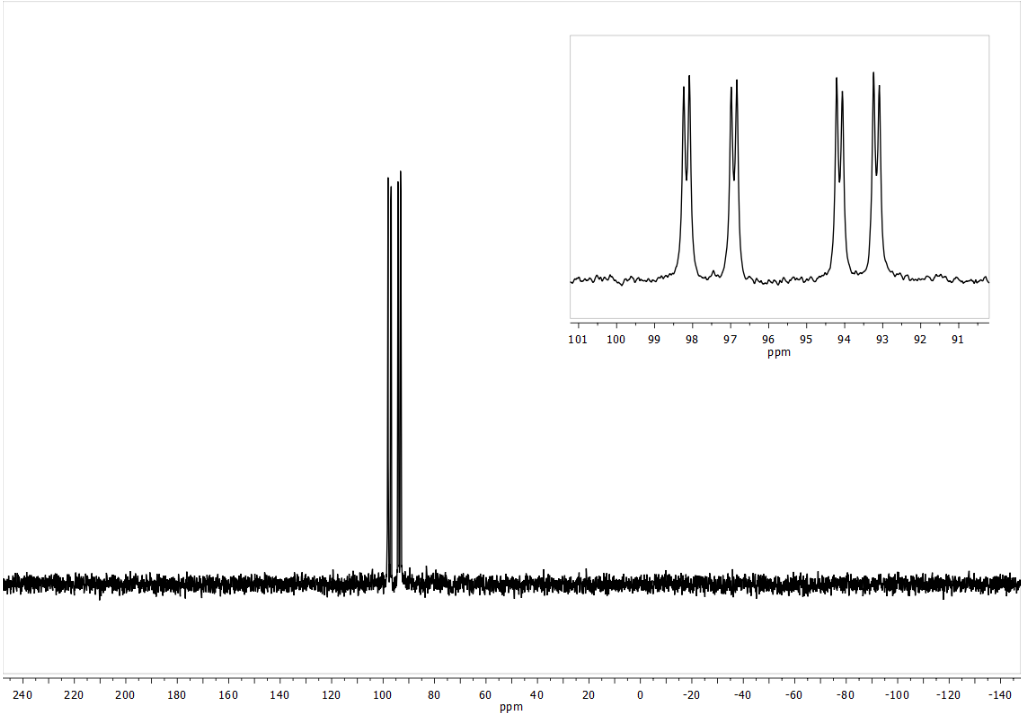

Figure S4: The solution $^{31}P\{^1H\}$ NMR (CD_2Cl_2, 183 K, 162 MHz) spectrum of **[1-C_4H_8][$BAr^F{}_4$]**.

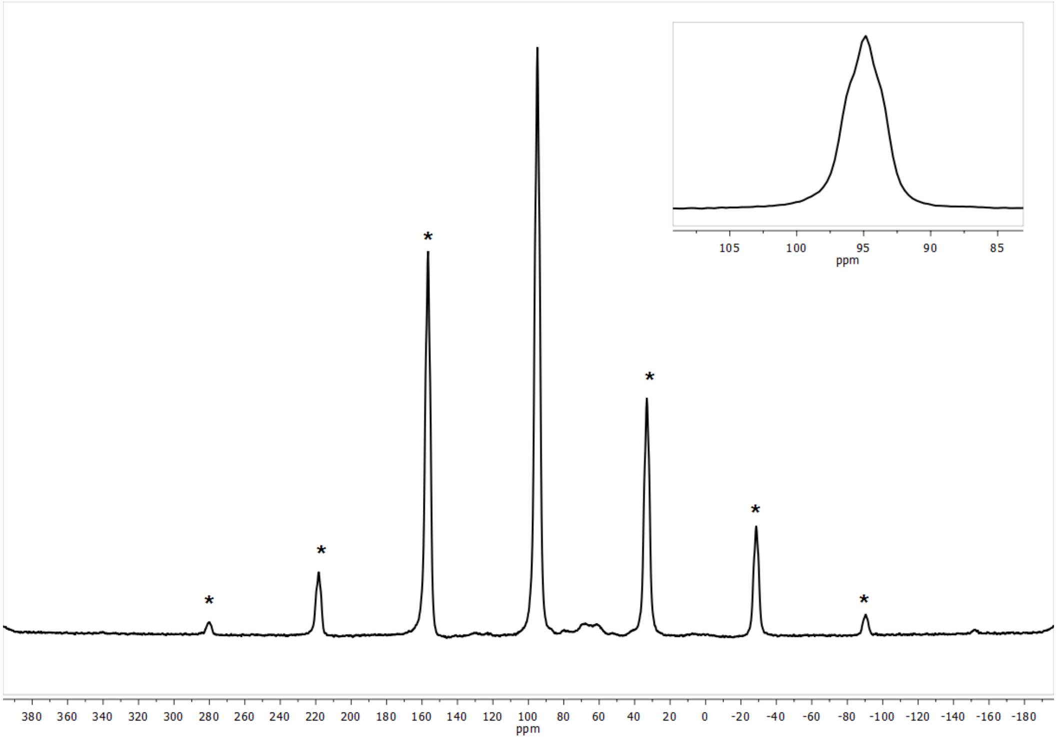

Figure S5: The $^{31}P\{^1H\}$ SSNMR (162 MHz, 158 K, 10 kHz spin rate) spectrum of **[1-C_4H_8][BAr$^F{}_4$].** The resonances marked * are due to spinning sidebands.

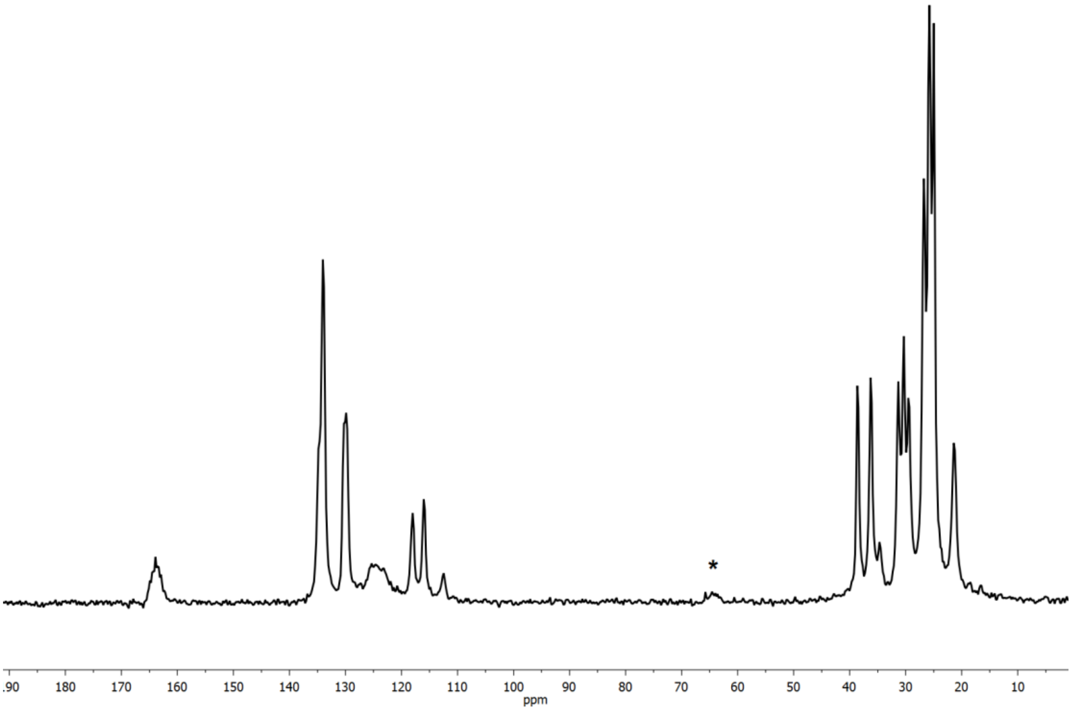

Figure S6: The $^{13}C\{^1H\}$ SSNMR (101 MHz, 298 K, 10 kHz spin rate) spectrum of **[1-C_4H_8][BAr$^F{}_4$]**. The resonances marked ***** are due to spinning sidebands.

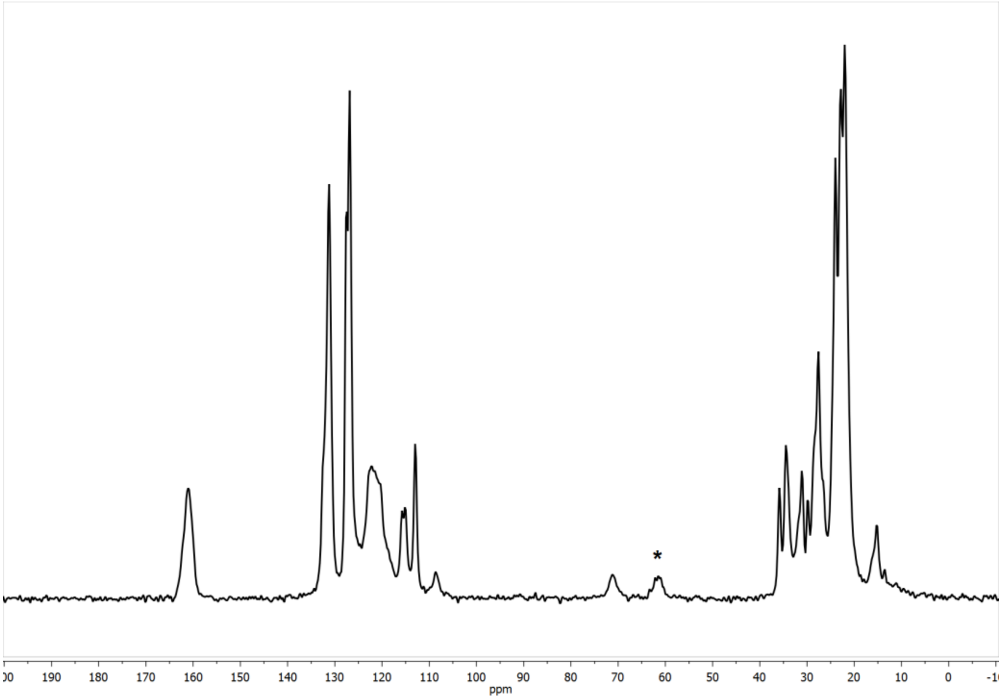

Figure S7: The $^{13}C\{^1H\}$ SSNMR (101 MHz, 158 K, 10 kHz spin rate) spectrum of **[1-C_4H_8][BAr$^F{}_4$]**. The resonances marked * are due to spinning sidebands.

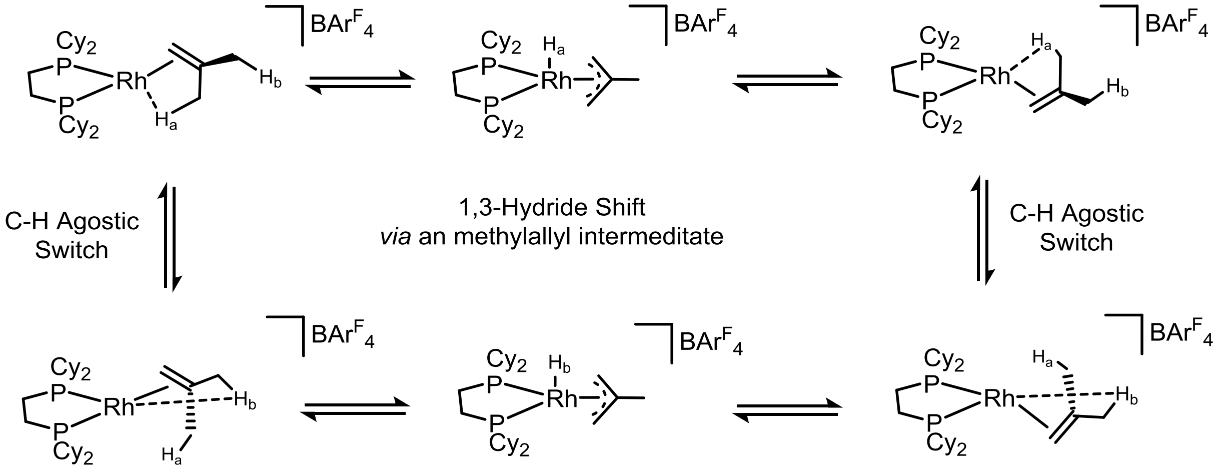

Figure S8: Proposed structural diagrams of the species and mechanism of the fluxional nature of the isobutene ligand of **[1-C_4H_8][BAr$^F{}_4$]**, in both solution and solid-states.

S.2.2. [Rh(Cy$_2$PCH$_2$CH$_2$PCy$_2$)(C$_4$H$_{10}$)][BAr^F$_4$], [1-C$_4$H$_{10}$][BAr^F$_4$]

S.2.2.1. Synthesis of [1-C$_4$H$_{10}$][BAr^F$_4$] for an x-ray diffraction study

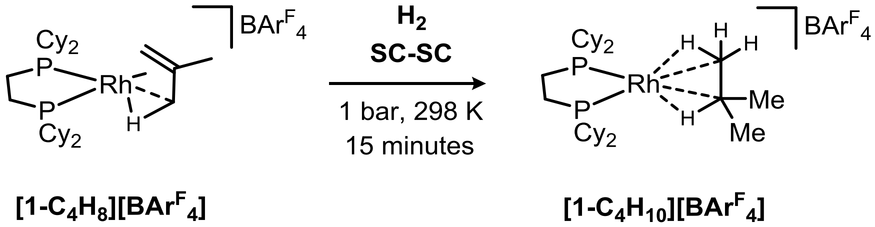

Orange crystals of **[1-C$_4$H$_8$][BAr^F$_4$]** were treated with H$_2$ (1 bar, 298 K, 15 mins) inside a J Young flask. The color of the crystals immediately turned a dark red. The crystalline material was then coated with Fomblin® Y oil under an argon-flush; a suitable crystal was rapidly selected and then transferred to the Cryostream of a diffractometer and an x-ray diffraction study was undertaken. For further details of structural refinement please refer to section S.5.

S.2.2.2. Synthesis of [1-C$_4$H$_{10}$][BAr^F$_4$] for SSNMR characterization

A powdered microcrystalline sample of **[1-C$_4$H$_8$][BAr^F$_4$]** (35 mg) was packed in a 3.2 mm SSNMR rotor, inside an argon filled glove box. The rotor was then placed in a custom built glass J Young flask [S7] and the sample was then exposed to H$_2$ (1 bar, 298 K). After 15 minutes, the rotor cap was fitted under a flush of H$_2$. The sample was immediately transferred to the bore of a pre-cooled (158 K) SSNMR spectrometer (~ 10 mins) and analyzed ^{31}P{^{1}H} and ^{13}C{^{1}H} solid state NMR spectroscopy.

These conditions were optimized to form **[1-C$_4$H$_{10}$][BAr^F$_4$]**. At 158K, no onward reactivity with H$_2$ is observed. When H$_2$ replaced by argon at 298K, as so the rotor is packed under an argon atmosphere, dehydrogenation to re-form **[1-C$_4$H$_8$][BAr^F$_4$]** is observed before cooling to 158K, see section S.4.1.1.

Further exposure to H$_2$ (90 mins) at 298 K results in complete decomposition to **[1-BAr^F$_4$]**, see section S.2.2.6.

S.2.2.3. Characterization data for [1-C_4H_{10}][$BAr^F{}_4$]

$^{31}P\{^1H\}$ SSNMR (162 MHz, 298K, 10 kHz spin rate): δ 106.4 (br m).

$^{31}P\{^1H\}$ SSNMR (162 MHz, 158 K, 10 kHz spin rate): δ 106.8 (br, environments overlapping)

$^{13}C\{^1H\}$ SSNMR (101 MHz, 158 K, 10 kHz spin rate): δ 160.5 (ArC), 132.9 (ArC), 127.1 (ArC), 121.6 (br, CF_3), 114.9 (ArC), 112.8 (ArC), 35.0, 32.1, 27.9, 22.8, 17.3, 15.9 (multiple aliphatic resonances).

^1H projection from $^1H/^{13}C$ FSLG HETCOR SSNMR (10 kHz spin rate, 158 K): δ 9.81 (br), 7.12 (br), 0.7 (br), -3.4 (br).

S.2.2.4. Solid State NMR spectra of [1-C_4H_{10}][BAr$^F{}_4$]

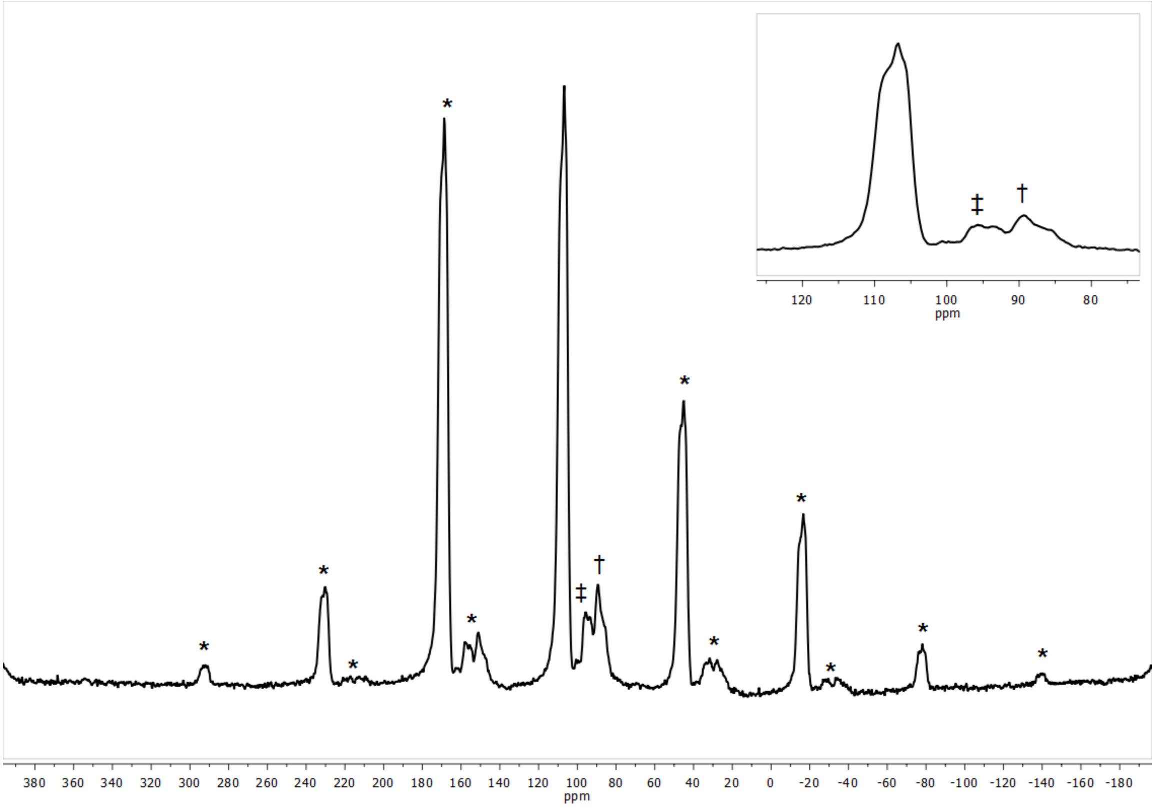

Figure S9: The $^{31}P\{^1H\}$ SSNMR (162 MHz, 158 K, 10 kHz spin rate) spectrum of **[1-C_4H_{10}][BAr$^F{}_4$]** prepared in situ after 15 mins under H_2 at 298K.

The resonances marked ‡ are assigned to **[1-C_6H_8][BAr$^F{}_4$]** from either incomplete hydrogenation or dehydrogenation of **[1-C_4H_{10}][BAr$^F{}_4$]** at 298K. The resonances marked † are assigned to an **[1-BAr$^F{}_4$]** decomposition product under H_2 at 298K. The resonances marked ***** are due to spinning sidebands. The inset is an enlargement of the central resonances.

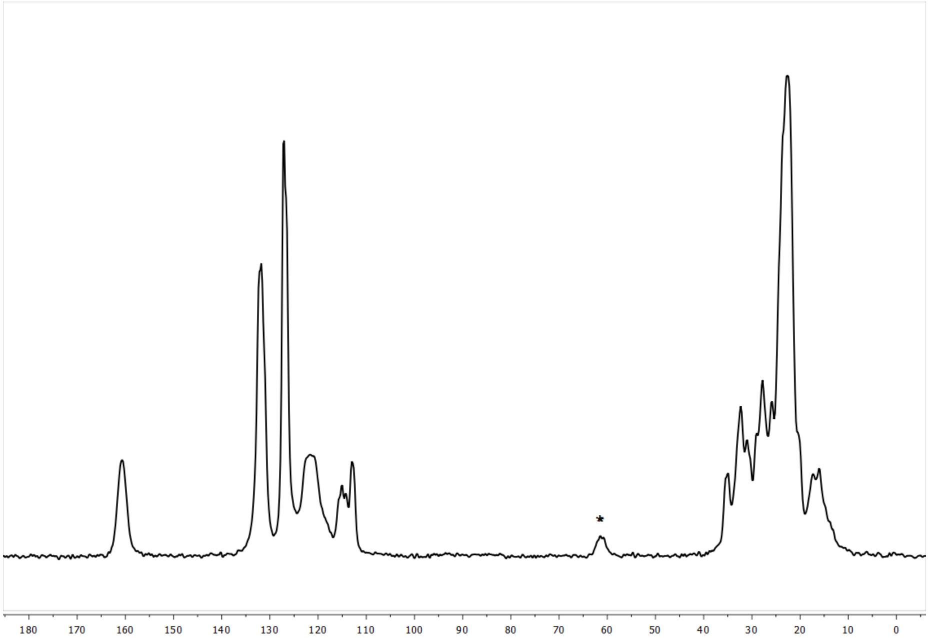

Figure S10: The $^{13}C\{^1H\}$ SSNMR (100 MHz, 158 K, under H_2, 10 kHz spin rate) spectrum of **[1-C_4H_{10}][BAr$^F{}_4$]** prepared in situ at time of measuring. The resonance marked * is due to a spinning sideband.

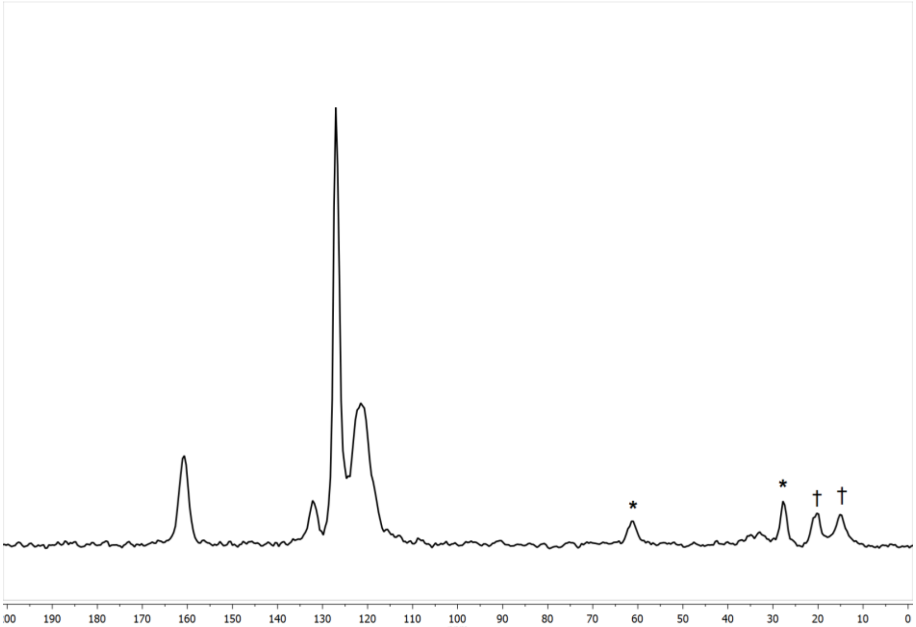

Figure S11: The $^{13}C\{^1H\}$ NQS SSNMR (100 MHz, 203 K, 10 kHz spin rate) spectrum of **[1-C_4H_{10}][BAr$^F{}_4$]** prepared in situ. The resonances marked * are due to spinning sidebands. Peaks marked † at δ ~ 21 and δ ~ 15 are assigned to the C_4H_{10} fragment undergoing motion at 203 K.

Note: When $^{13}C\{^1H\}$ NQS SSNMR was ran at 158 K; the peaks marked † are absent, suggesting freezing out of any motion.

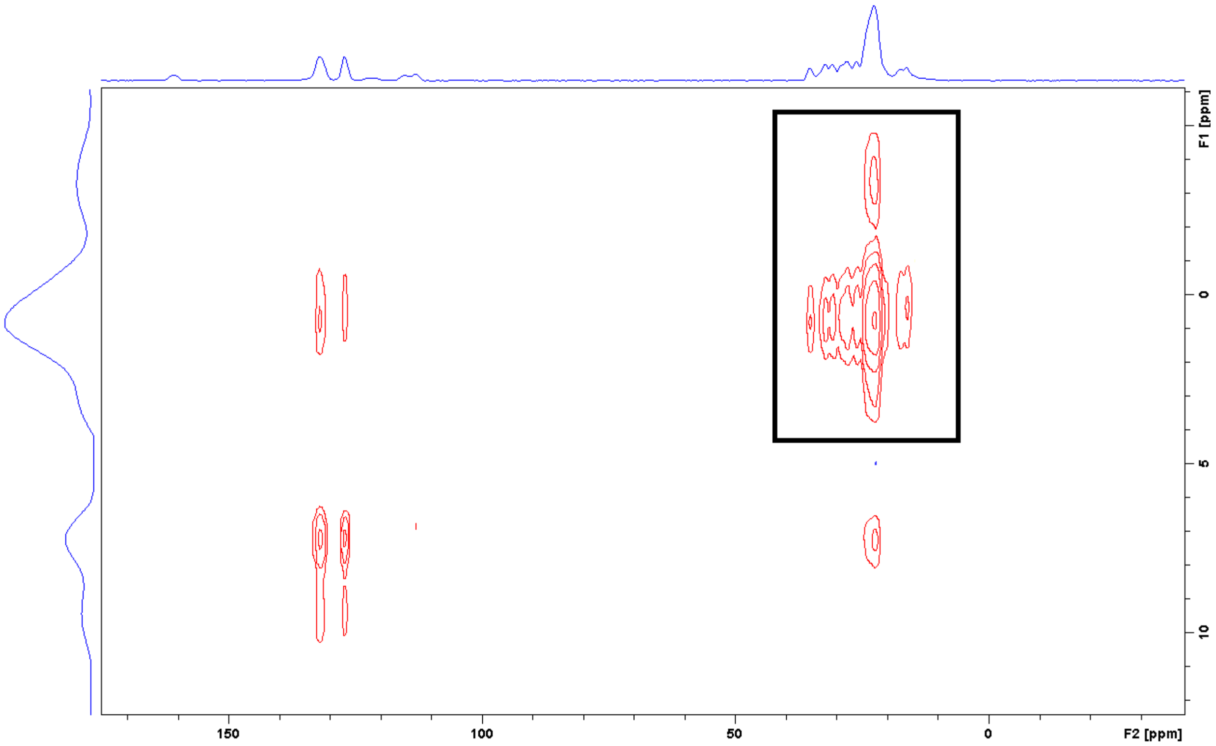

Figure S12: The ^{1}H/^{13}C FSLG HETCOR SSNMR (158 K, 10 kHz spin rate) full spectrum of **[1-C_4H_{10}][BAr$^F{}_4$]**. Enlargement of the alkyl region, shown by the black box, is shown below in Figure S13.

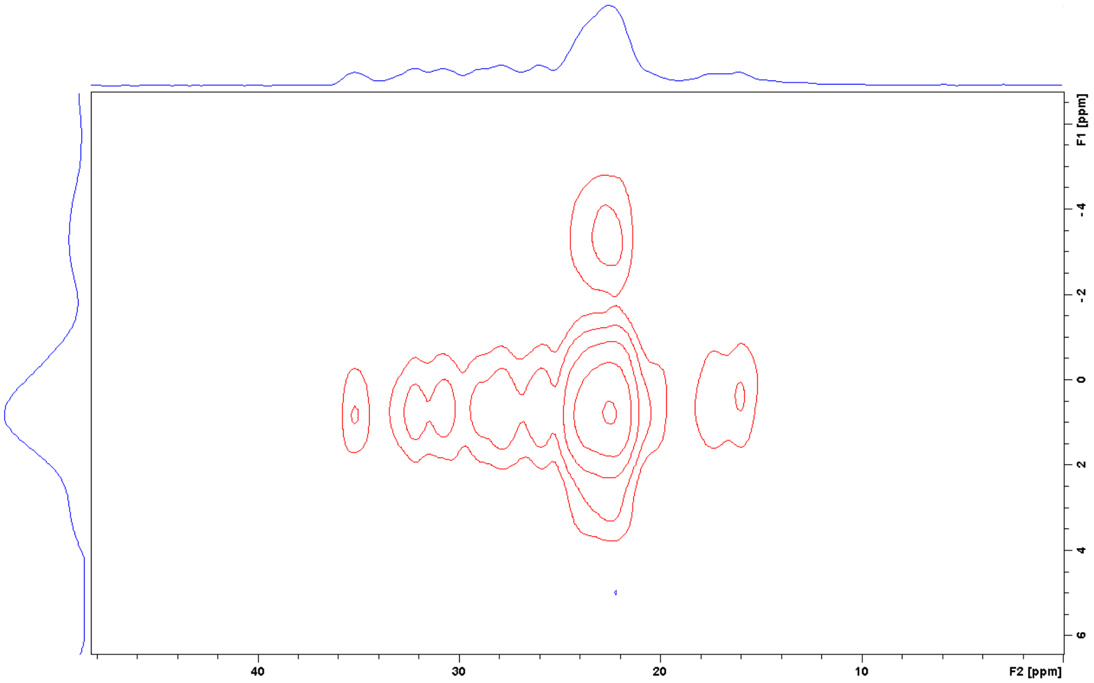

Figure S13: Enlargement of the ^{1}H/^{13}C FSLG HETCOR SSNMR (158 K, 10 kHz spin rate) spectrum of the alkyl region of **[1-C_4H_{10}][BAr$^F{}_4$]**.

S.2.2.5. Liberation of the bound isobutane from **[1-C_4H_{10}][BAr^F_4]**.

Orange crystals of **[1-C_4H_8][BAr^F_4]** (20 mgs) were treated with H_2 (1 bar, 298 K, 15 mins) inside a J Young flask. The color of the crystals immediately turned a dark red, yielding **[1-C_4H_{10}][BAr^F_4]**. The solid was then cooled to 77 K under liquid nitrogen and the J Young flask placed under vacuum to remove any H_2. CO (1 bar, 298K) was added and solid left for 1 hour; to which a vibrant yellow solid material had formed. The volatiles excluded from the lattice could be distilled into a fresh NMR tube with d_3-MeCN and analyzed by ^{1}H NMR spectroscopy.

^{1}H NMR (d_3-MeCN, 400 MHz): δ 1.72 (decet, 1H, $\underline{C}H(CH_3)_3$, J_{H-H} = 6.79 Hz), 0.89 (doublet, 9H, $CH(\underline{C}H_3)_3$, J_{H-H} = 6.79 Hz).

The resultant solid was confirmed to be [Rh(dcpe)$(CO)_2$][BAr^F_4] by solution ^{31}P{^{1}H} NMR spectroscopy (δ 85.22, d, J_{RhP} = 116 Hz).[S7]

S.2.2.6. Solid state decomposition products of [1-C_4H_{10}][$BAr^F{}_4$] under H_2

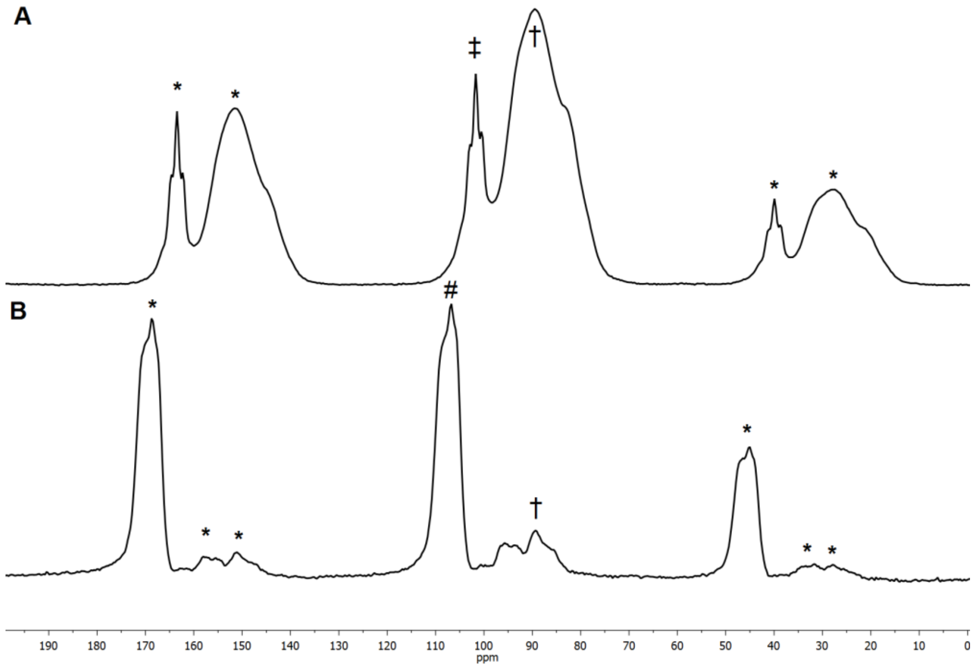

Figure S14: (A) The $^{31}P\{^1H\}$ SSNMR (162 MHz, 158 K, 10 kHz spin rate) spectrum of **[1-C_4H_{10}][$BAr^F{}_4$]** left in situ under an H_2 atmosphere at 298K for 90 mins. The peak assigned to † is the main decomposition product under H_2, **[1-$BAr^F{}_4$]**[S2] (approx. 70 %) and ‡ is an unidentified complex under H_2 (approx. 30 %).

(B) Repeat of Figure S9, showing the $^{31}P\{^1H\}$ SSNMR (162 MHz, 158 K, 10 kHz spin rate) spectrum, where # = **[1-C_4H_{10}][$BAr^F{}_4$]**, to show no signals in (A) relating to **[1-C_4H_{10}][$BAr^F{}_4$]** are present after hydrogenation for 90 mins.

S.2.3. [Rh(Cy$_2$PCH$_2$CH$_2$PCy$_2$)(C$_6$H$_8$)][BAr$^F{}_4$], [1-C$_6$H$_8$][BAr$^F{}_4$]

S.2.3.1. Synthesis of [1-C$_6$H$_8$][BAr$^F{}_4$]

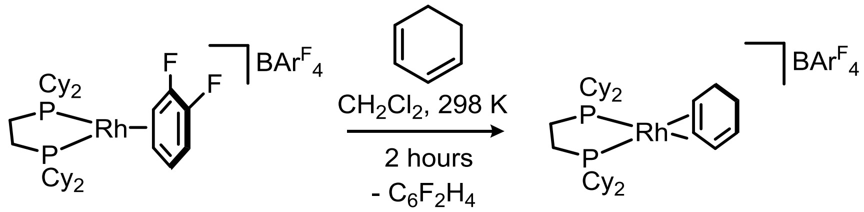

[1-C$_6$F$_2$H$_4$][BAr$^F{}_4$] **[1-C$_6$H$_8$][BAr$^F{}_4$]**

A solution of **[1-C$_6$H$_4$F$_2$][BAr$^F{}_4$]** (300 mg, 0.20 mmol) in CH$_2$Cl$_2$ (20 mL) was treated with 1,3-cyclohexadiene (200 µL) at ambient temperature. The resultant deep red solution was stirred at ambient temperature for 2 hours. Pentane (100 mL) was then added with vigorous stirring which resulted in the formation of a red precipitate. The solid was isolated by filtration, washed with pentane (2 × 20 mL) and then dried under vacuum. The solid was then dissolved in CH$_2$Cl$_2$ (~ 8 mL) and filtered. The filtrate was then layered with pentane. Deep red crystals were obtained upon storage at 4 °C after 1 week. Yield: 204 mg (70 %).

Note: **[1-C$_6$H$_8$][BAr$^F{}_4$]** displays poor stability in solution at room temperature, particularly at high concentrations. **[1-C$_6$H$_6$][BAr$^F{}_4$]** was identified as the major decomposition product (~ 50 %) as well as several other, as yet, unidentified species are also present. These are assumed to be the products of C-Cl activation from the solvent, as identified by ESI-MS.

S.2.3.2. Characterization data for [1-C_6H_8][BAr^F_4]

^{1}H NMR (CD_2Cl_2, 298 K, 400 MHz): δ 7.73 (s, 8H, ortho-ArH), 7.57 (s, 4H, para-ArH), 5.36-5.32 (br m, 5H, alkene CH and $CDHCl_2$), 2.16 (br s, 2H, aliphatic CH), 1.94-1.70 (br m, 28H, overlapping aliphatic CH), 1.61-1.58 (br m, 2H, aliphatic CH), 1.38-1.08 (br m, 16H, overlapping aliphatic CH), 0.99-0.96 (br m, 4H, overlapping aliphatic CH).

^{1}H NMR (CD_2Cl_2, 183 K, 400 MHz): δ 7.75 (s, 8H, ortho-ArH), 7.56 (s, 4H, para-ArH), 5.30-5.23 (br m, 4H, alkene), 2.11 (br s, 2H, aliphatic CH), 1.89-1.42 (br m, 30H, overlapping aliphatic CH), 1.31-0.74 (br m, 20H, overlapping aliphatic CH).

^{31}P{^{1}H} NMR (CD_2Cl_2, 298 K, 162 MHz): δ 78.7 (d, J_{RhP} 172 Hz).

^{31}P{^{1}H} NMR (CD_2Cl_2, 183 K, 162 MHz): δ 78.6 (d, J_{RhP} 172 Hz).

^{19}F{^{1}H} NMR (CD_2Cl_2, 298 K, 377 MHz): δ -62.9 (s).

^{13}C{^{1}H} NMR (CD_2Cl_2, 298 K, 126 MHz): δ 162.2 (q, J_{CB} 50 Hz, ipso-ArC), 135.3 (s, ortho-ArC), 129.3 (q, J_{CF} 32 Hz, meta-ArC), 125.1 (q, J_{CF} 272 Hz, CF_3), 117.9 (s, para-ArC), 95.0 (d, J_{CRh} 4.4 Hz, alkene-CH), 82.3 (m, alkene-CH), 37.9 (m, cyclohexyl-CH), 31.3 (s, cyclohexadiene-CH_2), 29.6 (m, cyclohexyl-CH_2), 29.1 (s, cyclohexyl-CH_2), 26.3 (m, PCH_2), 22.5 (m, cyclohexyl-CH_2), 21.1 (s, cyclohexyl-CH_2).

^{31}P{^{1}H} SSNMR (162 MHz, 294 K, 10 kHz spin rate): δ 78.6 (br m).

^{13}C{^{1}H} SSNMR (101 MHz, 294 K, 10 kHz spin rate): δ 163.9 (ipso-ArC), 133.9 (ortho-ArC), 130.0 (meta-ArC), 124.7 (br, CF_3), 117.8 (para-ArC), 116.0 (para-ArC), 95.8 (C=C), 94.1 (C=C), 83.3 (C=C), 80.7 (C=C), 37.7 (CH), 36.0 (CH), 31.4 (CH_2), 30.5 (CH_2), 29.5 (CH_2), 26.6 (CH_2), 25.3 (CH_2), 22.0 (CH_2), 21.1 (CH_2), 19.7 (CH_2), 18.7 (CH_2).

^{1}H projection from ^{1}H/^{13}C FSLG HETCOR SSNMR (10 kHz spin rate, 294 K): δ 7.1 (br), 3.9 (br), 0.5 (br).

ESI-MS found (calc. for [$Rh(Cy_2PCH_2CH_2PCy_2)(C_6H_8)$]$^+$): m/z 605.29 (605.29).

Elemental analysis found (calc. for $C_{64}H_{68}BF_{24}P_2Rh$): C 52.32 (52.33), H 4.52 (4.67).

S.2.3.3. NMR spectra of [1-C_6H_8][$BAr^F{}_4$]

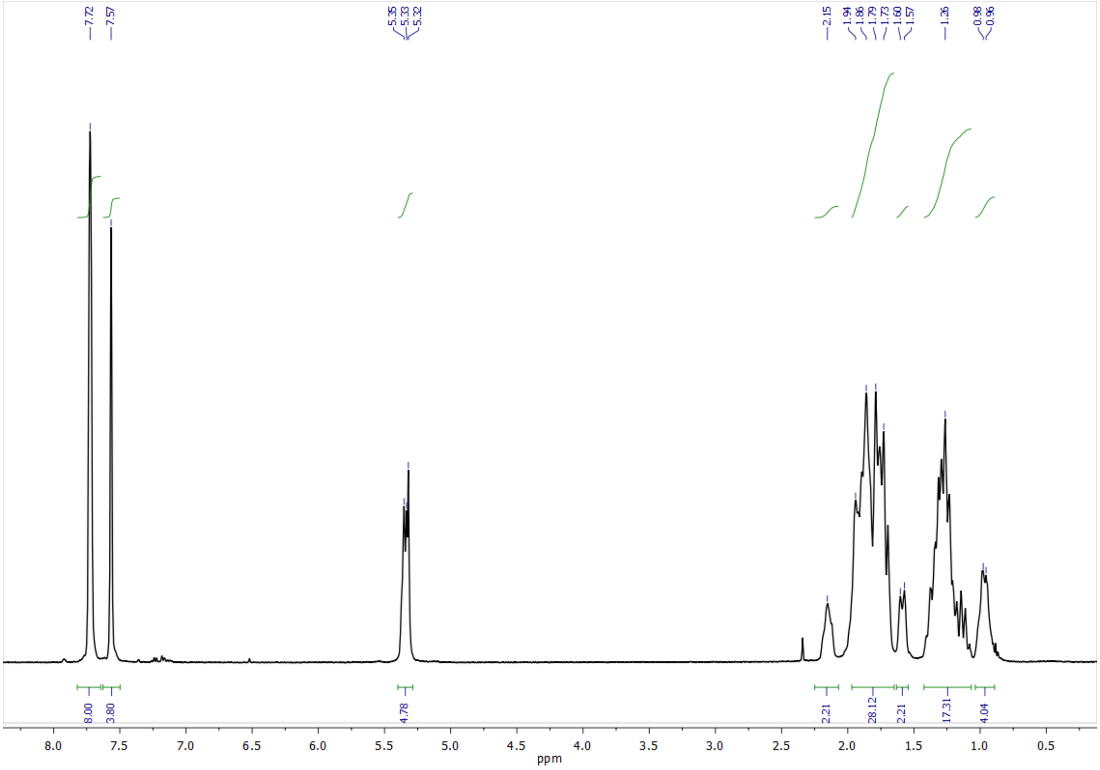

Figure S15: The solution ^{1}H NMR (CD_2Cl_2, 298 K, 400 MHz) spectrum of **[1-C_6H_8][$BAr^F{}_4$]**.

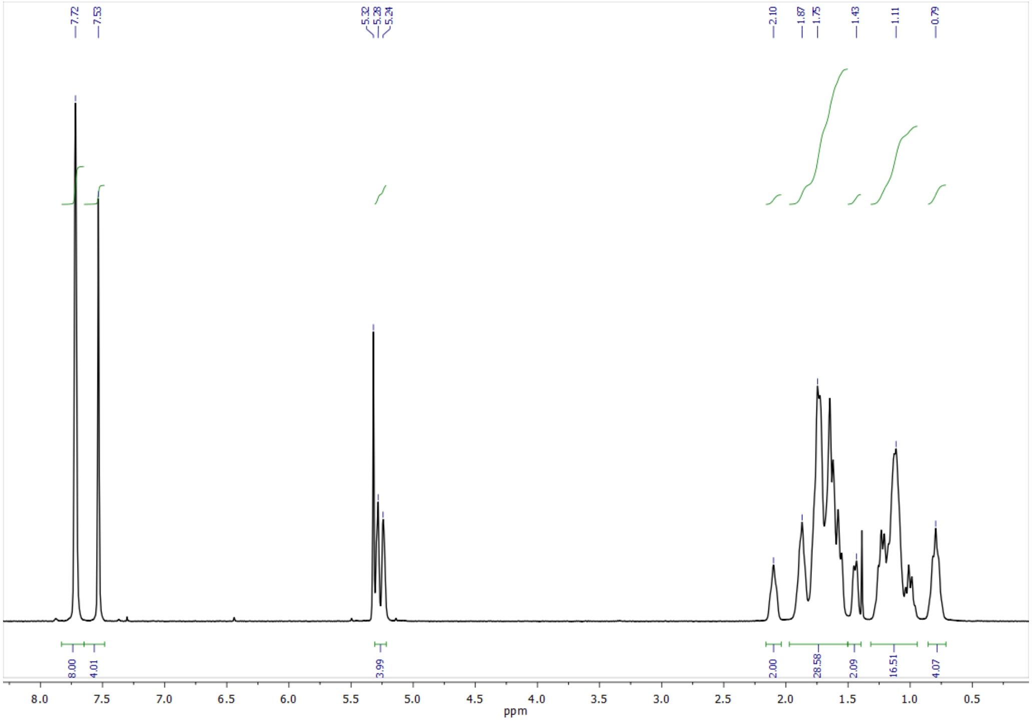

Figure S16: The solution ^{1}H NMR (CD_2Cl_2, 183 K, 400 MHz) spectrum of **[1-C_6H_8][$BAr^F{}_4$]**.

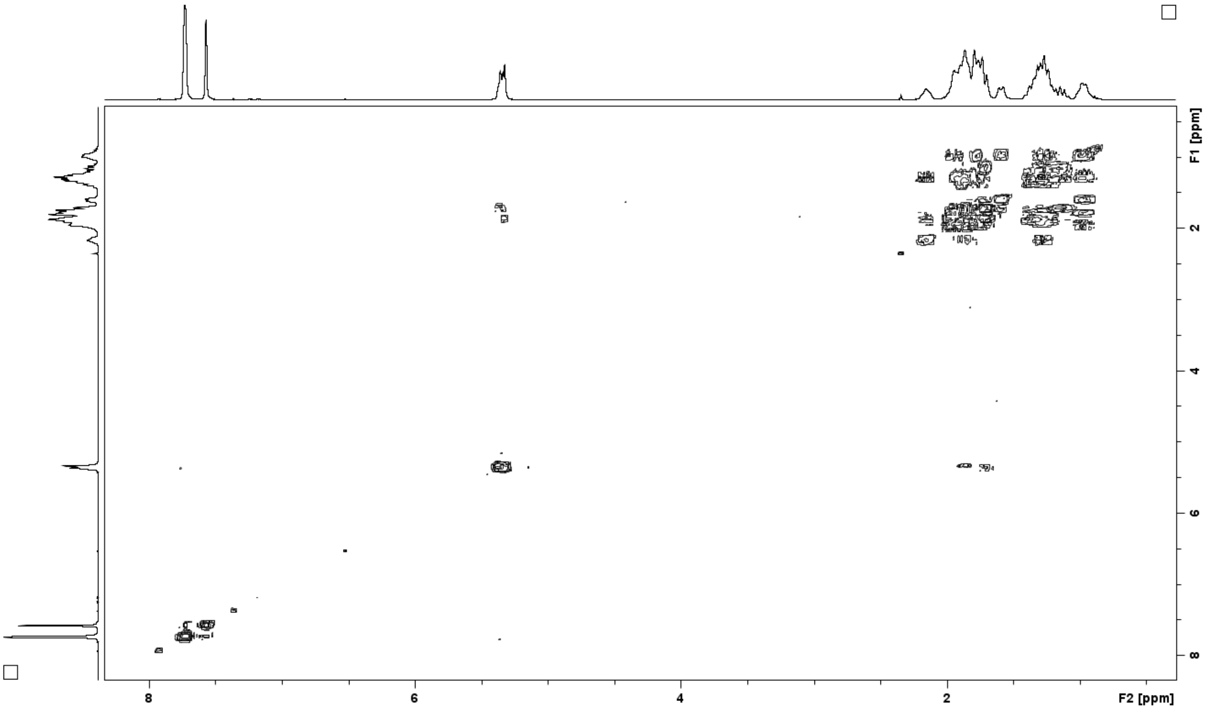

Figure S17: The solution $^{1}H/^{1}H$ COSY NMR (CD_2Cl_2, 298 K, 400 MHz) spectrum of **[1-C_6H_8][BAr$^F{}_4$]**.

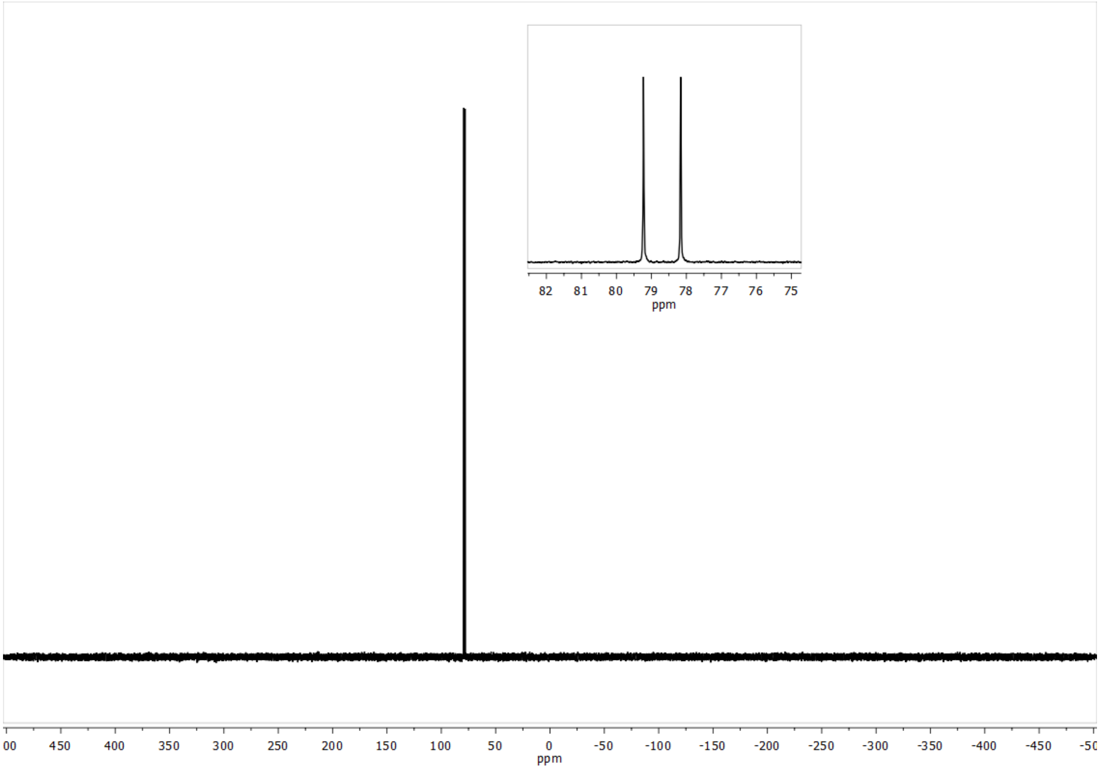

Figure S18: The solution $^{31}P\{^{1}H\}$ NMR (CD_2Cl_2, 298 K, 162 MHz) spectrum of **[1-C_6H_8][BAr$^F{}_4$]**.

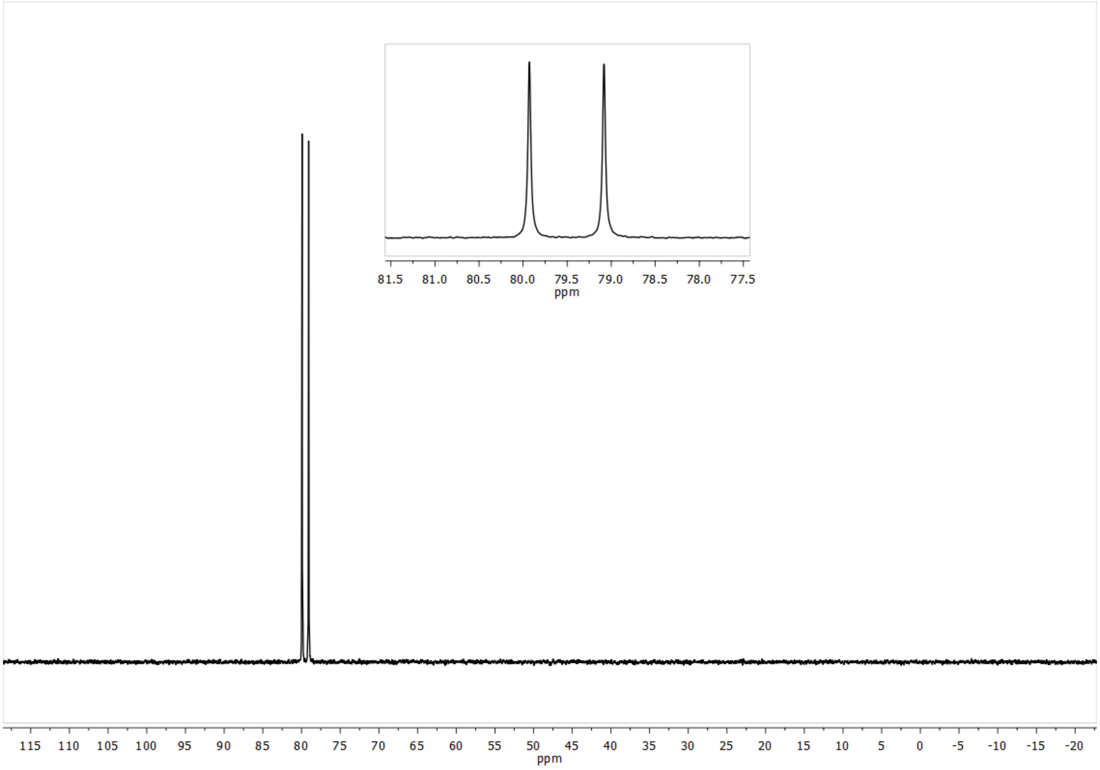

Figure S19: The solution $^{31}P\{^{1}H\}$ NMR (CD_2Cl_2, 183 K, 162 MHz) spectrum of **[1-C_6H_8][BAr$^F_4$]**.

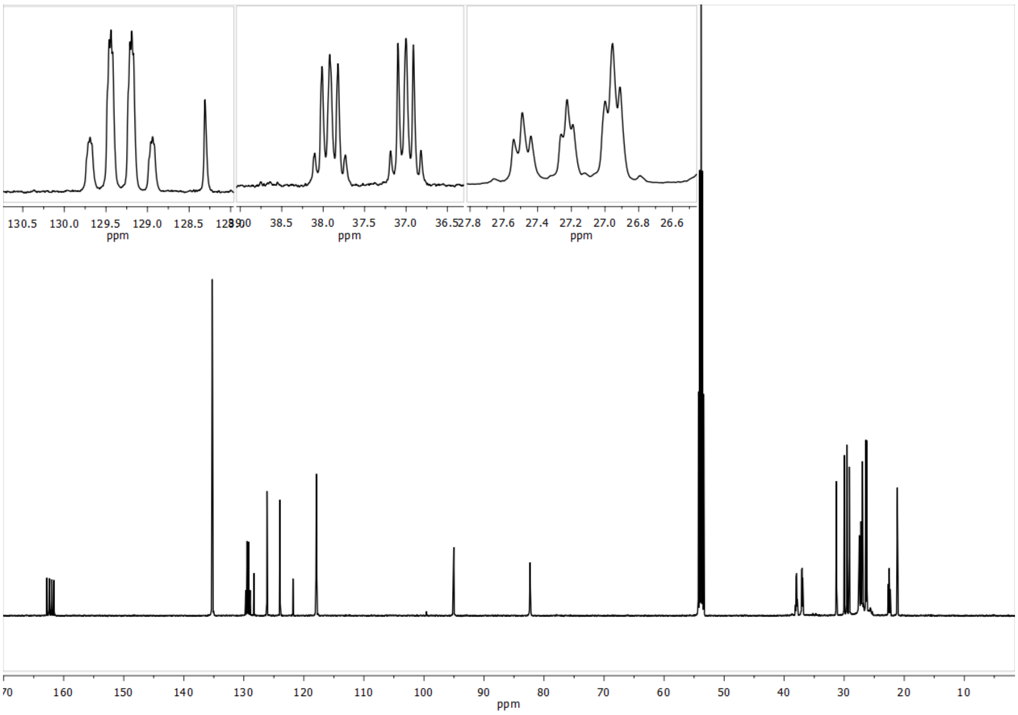

Figure S20: The solution $^{13}C\{^{1}H\}$ NMR (CD_2Cl_2, 298 K, 126 MHz) spectrum of **[1-C_6H_8][BAr$^F_4$]**.

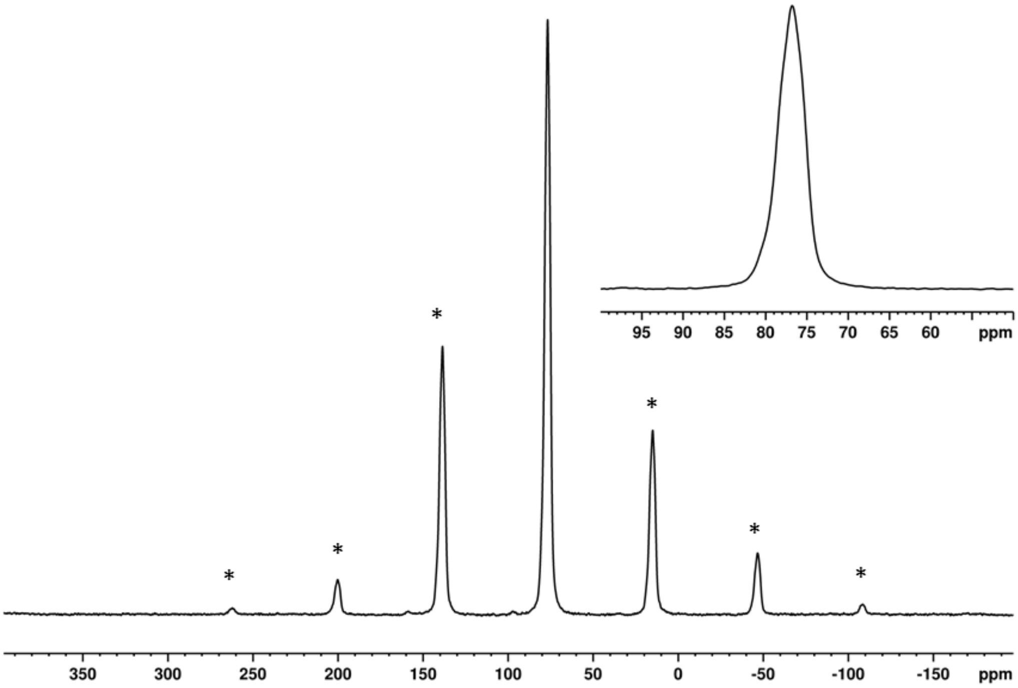

Figure S21: The $^{31}P\{^1H\}$ SSNMR (162 MHz, 294 K, 10 kHz spin rate) spectrum of **[1-C_6H_8][BAr$^F_4$]**. The resonances marked ***** are due to spinning sidebands. The inset is an enlargement of the central resonance.

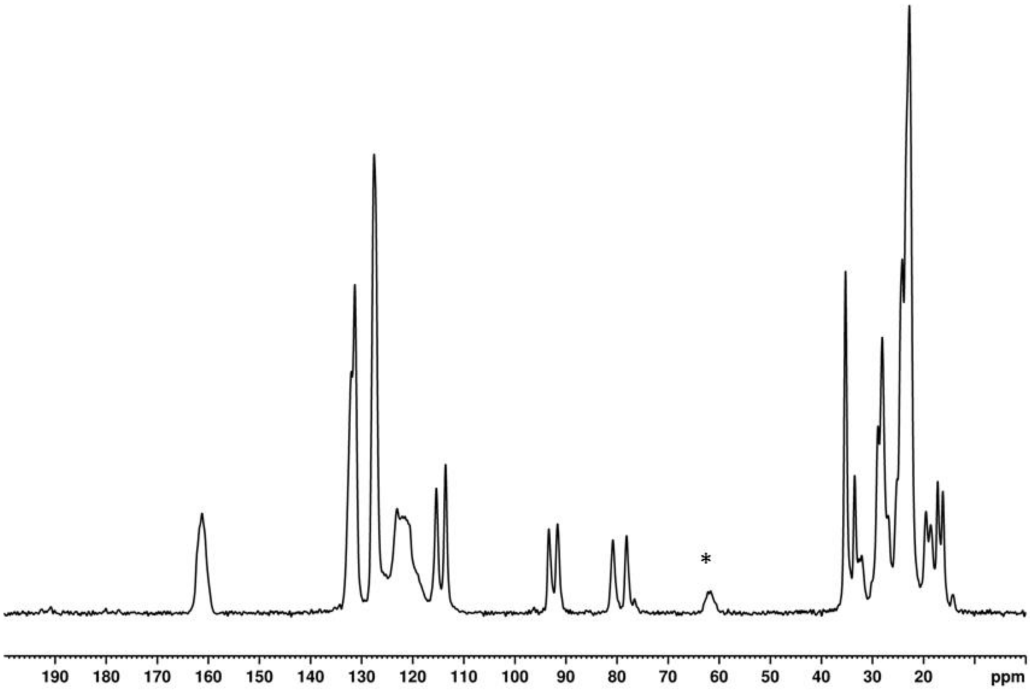

Figure S22: The $^{13}C\{^1H\}$ SSNMR (101 MHz, 294 K, 10 kHz spin rate) spectrum of **[1-C_6H_8][BAr$^F_4$]**. The resonance marked ***** is due to spinning sidebands.

S.2.4. [Rh(Cy$_2$PCH$_2$CH$_2$PCy$_2$)(C$_6$H$_{12}$)][BAr^F$_4$], [1-C$_6$H$_{12}$][BAr^F$_4$]

S.2.4.1. Synthesis of [1-C$_6$H$_{12}$][BAr^F$_4$] for an x-ray diffraction study

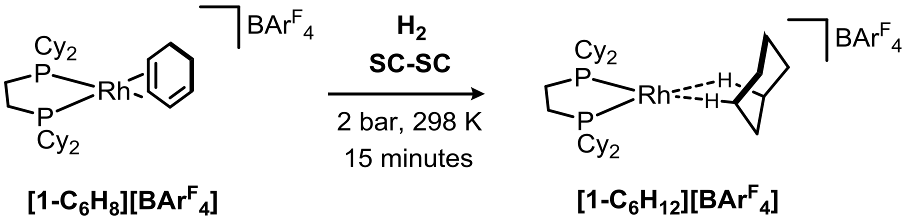

Deep red crystals of **[1-C$_6$H$_8$][BAr^F$_4$]** were treated with H_2 (2 bar, 298 K, 15 mins) inside a J Young flask. The colour of the crystals immediately darkens to a burgundy color. The crystalline material was then coated with Fomblin® Y oil under an argon flush, a suitable crystal was rapidly selected and then transferred to the Cryostream of a diffractometer and an x-ray diffraction study was undertaken. For further of the structural study, please refer to section S.5.

After 90 minutes under hydrogen, approx. 10 % of the sample has decomposed. This was shown by ^{31}P{^{1}H} SSNMR, see section S.2.4.6, figure S34.

S.2.4.2. Synthesis of **[1-C_6H_{12}][BAr^F_4]** for SSNMR characterization

A powdered microcrystalline sample of **[1-C_6H_8][BAr^F_4]** (35 mg) was packed in a 3.2 mm SSNMR rotor, inside an argon filled glove box. The rotor was then placed in a custom built glass J Young flask [S7] and the sample was then exposed to H_2 (1 bar, 298 K). After 20 minutes, the rotor cap was fitted under a flush of H_2. The sample was immediately transferred to the bore of a pre-cooled (158 K) SSNMR spectrometer (~ 10 mins) and analyzed $^{31}P\{^1H\}$ and $^{13}C\{^1H\}$ solid state NMR spectroscopy.

These conditions were optimized to form **[1-C_6H_{12}][BAr^F_4]**. At 158K, no onward reactivity with H_2 is observed. When H_2 replaced by argon at 298K, as so the rotor is packed under an argon atmosphere, spontaneous dehydrogenation is observed before cooling to 158K, to form **[1-C_6H_{10}][BAr^F_4]**, see section S.4.4.1.

S.2.4.3. Characterization data for **[1-C_6H_{12}][BAr^F_4]**

$^{31}P\{^1H\}$ SSNMR (162 MHz, 294 K, 10 kHz spin rate): δ 108.4 (two overlapping doublets, J_{RhP} = ~ 220 Hz.

$^{31}P\{^1H\}$ SSNMR (162 MHz, 158 K, 10 kHz spin rate): δ 107.1 (br), 104.5 (br).

$^{13}C\{^1H\}$ SSNMR (101 MHz, 198 K, 10 kHz spin rate): δ 161.1 (ArC), 131.8 (ArC), 127.2 (ArC), 121.8 (br, CF_3), 115.2 (ArC), 112.7 (ArC), 34.4, 32.4, 28.9, 27.8, 25.8, 24.2, 22.8, 22.3, 21.6, 17.2 (multiple aliphatic resonances).

$^{13}C\{^1H\}$ SSNMR (101 MHz, 158 K, 10 kHz spin rate): δ 161.1 (ArC), 131.8 (ArC), 127.1 (ArC), 121.6 (br, CF_3), 115.1 (ArC), 112.5 (ArC), 34.0, 32.1, 27.8, 24.1, 22.7, 19.7, 16.5 (multiple aliphatic resonances).

^1H projection from $^1H/^{13}C$ FSLG HETCOR SSNMR (198 K, 10 kHz spin rate): δ 7.1 (br), 1.0 (br).

^1H projection from $^1H/^{13}C$ FSLG HETCOR SSNMR (158 K, 10 kHz spin rate): δ 7.1 (br), 1.0 (br), -1.6 (br).

S.2.4.4. NMR spectra of [1-C_6H_{12}][BAr^F_4]

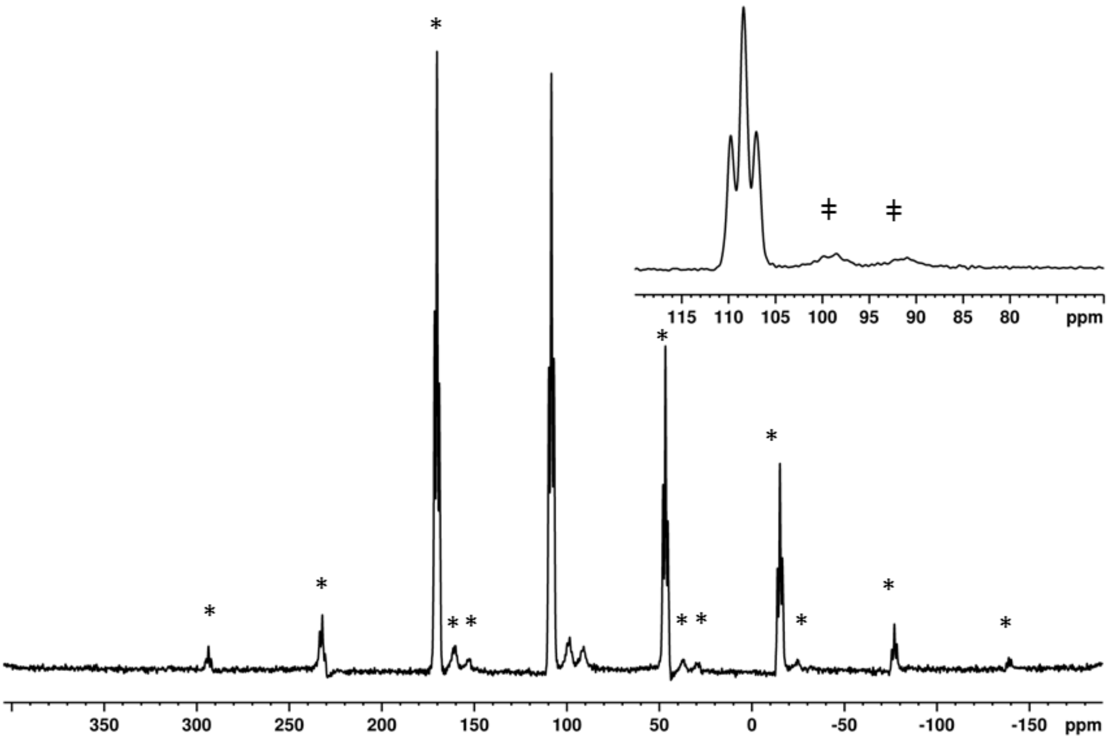

Figure S23: The $^{31}P\{^1H\}$ SSNMR (162 MHz, 298 K, 10 kHz spin rate) spectrum of **[1-C_6H_{12}][BAr^F_4]** prepared in situ, packed under at atmosphere of H_2. The resonances marked ‡ are assigned to **[1-C_6H_{10}][BAr^F_4]** which has formed by partial dehydrogenation, see section S.4.3. The resonances marked ***** are due to spinning sidebands. The inset is an enlargement of the central resonances.

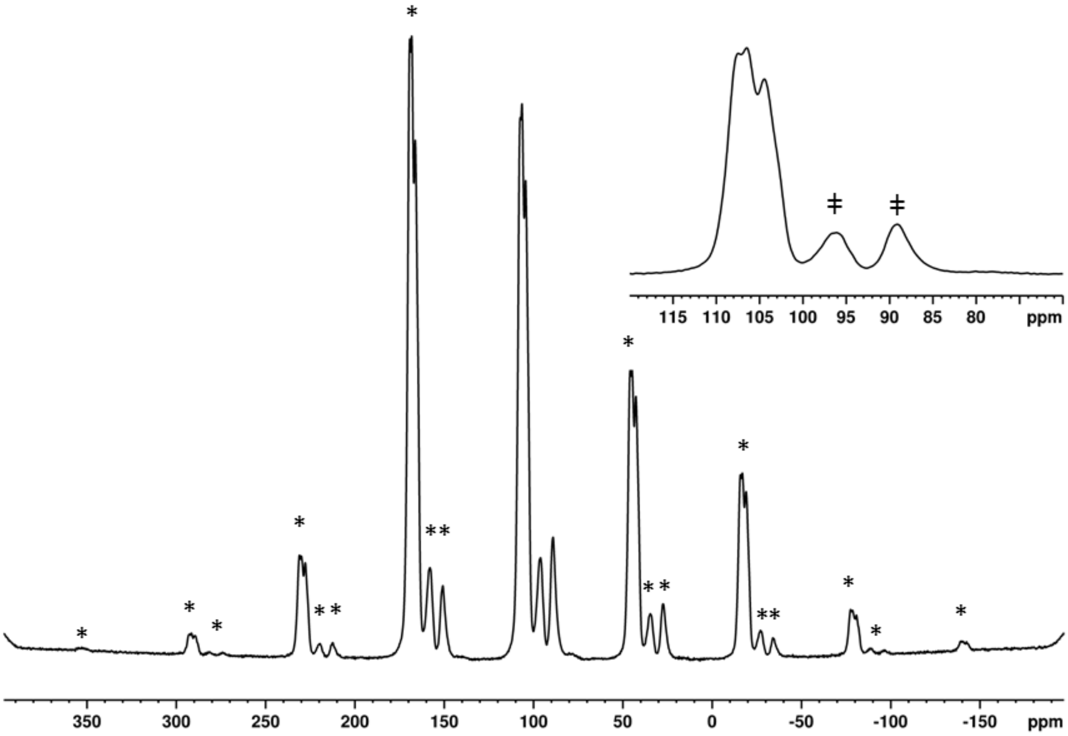

Figure S24: The ^{31}P{^{1}H} SSNMR (162 MHz, 158 K, 10 kHz spin rate) spectrum of **[1-C_6H_{12}][BAr$^F{}_4$]** prepared in situ. The resonances marked ‡ are assigned to **[1-C_6H_{10}][BAr$^F{}_4$]** which has formed by partial dehydrogenation. The resonances marked ***** are due to spinning sidebands. The inset is an enlargement of the central resonances. This spectrum was obtained from a different sample to that above, resulting in a different degree of dehydrogenation.

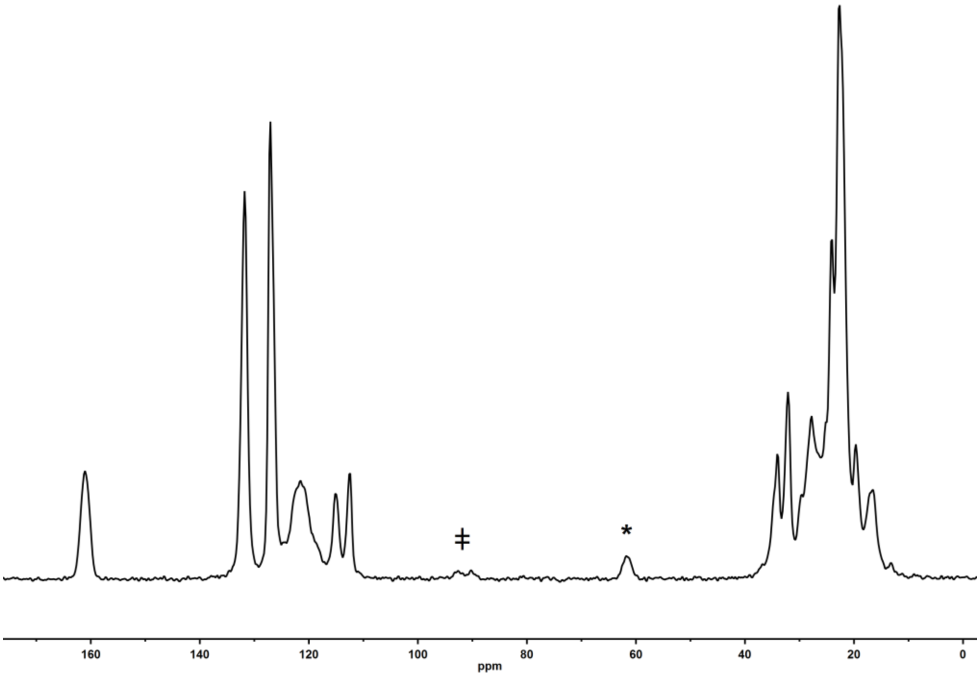

Figure S25: The $^{13}C\{^{1}H\}$ SSNMR (100 MHz, 158 K, 10 kHz spin rate) spectrum of **[1-C_6H_{12}][BAr$^F{}_4$]** prepared in situ. The resonances marked ‡ are assigned to **[1-C_6H_{10}][BAr$^F{}_4$]** which formed by partial dehydrogenation. The resonance marked * is due to a spinning sideband.

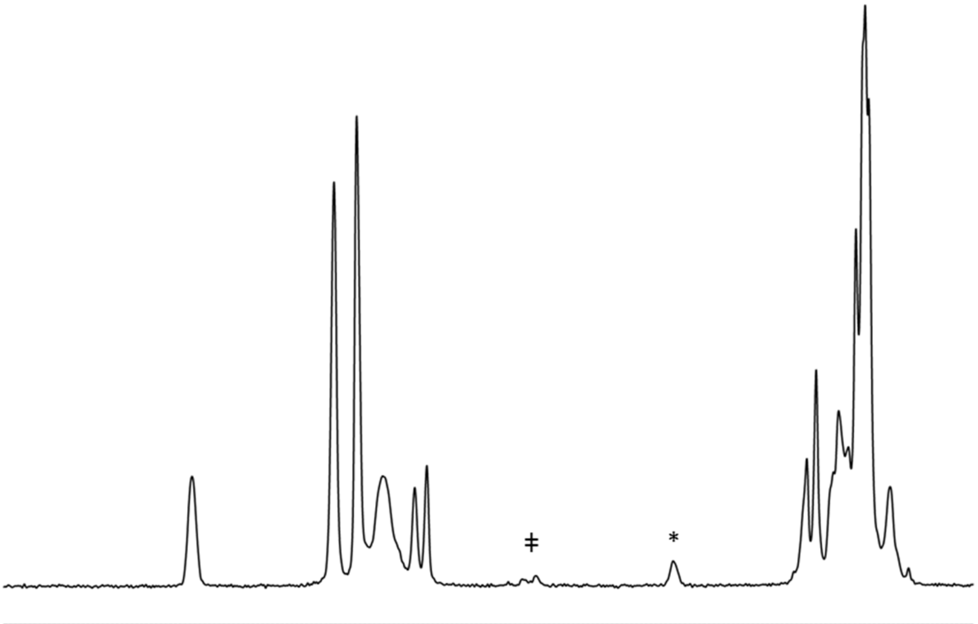

Figure S26: The $^{13}C\{^{1}H\}$ SSNMR (100 MHz, 198 K, 10 kHz spin rate) spectrum of **[1-C_6H_{12}][BAr$^F{}_4$]** prepared in situ. The resonances marked ‡ are assigned to **[1-C_6H_{10}][BAr$^F{}_4$]**, which formed by partial dehydrogenation. The resonance marked * is due to a spinning sideband.

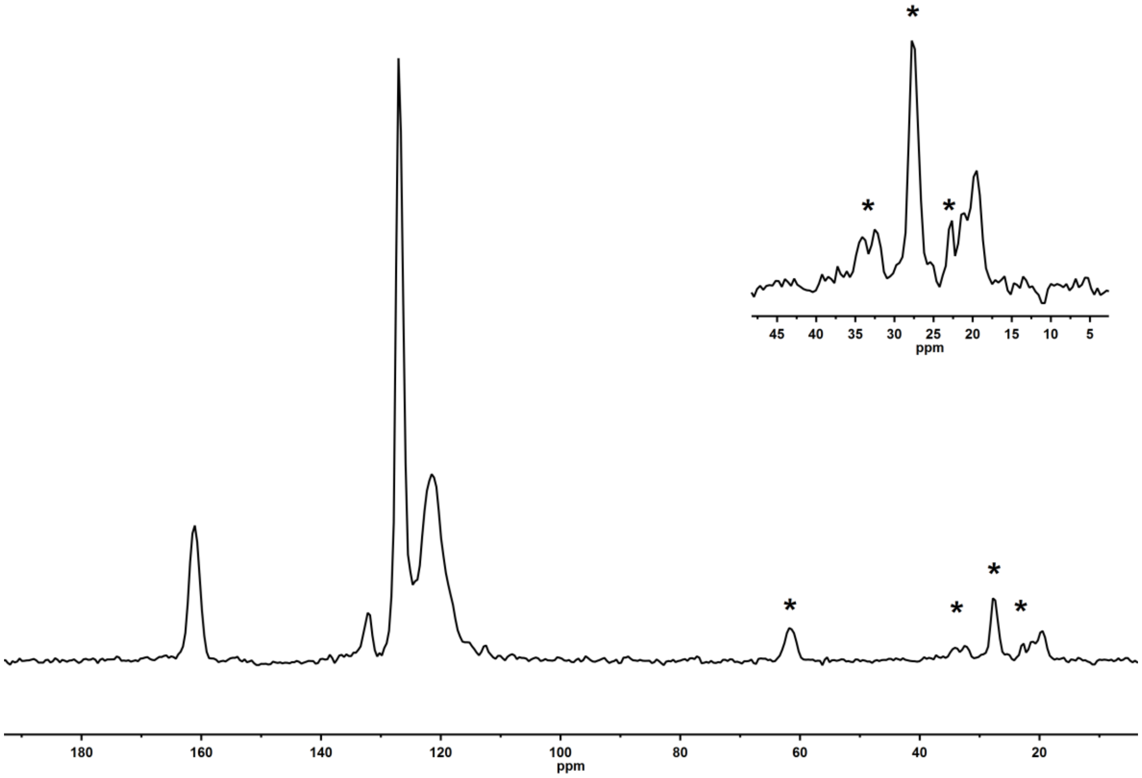

Figure S27: The $^{13}C\{^{1}H\}$ NQS SSNMR (100 MHz, 158 K, 10 kHz spin rate) spectrum of **[1-C_6H_{12}][BAr^F_4]** prepared in situ. The resonances marked * are due to spinning sidebands.

The inset is an enlargement of the resonances between δ 45 to 5, showing two peaks at δ 19.7 and 21.4. These peaks did not shift position in the analogous 8 kHz NQS SSNMR spectrum, suggestive of real signals and not sidebands.

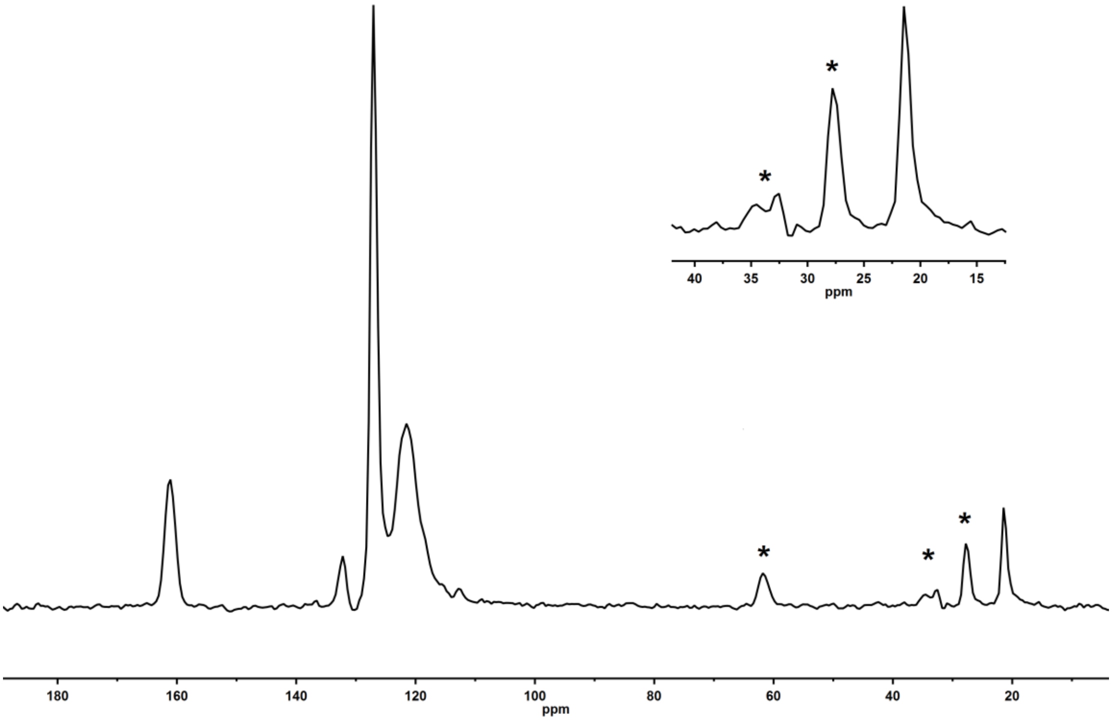

Figure S28: The $^{13}C\{^{1}H\}$ NQS SSNMR (100 MHz, 198 K, 10 kHz spin rate) spectrum of **[1-C_6H_{12}][BAr^F_4]** prepared in situ. The resonances marked * are due to spinning sidebands.

The inset is an enlargement of the resonances at δ 45 to 15, showing only a single resonance at δ 21.4. This peak did not shift position in the analogous 8 kHz NQS SSNMR spectrum, suggestive of a real signal and not a sideband.

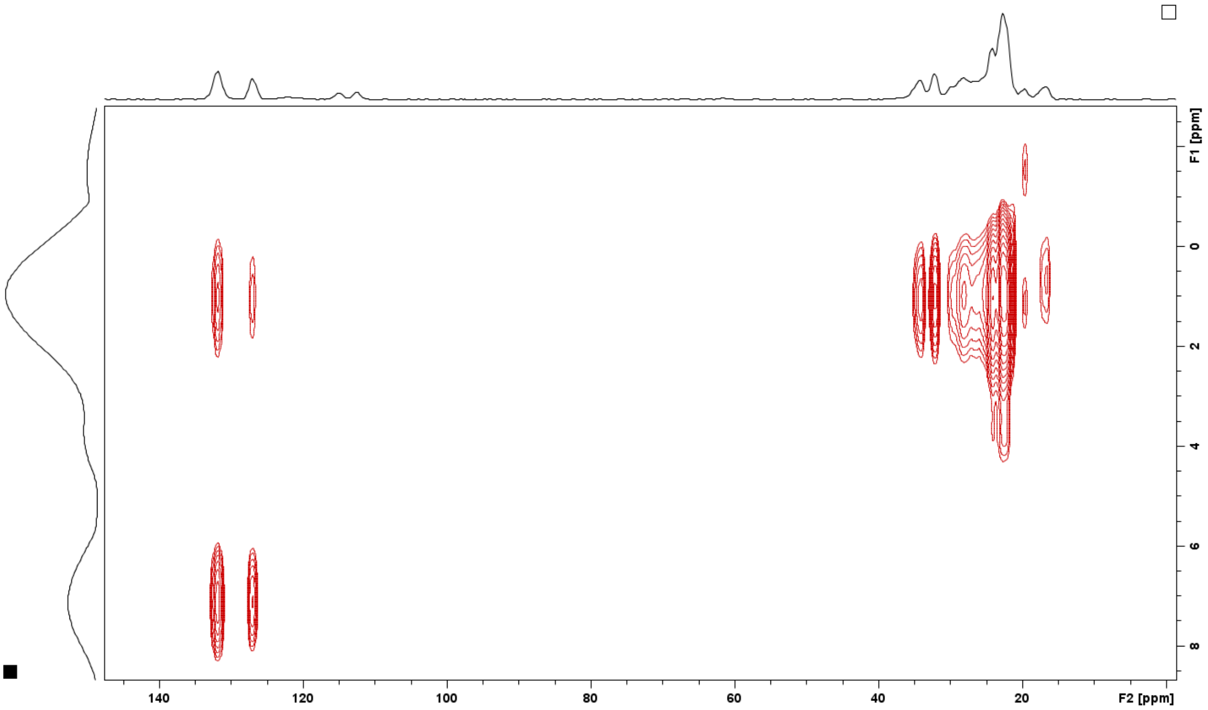

Figure S29: The ${}^{1}H/{}^{13}C$ FSLG HETCOR SSNMR (158 K, 10 kHz spin rate) spectrum of **[1-C_6H_{12}][BAr$^F{}_4$]** prepared in situ.

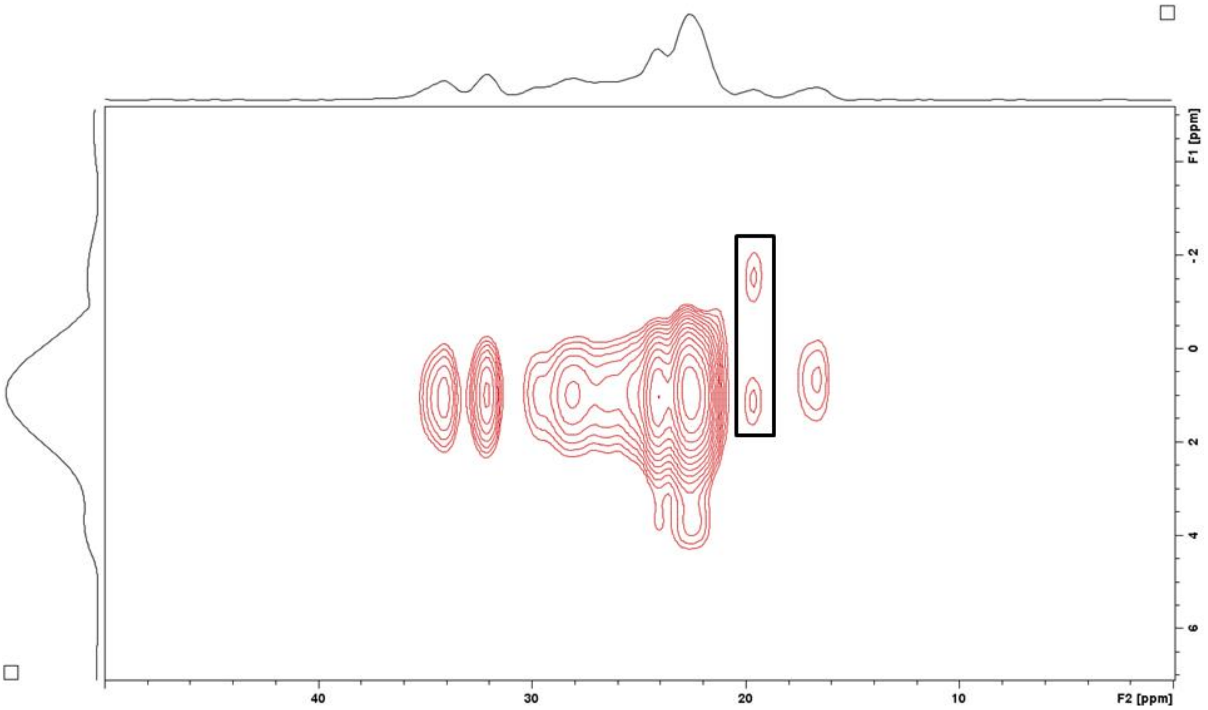

Figure S30: The ${}^{1}H/{}^{13}C$ FSLG HETCOR SSNMR (158 K, 10 kHz spin rate) spectrum of **[1-C_6H_{12}][BAr$^F{}_4$]** prepared in situ (top). Enlargement of the alkyl region (bottom). Black box added to guide the eye.

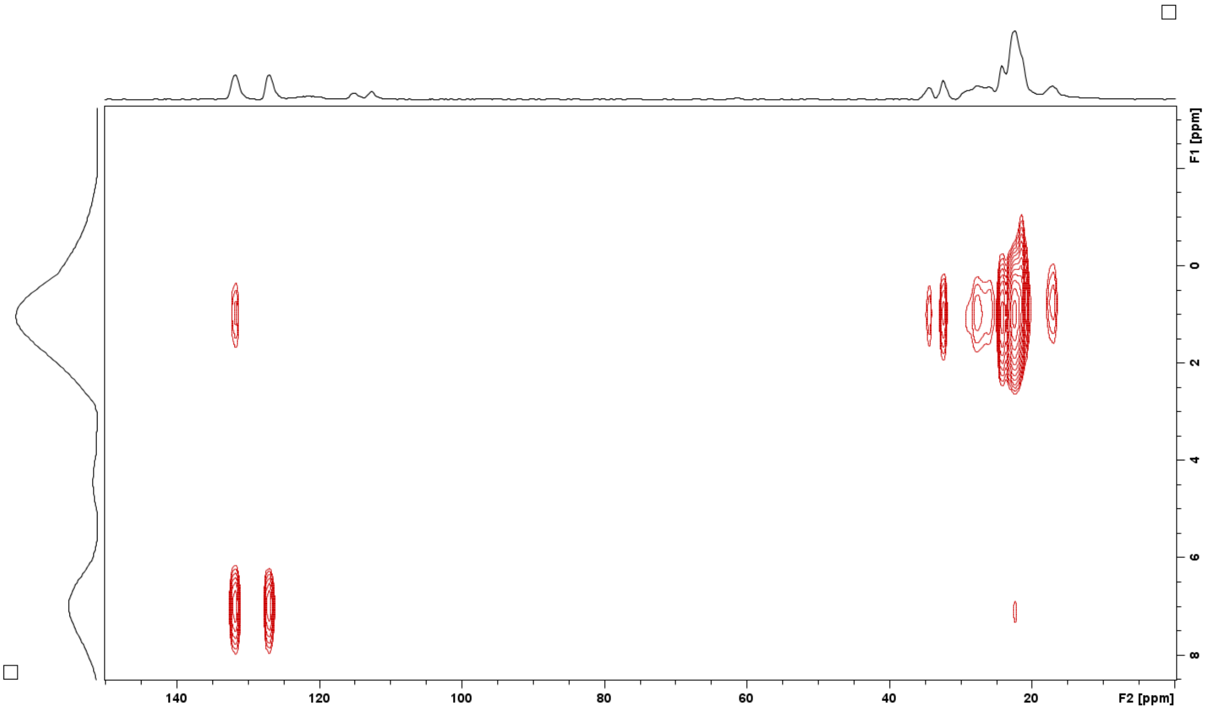

Figure S31: The ^{1}H/^{13}C FSLG HETCOR SSNMR (198 K, 10 kHz spin rate) spectrum of **[1-C_6H_{12}][BAr^F$_4$]** prepared in situ.

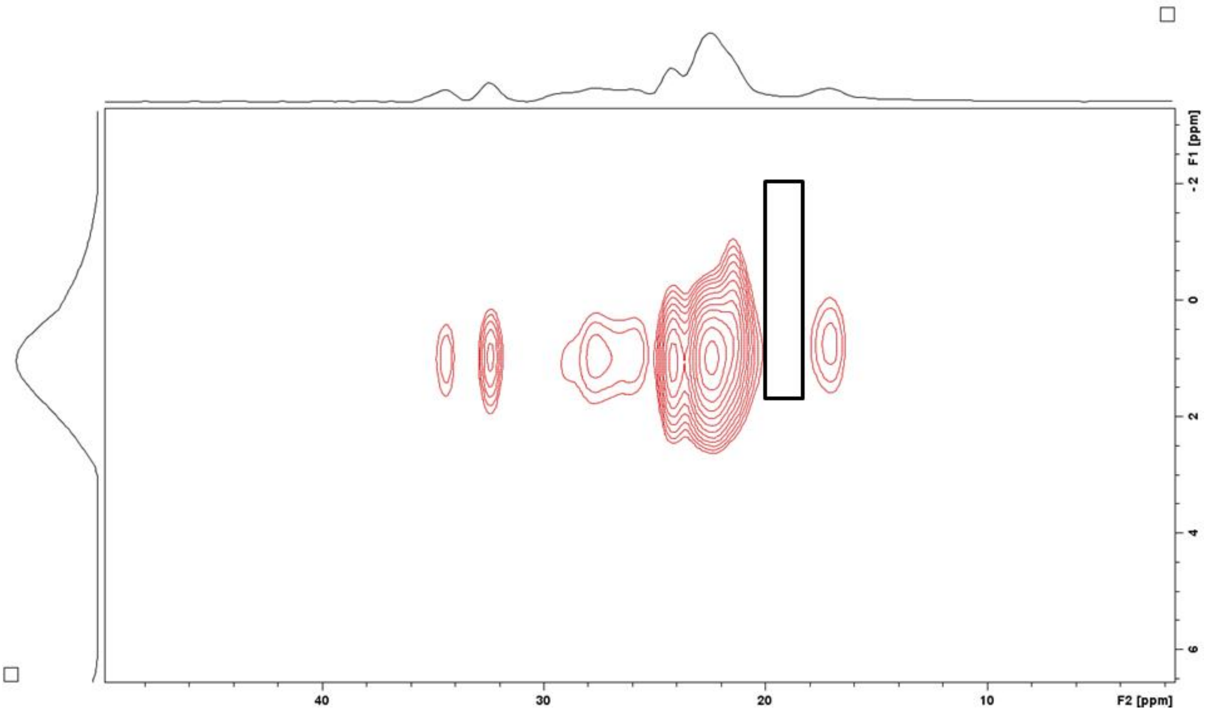

Figure S32: The ^{1}H/^{13}C FSLG HETCOR SSNMR (198 K, 10 kHz spin rate) spectrum of **[1-C_6H_{12}][BAr^F$_4$]** prepared in situ (top). Enlargement of the alkyl region (bottom). Black box added to guide the eye.

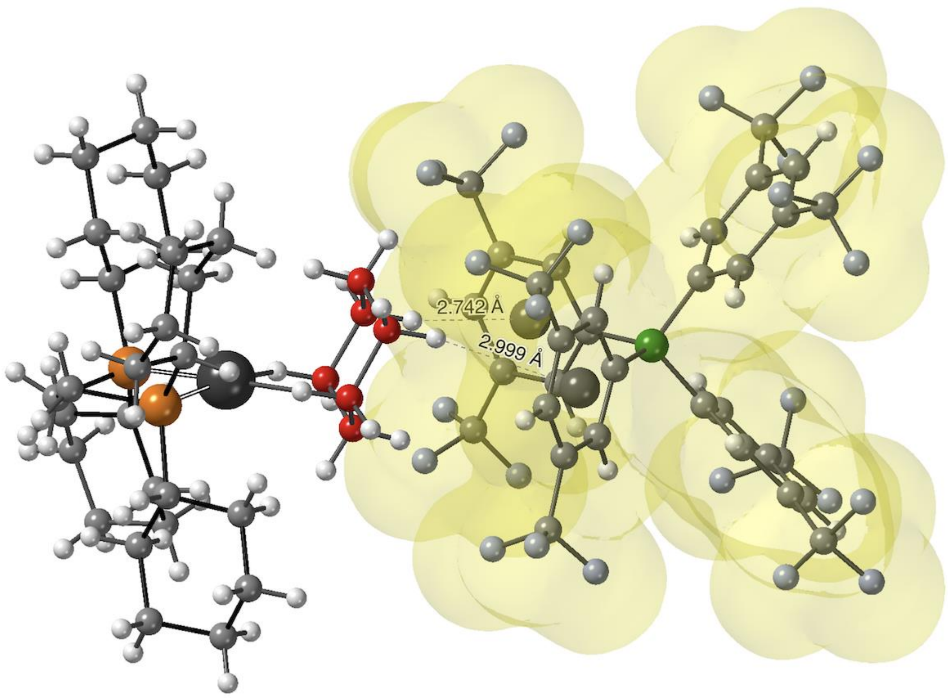

Figure S33: Molecular structure of **[1-C_6H_{12}][BAr^F_4]** showing C-H···F-C contacts (< 3.0Å) between the cyclohexane ligand and [BAr^F_4]$^-$ anion.

S.2.4.5. Liberation of the bound cyclohexane from [1-C_6H_{12}][BAr^F_4].

Deep red crystals of **[1-C_6H_8][BAr^F_4]** were treated with H_2 (2 bar, 298 K, 15 mins) inside a J Young flask. The colour of the crystals immediately darkens to a burgundy color, yielding **[1-C_6H_{12}][BAr^F_4]**. The solid was then cooled to 77 K under liquid nitrogen and the J Young flask placed under vacuum to remove any H_2. CO (1 bar, 298K) was added and solid left for 1 hour; to which a vibrant yellow solid material had formed. The solid was then dissolved in d_3-MeCN, to which the volatile component was isolated by trap-to-trap distillation and analyzed by ^1H NMR spectroscopy.

^1H NMR (d_3-MeCN, 400 MHz): δ 1.44 (s, 12 H, alkane-CH_2-)

The resultant solid was confirmed to be [Rh(dcpe)$(CO)_2$][BAr^F] by solution NMR $^{31}P\{^1H\}$ NMR spectroscopy (δ 85.22, d, J_{RhP} = 116 Hz).[S7]

S.2.4.6. Solid state decomposition products of $[1\text{-}C_6H_{12}][BAr^F_4]$ under H_2

A powdered microcrystalline sample of **$[1\text{-}C_6H_8][BAr^F_4]$** (35 mg) was packed in a 3.2 mm SSNMR rotor, inside an argon filled glove box. The rotor was then placed in a custom built glass J Young flask [S7] and the sample was then exposed to H_2 (1 bar, 298 K). After 80 minutes, the rotor cap was fitted under a flush of H_2. The sample was immediately transferred to the bore of a pre-cooled (158 K) SSNMR spectrometer (~ 10 mins, total time = 90 mins) and analyzed $^{31}P\{^1H\}$ and $^{13}C\{^1H\}$ solid state NMR spectroscopy.

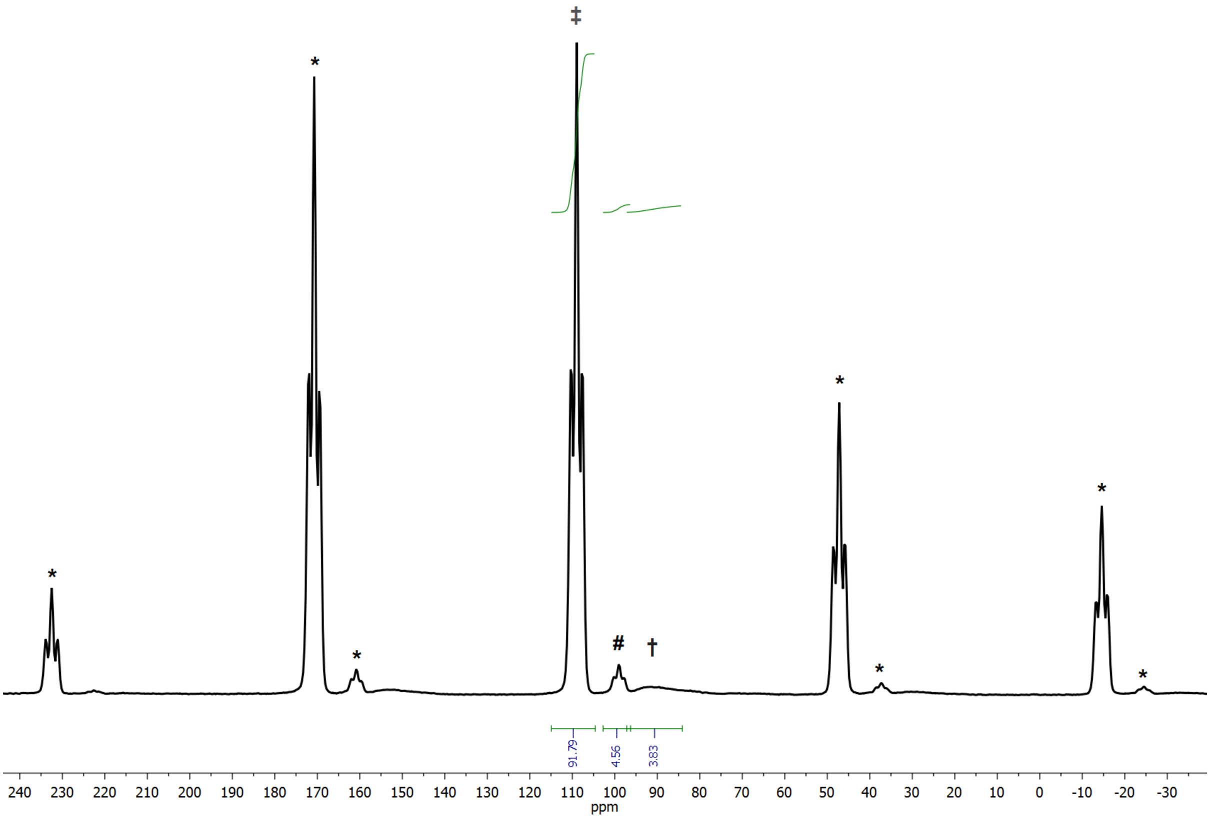

Figure S34: The $^{31}P\{^1H\}$ SSNMR (162 MHz, 295 K, 10 kHz spin rate) spectrum of the solid state decomposition products of **$[1\text{-}C_6H_{12}][BAr^F_4]$** under H_2 after 90 minutes. The resonances ‡ marked are assigned to **$[1\text{-}C_6H_{12}][BAr^F_4]$** (approx. 90%) and the resonances marked † are assigned to **$[1\text{-}BAr^F_4]$**[S2] (approx. 5%). The resonance marked # at δ 100 is unidentified complex under H_2 (approx. 5%), also seen in the decomposition of **$[1\text{-}C_4H_{10}][BAr^F_4]$** also under hydrogen atmosphere (section S.2.2.6.). The resonances marked ***** are due to spinning sidebands.

S.2.5. [Rh($Cy_2PCH_2CH_2PCy_2$)(C_6H_6)][$BAr^F{}_4$], [1-C_6H_6][$BAr^F{}_4$]

S.2.5.1. Synthesis of [1-C_6H_6][$BAr^F{}_4$]

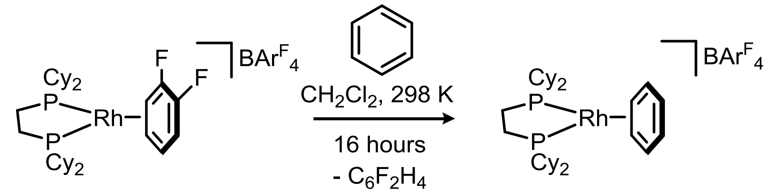

[1-$C_6H_4F_2$][$BAr^F{}_4$] **[1-C_6H_6][$BAr^F{}_4$]**

A solution of **[1-$C_6H_4F_2$][$BAr^F{}_4$]** (70 mg, 46.6 μmol) in CH_2Cl_2 (5 mL) was treated with C_6H_6 (100 μL) at ambient temperature. The resultant yellow solution was stirred at ambient temperature for 16 hours, and then filtered. Addition of pentane afforded a yellow powder, which was washed with further pentane and then dried under vacuum. Yield: 59 mg (86 %).

S.2.5.2. Characterization data for [1-C_6H_6][$BAr^F{}_4$]

^1H NMR (CD_2Cl_2, 298 K, 400 MHz): δ 7.72 (s, 8H, ortho-ArH), 7.57 (s, 4H, para-ArH), 6.52 (s, 6H, C_6H_6), 1.91-1.59 (br m, 28H, overlapping aliphatic CH), 1.37-1.14 (br m, 16H, aliphatic CH), 1.04-0.94 (br m, 4H, overlapping aliphatic CH).

^1H NMR (CD_2Cl_2, 183 K, 400 MHz): δ 7.72 (s, 8H, ortho-ArH), 7.54 (s, 4H, para-ArH), 6.44 (s, 6H, C_6H_6), 1.78-1.44 (br m, 28H, overlapping aliphatic CH), 1.26-0.96 (br m, 16H, aliphatic CH), 0.92-0.79 (br m, 4H, overlapping aliphatic CH).

$^{31}P\{^1H\}$ NMR (CD_2Cl_2, 298 K, 162 MHz): δ 99.7 (d, J_{RhP} 201 Hz).

$^{31}P\{^1H\}$ NMR (CD_2Cl_2, 183 K, 162 MHz): δ 99.4 (d, J_{RhP} 201 Hz).

$^{19}F\{^1H\}$ NMR (CD_2Cl_2, 298 K, 377 MHz): δ -62.9 (s).

$^{13}C\{^1H\}$ NMR (CD_2Cl_2, 298 K, 126 MHz): δ 162.2 (q, J_{CB} 50 Hz, ipso-ArC), 135.2 (s, ortho-ArC), 129.3 (q, J_{CF} 32 Hz, meta-ArC), 125.0 (q, J_{CF} 272 Hz, CF_3), 117.9 (m, para-ArC), 99.6 (d, J_{CRh} 1.9 Hz, C_6H_6), 38.6 (m, cyclohexyl-CH), 29.4 (m, cyclohexyl-CH_2), 27.1 (m, cyclohexyl-CH_2), 26.4 (s, cyclohexyl-CH_2), 22.9 (m, cyclohexyl-CH_2).

ESI-MS found (calc. for [Rh($Cy_2PCH_2CH_2PCy_2$)(C_6H_6)]$^+$): m/z 603.29 (603.28).

Elemental analysis found (calc. for $C_{64}H_{66}BF_{24}P_2Rh$): C 52.29 (52.40), H 4.35 (4.54).

S.2.5.3. Spectra of [1-C_6H_6][BAr^F_4]

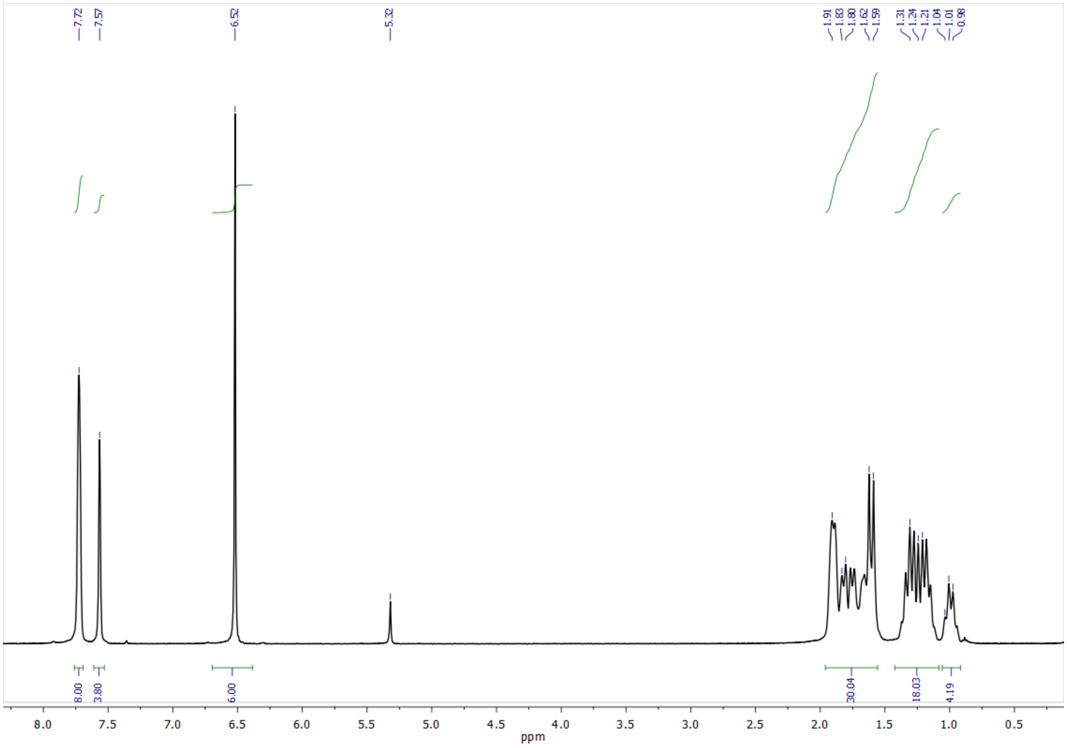

Figure S35: The solution ^1H NMR (CD_2Cl_2, 298 K, 400 MHz) spectrum of **[1-C_6H_6][BAr^F_4].**

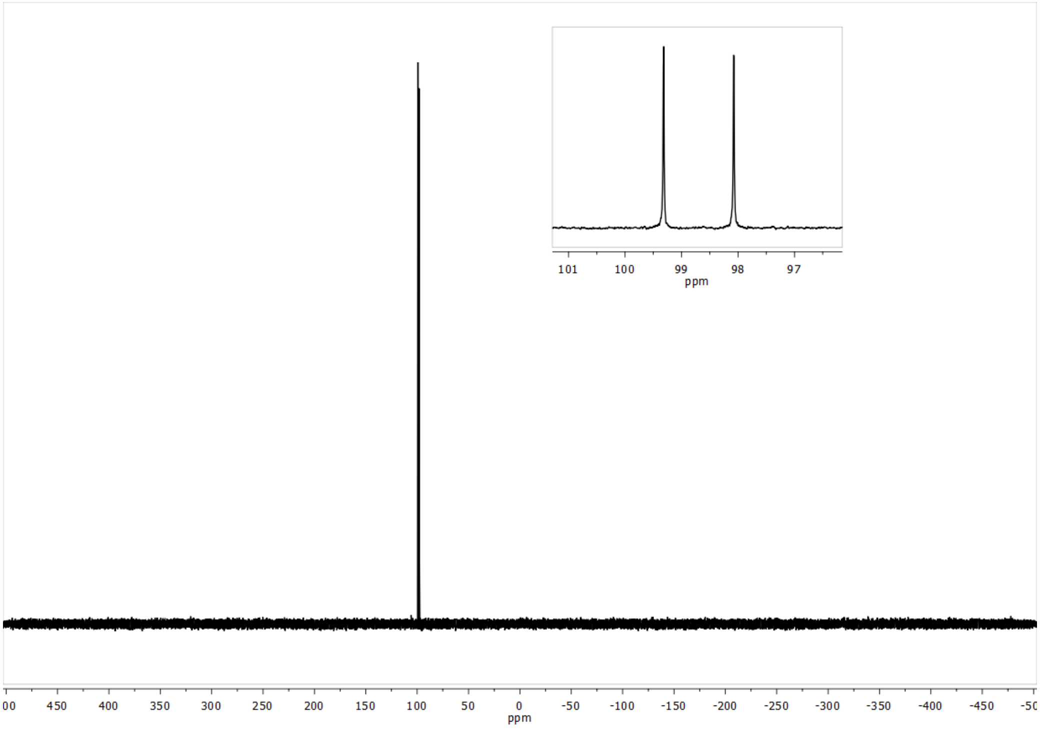

Figure S36: The solution $^{31}P\{^1H\}$ NMR (CD_2Cl_2, 298 K, 162 MHz) spectrum of **[1-C_6H_6][BAr^F_4].**

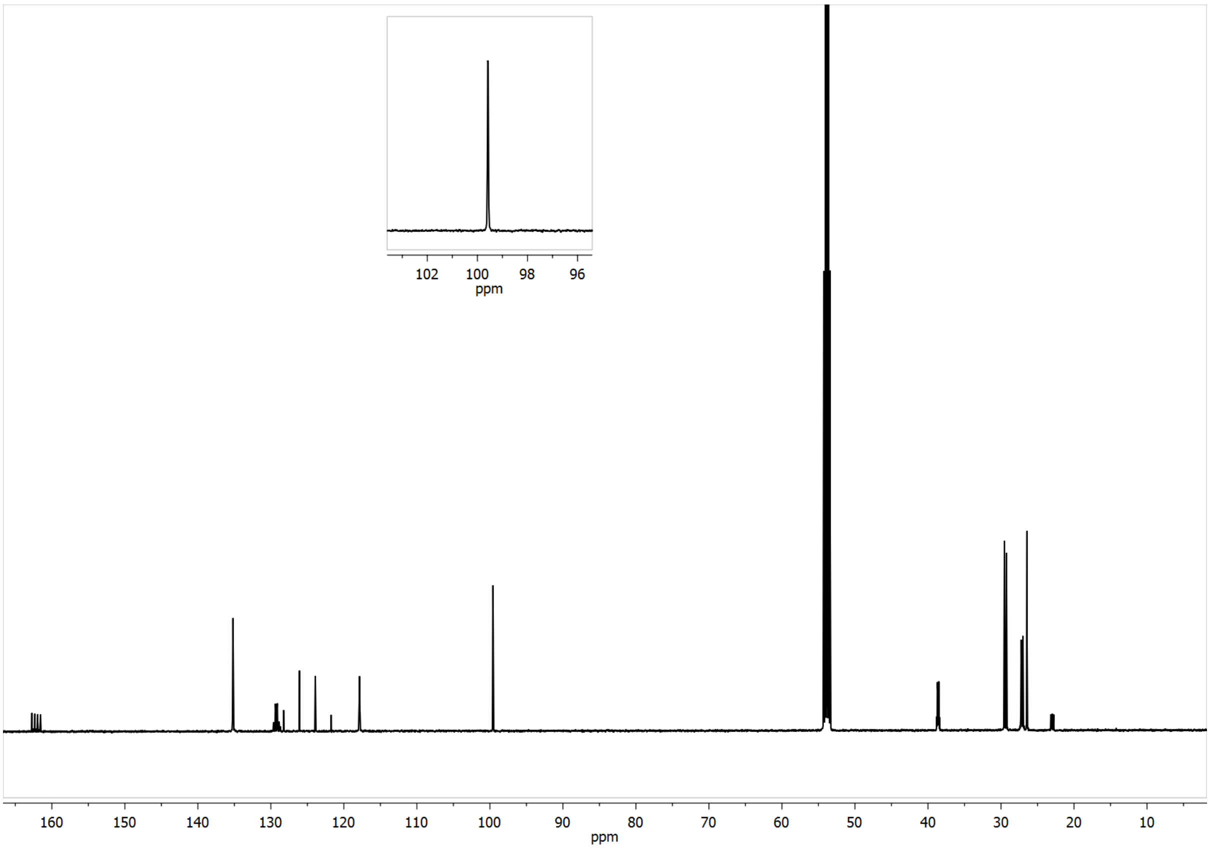

Figure S37: The solution $^{13}C\{^1H\}$ NMR (CD_2Cl_2, 298 K, 126 MHz) spectrum of **[1-C_6H_6][$BAr^F{}_4$]**. The inset shows an enlargement of the benzene carbon signals at δ 99.6.

S.2.6. [Rh($Cy_2PCH_2CH_2PCy_2$)(C_6D_6)][BAr^F_4], [1-C_6D_6][BAr^F_4]

S.2.6.1. Synthesis of [1-C_6D_6][BAr^F_4]

A solution of **[1-$C_6H_4F_2$][BAr^F_4]** (35 mg, 23.3 µmol) in CH_2Cl_2 (3 mL) was treated with C_6D_6 (50 µL) at ambient temperature. The resultant yellow solution was stirred at ambient temperature for 16 hours and then filtered. Addition of pentane afforded a yellow powder, which was washed with further pentane and then dried under vacuum. Yield: 17 mg (50 %).

S.2.6.2. Characterization data for [1-C_6D_6][BAr^F_4]

^{1}H NMR (CD_2Cl_2, 298 K, 400 MHz): δ 7.72 (s, 8H, ortho-ArH), 7.56 (s, 4H, para-ArH), 1.91-1.59 (br m, 28H, overlapping aliphatic CH), 1.37-1.14 (br m, 16H, aliphatic CH), 1.04-0.94 (br m, 4H, overlapping aliphatic CH).

^{1}H NMR (CD_2Cl_2, 183 K, 400 MHz): δ 7.72 (s, 8H, ortho-ArH), 7.54 (s, 4H, para-ArH), 1.78-1.44 (br m, 28H, overlapping aliphatic CH), 1.26-0.96 (br m, 16H, aliphatic CH), 0.92-0.79 (br m, 4H, overlapping aliphatic CH).

^{2}H NMR (CD_2Cl_2, 298 K, 61 MHz): δ 6.56 (s, C_6D_6).

$^{31}P\{^1H\}$ NMR (CD_2Cl_2, 298 K, 162 MHz): δ 98.7 (d, J_{RhP} 201 Hz).

$^{31}P\{^1H\}$ NMR (CD_2Cl_2, 183 K, 162 MHz): δ 99.5 (d, J_{RhP} 201 Hz).

$^{19}F\{^1H\}$ NMR (CD_2Cl_2, 298 K, 377 MHz): δ -62.9 (s).

$^{13}C\{^1H\}$ NMR (CD_2Cl_2, 298 K, 126 MHz): δ 162.2 (q, J_{CB} 50 Hz, ipso-ArC), 135.2 (s, ortho-ArC), 129.3 (q, J_{CF} 32 Hz, meta-ArC), 125.0 (q, J_{CF} 272 Hz, CF_3), 117.9 (m, para-ArC), 99.2 (t, J_{CD} 26.1 Hz, C_6H_6), 38.6 (m, cyclohexyl-CH), 29.5 (s, cyclohexyl-CH_2), 29.2 (s, cyclohexyl-CH_2), 27.2 (m, cyclohexyl-CH_2), 27.0 (m, cyclohexyl-CH_2), 26.4 (s, cyclohexyl-CH_2), 23.1 (m, cyclohexyl-CH_2), 23.0 (m, cyclohexyl-CH_2), 23.0 (br s, cyclohexyl-CH_2), 22.8 (m, cyclohexyl-CH_2).

ESI-MS found (calc. for [Rh($Cy_2PCH_2CH_2PCy_2$)(C_6D_6)]$^+$): m/z 609.32 (609.31).

S.3. H/D Exchange Experiments

S.3.1. Solid-state H/D exchange on [1-C_4H_8][BAr^F_4]

S.3.1.1. General Experimental of H/D Exchange on [1-C_4H_8][BAr^F_4]

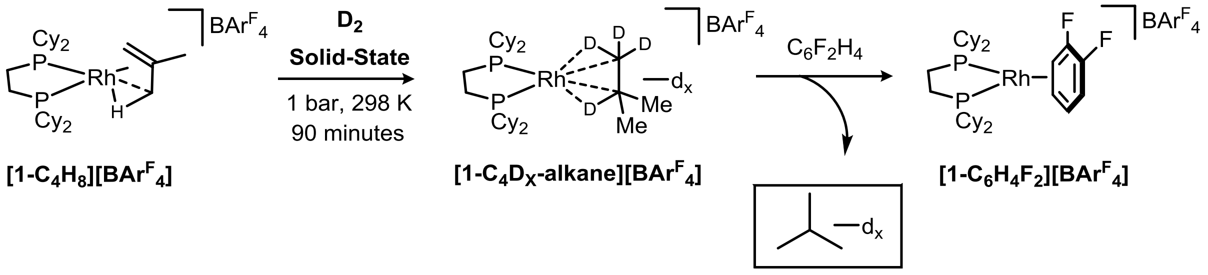

[1-C_4H_8][BAr^F_4] **[1-C_4D_X-alkane][BAr^F_4]** **[1-$C_6H_4F_2$][BAr^F_4]**

Isobutane-d_x (x = 10 - 7)

A J Young NMR tube (~ 2 mL) was charged with 25 mgs of an orange crystalline sample of **[1-C_4H_8][BAr^F_4]**. The tube was evacuated (< 3 × 10^{-2} mbar) and D_2 (1 bar, 298 K) was added. The color of the crystals immediately turned a dark red, yielding the deuterated analogue of **[1-C_4H_{10}][BAr^F_4]**; **[1-C_4D_x-alkane][BAr^F_4]**.

The reaction was left for 90 minutes; after which the crystal color changed to a dark orange. After this time, it was found isobutane-d_x (x = 10 - 7) had been expelled from the crystal lattice, shown by gas phase ^1H and ^2H NMR spectroscopy of the NMR tube headspace.[S6] The volatiles were then distilled into a clean NMR tube with CD_2Cl_2 and analyzed by ^1H, ^2H, $^{13}C\{^1H\}$ NMR spectroscopy and GC EI-MS.

The remaining solid material was dissolved in $C_6F_2H_4$ to quantitatively yield **[1-$C_6F_2H_4$][BAr^F_4]** complex. No isobutane could be identified in the solution ^1H or ^2H NMR spectrum, suggesting total expulsion of isobutane from the lattice by D_2 is complete after 90 minutes.

S.3.1.2. Characterization data for isobutane-d_x

^1H NMR (CD_2Cl_2, 400 MHz, 183 K): δ 0.86 (br m, CH_3, residual protio-isobutane)

^2H NMR (CD_2Cl_2, 61 MHz, 183 K): δ 1.66 (br s, CD), 0.85 (br s, CD_3).

$^{13}C\{^1H\}$ NMR (CD_2Cl_2, 126 MHz, 183 K): δ 23.6 (septet, CD_3, J_{CD} = 18.8), 22.5 (triplet, CD, J_{CD} = 20.1), for C_4D_{10}, but also formed is C_4HD_9, $C_4H_2D_8$ and $C_4H_3D_7$.

GC EI-MS found (calc. for $C_4D_9^+$): m/z 66.127 (66.127).

S.3.1.3. NMR Spectra of isobutane-d_x (x = 10 – 7)

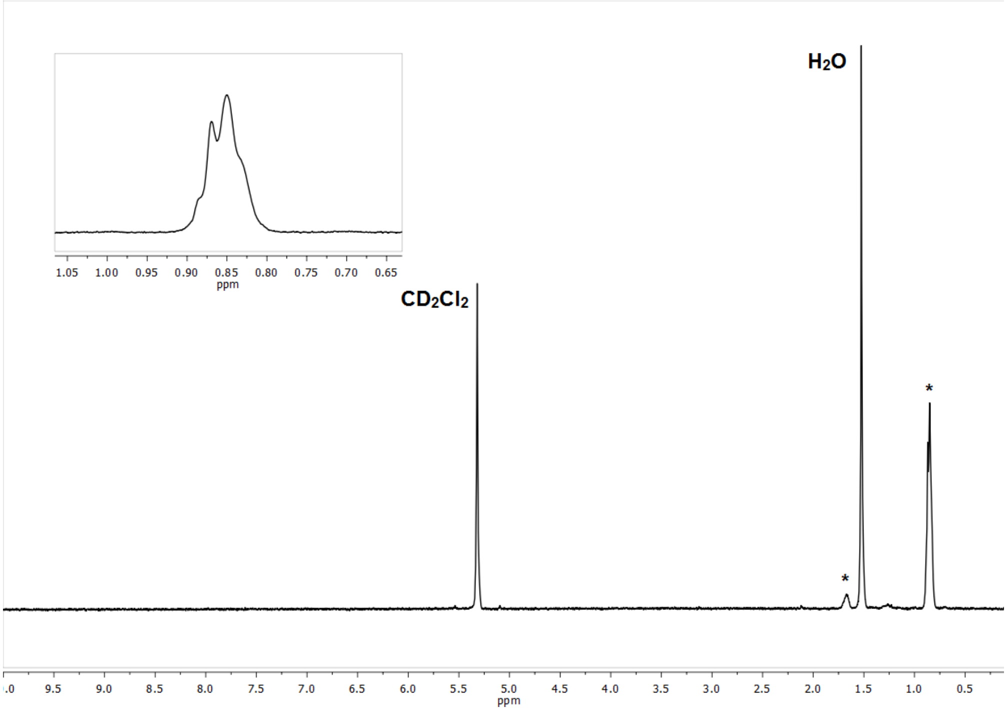

Figure S38: The solution ^{1}H NMR (CD_2Cl_2, 298 K, 400 MHz) spectrum of isolated volatiles. Residual protio-isobutane signals observed are marked with *.

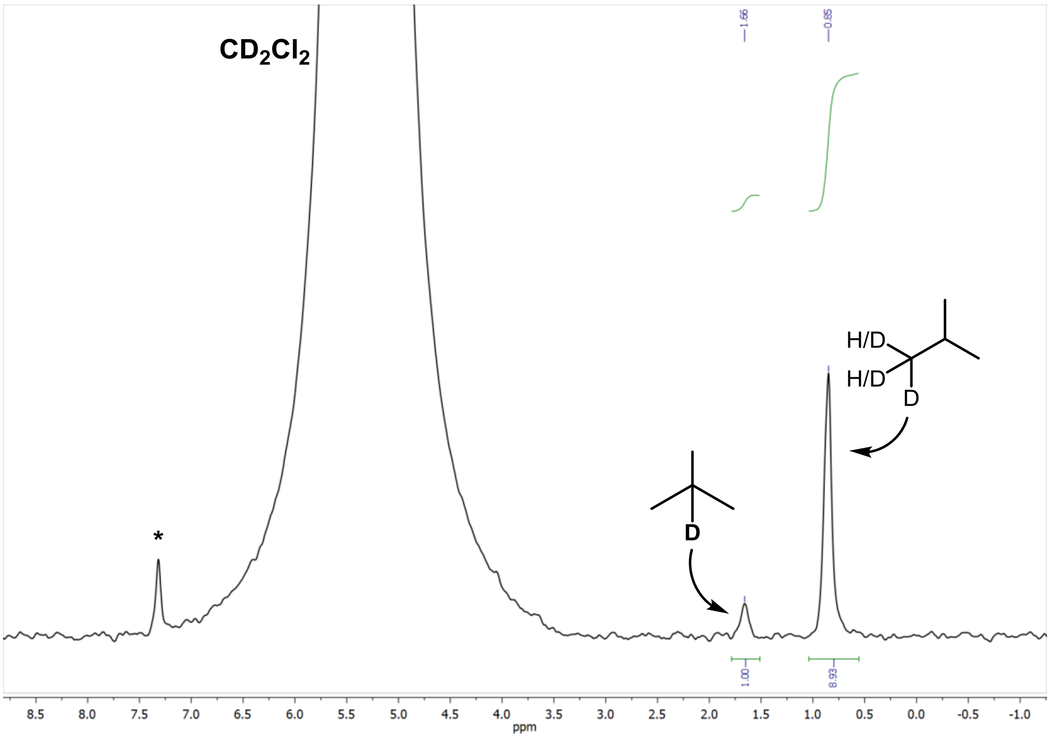

Figure S39: The solution ^{2}H NMR (CD_2Cl_2, 298 K, 61 MHz) spectrum of isolated volatiles. The signal marked * is from a $CDCl_3$ impurity.

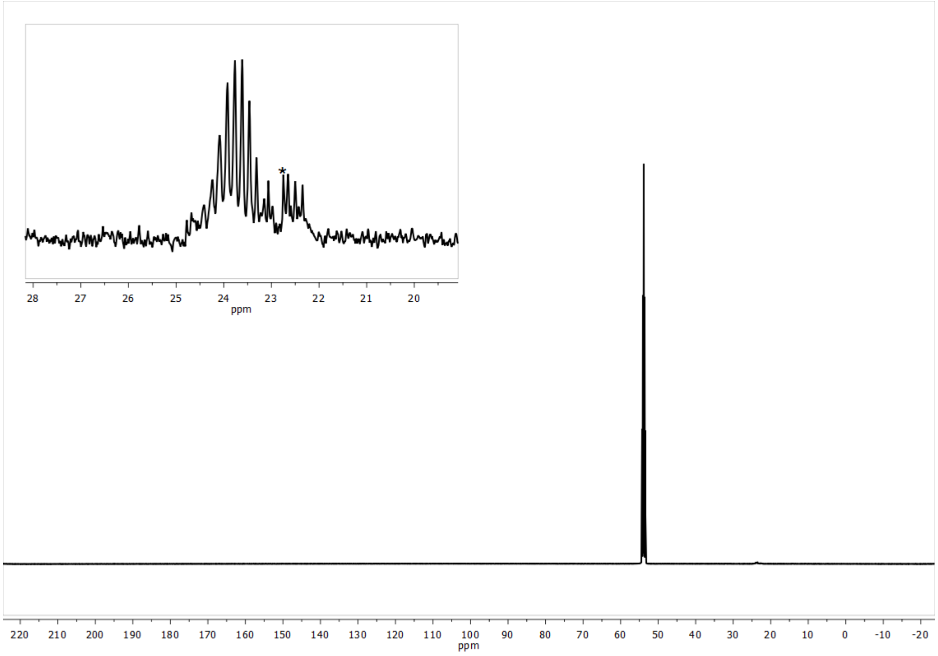

Figure S40: The solution $^{13}C\{^{1}H\}$ NMR (CD_2Cl_2, 298 K, 126 MHz) spectrum of isolated volatiles. The inset in an enlargement of the resonances between δ 27 – 20, where the signal marked * is from a pentane impurity.

S.3.1.3. GC EI-MS Spectra of isobutane-d$_x$ (x = 10 – 7) and isobutane-h$_{10}$

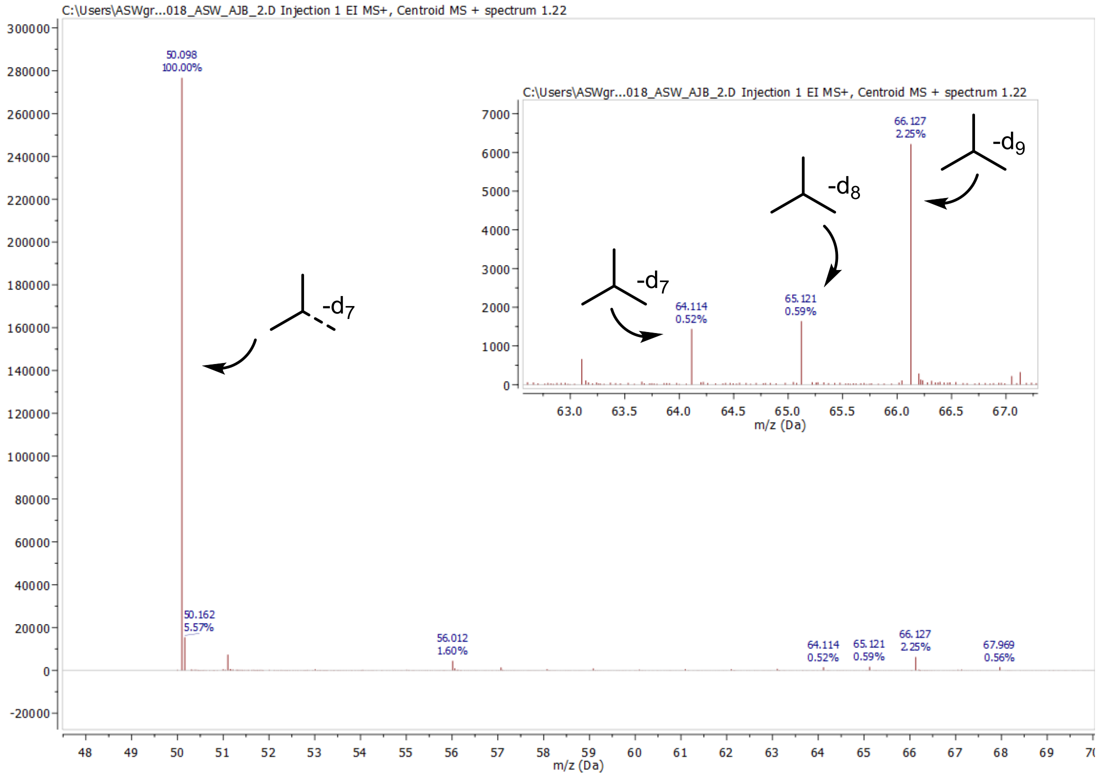

Figure S41: Mass spectrum of the isolated isobutane-d$_x$ with enlargement of m/z = 62 – 69 region. Due to relative ease of fragmentation of isobutane,[S8] the molecular ion peak is that of $C_4D_9^+$, m/z = 66.127 (calc. 66.1269) with greatest intensity fragment of $C_3D_7^+$, m/z = 50.098 (calc. = 50.098). Other main isotopologues are of $C_4HD_8^+$, m/z = 65.121 (calc. 65.120), C4$H_2D_7^+$, m/z = 64.114 (calc. 64.114).

To further show the relative ease of fragmentation; commercially bought isobutane-H$_{10}$ was studied using GC EI-MS, shown in Figure S42.

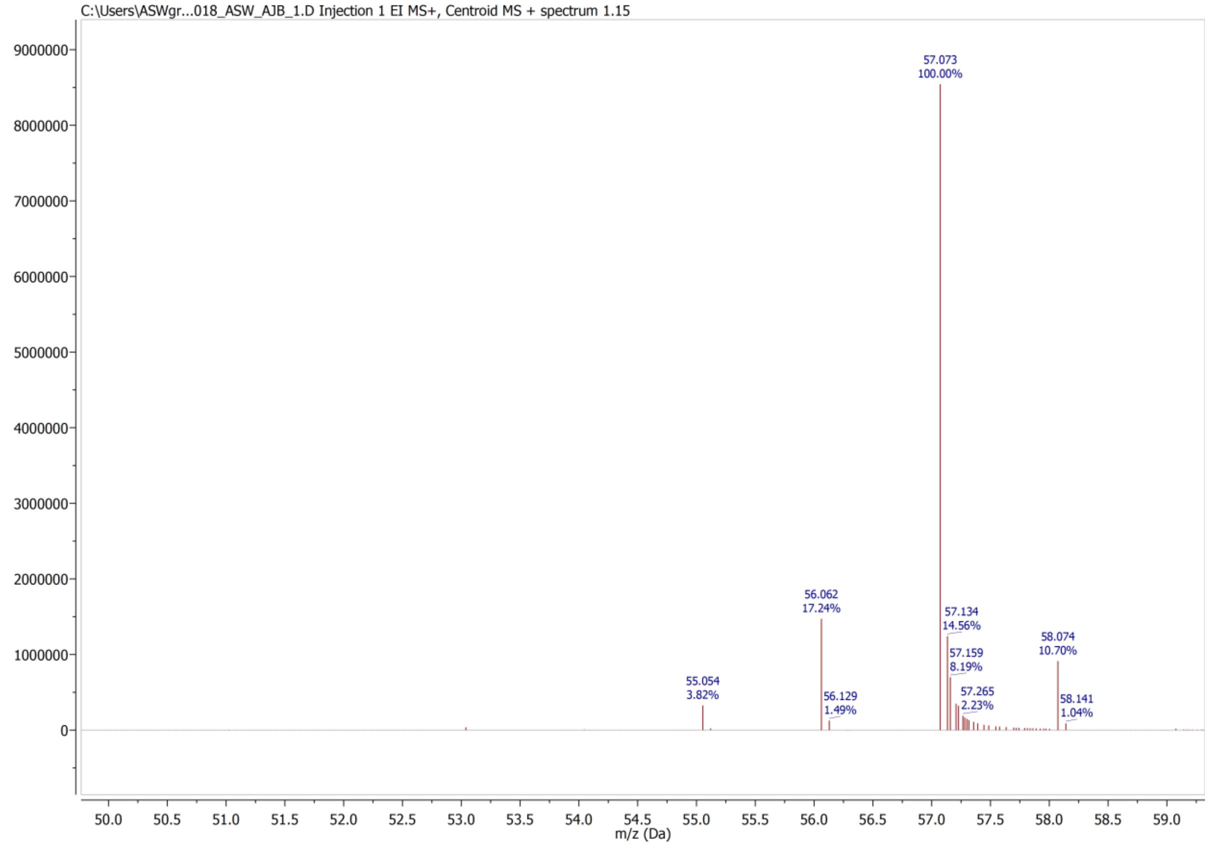

Figure S42: GC EI-Mass spectrum of commercially bought isobutane-H_{10}. Due to relative ease of fragmentation of isobutane,[S8] the molecular ion peak is that of $C_4H_9^+$, m/z = 57.073 (calc. 57.078).

Although approx. 10 % $C_4H_{10}^+$, m/z = 58.074 (calc. 58.078) can be located, in the experimental condition presented above, the percentage of $C_4D_{10}^+$ in the isobutane-d_x sample is below the detection intensity of the equipment, and hence cannot be unequivocally identified.

S.3.1.4. Simulated solution $^{13}C\{^{1}H\}$ NMR spectra of isobutane-d$_x$ (x = 10 – 7)

The solution $^{13}C\{^{1}H\}$ NMR spectrum of isolated isobutane-d$_x$ (x = 10 – 7) (Figure S40) was de-convoluted using the Spin Simulation function on MestReNova, shown in Figure S43. The line width was kept at 6.0 Hz throughout, only changing the levels of population in each simulated environment.

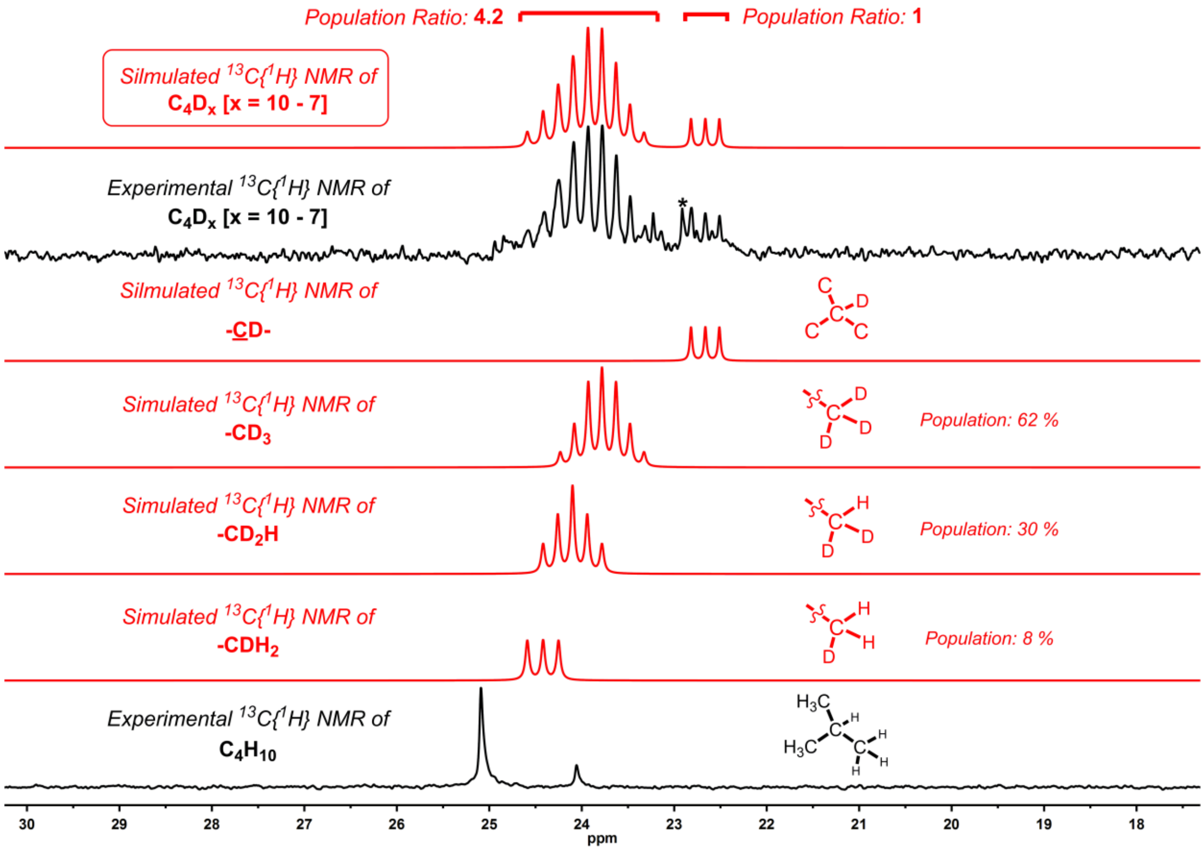

Figure S43: Simulated solution $^{13}C\{^{1}H\}$ NMR spectra of isobutane-d$_x$ (x = 10 – 7), showing approximated populations of varyingly level of deuteration in the –CX$_3$ groups of isobutane. The signal marked by * is from a pentane impurity.

Three systems were used to recreate the multiplet at δ 23.85, modelling the ^{13}C methyl environments as –CD$_3$, -CD$_2$H and -CDH$_2$. No evidence of -CH$_3$ could be seen in the experimental data so was not modelled. A separate fourth system was also modelled describing the triplet at δ 22.66; reported as the methine carbon of isobutane-d$_x$, split by a single bound deuterium. The proto-methine group could not be modelled, as signals obscured by multiplet at δ 23.85.

The simulation suggests that 62 % of the $–CX_3$ groups were of $–CD_3$, 30 % are $-CD_2H$ and 8 % are $–CDH_2$. This is consistent with the GC EI-MS shown in Figure S41, which showed a high proportion of $C_4D_9^+$ and $C_4D_8^+$ from the signals at 66.127 and 65.121 respectively as well as the molecular ion of 50.098^+ from $C_3D_7^+$.

The population ratio of each ^{13}C environment in the simulated spectra was calculated from the sum of each individual $–CD_xH_Y$ component in each environment compared between the environments. These ratios suggest an approximate 1:4.2 ratio of carbon environments; albeit a little higher than predicted (1:3). This may be due to unmodelled –C-H methine group's signals obscured by the multiplet at δ 23.85, affecting this ratio.

S.3.2. Solution-state deuteration of [1-C_4H_8][BAr$^F_4$]

A solution of **[1-C_4H_8][BAr$^F_4$]** (10 mg) in $C_6F_2H_4$ in a thick walled NMR tube was freeze-pump-thaw degassed three times and backfilled with D_2 (1 bar, 298 K). Upon agitation the color of the solution changed from red to yellow. Solution $^{31}P\{^1H\}$ NMR showed total conversion of the organometallic fragment to be **[1-$C_6H_4F_2$][BAr$^F_4$]**, where the volatile component was then isolated by trap-to-trap distillation. The products were identified as $C_4H_8D_2$ by ^1H and ^2H NMR spectroscopy which is the product of deuteration across the double bond only.

^1H NMR (CD_2Cl_2, 400 MHz, 183 K): δ 0.89 (br s, CH).

^2H NMR (CD_2Cl_2, 61 MHz, 183 K): δ 1.66 (br s, 1D, CD), 0.85 (br s, 1D, CD).

S.3.3. Solid-state H/D exchange on [1-C_6H_{12}][BAr^F_4]

S.3.3.1. General Experimental of H/D Exchange on [1-C_6H_{12}][BAr^F_4]

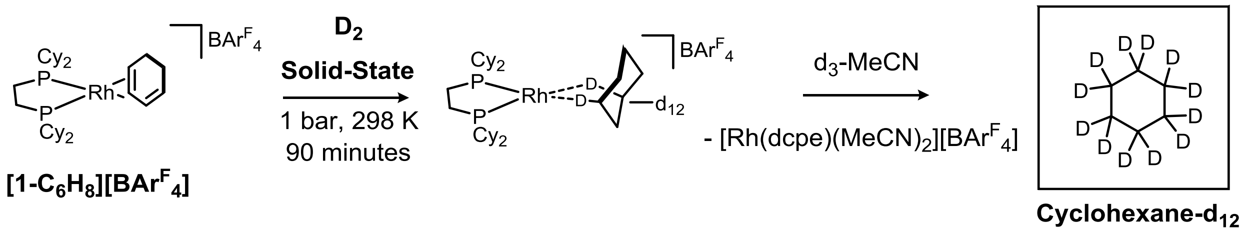

A thick walled NMR tube was charge with powdered microcrystalline **[1-C_6H_8][BAr^F_4]** (10 mg) in an argon filled glove box. The sample was then cooled to 77 K in liquid nitrogen, evacuated and backfilled with D_2 (1 bar, 298 K). After 30 min, sample was then cooled again to 77 K in liquid nitrogen, evacuated and backfilled with D_2 (1 bar, 298 K). This cycle was repeated once more, to give a total of 3 x 30 mins cycles, totaling 90 minutes under D_2. The reaction was then quenched by condensing d_3-MeCN (0.4 mL) into the NMR tube. The volatiles were then isolated by trap-to-trap distillation.

^{2}H NMR (d_3-MeCN, 61 MHz): δ 1.37 (s).

^{13}C{^{1}H} NMR (d_3-MeCN, 126 MHz): δ 25.3 (1:2:3:2:1 quintet, J_{CD} = 19 Hz).

S.3.3.2. NMR Spectra

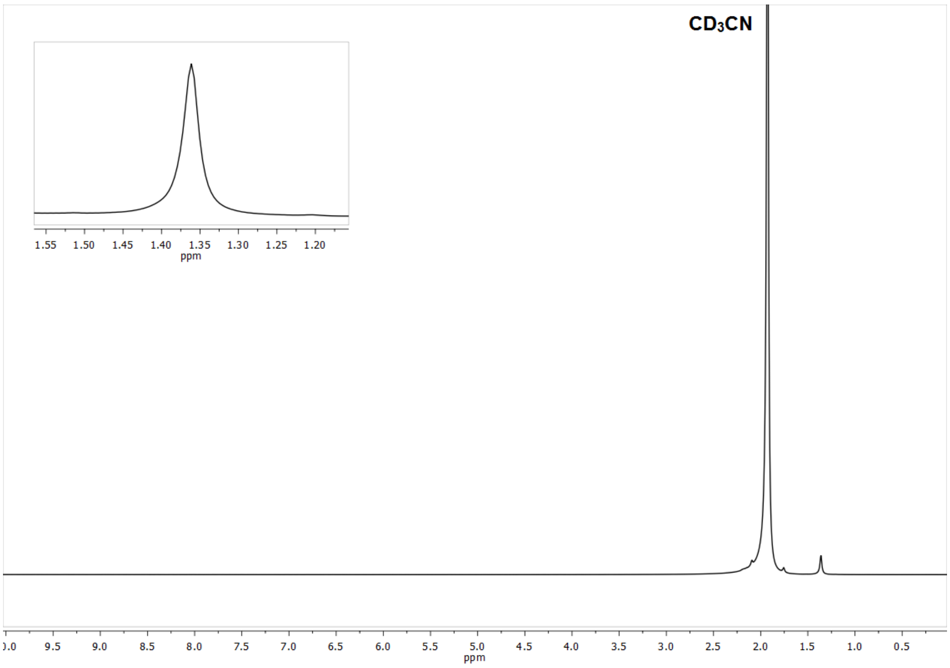

Figure S44: The solution ^{2}H NMR (d_3-MeCN, 298 K, 61 MHz) spectrum of cyclohexane-d_{12}.

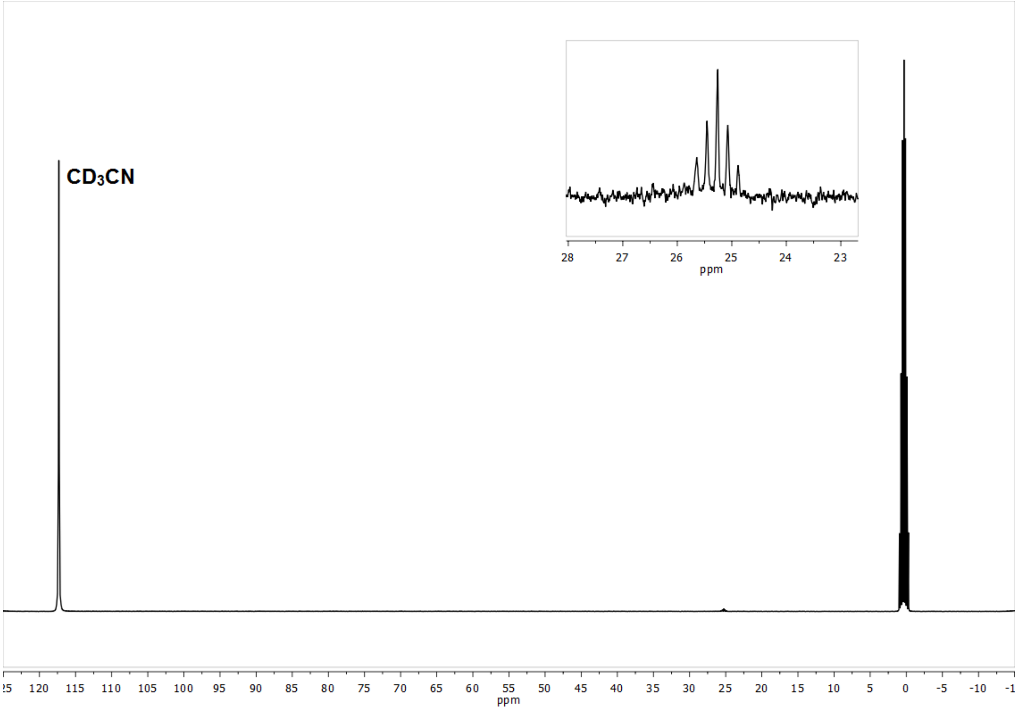

Figure S45: The solution ^{13}C{^{1}H} NMR (d_3-MeCN, 298 K, 100 MHz) spectrum of cyclohexane-d_{12}, δ 25.3 (1:2:3:2:1 quintet, J_{CD} = 19 Hz).

S.3.3.3. GC EI-Mass spectra

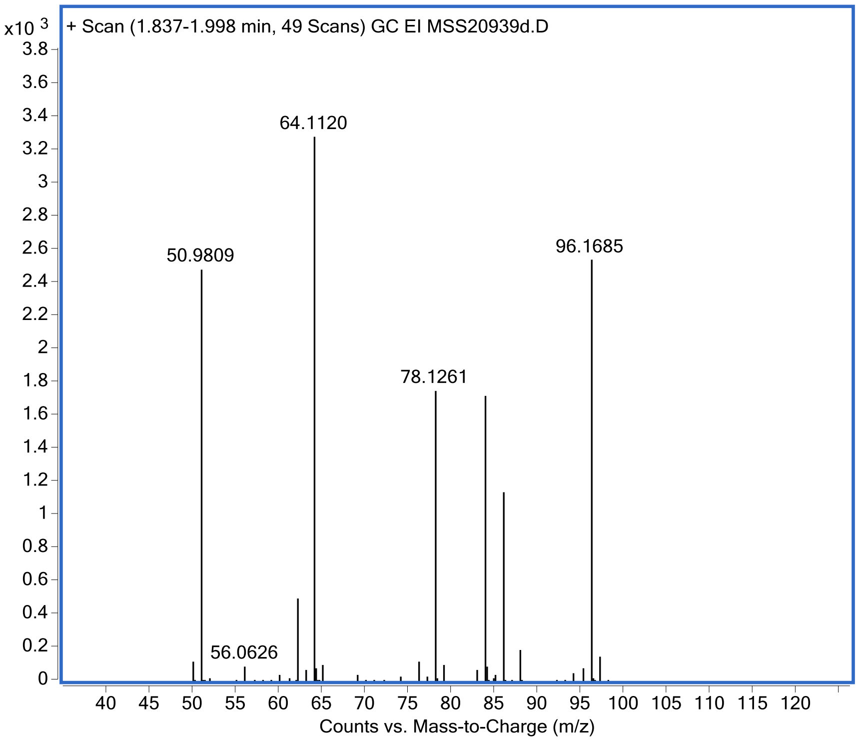

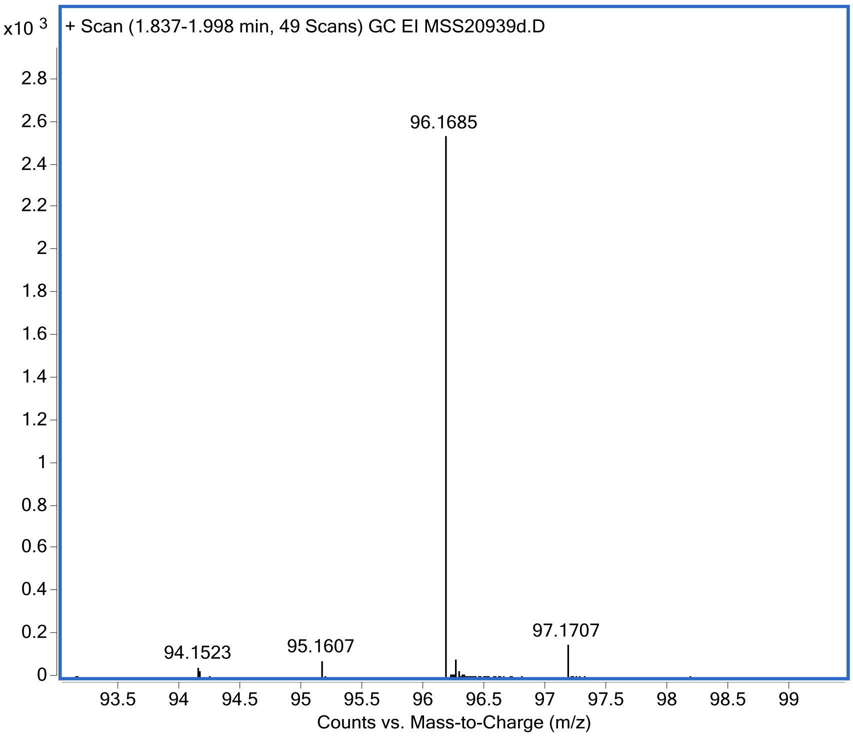

Figure S46: Mass spectrum of the isolated volatiles where the time of D_2 exposure was 30 minutes per cycle (top). Enlargement of m/z = 93 – 100 region (bottom). The signal at m/z = 96.1685 matches that of C_6D_{12} (calc. 96.1687). Signals at m/z = 84 and 86 are due to CH_2Cl_2.

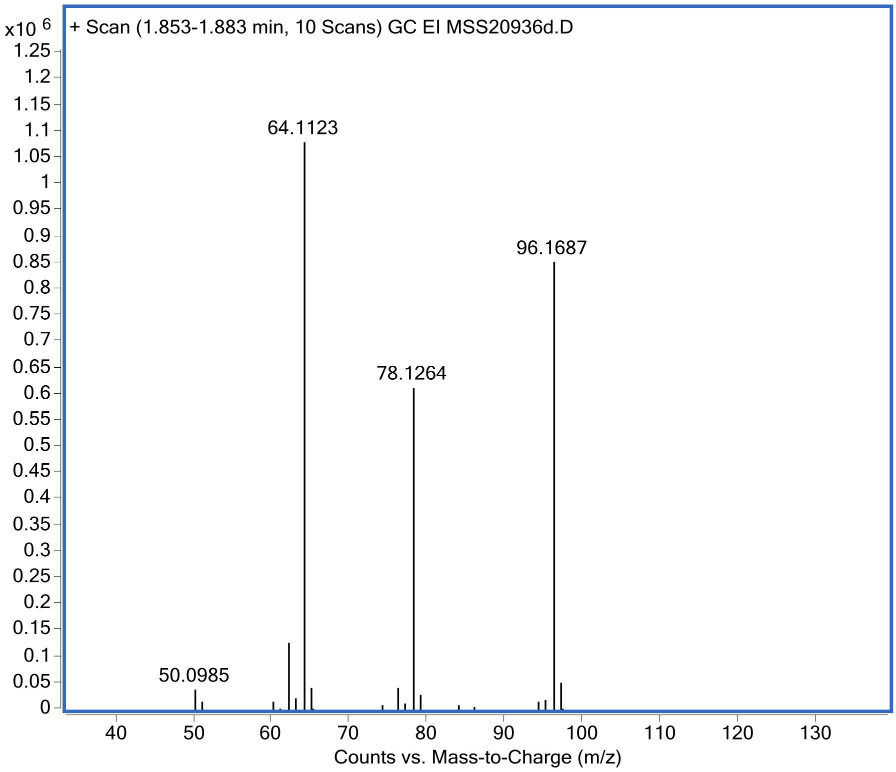

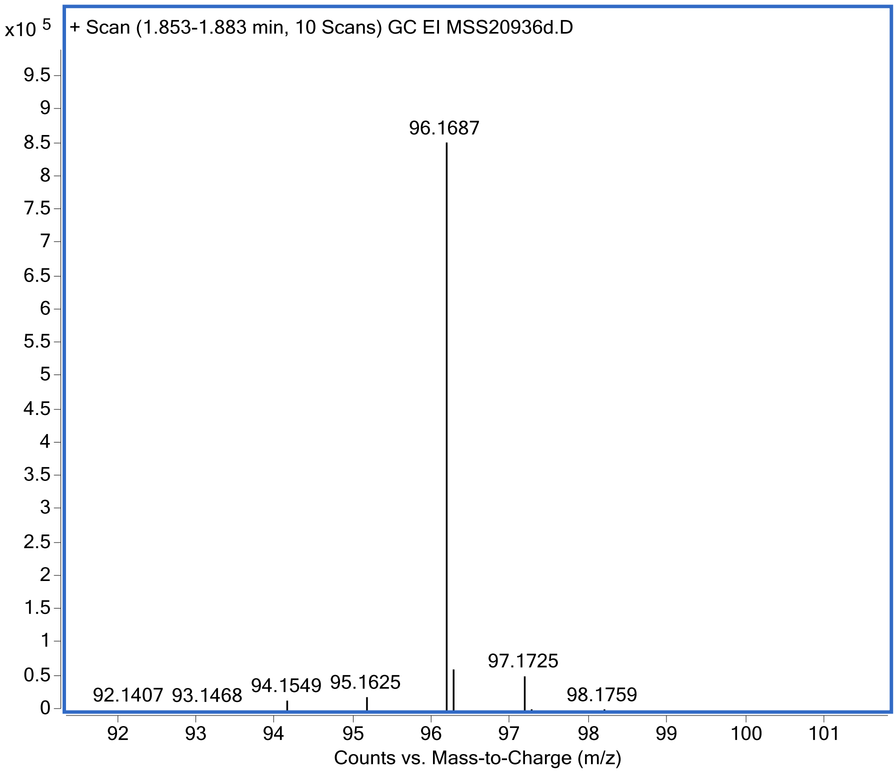

Figure S47: Mass spectrum of a commercially sourced sample of D_{12}-cyclohexane (top). Enlargement of m/z = 91 – 100 region (bottom).

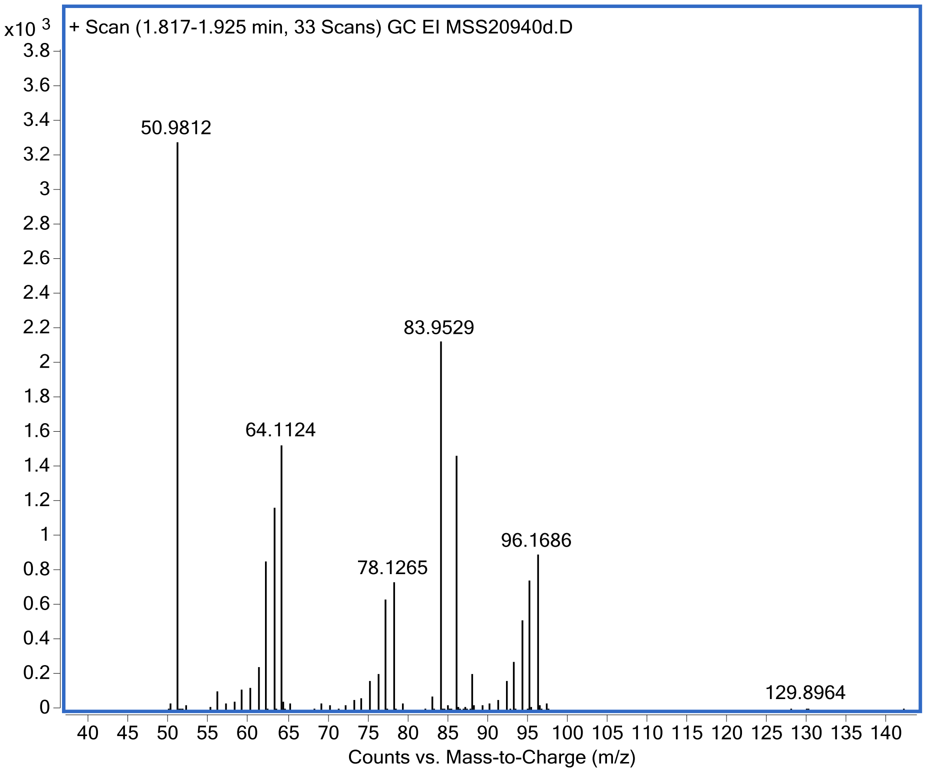

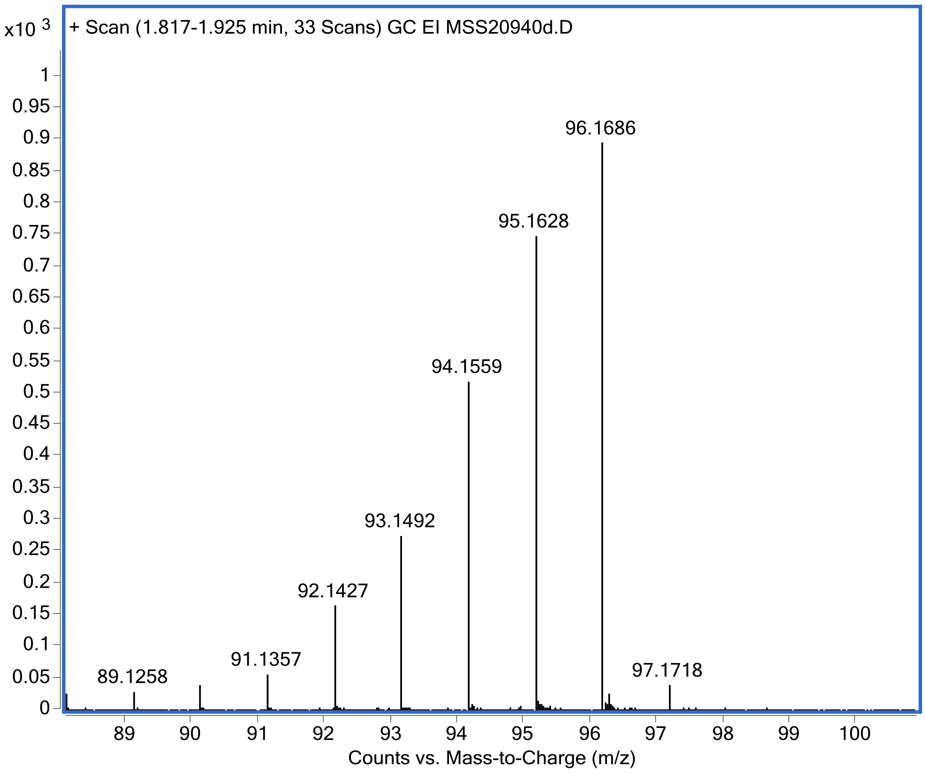

Figure S48: Mass spectrum of the isolated volatiles where the time of D_2 exposure was 5 minutes per cycle rather than 30 minutes (top). Enlargement of m/z = 88 – 100 region (bottom). Signals at m/z = 84 and 86 are due to CD_2Cl_2.

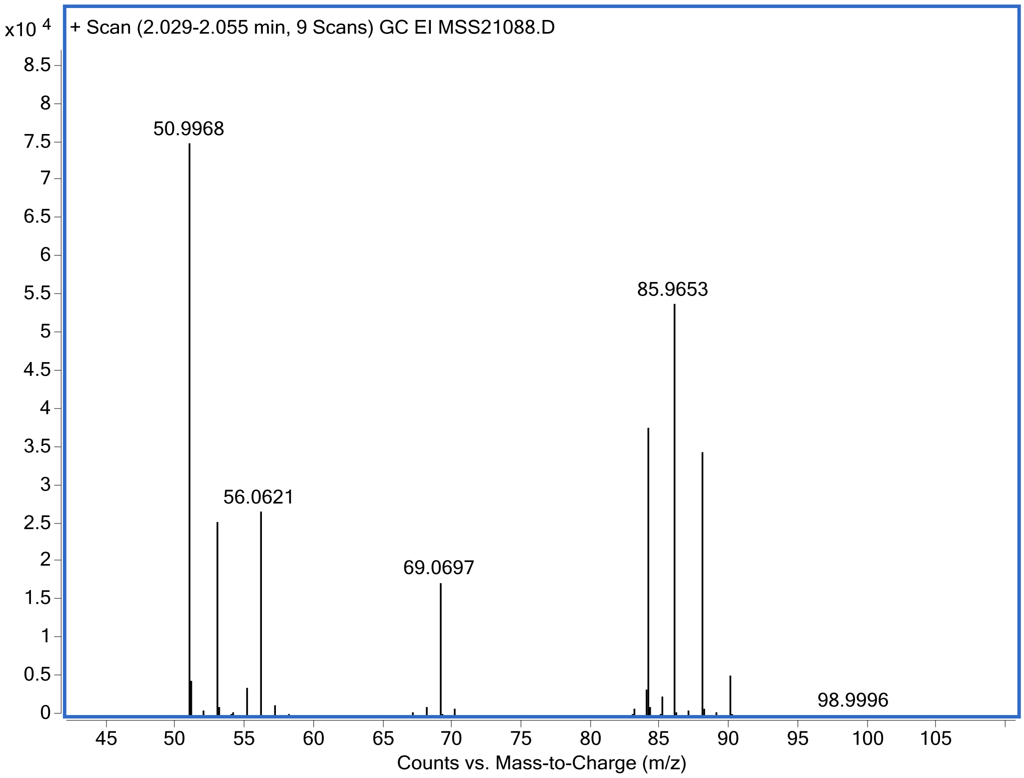

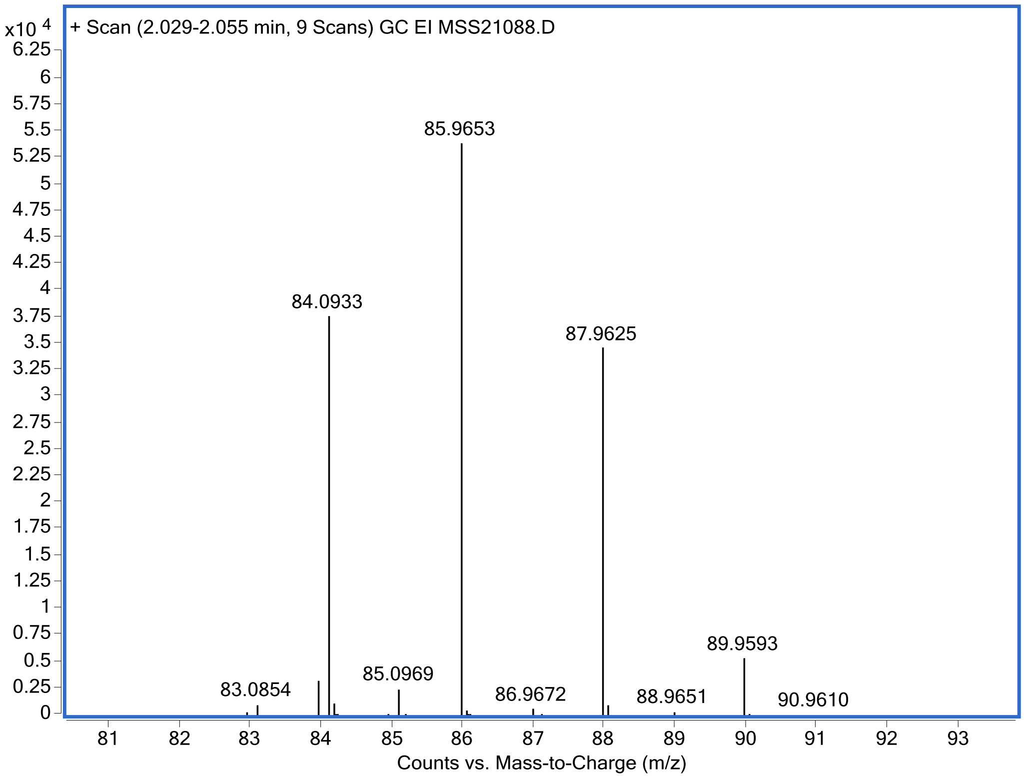

Figure S49: Mass spectrum of the isolated volatiles where the time of D_2 exposure was 0 minutes per cycle rather than 30 minutes (top), i.e., no D_2 exposure. Enlargement of m/z = 81 – 93 region (bottom). The signal at m/z = 84.0933 matches that of C_6H_{12} (calc. 84.0933). Signals at m/z = 86 and 88 are due to CD_2Cl_2.

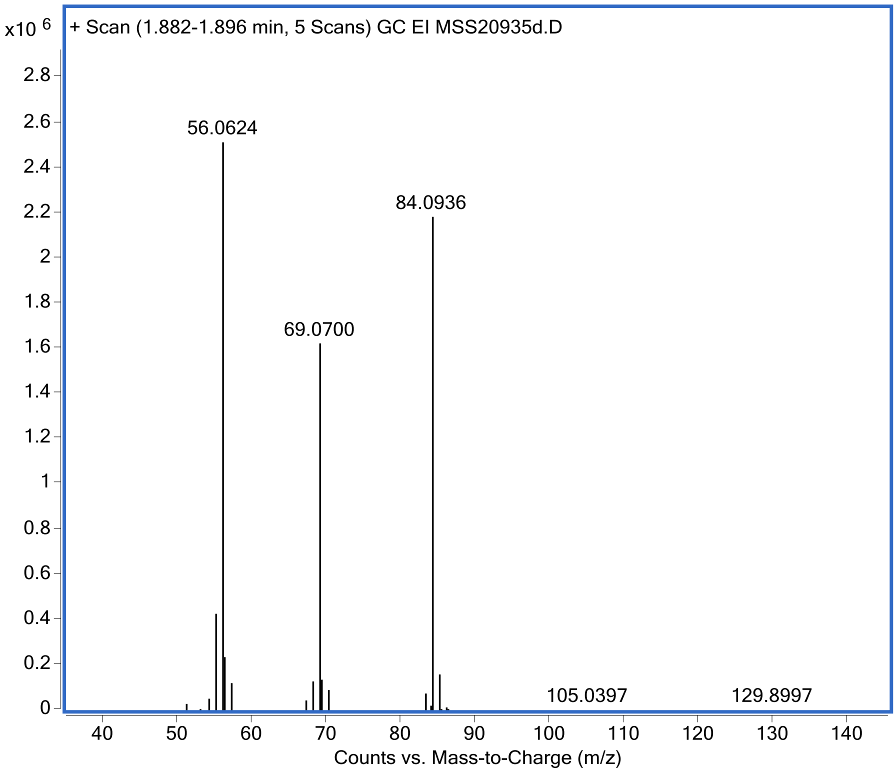

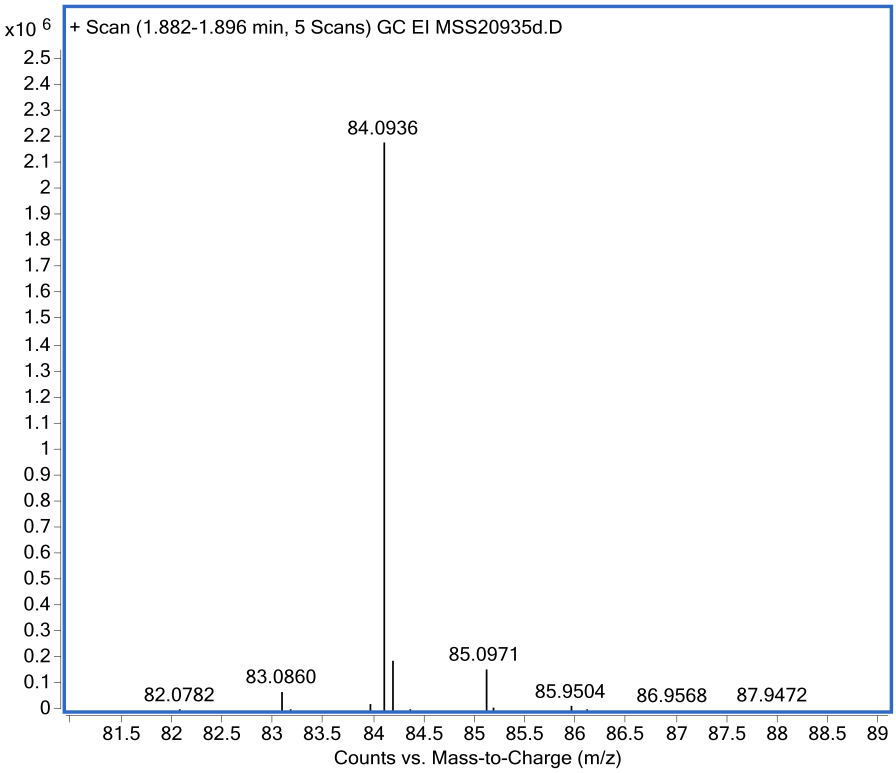

Figure S50: Mass spectrum of a commercially sourced sample of cyclohexane (top). Enlargement of m/z = 81 – 89 region (bottom).

S.3.4. Solution-state deuteration of [1-C_6H_8][BAr$^F_4$]

S.3.4.1. Procedure for the solution-state deuteration of [1-C_6H_8][BAr$^F_4$]

A solution of **[1-C_6H_8][BAr$^F_4$]** (10 mg) in CD_2Cl_2 in a thick walled NMR tube was freeze-pump-thaw degassed three times and backfilled with D_2 (1 bar, 298 K). Upon agitation the color of the solution changed from red to yellow. The volatile component was then isolated by trap-to-trap distillation. The product was identified as $C_6H_8D_4$, which is the product of deuteration across the double bonds only.

^{1}H NMR (CD_2Cl_2, 400 MHz, 183 K): δ 1.52 (br s, 4H, CH), 1.05 (br s, 4H, CH).

^{2}H NMR (CD_2Cl_2, 61 MHz, 183 K): δ 1.54 (br s, 2D, CD), 1.08 (br s, 2D, CD).

S.3.4.2. GC EI-Mass Spectra

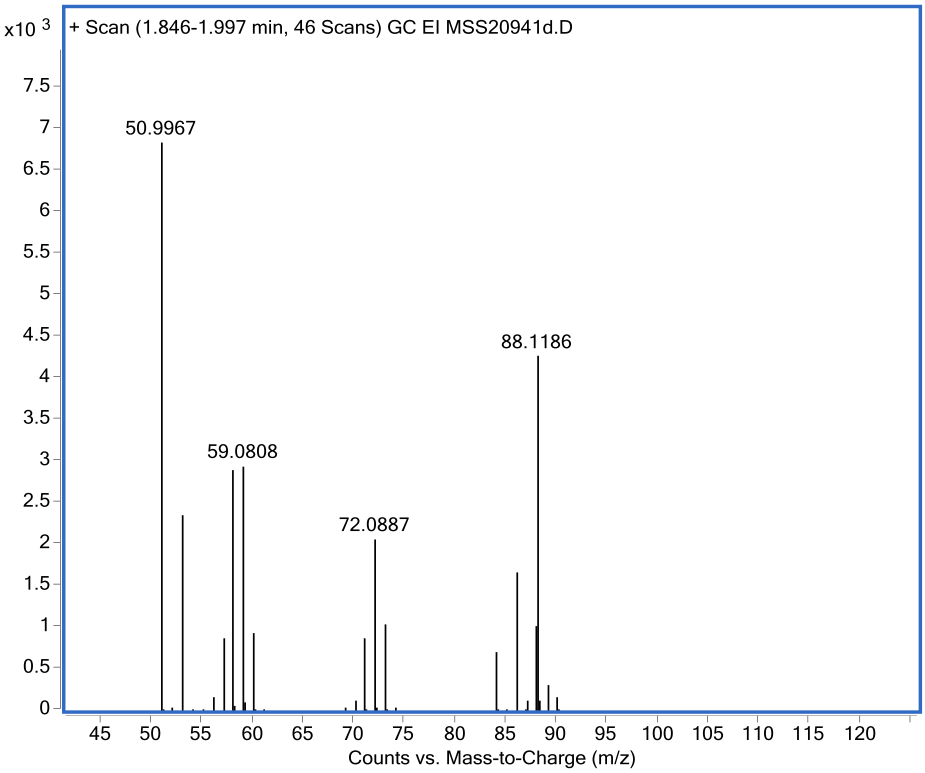

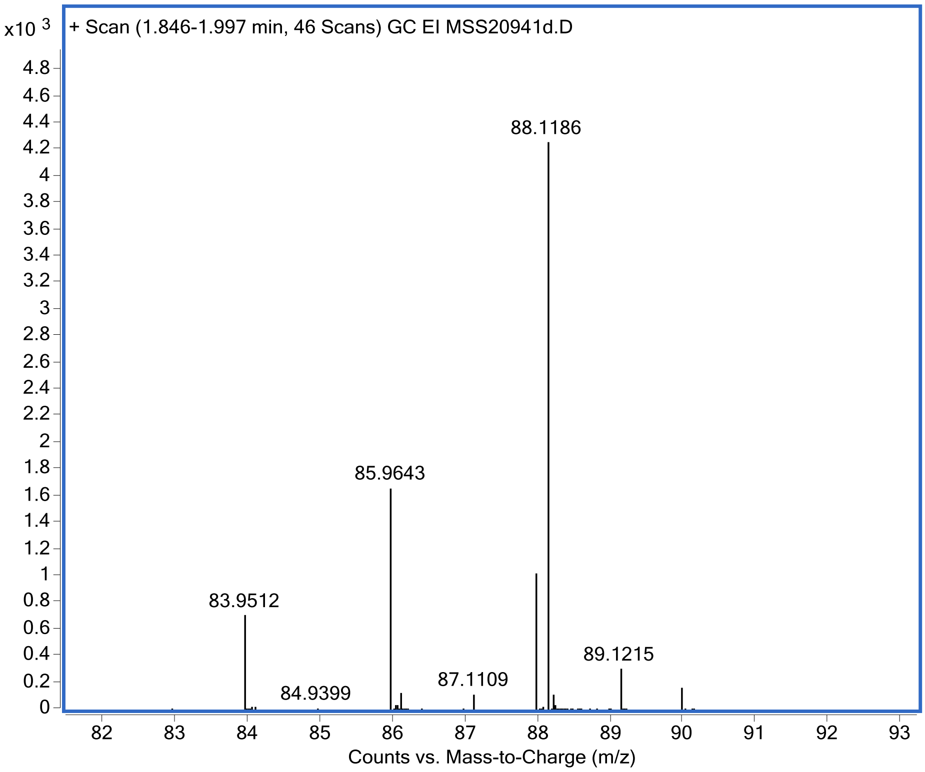

Figure S51: Mass spectrum of the isolated volatiles (top). Enlargement of m/z = 81 – 89 region (bottom). The signal at m/z = 88.1186 matches that of $C_6H_8D_4^+$ (calc. 88.1185). Signals at m/z = 84 and 86 are due to CH_2Cl_2.

S.4. Alkane Dehydrogenation Experiments

S.4.1. Dehydrogenation of **[1-C_4H_{10}][BAr$^F{}_4$]** to form **[1-C_4H_8][BAr$^F{}_4$]**

S.4.1.1. Solid-state dehydrogenation of [1-C_4H_{10}][BAr$^F{}_4$] under *argon flow* to form [1-C_4H_8][BAr$^F{}_4$]

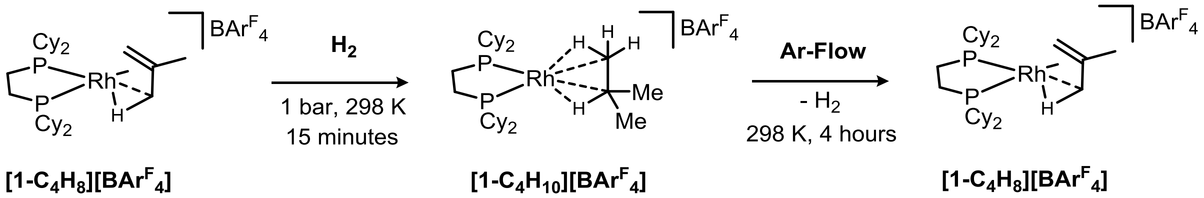

A J Young flask (ca. 50 mL) was charged with 50 mgs of block like crystalline material of **[1-C_4H_8][BAr$^F{}_4$]**. The flask was evacuated (1×10^{-2} mbar) and H_2 (1 bar, 298 K) was added for 15 minutes; to yield deep red coloured crystallites of **[1-C_4H_{10}][BAr$^F{}_4$]**.

A portion of this (approx. 10 mgs) was taken at this point, dissolved in CH_2Cl_2 and solution $^{31}P\{^1H\}$ NMR spectrum taken. No signals relating to **[1-C_4H_8][BAr$^F{}_4$]** could be identified, only signals relating to **[1-BAr$^F{}_4$]** and further solvent activated complexes – confirming the hydrogenation of total **[1-C_4H_8][BAr$^F{}_4$]** had occurred.

The remaining solid was placed under an argon flow for 4 hours. This was done by placing an exit needle into the suba sealed J Young flask which was open to argon flow, with regulator pressure set at 0.5 bar. After 4 hours, the sample was sealed, transferred to a glove box and packed inside a solid state NMR rotor and analyzed $^{31}P\{^1H\}$ and $^{13}C\{^1H\}$ solid state NMR spectroscopy.

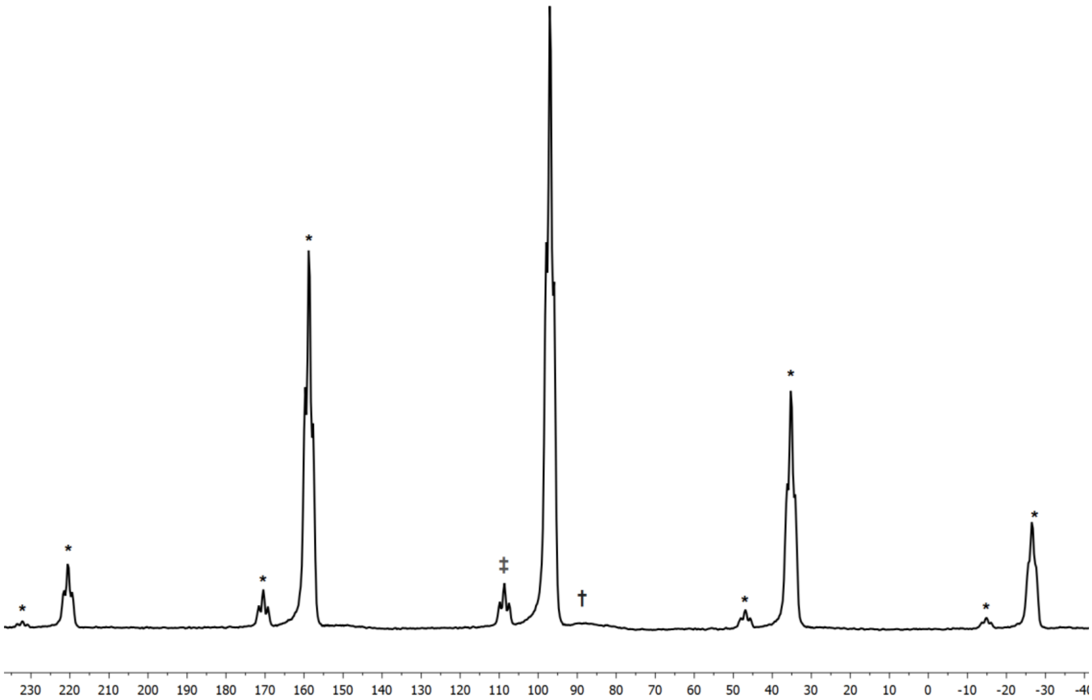

Figure S52: The $^{31}P\{^{1}H\}$ SSNMR (162 MHz, 295 K, 10 kHz spin rate) spectrum of the dehydrogenation of powdered microcrystalline **[1-C_4H_{10}][BAr$^F_4$]** under argon flow to form **[1-C_4H_8][BAr$^F_4$]** (approx. 90 %). The rotor is packed under an argon atmosphere. The resonances ‡ marked are assigned to **[1-C_4H_{10}][BAr$^F_4$]** (approx. 7%), from incomplete dehydrogenation and the resonances marked † are assigned to the decomposition product of **[1-BAr$^F_4$]**[S2] (approx. 3 %), formed during the initial hydrogenation. The resonances marked ***** are due to spinning sidebands.

S.4.1.2. Kinetics of the solid-state **[1-C_4H_{10}][BAr$^F{}_4$]** dehydrogenation ***under vacuum*** to form **[1-C_4H_8][BAr$^F{}_4$]**

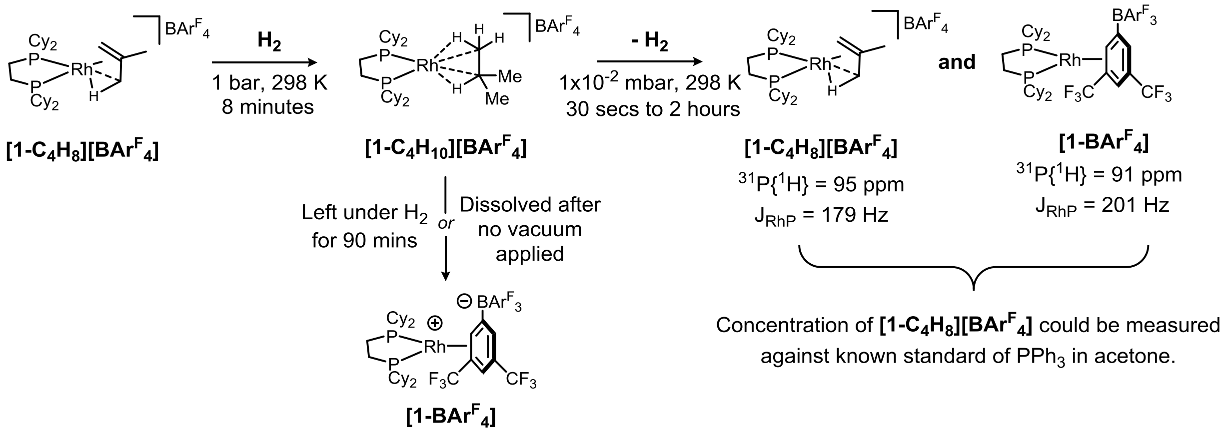

A J Young NMR tube (~ 2.1 mL) was charged with 10 mgs powdered crystalline material of **[1-C_4H_8][BAr$^F{}_4$]**. The tube was evacuated (1 × 10^{-2} mbar) and H_2 (1 bar, 298 K) was added for 8 minutes to yield deep red powder of **[1-C_4H_{10}][BAr$^F{}_4$]**. The samples were placed under vacuum (1 × 10^{-2} mbar) for varying times between 0 seconds and 2 hours, then dissolved in CD_2Cl_2 and analyzed by $^{31}P\{^1H\}$ NMR spectroscopy.

The above procedure was repeated on numerous occasions, varying the period of time the sample was exposed to vacuum at room temperature. When time = 0 seconds, no signals relating to **[1-C_4H_8][BAr$^F{}_4$]** could be identified, confirming the complete hydrogenation of the sample.

After dissolution in CD_2Cl_2, two doublets were observed in the $^{31}P\{^1H\}$ NMR spectra at 298 K; the dehydrogenation product **[1-C_4H_8][BAr$^F{}_4$]** (δ 95) and decomposition product **[1-BAr$^F{}_4$]**[S2] (δ 91). The concentration of re-formed **[1-C_4H_8][BAr$^F{}_4$]** could be accurately measured by use of an separate, sealed capillary of PPh_3 in acetone.

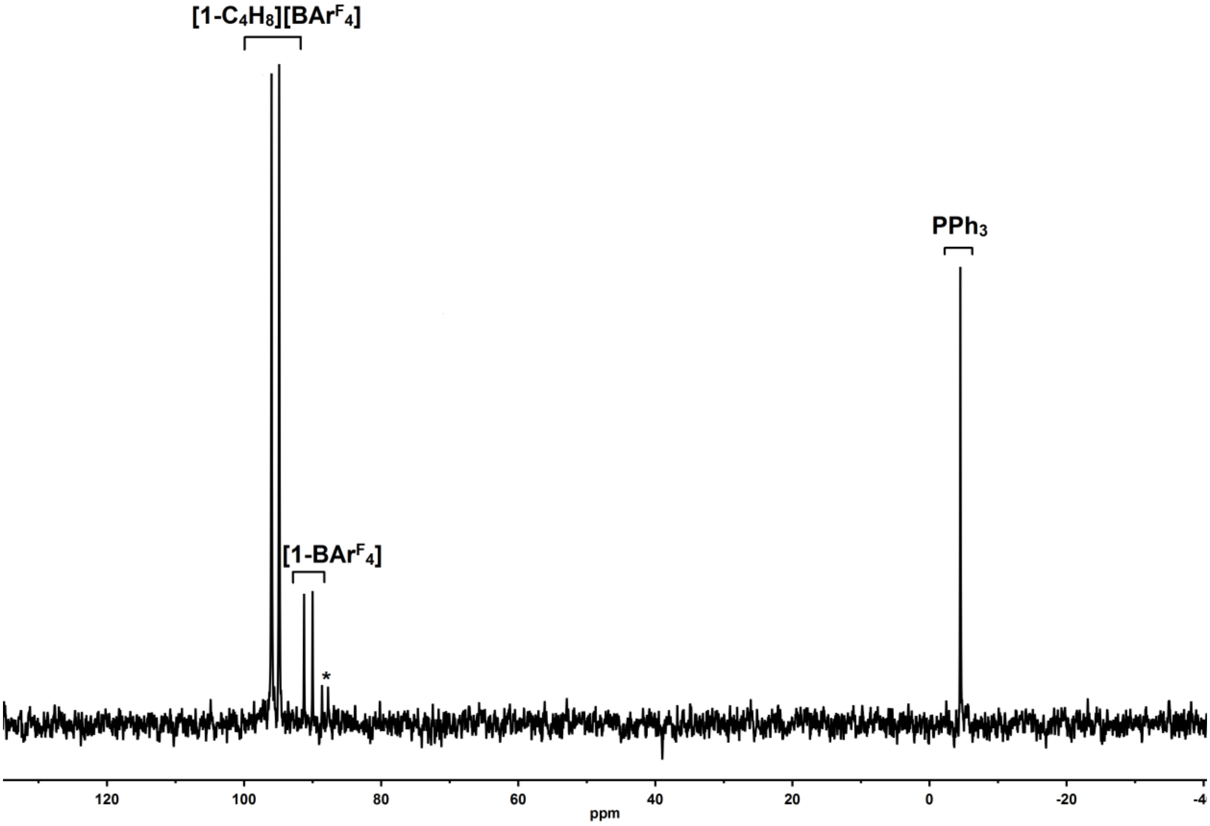

Figure S53: Example of a solution ^{31}P{^{1}H} NMR (CD_2Cl_2, 298 K, 162 MHz) spectra of the dehydrogenation of **[1-C_4H_8][BAr$^F_4$]** under vacuum for 1 hour. Signals can be observed from **[1-C_4H_8][BAr$^F_4$]** (δ 95, d., 179 Hz) and **[1-BAr$^F_4$]** (δ 91, d., J_{RhP} = 201 Hz) with PPh_3 (δ -6, in acetone within sealed capillary). * = a further, unidentified CH_2Cl_2 decomposition product of **[1-BAr$^F_4$]**.[S2]

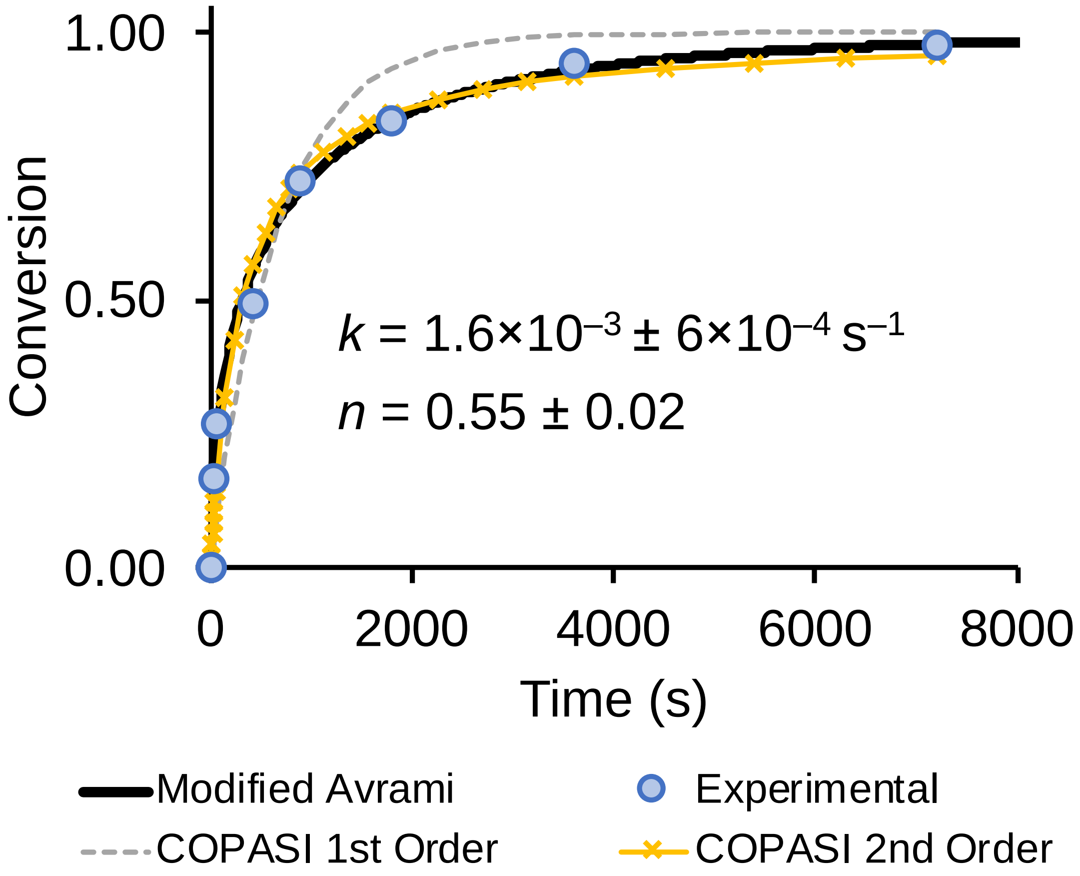

Figure S54: Modified JAMK Plot of Conversion[S9] (f) = $(1–e^{(–kt)n})$ versus time for the dehydrogenation of **[1-C_4H_{10}][BAr$^F_4$]** to **[1-C_4H_8][BAr$^F_4$]** in the solid-state. Where k = growth rate constant and n = Avrami exponent.

Shown with comparison to a COPASI[S10] modelled first order process for dehydrogenation (**[1-C_4H_{10}][BAr$^F_4$] → [1-C_4H_8][BAr$^F_4$]**, k = 1.5(2) × $10^{–3}$ $s^{–1}$) and a second order process (2 x **[1-C_4H_{10}][BAr$^F_4$] → [1–C_4H_8][BAr$^F_4$] + [1–C_4H_{10}][BAr$^F_4$]**, k = 1.6(2) × $10^{–4}$ $M^{–1}s^{–1}$). Initial concentration of dissolved samples = 19.8 mM (conversion = 0 %).

S.4.1.3. *Single-Crystal* to *Single-Crystal* dehydrogenation of [1-C_4H_{10}][BAr^F_4] under *vacuum* to form [1-C_4H_8][BAr^F_4] for an x-ray diffraction study

A J Young NMR tube (~ 2 mL) was charged with 10 mgs of orange coloured, block like crystalline material of **[1-C_4H_8][BAr^F_4]**. The flask was evacuated (1 × 10^{-2} mbar) and H_2 (1 bar, 298 K) was added for 15 minutes to yield deep red crystallites of **[1-C_4H_{10}][BAr^F_4]**. The sample was then placed under vacuum (2 × 10^{-2} mbar) for 4 hours, to which the colour of the crystals after this time had returned to orange.

The crystalline material was then coated with Fomblin® Y oil under an argon flush, a suitable crystal was rapid selected and then transferred to the cryostream of a diffractometer and an x-ray diffraction study was undertaken.

The crystals were of sufficient quality to be collected, and solved, as **[1-C_4H_8][BAr^F_4]-SC-SC**. For further details of the structural study, please refer to section S.5.

S.4.2. Dedeuteration of [1-C_4D_x-alkane][BAr^F_4] under vacuum to form [1-C_4D_x-alkene][BAr^F_4]

S.4.2.1. Solid state dedeuteration of [1-C_4D_x-alkane][BAr^F_4] *under vacuum* to form [1-C_4D_x-alkene][BAr^F_4]

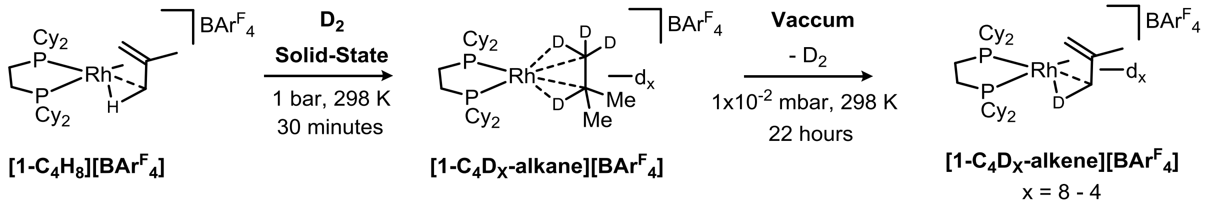

A J Young NMR tube (~ 3 mL) was charged 30 mgs of block-like crystallites of **[1-C_4H_8][BAr^F_4]**. The flask was evacuated (1 × 10^{-2} mbar) and D_2 (1 bar, 298 K) was added to yield red crystalline powder of **[1-C_4D_x-alkane][BAr^F_4]**, and left for 30 minutes. After this time, the sample was placed under vacuum at room temperature for 22 hours to yield **[1-C_4D_x-alkene][BAr^F_4]**, where (x = 8 – 6).

S.4.2.2. Characterization data for [1-C_4D_x-alkene][BAr^F_4]

^{1}H NMR (CD_2Cl_2, 298 K, 400 MHz): δ 7.73 (s, 8H, ortho-ArH), 7.57 (s, 4H, para-ArH), 5.32 ($CDHCl_2$), 2.09-1.64 (br m, 24H, overlapping aliphatic CH), 1.40-1.0.96 (br m, 20H, overlapping aliphatic CH).

^{1}H NMR (CD_2Cl_2, 183 K, 400 MHz): δ 7.75 (s, 8H, ortho-ArH), 7.56 (s, 4H, para-ArH), 5.32 ($CDHCl_2$), 2.22-1.38 (br m, 24H, overlapping aliphatic CH), 1.38-0.63 (br m, 24H, overlapping aliphatic CH).

^{2}H NMR (CD_2Cl_2, 298 K, 400 MHz): δ 1.55 (br. s)

^{2}H NMR (CD_2Cl_2, 183 K, 400 MHz): δ 0.72 (br. m)

^{31}P{^{1}H} NMR (CD_2Cl_2, 298 K, 162 MHz): δ 95.3 (d, J_{RhP} 179 Hz).

^{31}P{^{1}H} NMR (CD_2Cl_2, 183 K, 162 MHz): δ 97.6 (d. of d., J_{RhP} 201 Hz, J_{PP} 26 Hz), 93.6 (d. of d., J_{RhP} 158 Hz, J_{PP} 26 Hz) .

ESI-MS: Not stable under mass spectrometric conditions (20eV, 333K). Species with appropriate isotopic distributions at m/z found = 581.240, calculated to $[(Cy_2PCH_2CH_2PCy_2)Rh(N_2)_2]^+$ (581.242). There is no evidence for the nitrogen compound in bulk samples so it is assumed to form via an in-situ ESI-MS process.

S.4.2.3. NMR Spectra of [1-C_4D_x-alkene][BAr^F_4]

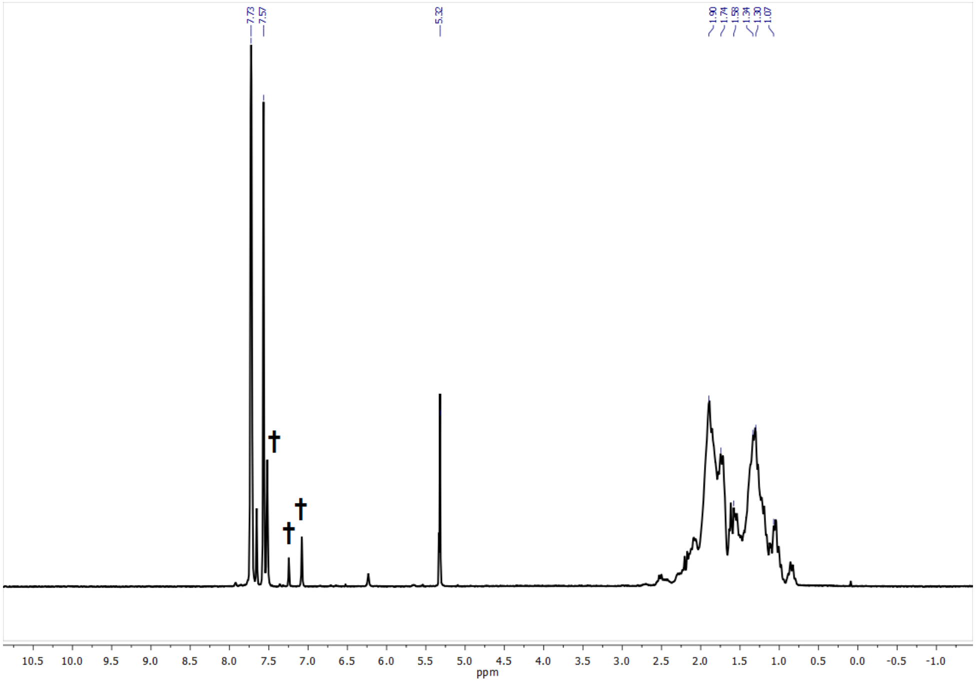

Figure S55: The solution ^{1}H NMR (CD_2Cl_2, 298 K, 400 MHz) spectrum of **[1-C_4D_x-alkene][BAr^F_4]**. Signals marked **†** are due to **[1-BAr^F_4]**.

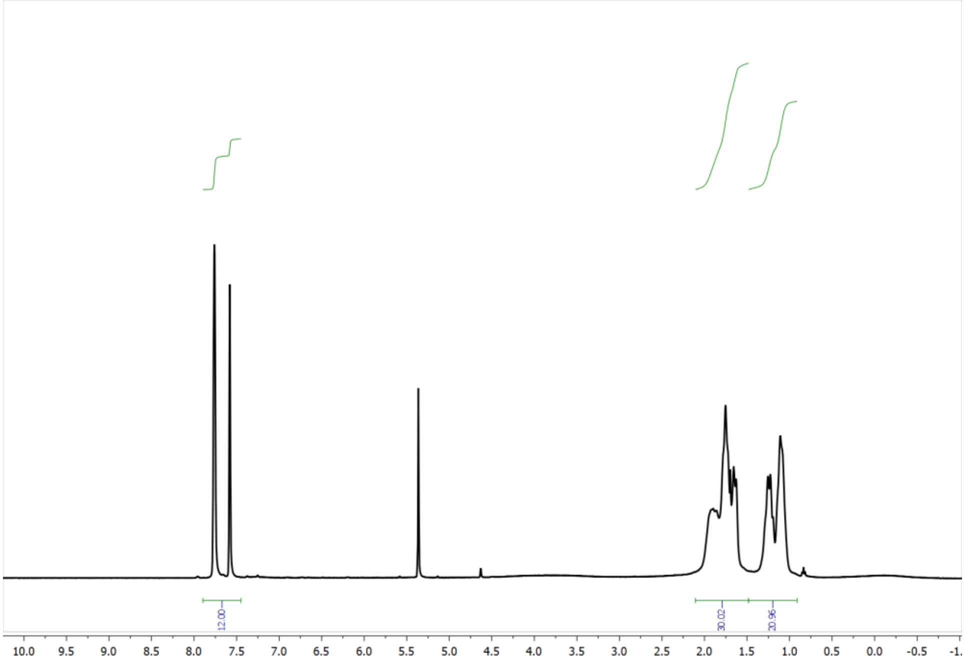

Figure S56: The solution ^{1}H NMR (CD_2Cl_2, 183 K, 400 MHz) spectrum of **[1-C_4D_x-alkene][BAr^F_4]**. Protio-alkene signals are not observed, unlike in Figure S2 of **[1-C_4H_8][BAr^F_4]** at 183 K, suggestive of isotopic substitution of these protons.

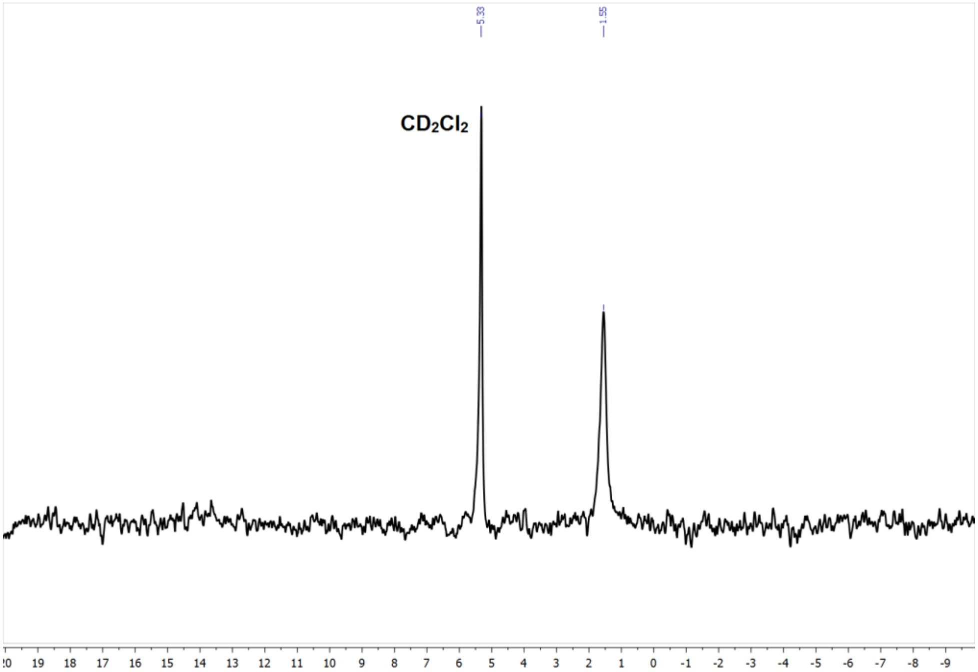

Figure S57: The solution ^{2}H NMR (CH_2Cl_2, 298 K, 61 MHz) spectrum of **[1-C_4D_x-alkene][BAr^F$_4$]**.

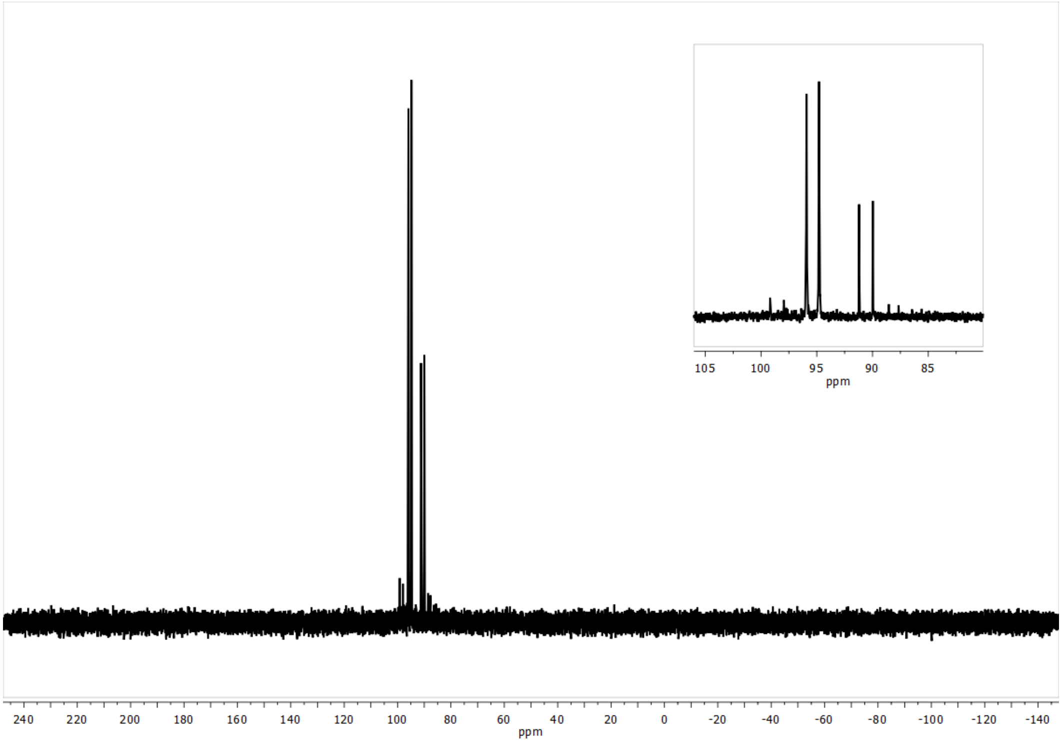

Figure S58: The solution ^{31}P {^{1}H} NMR (CD_2Cl_2, 298 K, 162 MHz) spectrum of **[1-C_4D_x-alkene][BAr^F$_4$]**, with ~ 40 % decomposition to **[1-BAr^F$_4$]**. This decomposition to **[1-BAr^F$_4$]** has occurred after an extended time under D_2, see section S.2.2.6.

S.4.2.4. Liberation of bound isobutene-d_x (x = 8 – 6)

After preparation of **[1-C_4D_x-alkene][BAr$^F{}_4$]** following the procedure in section S.4.2.1., **[1-C_4D_x-alkene][BAr$^F{}_4$]** was dissolved in CD_2Cl_2 in a J Young NMR tube and the solution was freeze pump thawed degassed three times. CO (1 bar, 298K) was added and after 2 minutes, a vibrant yellow solution had formed of [Rh(dcpe)(CO)$_2$][BAr$^F{}_4$], confirmed by solution ^{31}P{^{1}H} NMR spectroscopy (δ 85.22, d, J_{RhP} = 116 Hz),[S7] as well as liberated isobutene-d_x. The solvent and volatiles were distilled into a fresh NMR tube and analyzed by ^{1}H, ^{2}H, ^{13}C {^{1}H} NMR spectroscopy and GC EI-MS.

S.4.2.5. Characterization data for isobutene-d_x (x = 8 – 6)

^{1}H NMR (CD_2Cl_2, 400 MHz, 298 K): Residual protio Signals at δ 4.69 (s, C=CH_2), 1.71 br. m., CH_3)

^{2}H NMR (CD_2Cl_2, 61 MHz, 298 K): δ 4.71 (br s, 2D, CD), 1.70 (br s, 5.6D, CD_3).

^{13}C{^{1}H} NMR (CD_2Cl_2, 126 MHz, 298 K): δ 142.7 (s, $\underline{C}$=CD_2.), 110.1 (m, C=$\underline{C}D_2$, J_{C-D} = 22.8), 23.4 (m, -CD_3, J_{C-D} = 20.1).

ESI-MS found (calc. for $C_4D_8^+$): m/z 64.112 (64.1128).

S.4.2.6. Solution NMR for isobutene-d_x (x = 8 – 6)

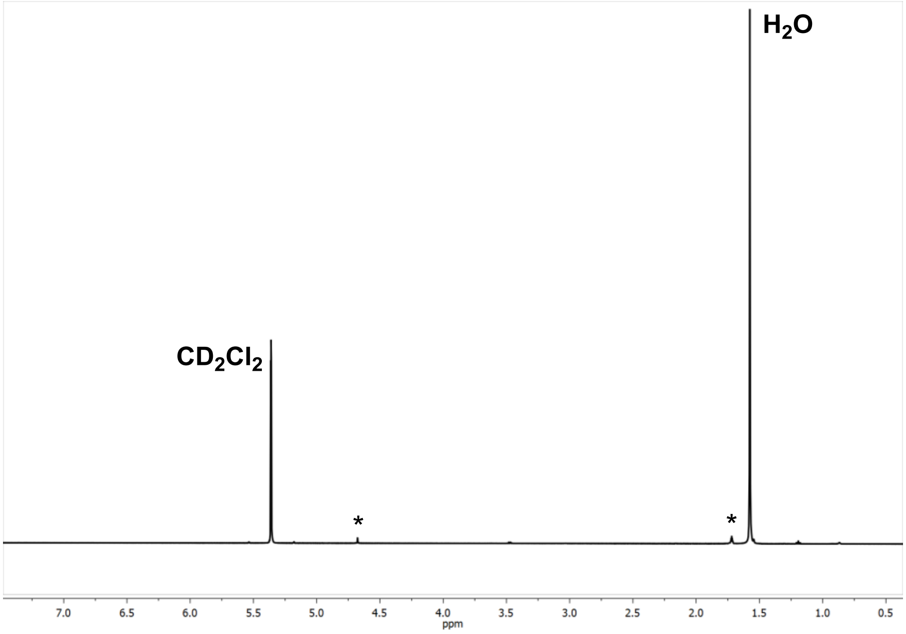

Figure S59: The solution ^{1}H NMR (C_6D_6, 298 K, 400 MHz) spectrum of isolated volatiles of isobutene-d_x. The signals marked * are from residual protio-isobutene.

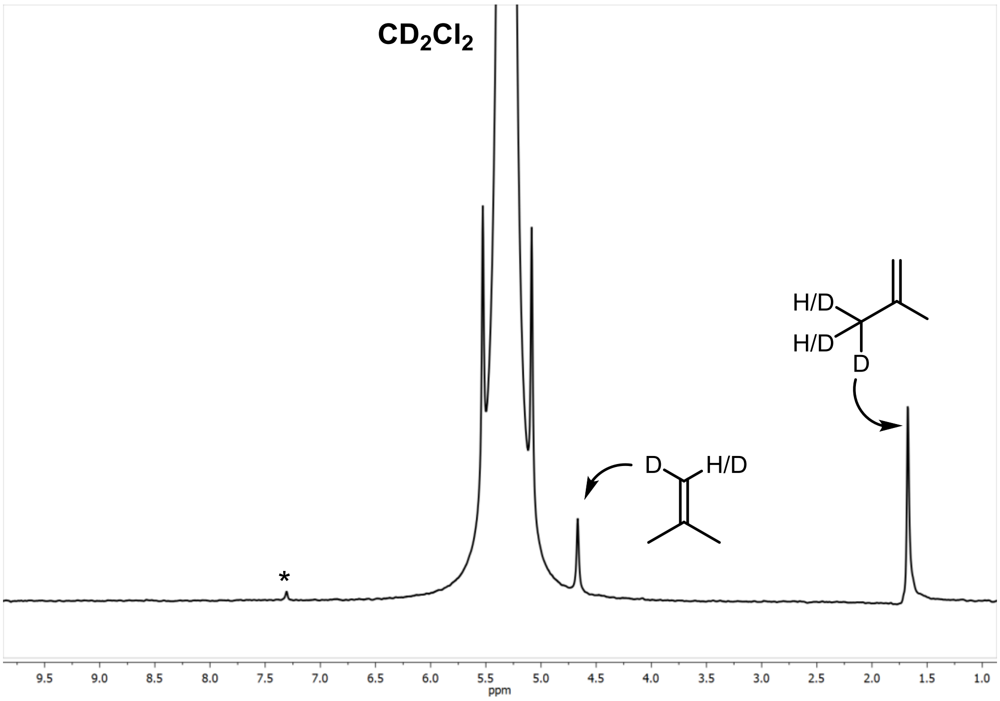

Figure S60: The solution ^{2}H NMR (CD_2Cl_2, 298 K, 61 MHz) spectrum of isolated volatiles of isobutene-d$_x$. The signals marked * are from a $CDCl_3$ impurity.

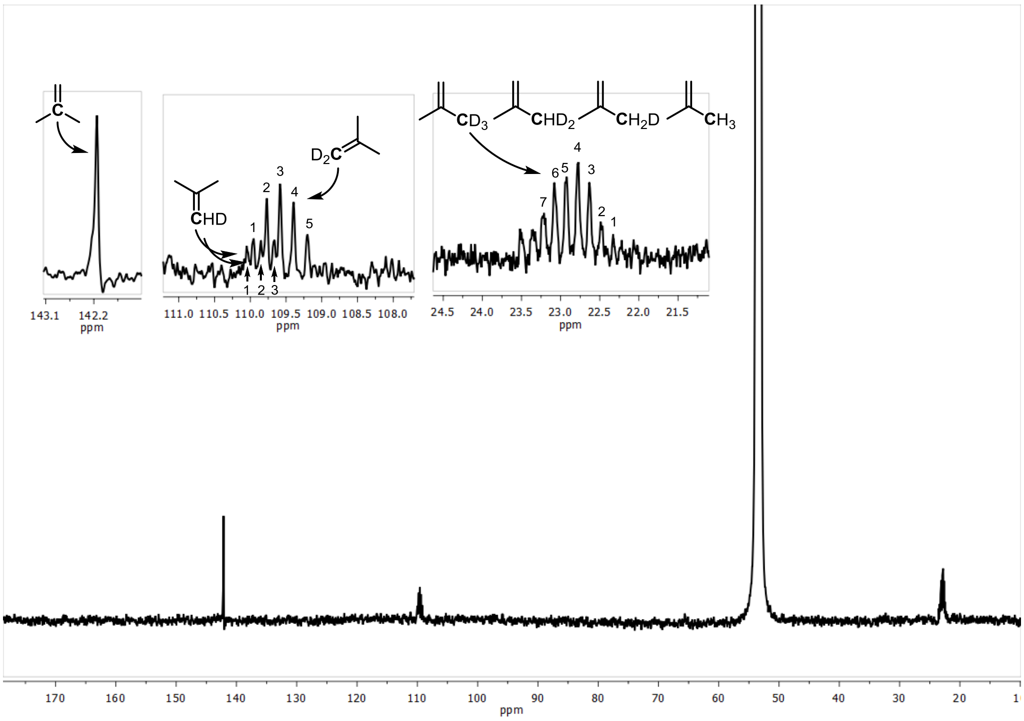

Figure S61: The solution $^{13}C\{^{1}H\}$ NMR (CD_2Cl_2, 298 K, 126 MHz) spectrum of isolated volatiles of isobutene-d$_x$.

S.4.2.7. GC EI-MS Mass Spectra of isobutene-d_x (x = 8 – 6)

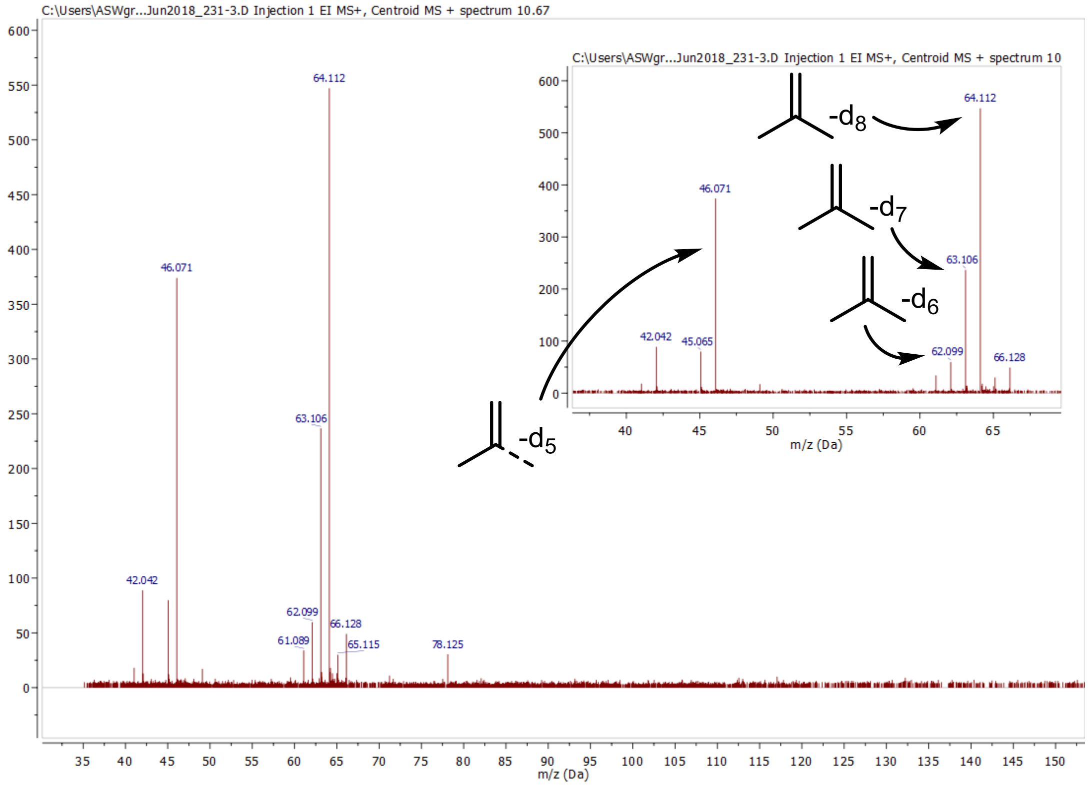

Figure S62: Mass spectrum of the isolated isobutene-d_x with enlargement of m/z = 35 – 70 region. The molecular ion peak is that of $C_4D_8^+$, m/z = 64.112 (calc. 64.1128) with greatest intensity fragment of $C_3D_5^+$, m/z = 46.071 (calc. = 46.0705). The 3 major isotopic contributions are that of $C_4D_8^+$, $C_4HD_7^+$ and $C_4H_2D_6^+$, as shown by signals at 64.112, 63.106 and 62.099 respectively.

S.4.2.8. Simulated solution $^{13}C\{^1H\}$ NMR spectra of isobutene-d_x (x = 8 – 6)

As per section S.3.1.4., the solution $^{13}C\{^1H\}$ NMR of isolated isobutene-d_x (x = 8 – 6) (Figure S61) was de-convoluted using the Spin Simulation function on MestReNova, shown in Figure S63. Line width was kept at 4.5 Hz throughout, only changing levels of population in each simulated environment.

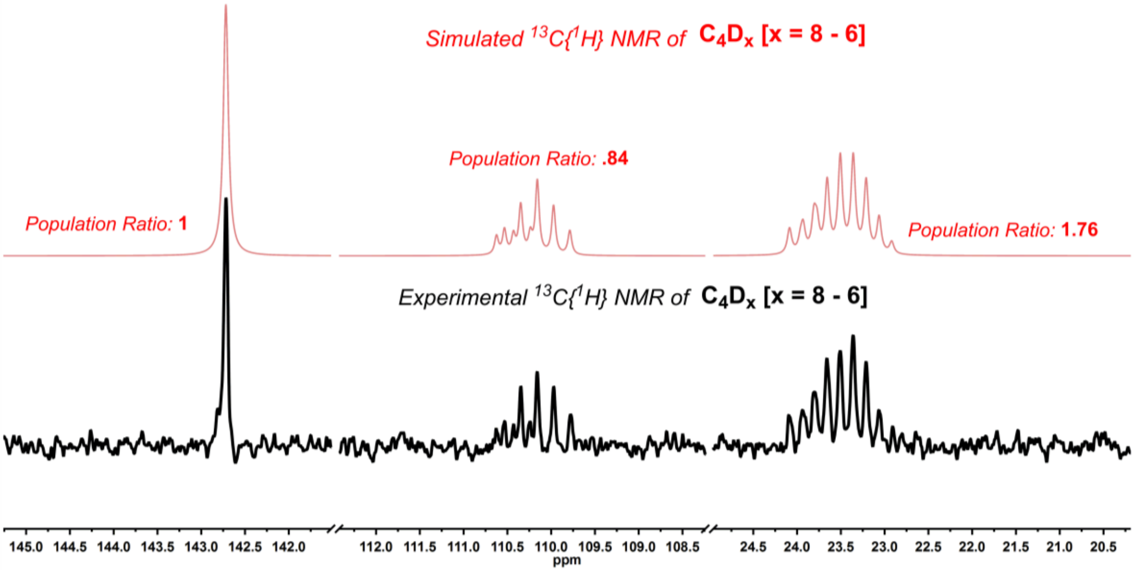

Figure S63: Simulated and partial experimental solution $^{13}C\{^1H\}$ NMR spectra of isobutene-d_x (x = 8 – 6). The three separate ^{13}C-environments are assigned to methyl ^{13}C (δ ~ 23), methylene ^{13}C (δ ~ 110) and quaternary ^{13}C (δ ~ 142).

The population ratio of each ^{13}C environment in the simulated spectra was calculated from the sum of each individual $–CD_XH_Y$ component in each environment compared between environments. These ratios suggest an approximate 1:1:2 ratios of carbon environments, in line with that of isobutene.

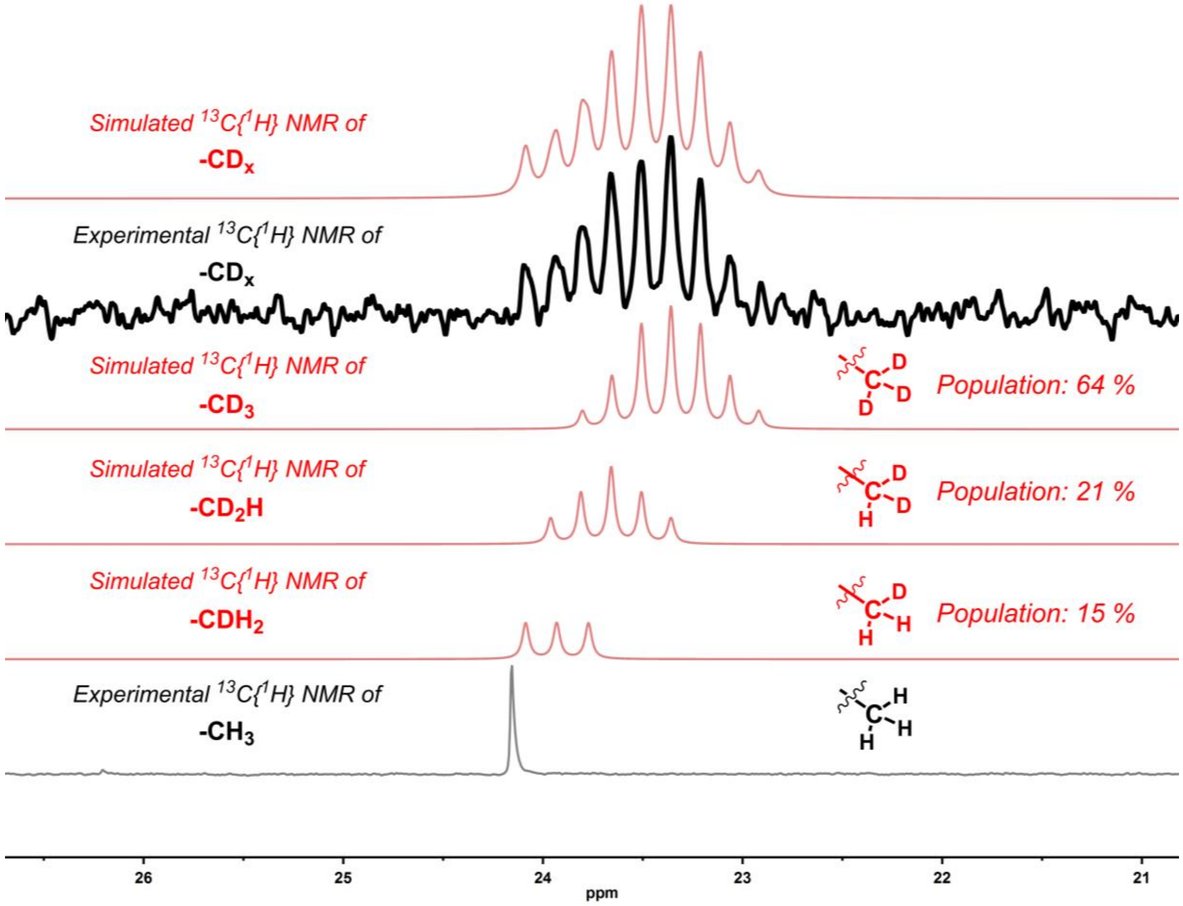

Figure S64: Three systems were used to recreate the multiplet at δ 23.5 from the methyl environment, modelling –CD_3, -CD_2H and -CDH_2 groups. No evidence of –CH_3 could be seen in the experimental data so was not modelled. The simulation from this environments suggests that 64 % of –CX_3 groups are were of –CD_3 in nature, 21 % –CD_2H and 15 % –CDH_2.

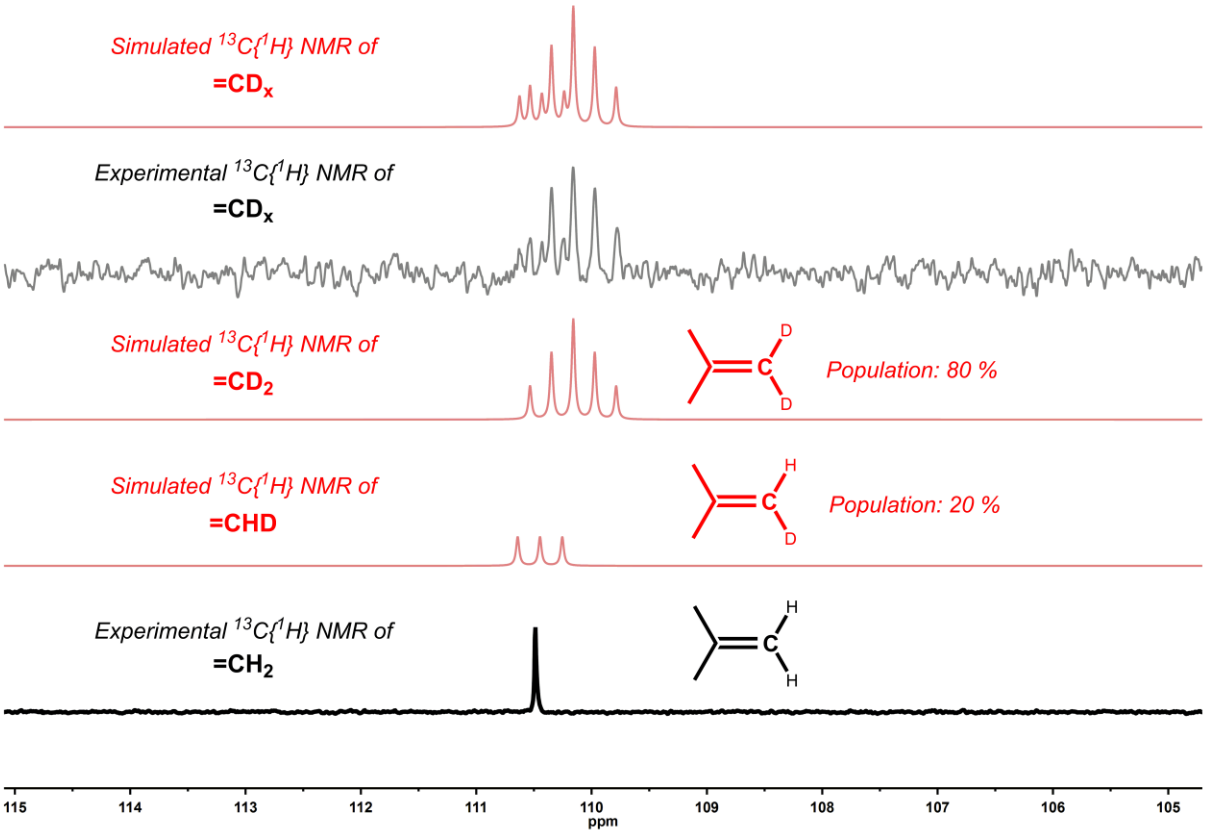

Figure S65: Two systems were used to recreate the multiplet at δ 110 from the methylene environment, modelling =CD$_2$ and =CDH groups. No evidence of =CH$_2$ could be seen in the experimental data so was not modelled. The simulation from these environments suggests that 80 % of =CD$_x$ groups are =CD$_2$, and 20 % = -CDH.

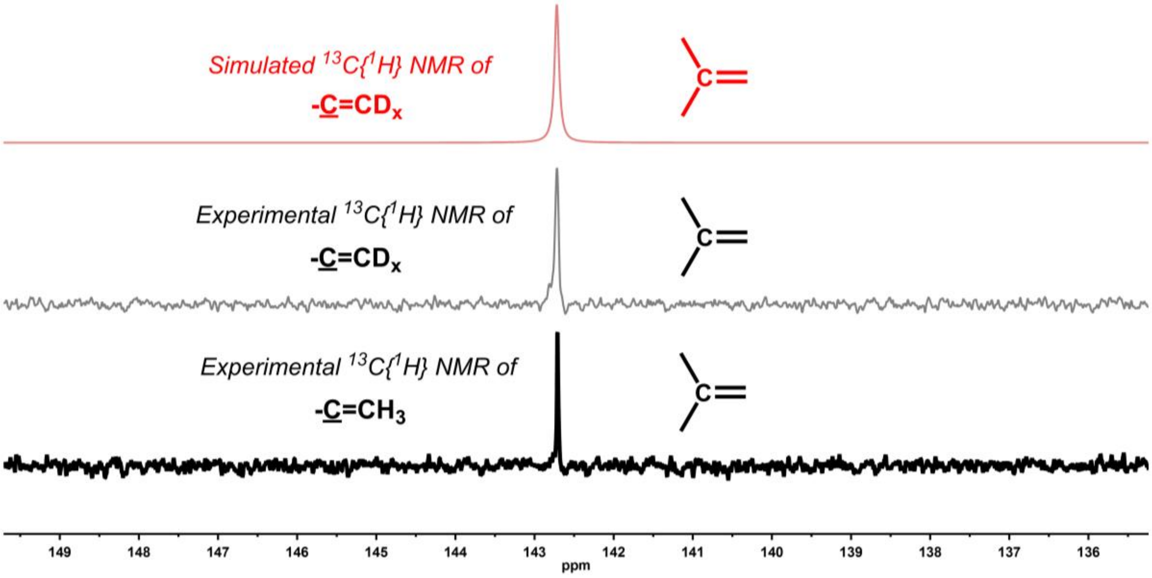

Figure S66: The singlet from the quaternary carbon at δ 142 was also modeled. This simulation was used as an approximate internal standard. The slight variation in chemical shift between the deuterated and proto isobutene (δ ~ .05) we have assign to secondary isotope effects.

Overall, the three figures (S64 – S66) describe the full calculated breakdown of deuterated isobutene, confirming a high level of deuteration incorporation. This is consistent with the GC EI-MS shown in Figure S62, which showed a high amount of deuterated isobutene ($C_4D_8^+$ to $C_4D_6^+$).

However, overall, lower levels of deuteration are observed compared to isobutane-d$_x$ (Section S.3.1.), as consistent with reduction of experimental time of **[1-C_4H_8][BAr^F_4]** under an D_2 atmosphere (30 vs 90 mins), see sections S.3.1. and S.4.2.

S.4.3. Solid-state dehydrogenation of [1-C_6H_{12}][BAr^F_4] to form [1-C_6H_8][BAr^F_4]

S.4.3.1. Solid-state dehydrogenation of [1-C_6H_{12}][BAr^F_4] under *argon flow* to form [1-C_6H_8][BAr^F_4]

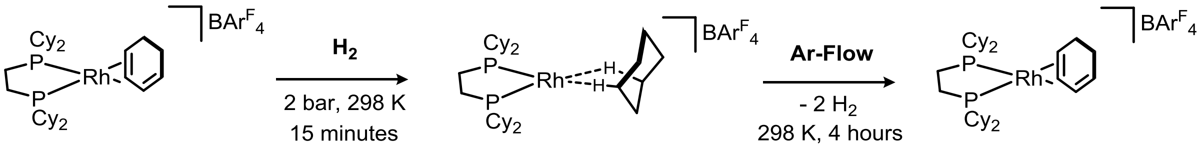

[1-C_6H_8][BAr^F_4] **[1-C_6H_{12}][BAr^F_4]** **[1-C_6H_8][BAr^F_4]**

A powdered microcrystalline sample of **[1-C_6H_8][BAr^F_4]** (35 mg) was packed in a 3.2 mm SSNMR rotor, inside an argon filled glove box. The rotor was then placed in a custom built glass J Young flask [S7] and the sample was then exposed to H_2 (1 bar, 298 K) for 20 minutes, to yield deep red crystalline powder of **[1-C_6H_{12}][BAr^F_4]**.

The sample was then placed under an argon flow for 18 hours. This was done by placing an exit needle into the suba sealed J Young flask which was open to argon flow, with regulator pressure set at 0.5 bar. After 18 hours, the rotor cap was fitted under a flush of Ar, and immediately transferred to the bore of a SSNMR spectrometer and analyzed $^{31}P\{^1H\}$ and $^{13}C\{^1H\}$ solid state NMR spectroscopy.

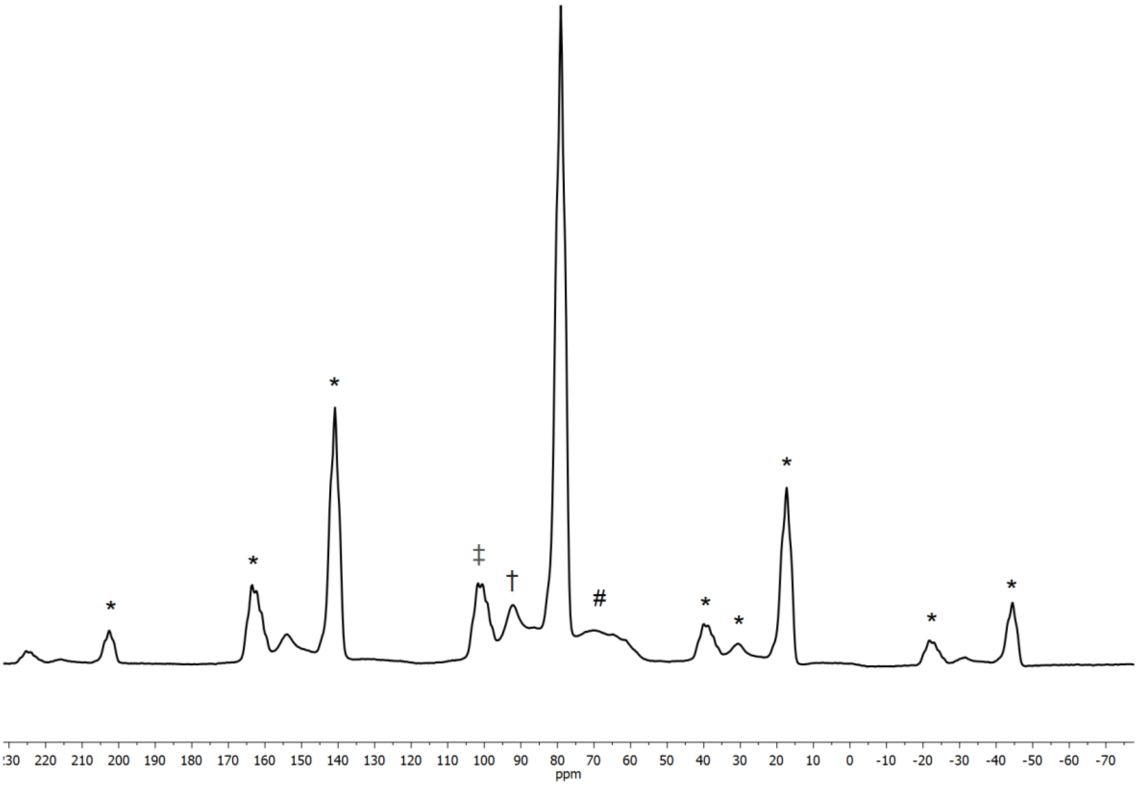

Figure S67: The ^{31}P{^{1}H} SSNMR (162 MHz, 295 K, 10 kHz spin rate) spectrum of the dehydrogenation of powdered microcrystalline **[1-C_6H_{12}][BAr$^F{}_4$]** under an argon flow. The resonance at δ 78 corresponds to **[1-C_6H_8][BAr$^F{}_4$]**, in comparison to clean **[1-C_6H_8][BAr$^F{}_4$]** shown in Figure S21. The resonances ‡ marked are assigned to **[1-C_6H_{10}][BAr$^F{}_4$]**, from incomplete dehydrogenation and † from **[1-BAr$^F{}_4$]**, formed from a side reaction when under H_2 atmosphere. The resonances marked # are assigned to as yet unidentified decomposition products. The resonances marked ***** are due to spinning sidebands.

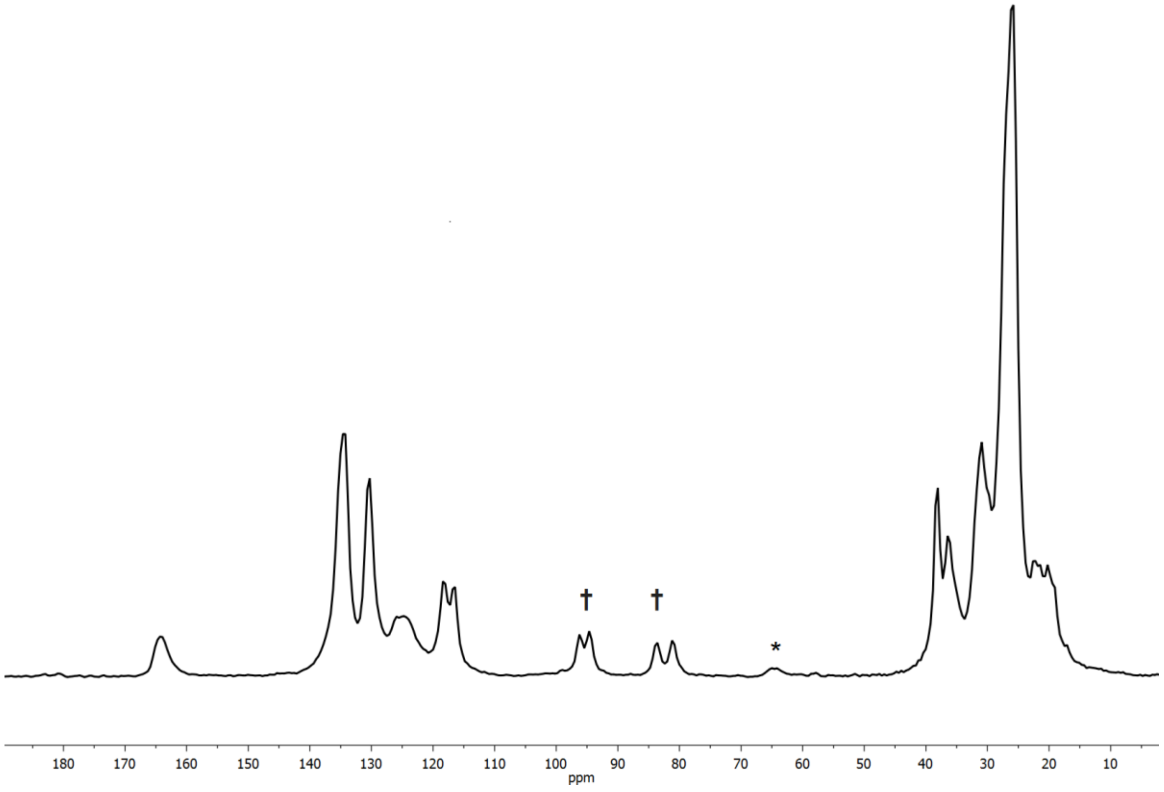

Figure S68: The $^{13}C\{^{1}H\}$ SSNMR (100 MHz, 295 K, 10 kHz spin rate) spectrum of the dehydrogenation of powdered microcrystalline **[1-C_6H_{12}][BAr$^F{}_4$]** under an argon flow. The resonances marked † correspond to the alkene signals in **[1-C_6H_8][BAr$^F{}_4$]**, in comparison to clean **[1-C_6H_8][BAr$^F{}_4$]** shown in Figure S22. The resonances marked ***** are due to spinning sidebands.

S.4.3.2. Solid-state dehydrogenation of $[1\text{-}C_6H_{12}][BAr^F_4]$ *under vacuum* to form $[1\text{-}C_6H_8][BAr^F_4]$

A J Young NMR tube was charged with powdered microcrystalline **$[1\text{-}C_6H_8][BAr^F_4]$** (10 mgs) in an argon filled glove box. The sample was then evacuated (2×10^{-2} mbar) and backfilled with H_2 (1 bar, 298 K) for 15 minutes. The sample was then cooled to 77 K in liquid nitrogen and evacuated. After a steady vacuum was achieved (2×10^{-2} mbar) the sample was rapidly warmed to 298 K and a timer was simultaneously started. After a set period of time (5 mins to 960 mins), the sample was cooled to 77 K in liquid nitrogen and CH_2Cl_2 (0.40 mL) was condensed into the NMR tube. The sample was expediently thawed and rapidly transferred to the bore of a precooled (183 K) NMR spectrometer which was previously locked and shimmed to a sample of CD_2Cl_2. A $^{31}P\{^1H\}$ NMR spectrum was then acquired.

The above procedure was repeated on numerous occasions, varying the period of time the sample was exposed to vacuum at room temperature.

Note: Vacuum pressure was used to normalize the conditions, opposed to an argon flow as per section S.4.3.1.

Three species are identified in the $^{31}P\{^1H\}$ solution NMR spectra;

$[1\text{-}(CH_2Cl_2)_n][BAr^F_4]$: δ 97.2 (br d, J_{RhP} 203 Hz).
$[1\text{-}C_6H_{10}][BAr^F_4]$: δ 96.9 (dd, J_{RhP} 207 Hz, J_{PP} 24 Hz), 90.4 (dd, J_{RhP} 159 Hz, J_{PP} 24 Hz).
$[1\text{-}C_6H_8][BAr^F_4]$: δ 78.3 (d, J_{RhP} 172 Hz).

Note: A powdered crystalline sample of **$[1\text{-}C_6H_8][BAr^F_4]$** was placed under vacuum (1×10^{-2} mbar) for a period of 2 weeks. ^1H and $^{31}P\{^1H\}$ NMR spectra of the dissolved solid (CD_2Cl_2) showed no significant change, and no **$[1\text{-}C_6H_6][BAr^F_4]$** was observed.

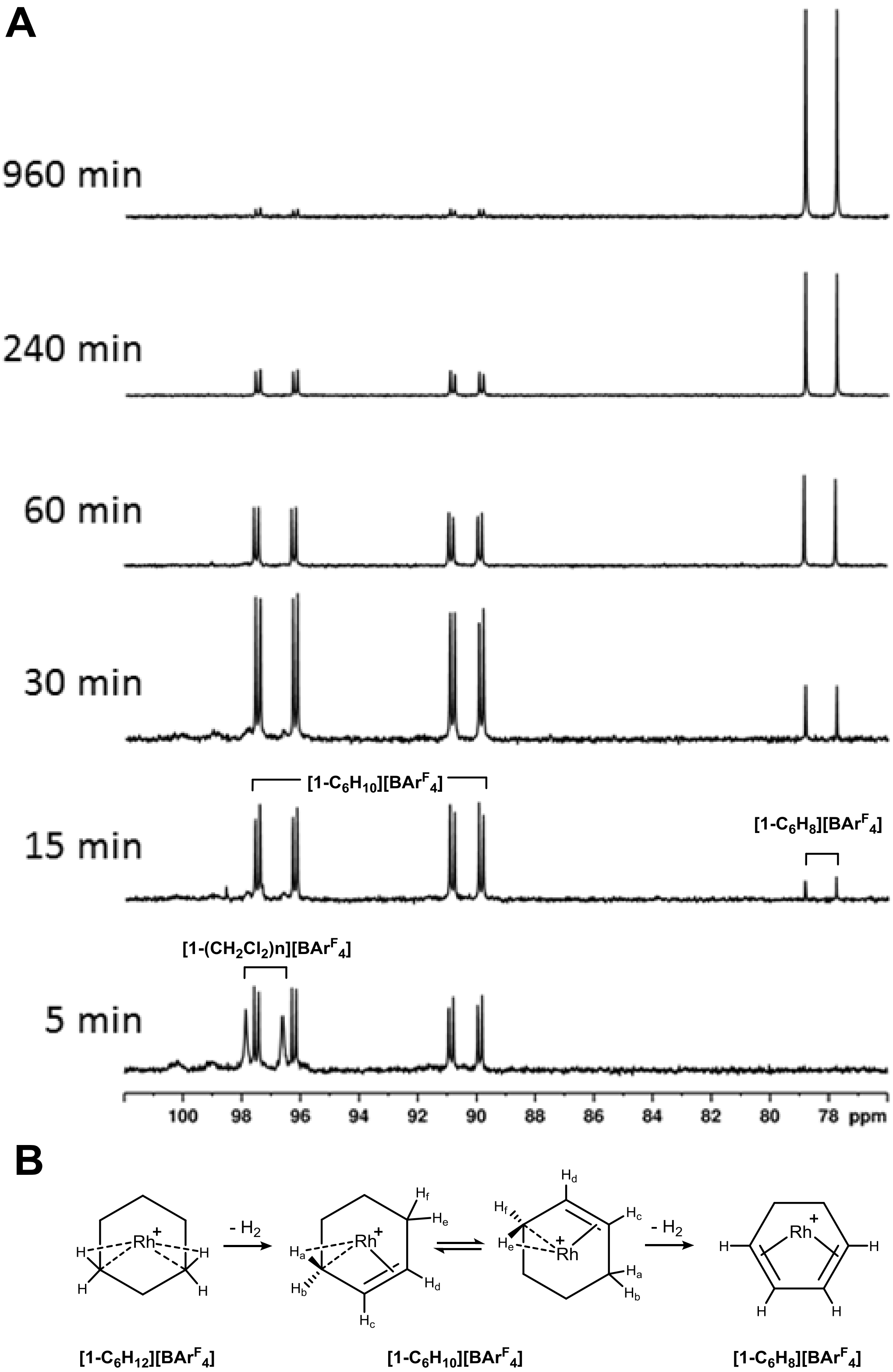

Figure S69: (A) Representative solution $^{31}P\{^1H\}$ NMR (CH_2Cl_2, 183 K, 162 MHz) spectra of **[1-C_6H_{12}][BAr^F_4]** exposed to vacuum for various periods of time in the solid-state then quenched by condensing CH_2Cl_2 onto the sample. **(B)** Structural diagrams of the species present during the dehydrogenation reactions; phosphine units and $[BAr^F_4]^-$ anions removed for clarity.

S.4.3.3. Kinetics of the solid-state $[1\text{-}C_6H_{12}][BAr^F{}_4]$ dehydrogenation *under vacuum* to form $[1\text{-}C_6H_8][BAr^F{}_4]$

In contrast to the dehydrogenation of **$[1\text{-}C_4H_{10}][BAr^F{}_4]$**, the dehydrogenation of **$[1\text{-}C_6H_{12}][BAr^F{}_4]$** proceeds in two stages. Given the poor stability of the intermediate complex of **$[1\text{-}C_6H_{10}][BAr^F{}_4]$** in solution, the $^{31}P\{^1H\}$ NMR spectra used in the kinetic study were collected at 183 K. As previously noted **$[1\text{-}C_6H_{12}][BAr^F{}_4]$** imminently reacts with CH_2Cl_2 even at low temperatures to form several species two of which we have tentatively assigned as **$[1\text{-}(CH_2Cl_2)_n][BAr^F{}_4]$** and **$[1\text{-}BAr^F{}_4]$**. At 183 K, the resonances of these species are typically very broad.

Dehydrogenation reactions were undertaken in J Young NMR tubes containing capillaries of a ^{31}P NMR standard (PPh_3 in d_6-acetone), in which a known amount of powdered crystalline **$[1\text{-}C_6H_8][BAr^F{}_4]$** was hydrogenated, then subjected to vacuum for a range of times from 15 mins to 960 mins, and worked up as per the procedure outlined in section S.4.3.3. The concentration of each capillary was calibrated to a sample of $Cy_2PCH_2CH_2PCy_2$ in CH_2Cl_2 at 183 K. The concentrations of the species involved were referenced against the internal standard.

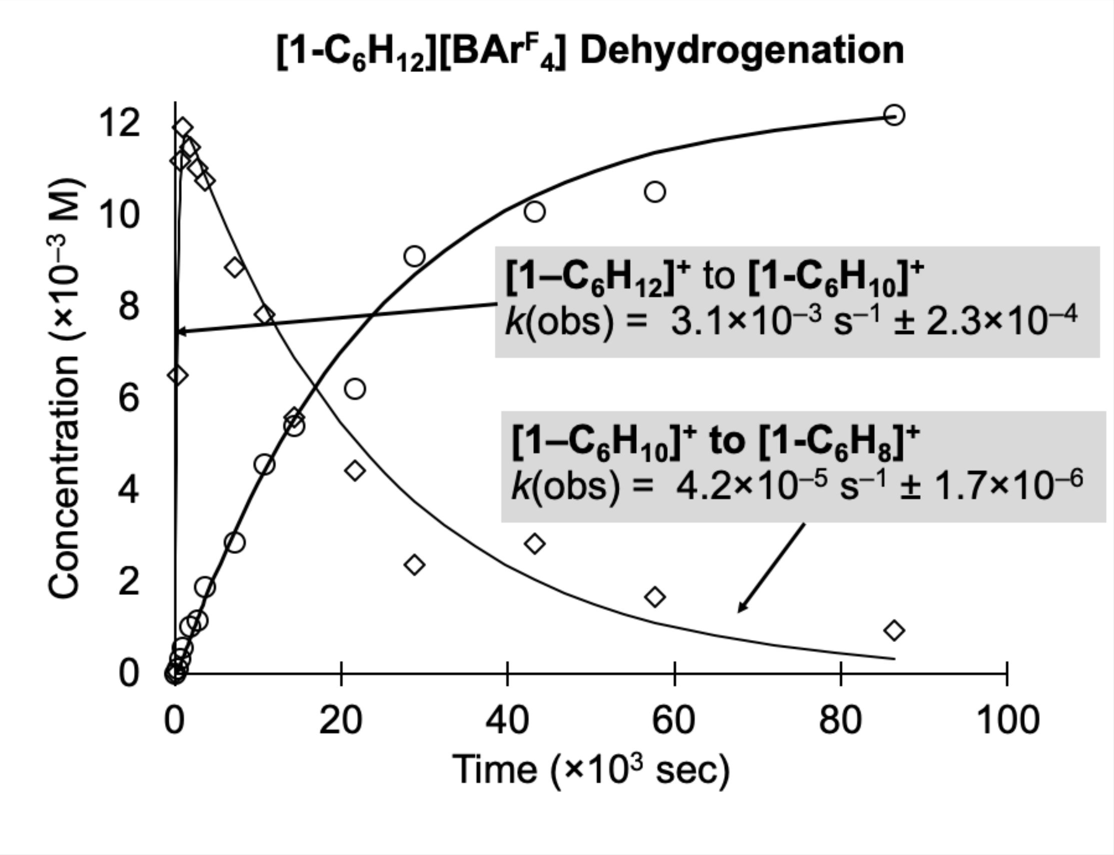

Figure S70: Temporal evolution of dehydrogenation of **[1-C_6H_{12}][BAr^F_4]** under vacuum (1 x 10^{-2} mbar). Each data point comes from a separate experiment using 10 mg crystalline material, subjected to a vacuum for a set period of time and dissolved in cold CD_2Cl_2 (0.4 mL) that has been vacuum transferred into the sample.

This gives a $[Rh]_{TOT}$ = 13 ×10^{-3} M. Integrals measured using quantitative $^{31}P\{^1H\}$ NMR spectroscopy at 183 K of the resulting Rh–complexes, **[1-BAr^F_4]** (a proxy for **[1-C_6H_{12}][BAr^F_4]**), **[1-C_6H_{10}][BAr^F_4]** and **[1-C_6H_8][BAr^F_4]** which have been calibrated from use of an internal standard of PPh_3 in a sealed capillary.

Solid–lines are fits for COPASI[S10] modelled processes for the sequential dehydrogenation (**[1-C_6H_{12}][BAr^F_4]** → **[1-C_6H_{10}][BAr^F_4]** → **[1-C_6H_8][BAr^F_4]**), where the *second* dehydrogenation is 1st order (k = 3.1(2) × 10^{-5} s^{-1}) and the *first* is either 1st or 2nd order. Initial concentration of dissolved samples = 12.5 mM (conversion = 0%).

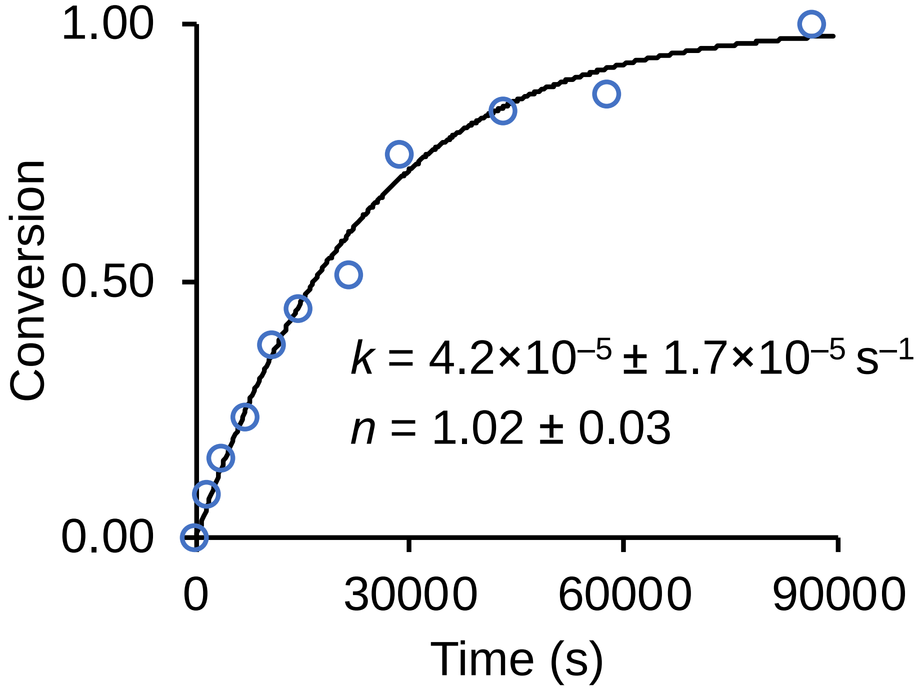

Figure S71: Modified JAMK Plot of conversion[S9] (f) = $(1\text{–}e^{(-kt)2})$ versus time for the dehydrogenation process **[1-C_6H_{10}][BAr^F_4]** to **[1-C_6H_8][BAr^F_4]** in the solid-state; which is the second dehydrogenation process of **[1-C_6H_{12}][BAr^F_4]**. Where *k* = growth rate constant and *n* = Avrami exponent.

S.4.4. Solid-state dehydrogenation of [1-C_6H_{12}][BAr$^F{}_4$] to form [1-C_6H_{10}][BAr$^F{}_4$]

S.4.4.1. Solid-State Synthesis of [1-C_6H_{10}][BAr$^F{}_4$]

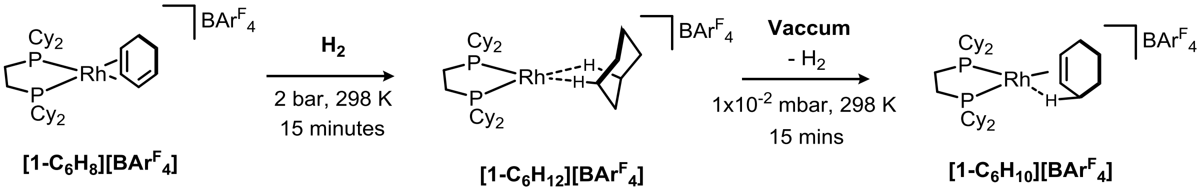

Attempts to trap **[1-C_6H_{10}][BAr$^F{}_4$]** in the solid-state were conducted using the following method:

A powdered microcrystalline sample of **[1-C_6H_8][BAr$^F{}_4$]** (35 mg) was packed in a 3.2 mm SSNMR rotor, inside an argon filled glove box. The rotor was then placed in a custom built glass J Young flask [S7] and the sample was then exposed to H_2 (1 bar, 298 K) for 20 minutes, to yield deep red crystalline powder of **[1-C_6H_{12}][BAr$^F{}_4$]**. The sample was then placed under a steady vacuum (2 × 10^{-2} mbar) at 298 K. After 15 minutes, the rotor cap was fitted under a flush of Ar, and immediately transferred to the bore of a SSNMR spectrometer and analyzed by ^{31}P{^{1}H} and ^{13}C{^{1}H} solid state NMR spectroscopy.

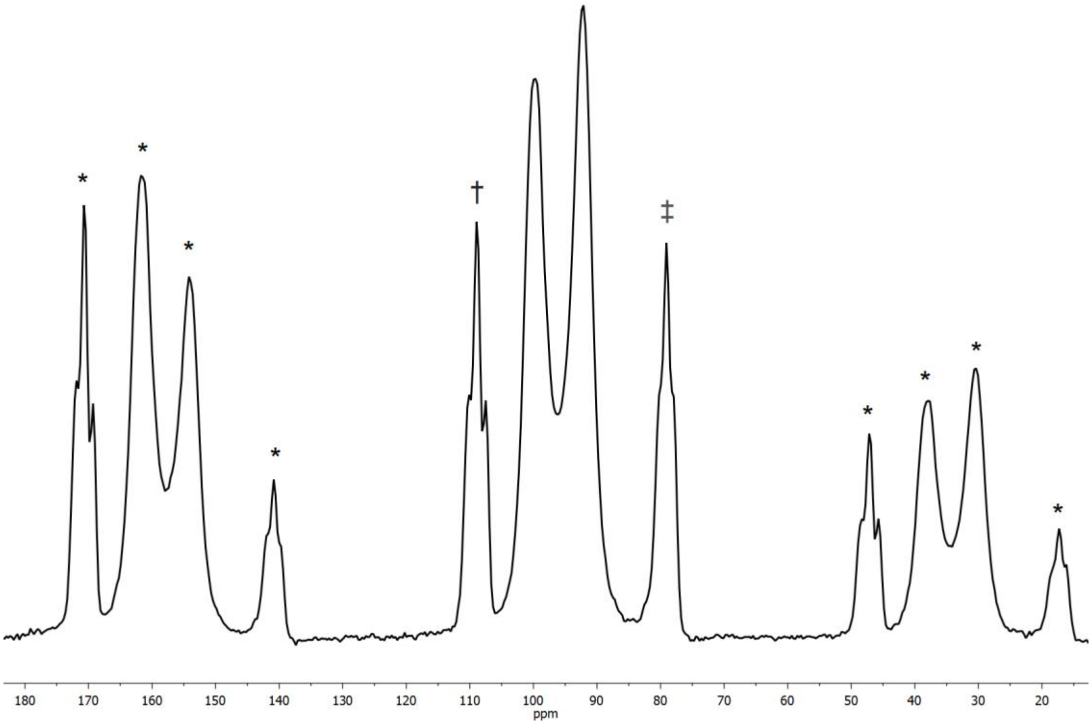

Figure S72: The ^{31}P{^{1}H} SSNMR (162 MHz, 295 K, 10 kHz spin rate) spectrum of the dehydrogenation of powdered microcrystalline **[1-C_6H_{12}][BAr$^F{}_4$]** under 15 minutes of vacuum. The resonances at δ 100 and δ 92 correspond to **[1-C_6H_{10}][BAr$^F{}_4$]** (~ 70 %), and the resonances † marked are assigned to **[1-C_6H_{12}][BAr$^F{}_4$]** (~ 15 %) and the resonances marked ‡ (~ 15 %) are assigned to **[1-C_6H_8][BAr$^F{}_4$].** The resonances marked ***** are due to spinning sidebands.

We postulate this mixture of species arises in the solid-state from non-uniform vacuum being applied throughout the densely packed solid-state rotor, leading to slightly different kinetics then observed in Section S.4.3.3.

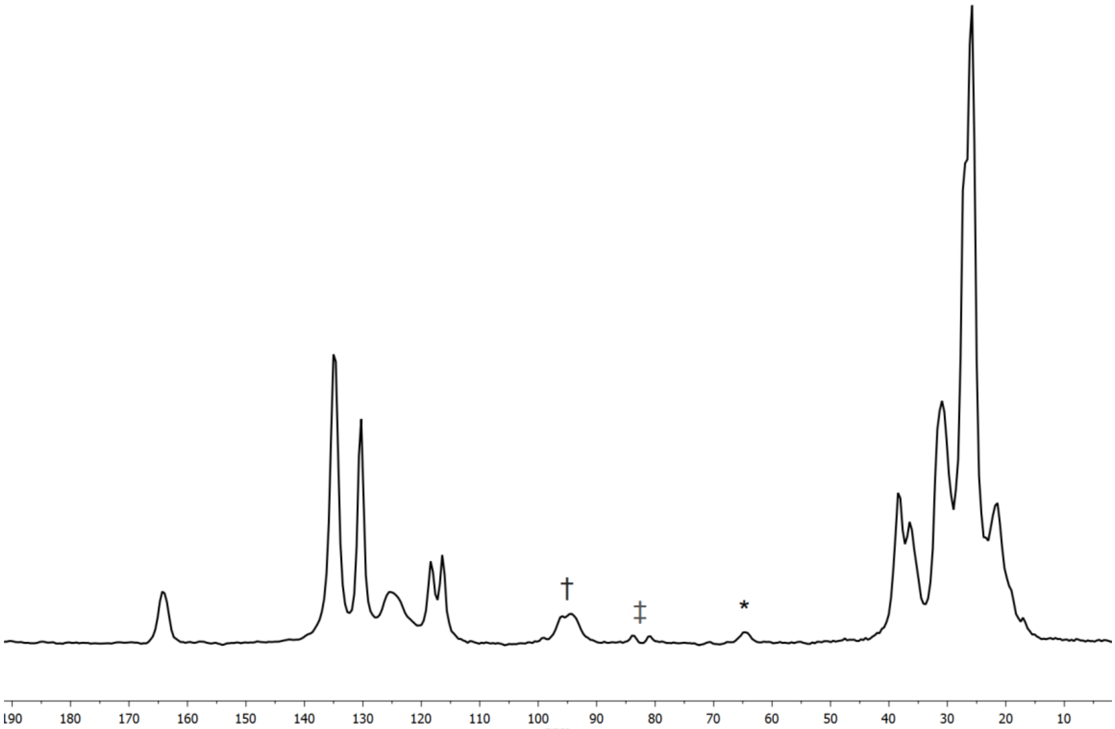

Figure S73: The $^{13}C\{^1H\}$ SSNMR (100 MHz, 295 K, 10 kHz spin rate) spectrum of the dehydrogenation of powdered microcrystalline **[1-C_6H_{12}][BAr$^F_4$]** under 15 minutes of vacuum. The resonance marked † are from the carbons in alkene environments of **[1-C_6H_{10}][BAr$^F_4$]**, and resonances ‡ marked are assigned to **[1-C_6H_8][BAr$^F_4$]**, see Figure S22. The resonances marked ***** are due to spinning sidebands.

S.4.4.2. Isolation and solution-state characterization data for [1-C_6H_{10}][BAr$^F_4$]

Attempts to trap **[1-C_6H_{10}][BAr$^F_4$]** in solution were conducted using the following method:

A J Young NMR tube was charge with powdered microcrystalline **[1-C_6H_8][BAr$^F_4$]** (10 mg) in a glove box. The sample was then evacuated and backfilled with H_2 (2 bar, 298 K) for 15 minutes. The sample was then cooled to 77 K in liquid nitrogen and evacuated. After a steady vacuum was achieved (2 × 10^{-2} mbar) the sample was rapidly warmed to 298 K and a timer was simultaneously started. After 15 minutes, the sample was cooled to 77 K in liquid nitrogen and CH_2Cl_2 (0.40 mL) was condensed into the NMR tube. The sample was expediently thawed and rapidly transferred to the bore of a precooled (183 K) NMR spectrometer which was previously locked and shimmed to a sample of CD_2Cl_2. A $^{31}P\{^1H\}$ NMR spectrum was then acquired.

^{1}H NMR (CD_2Cl_2, 400 MHz, 183 K, selected resonances): δ 7.72 (s, 14H, ortho-ArH), 7.54 (s, 7H, para-ArH), 5.23 (s, ~ 2H, alkene-CH), 2.47 (br d, J_{HH} 14 Hz, cyclohexene-CH), 2.05-1.38 (br m, 73H, overlapping aliphatic CH), 1.30-0.98 (br m, 53H, overlapping aliphatic CH), -1.01 (br s, ~ 2H, agostic CH).

Note: The low temperature limit was not reached at 183K, so integrated values are approximate. As well, the integrals of the $[BAr^F{}_4]^-$ and alkyl resonances are higher than expected presumably due to contamination decomposition products of **[1-BAr$^F{}_4$]**,[S2] **[1-(CD_2Cl_2)$_n$][BAr$^F{}_4$]** [S1] and liberated cyclohexane.

^{31}P{^{1}H} NMR (CD_2Cl_2, 162 MHz, 183 K, selected resonances): δ 98.0 (dd, J_{RhP} 207 Hz, J_{PP} 24 Hz), 91.5 (dd, J_{RhP} 159 Hz, J_{PP} 24 Hz).

^{19}F{^{1}H} NMR (CD_2Cl_2, 377 MHz, 183 K, selected resonances): δ -62.9 (s).

Note: Samples rapidly decomposed in solution at room temperature. The decomposition products **[1-C_6H_8][BAr$^F{}_4$]**, **[1-C_6H_6][BAr$^F{}_4$]**, **[1-BAr$^F{}_4$]** and liberated cyclohexane were identified by ^{1}H and ^{31}P{^{1}H} NMR spectroscopy.

S.4.4.3. Solution NMR spectra of $[\mathbf{1}\text{-}C_6H_{10}][BAr^F_4]$

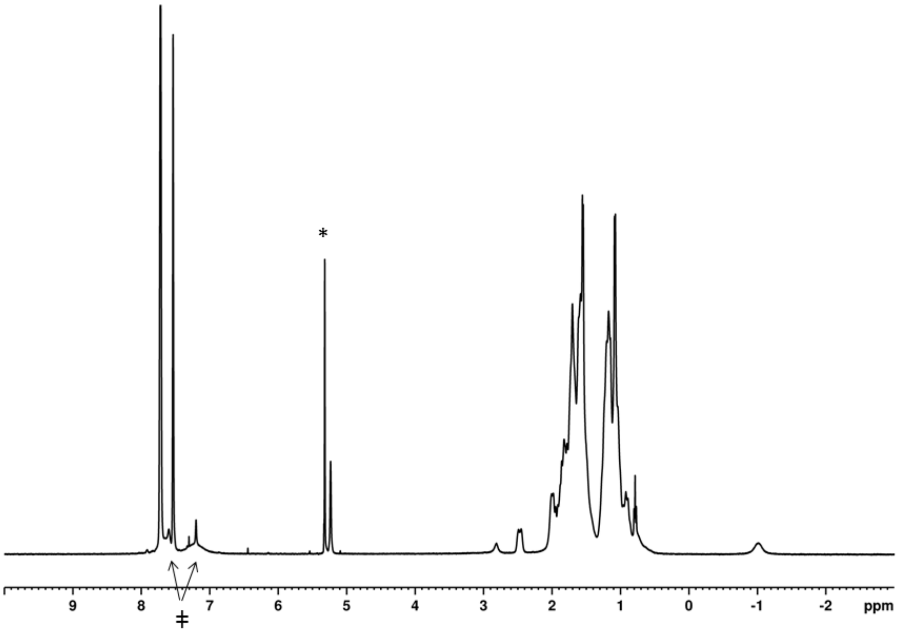

Figure S74: The solution ^{1}H NMR (CD_2Cl_2, 183 K, 400 MHz) spectrum of the intermediate stage of dehydrogenation. The resonance marked ***** is due to $CHDCl_2$. The resonances marked ‡ are tentatively assigned to **$[\mathbf{1}\text{-}BAr^F_4]$**.

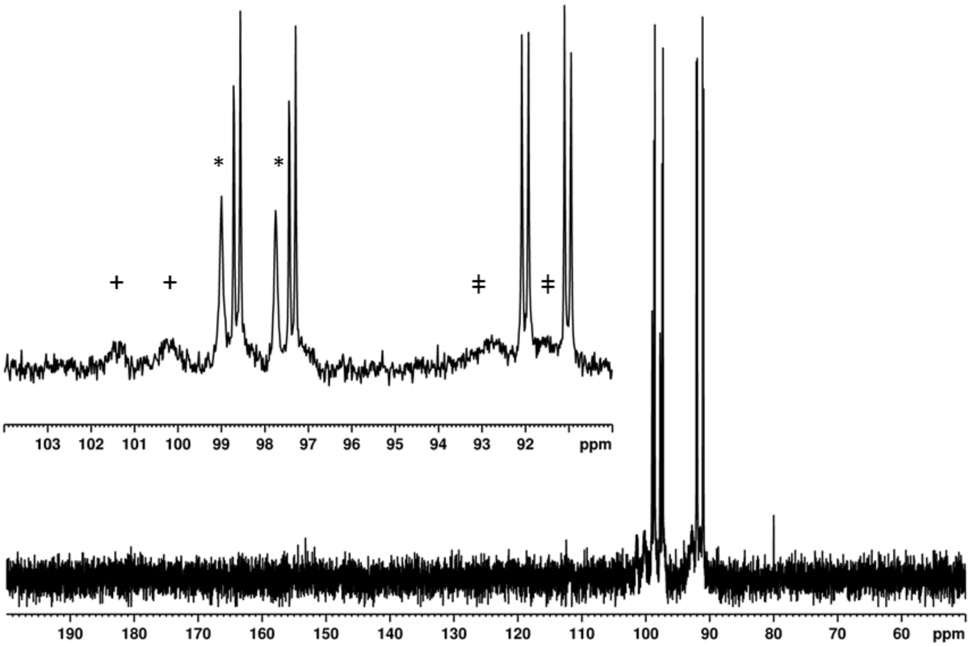

Figure S75: The ^{31}P{^{1}H} NMR (CD_2Cl_2, 183 K, 162 MHz) spectrum of the intermediate stage of dehydrogenation. The resonance marked ***** are tentatively assigned to **$[\mathbf{1}\text{-}(CD_2Cl_2)_n][BAr^F_4]$**. The resonances marked ‡ are assigned to **$[\mathbf{1}\text{-}BAr^F_4]$**.[S2] The resonances marked + could not be assigned.

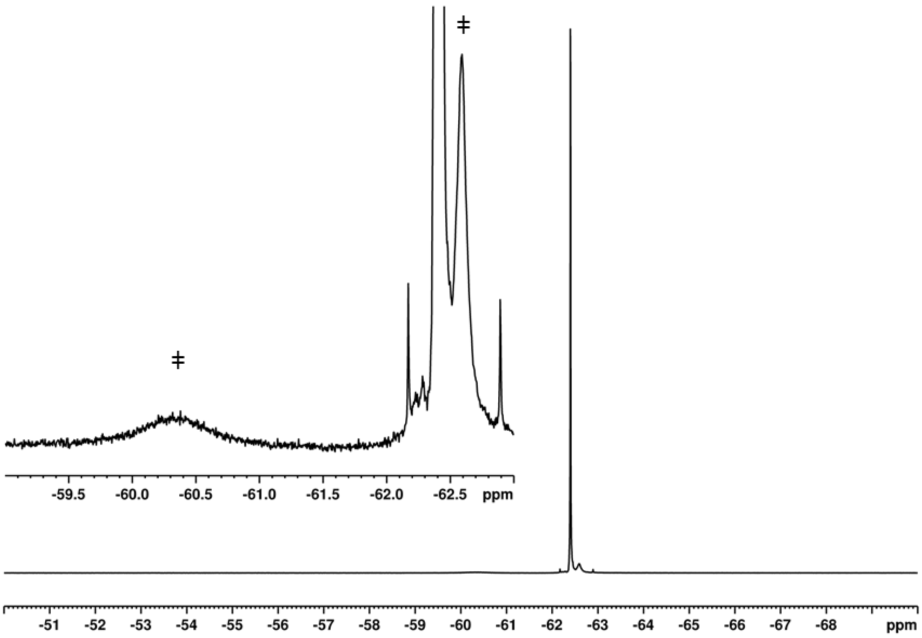

Figure S76: The $^{19}F\{^{1}H\}$ NMR (CD_2Cl_2, 183 K, 377 MHz) spectrum of the intermediate stage of dehydrogenation. The inset is an enlargement of the baseline around the central resonance. The resonance marked ‡ is tentatively assigned to **[1-BAr$^F{}_4$]**.

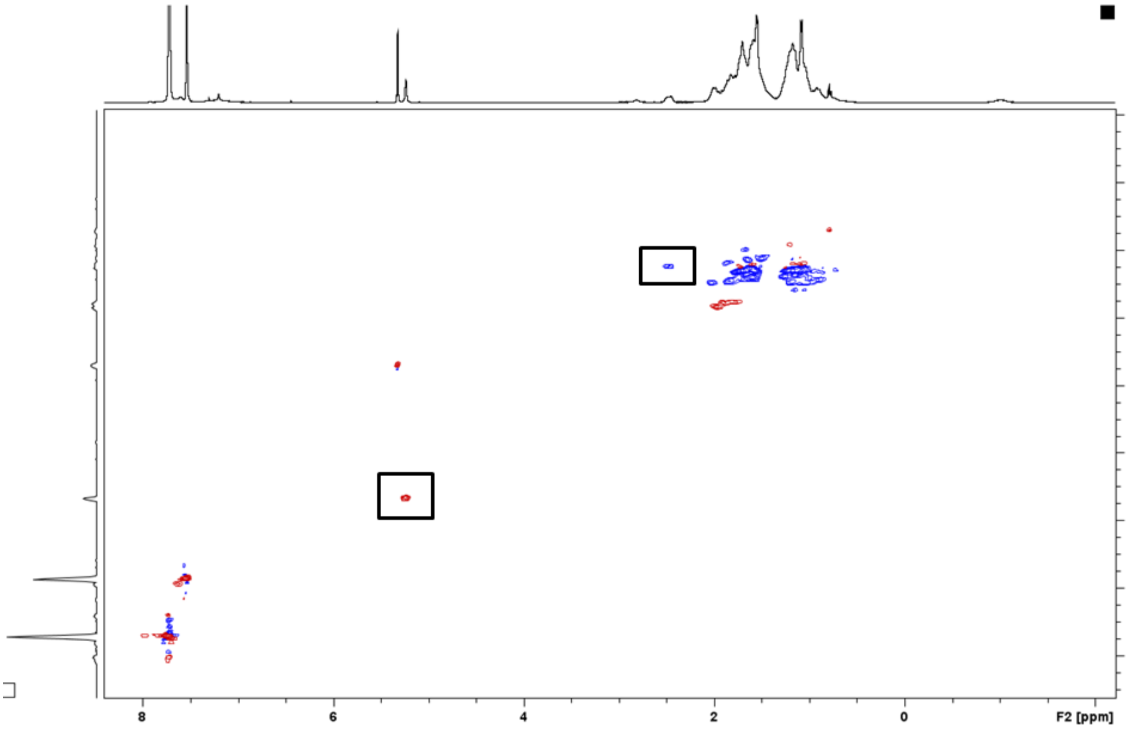

Figure S77: The solution $^{1}H/^{13}C$ HSQC NMR (CD_2Cl_2, 183 K) spectrum of intermediate in the dehydrogenation. Black boxes added to guide the eye. A cross peak for the high field ^{1}H resonance was not unambiguously identified.

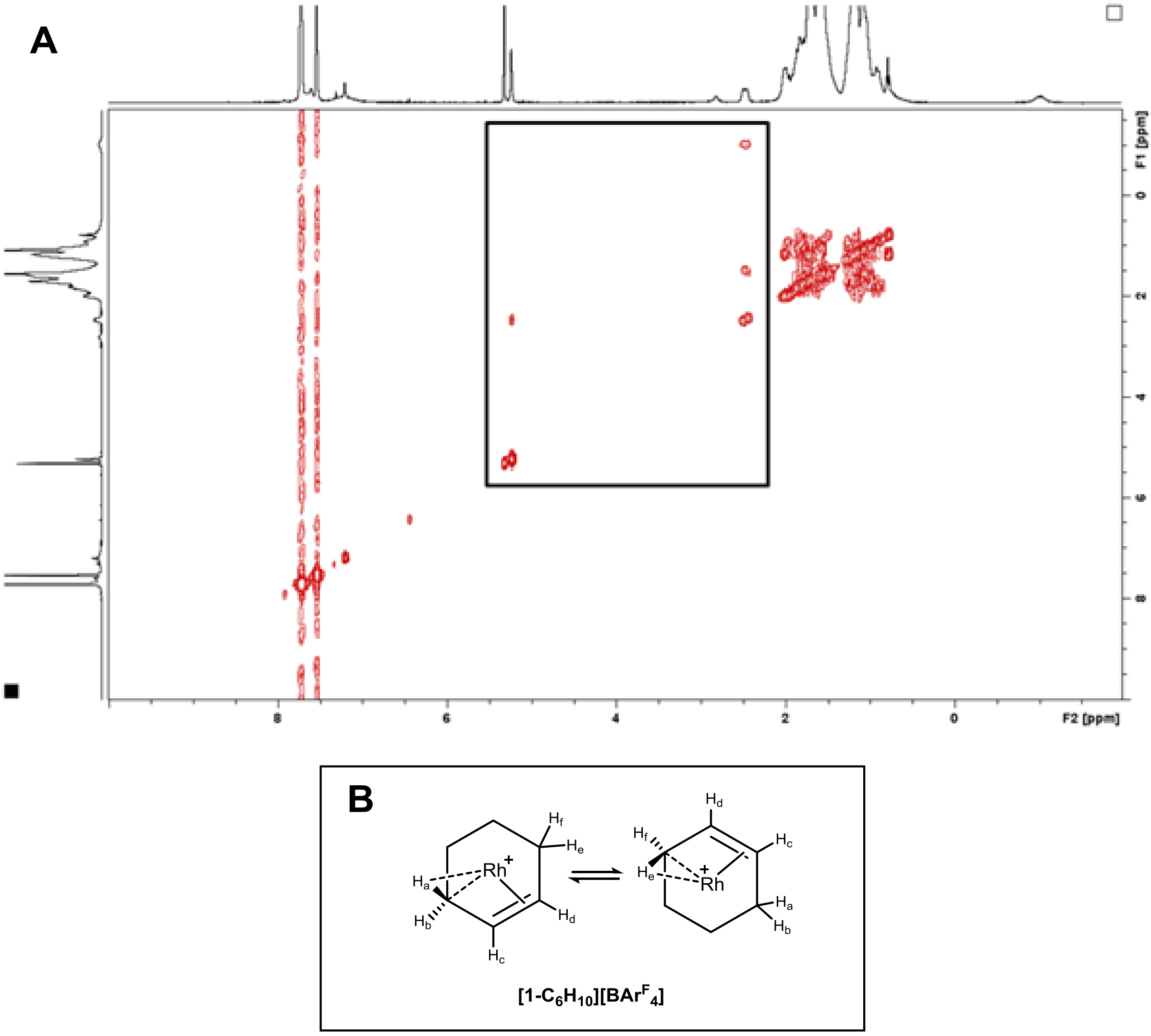

Figure S78: (A) The solution $^1H/^1H$ COSY NMR (CD_2Cl_2, 183 K) spectrum of intermediate in the dehydrogenation. Black box added to guide the eye, showing $^1H/^1H$ correlation between agostic and alkene protons in **[1-C_6H_{10}][$BAr^F{}_4$]**. **(B)** Structual diagrams of the fluxioanitly at room tempreture of **[1-C_6H_{10}][$BAr^F{}_4$]**; phosphine units and $[BAr^F{}_4]^-$ anions removed for clarity.

S.4.4.4. Liberation of the bound cyclohexene from [1-C_6H_{10}][BAr$^F{}_4$].

A J Young NMR tube was charge with powdered microcrystalline **[1-C_6H_8][BAr$^F{}_4$]** (10 mg) in a glove box. The sample was then evacuated and backfilled with H_2 (2 bar, 298 K). The sample was then cooled to 77 K in liquid nitrogen and evacuated. After a steady vacuum was achieved (2×10^{-2} mbar) the sample was rapidly warmed to 298 K and a timer was simultaneously started. After 15 mins, the sample was cooled to 77 K in liquid nitrogen and CH_2Cl_2 (0.40 mL) was condensed into the NMR tube. When thawing, care was taken such that the sample was not warmed above 233 K. The cool sample was then carefully refilled with CO (1 bar, 233 K). After 5 minutes, a vibrant yellow solution had formed of [Rh(dcpe)$(CO)_2$][BAr$^F{}_4$],[S7] confirmed by solution $^{31}P\{^1H\}$ NMR spectroscopy (δ 85.22, d, J_{RhP} = 116 Hz), as well as liberated cyclohexene. The volatile component was then isolated by trap-to-trap distillation and analyzed by ^1H NMR spectroscopy and GC EI-MS.

^1H NMR (CD_2Cl_2, 400 MHz): δ 5.66 (s, 2H, alkene-CH), 1.98 (br m, 4H, CH), 1.61 (m, 4H, CH).

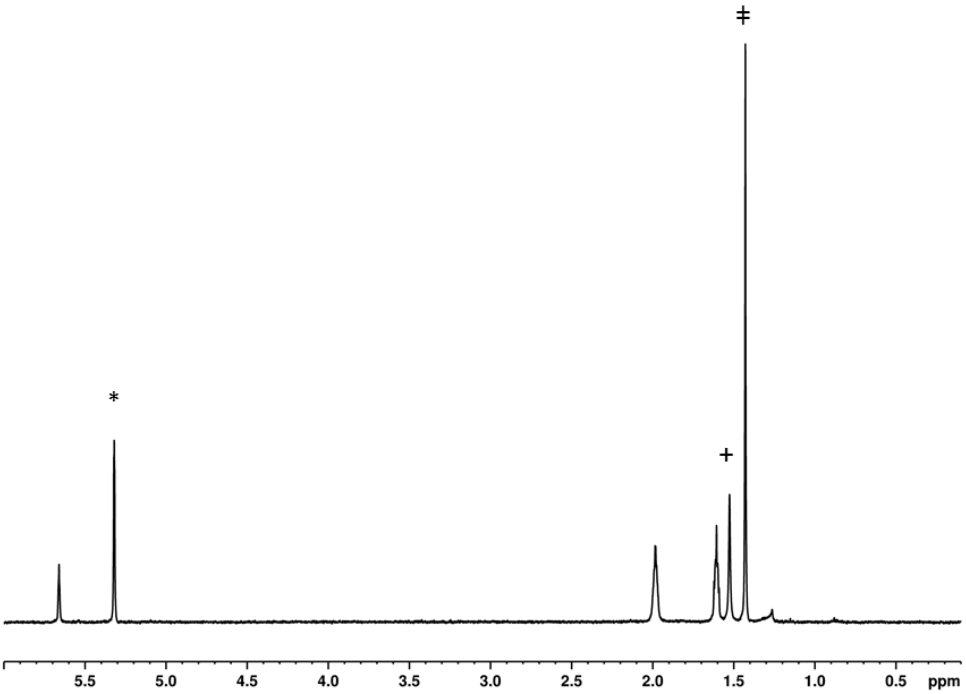

Figure S79: The ^{1}H NMR (CD_2Cl_2, 298 K, 400 MHz) spectrum of volatiles isolated post carbonylation. The resonance marked * is due to $CHDCl_2$. The resonance marked ‡ is assigned to cyclohexane. The resonance marked + is assigned to H_2O.

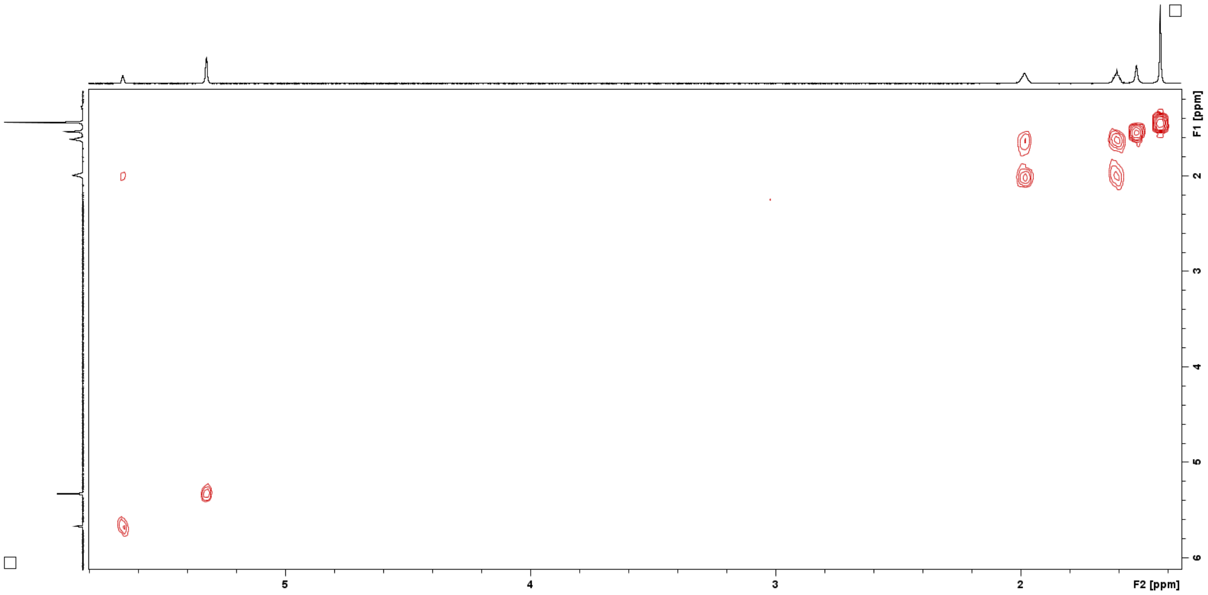

Figure S80: The ^{1}H/^{1}H COSY NMR (CD_2Cl_2, 298 K, 400 MHz) spectrum of volatiles isolated post carbonylation.

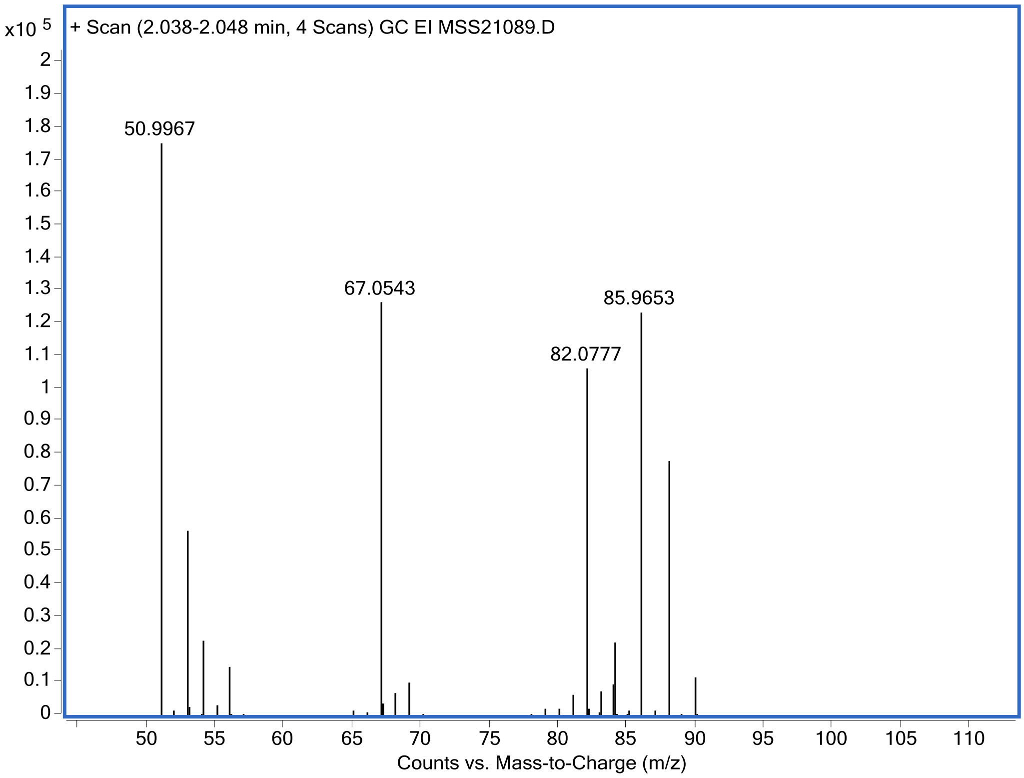

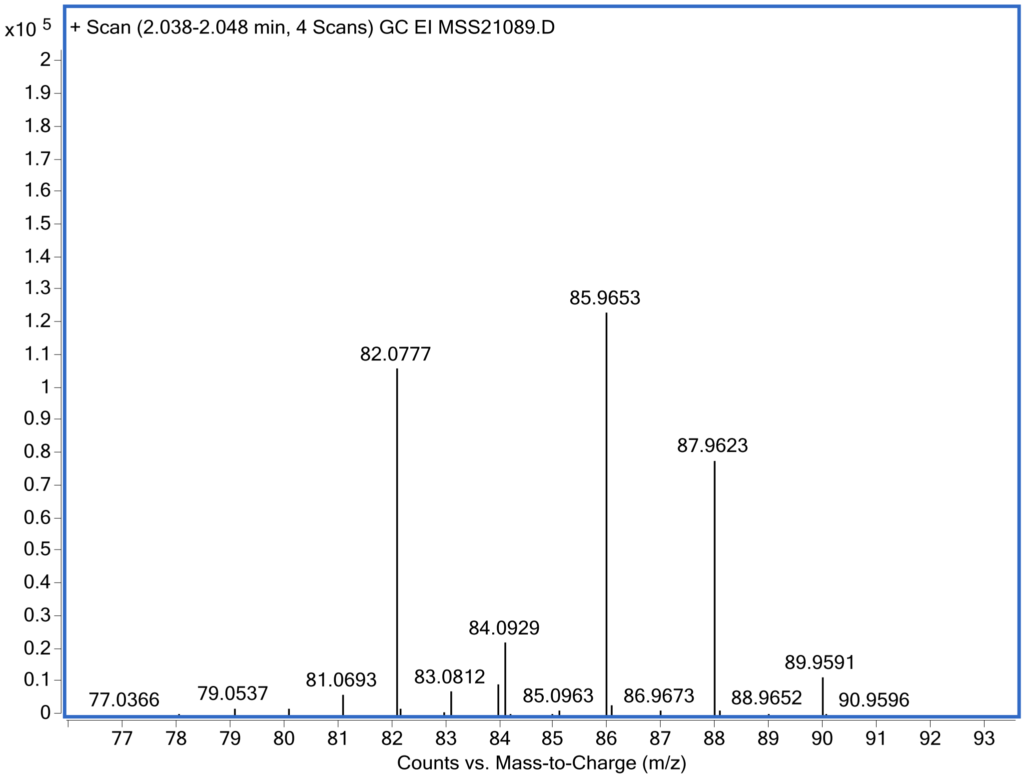

Figure S81: Mass spectrum of the isolated volatiles (top). Enlargement of m/z = 77 – 93 region (bottom). The signal at m/z = 82.0777 matches that of C_6H_{10} (calc. 82.0777). The signal at m/z = 84.0929 matches that of C_6H_{12} (calc. 84.0933). Signals at m/z = 86 and 88 are due to CD_2Cl_2.

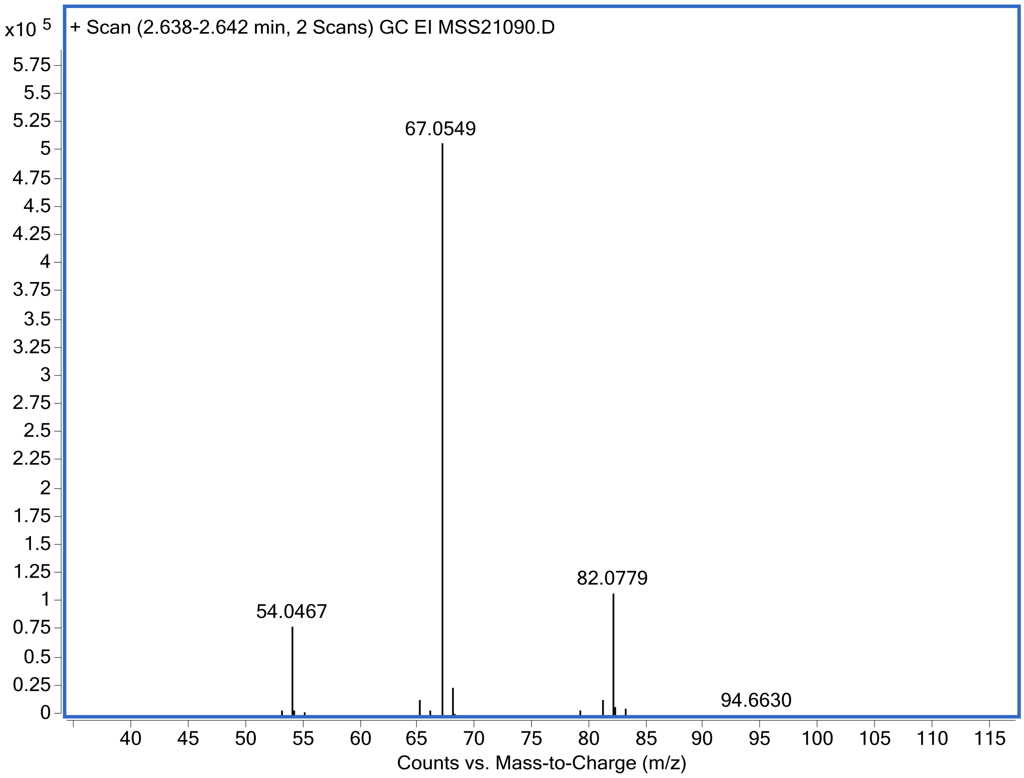

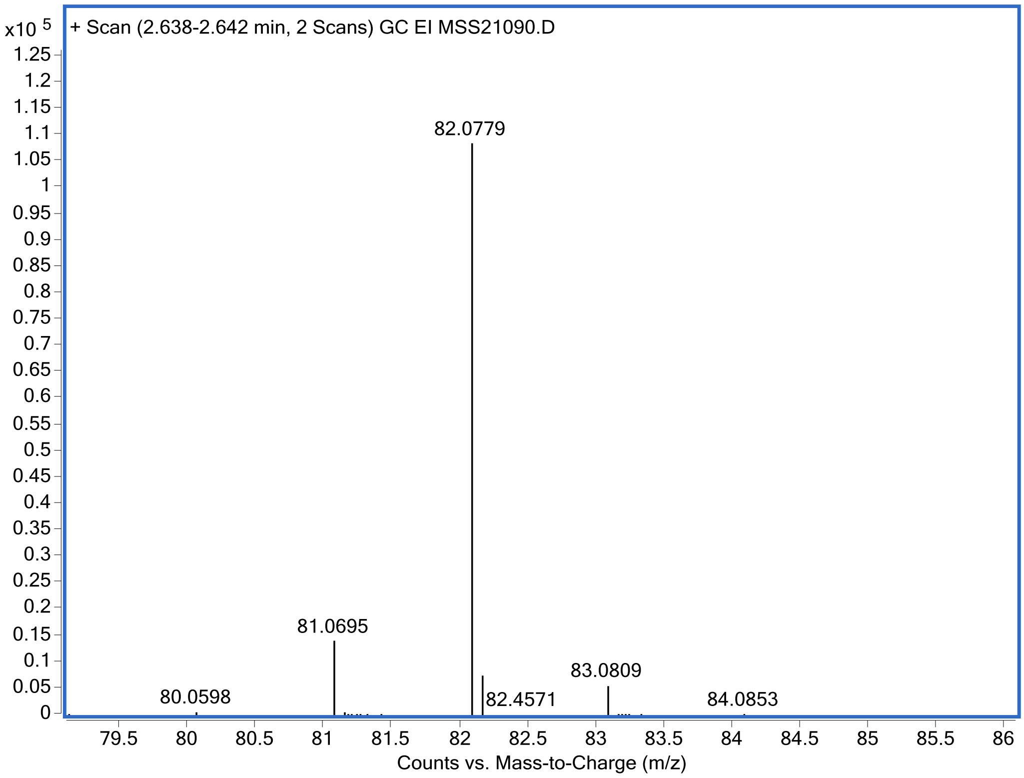

Figure S82: Mass spectrum of a commercially sourced sample of cyclohexene (top). Enlargement of m/z = 79 – 86 region (bottom).

S.4.5. Solid state dedeuteration of [1-C_6D_{12}][BAr^F_4] *under vacuum* to form [1-C_6D_8][BAr^F_4]

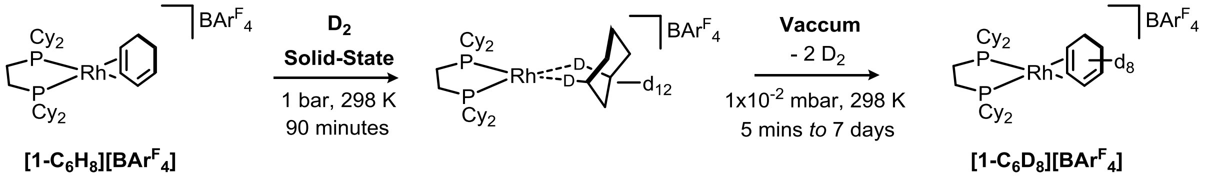

A thick walled NMR tube was charge with powdered microcrystalline **[1-C_6H_8][BAr^F_4]** (10 mg) and sample was cooled to 77 K in liquid nitrogen, evacuated and backfilled with D_2 (1 bar, 298 K). After 30 min, sample was then cooled to 77 K in liquid nitrogen, evacuated and backfilled with D_2 (1 bar, 298 K). This cycle was repeated once more, to give a total of 3 x 30 minute cycles, totaling 90 minutes under D_2. The sample was placed under a steady vacuum (2×10^{-2} mbar), was rapidly warmed to 298 K and a timer was simultaneously started. After set periods of time (5 mins to approx. 3 days) the sample was cooled to 77 K in liquid nitrogen and CH_2Cl_2 (0.40 mL) was condensed into the NMR tube. The sample was expediently thawed and rapidly transferred to the bore of a precooled (183 K) NMR spectrometer which was previously locked and shimmed to a sample of CD_2Cl_2. A $^{31}P\{^1H\}$ NMR spectrum was then acquired.

The above procedure was repeated on numerous occasions, varying the period of time the sample was exposed to vacuum at room temperature.

S.4.5.1. Kinetics of the solid state dedeuteration of **[1-C_6D_{12}][BAr$^F_4$]** *under vacuum* to form **[1-C_6D_8][BAr$^F_4$]**

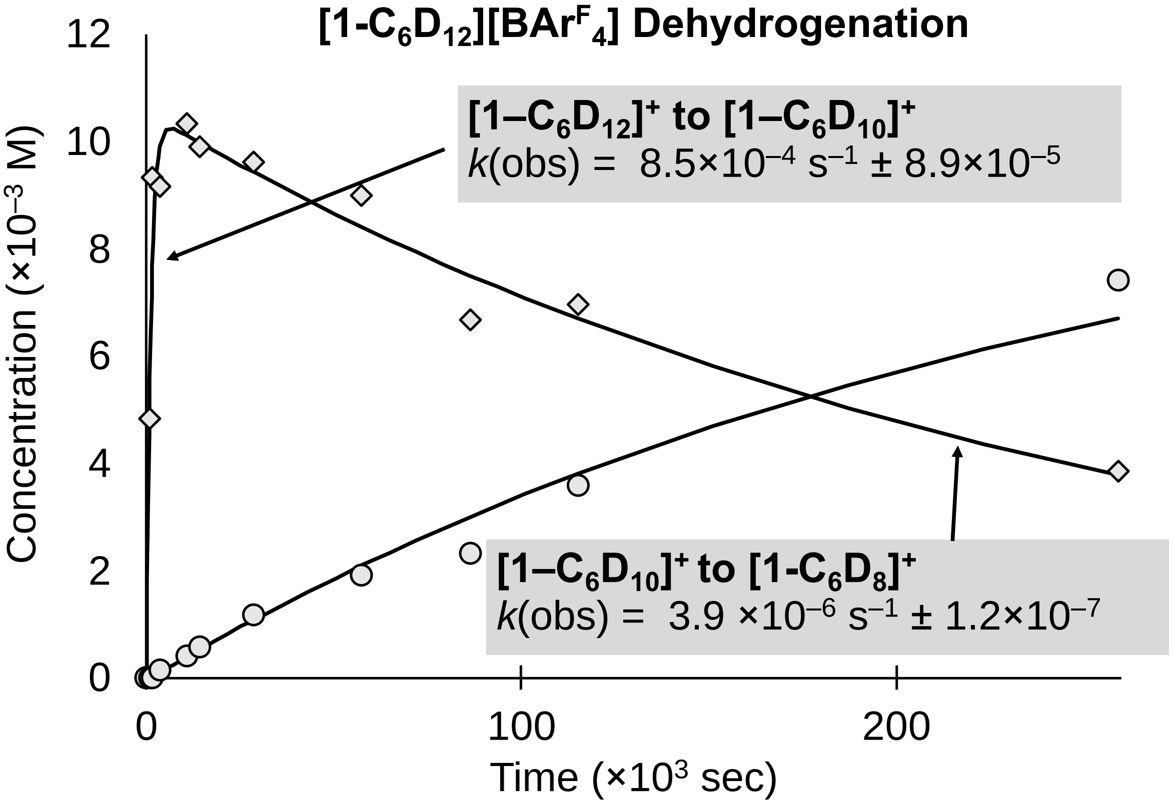

Figure S83: Temporal evolution of the dehydrogenation of **[1-C_6D_{12}][BAr$^F_4$]** under vacuum (1 × 10^{-2} mbar). A sample of **[1-C_6D_{12}][BAr$^F_4$]** was initially prepared by exposing samples of **[1-C_6H_{12}][BAr$^F_4$]** to 3 × 30 minutes of D_2 (1 bar, 298 K). This prolonged exposure resulted in a small but significant systematic decomposition of **[1-C_6H_{12}][BAr$^F_4$]**. This shown by ^{13}P{^{1}H} SSNMR to be ~ 10 % (Section S.2.4.6.). The best COPASI simulated fits (both first order) agree well with this attenuation in **[1-C_6D_{12}][BAr$^F_4$]**.

S.4.5.2. Characterization data for [1-C_6D_8][BAr^F_4]

^{1}H NMR (CD_2Cl_2, 298 K, 400 MHz): δ 7.73 (s, 8H, ortho-ArH), 7.57 (s, 4H, para-ArH), 2.15 (br s, 2H, aliphatic CH), 1.99-1.66 (br m, 24H, overlapping aliphatic CH), 1.61-1.58 (br m, 2H, aliphatic CH), 1.38-1.08 (br m, 16H, overlapping aliphatic CH), 0.99-0.96 (br m, 4H, overlapping aliphatic CH).

^{2}H NMR (CH_2Cl_2, 298 K, 61 MHz): δ 5.30 (br s, 4D, alkene-CD), 1.76 (br s, 2D, aliphatic-CD), 1.62 (br s, 2D, aliphatic-CD).

^{31}P{^{1}H} NMR (CD_2Cl_2, 298 K, 162 MHz): δ 78.7 (d, J_{RhP} 172 Hz).

^{19}F{^{1}H} NMR (CD_2Cl_2, 298 K, 377 MHz): δ -62.9 (s).

^{13}C{^{1}H} NMR (CD_2Cl_2, 298 K, 126 MHz): δ 162.2 (1:1:1:1 q, J_{CB} 50 Hz, ipso-ArC), 135.2 (s, ortho-ArC), 129.3 (q, J_{CF} 32 Hz, meta-ArC), 125.0 (q, J_{CF} 272 Hz, CF_3), 117.9 (s, para-ArC), 94.7 (1:1:1 t, J_{CD} 26 Hz, alkene-CD), 82.3 (1:1:1 t, J_{CD} 23 Hz, alkene-CD), 37.9 (dt, J_{CP} 24.4 Hz, J_{CRh} 11.5 Hz, cyclohexyl-CH), 37.0 (dt, J_{CP} 23.3 Hz, J_{CRh} 11.4 Hz, cyclohexyl-CH), 31.2 (s, cyclohexyl-CH_2), 30.0 (s, cyclohexyl-CH_2), 29.5 (s, cyclohexyl-CH_2), 29.1 (s, cyclohexyl-CH_2), 27.5 (t, J_{CP} 6.4 Hz, cyclohexyl-CH_2), 27.2 (t, J_{CP} 4.3 Hz, cyclohexyl-CH_2), 27.0 (t, J_{CP} 5.8 Hz, cyclohexyl-CH_2), 26.3 (d, J_{CP} 18.6 Hz, PCH_2), 22.6 (d, J_{CP} 3.4 Hz, cyclohexyl-CH_2), 22.5 (br s, cyclohexyl-CH_2), 22.3 (d, J_{CP} 3.2 Hz, cyclohexyl-CH_2), 21.3 (1:2:3:2:1 quintet, J_{CD} = 20 Hz, CD_2).

ESI-MS found (calc. for $[Rh(Cy_2PCH_2CH_2PCy_2)(C_6D_8)]^+$): m/z 613.34 (613.34).

S.4.5.3. Solution NMR and mass spectra of [1-C_6D_8][BAr$^F{}_4$]

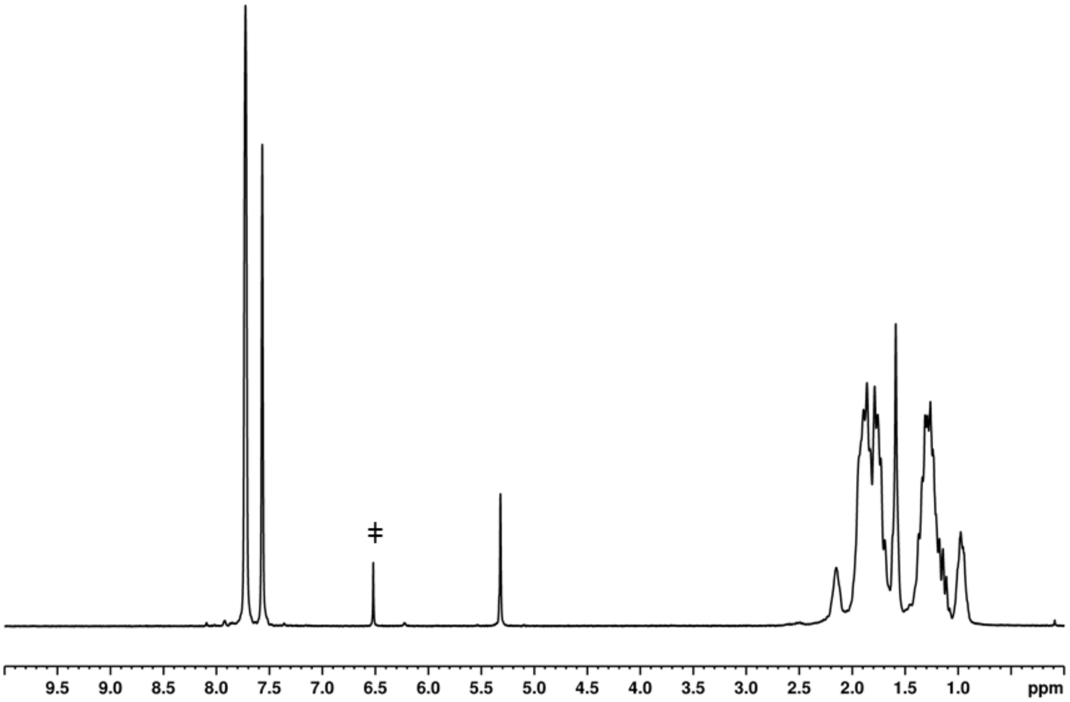

Figure S84: The solution ^{1}H NMR (CD_2Cl_2, 298 K, 400 MHz) spectrum of **[1-C_6D_8][BAr$^F{}_4$]**. The resonance marked ‡ is due to **[1-C_6H_6][BAr$^F{}_4$]** which is present as a minor (~ 5 %) contaminant in the **[1-C_6H_8][BAr$^F{}_4$]** starting material in this experiment.

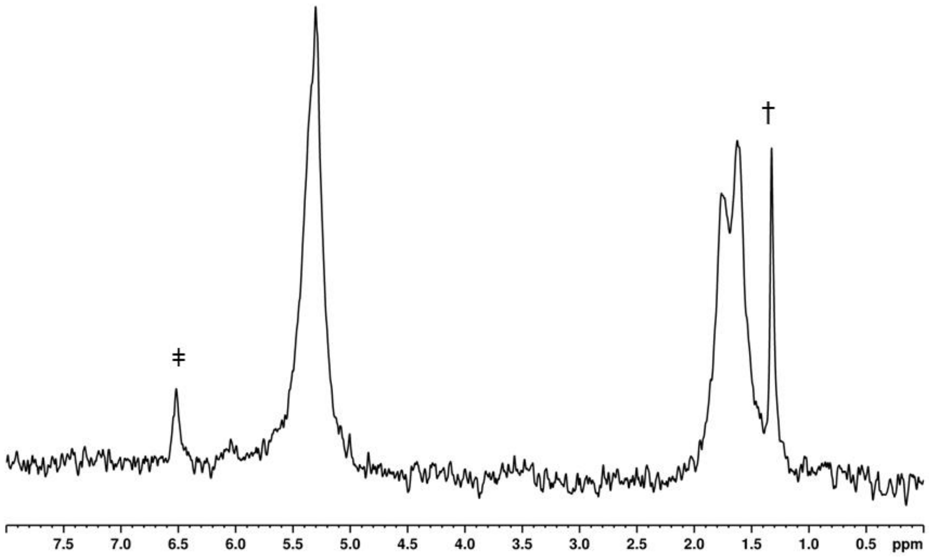

Figure S85: The solution ^{2}H NMR (CH_2Cl_2, 298 K, 61 MHz) spectrum of **[1-C_6D_8][BAr$^F{}_4$]**. The resonances marked ‡ and † are due to **[1-C_6D_6][BAr$^F{}_4$]** and liberated C_6D_{12} respectively, which arise due to the solution decomposition of **[1-C_6D_8][BAr$^F{}_4$]** and incomplete dehydrogenation.

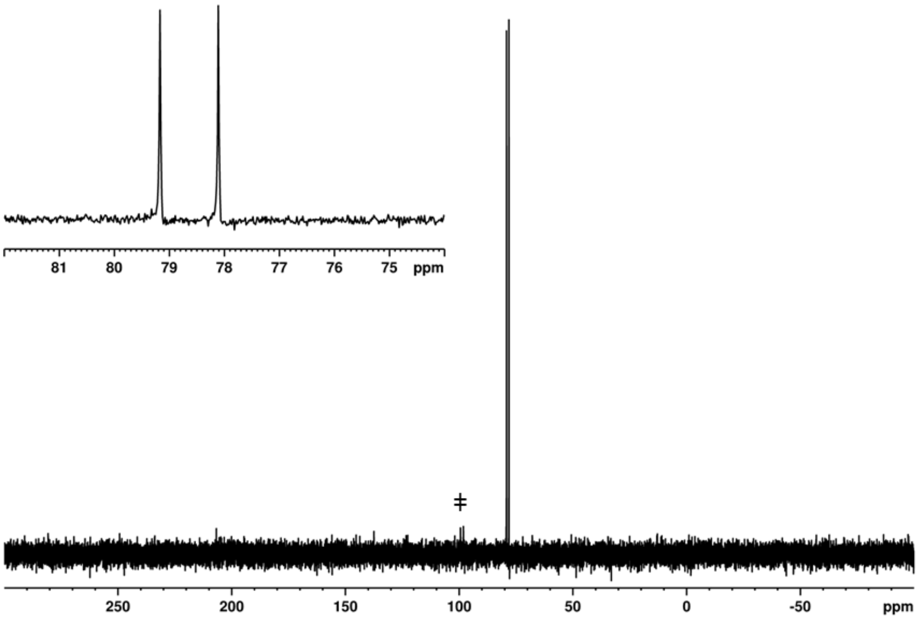

Figure S86: The solution $^{31}P\{^{1}H\}$ NMR (CD_2Cl_2, 298 K, 162 MHz) spectrum of **[1-C_6D_8][BAr$^F{}_4$]**. The resonance marked ‡ is due to **[1-C_6H_6][BAr$^F{}_4$]**.

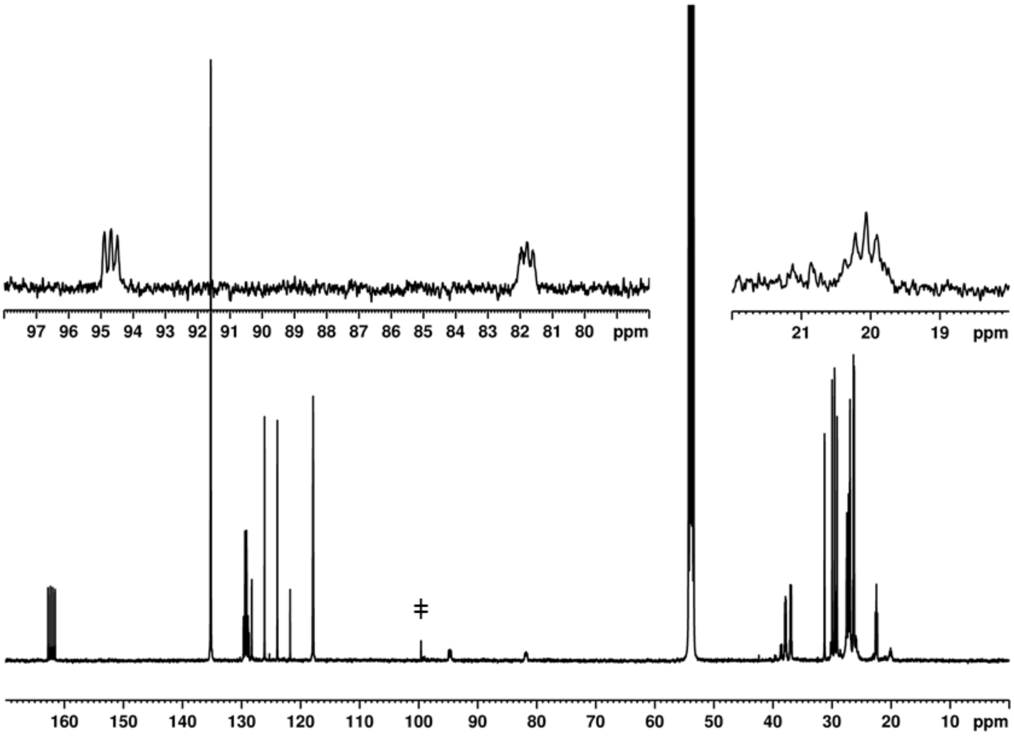

Figure S87: The solution $^{13}C\{^{1}H\}$ NMR (CD_2Cl_2, 298 K, 126 MHz) spectrum of **[1-C_6D_8][BAr$^F{}_4$]**. The resonance marked ‡ is due to **[1-C_6H_6][BAr$^F{}_4$]**.

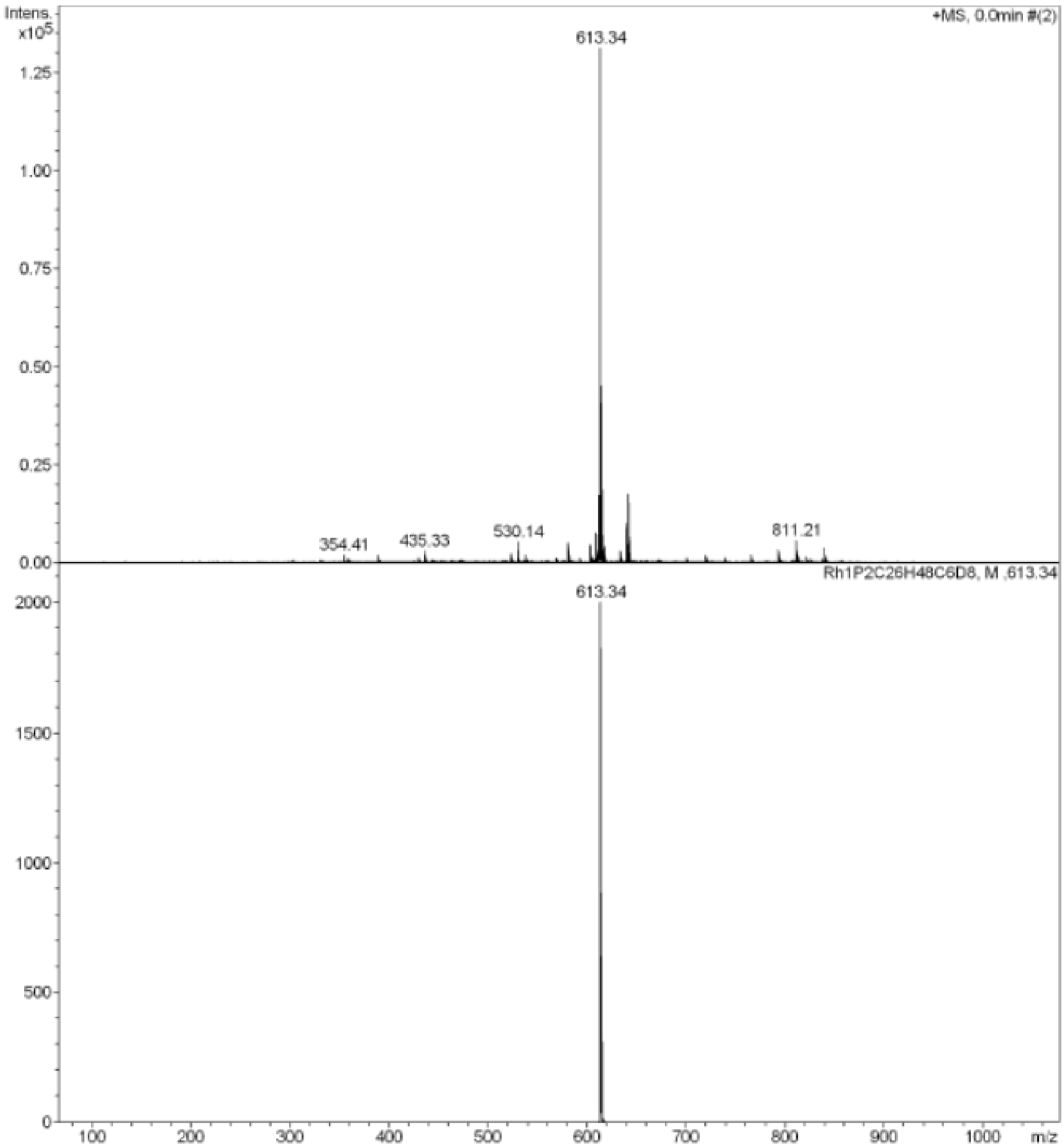

Figure S88: The experimental (top) and simulated (bottom) ESI mass spectra of **[1-C_6D_8][BAr$^F{}_4$]**.

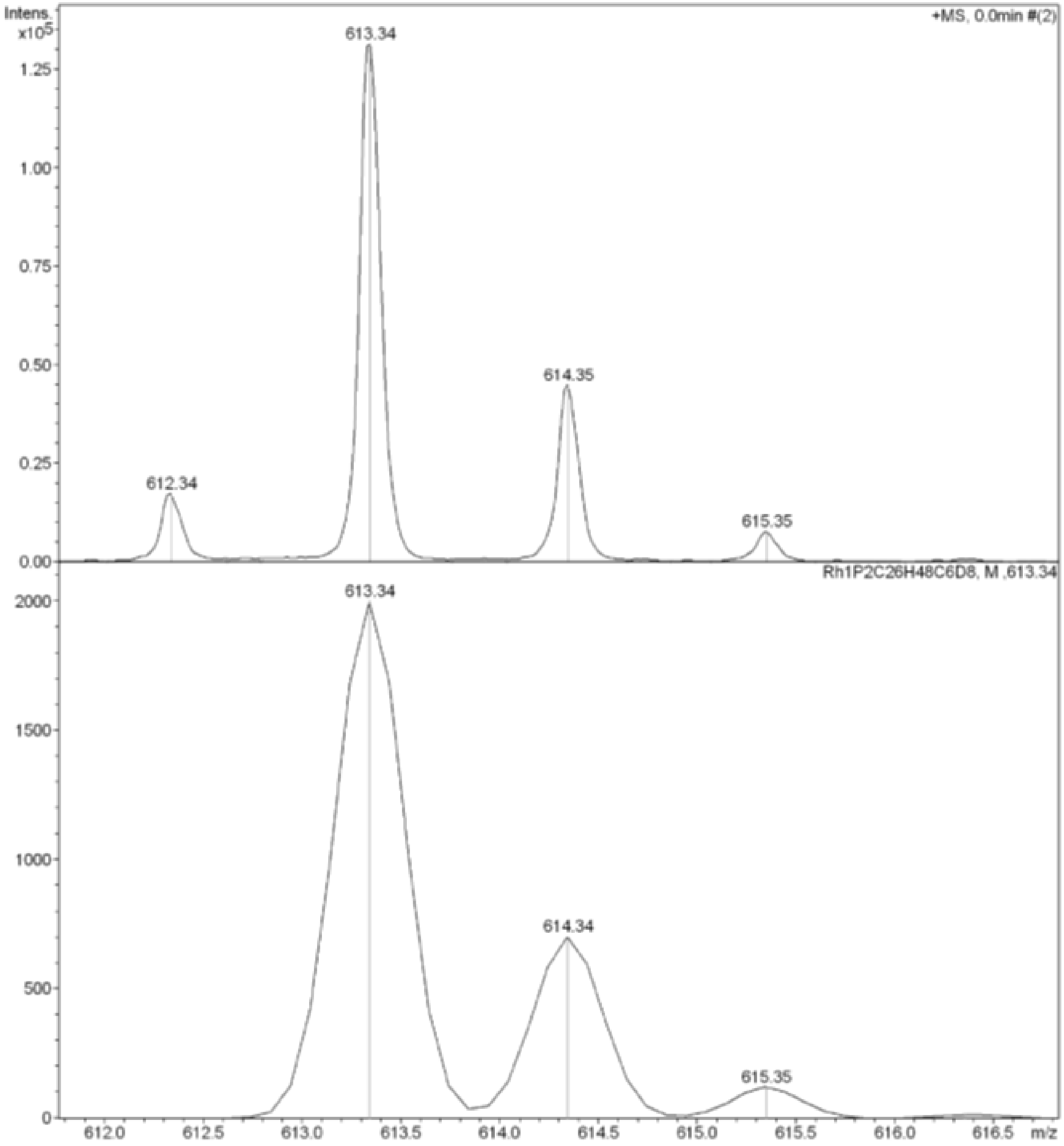

Figure S89: An enlargement of the ESI mass spectra of **[1-C_6D_8][BAr$^F_4$]** showing the matching isotope patterns. The small peak at m/z = 612.34 is [1-C_6HD_7]$^+$ (calc. 612.34), which is presumably due to trace incomplete H/D exchange.

S.4.5.4. Liberation of cyclohexadiene-d_8

A CD_2Cl_2 or CH_2Cl_2 (0.4 mL) solution of **[1-C_6D_8][BAr$^F{}_4$]** in a J Young NMR tube was freeze-pump-thaw degassed three times. The sample was then carefully refilled with CO (1 bar, 298 K). Brief agitation of the sample resulted in a rapid change in the color of the solution from orange to yellow. The volatile component was then isolated by trap-to-trap distillation. The resultant solid was confirmed to be [Rh(dcpe)$(CO)_2$][BAr$^F{}_4$] by solution $^{31}P\{^1H\}$ NMR spectroscopy (δ 85.22, d, J_{RhP} = 116 Hz).[S7]

^2H NMR (CH_2Cl_2, 298 K, 61 MHz): δ 5.91 (s, 2D), 5.81 (s, 2D), 2.08 (s, 4D).

$^{13}C\{^1H\}$ NMR (CD_2Cl_2, 298 K, 126 MHz): δ 126.1 (1:1:1 t, J_{CD} 24.5 Hz, alkene CD), 124.1 (1:1:1 t, J_{CD} 24.3 Hz, alkene CD), 21.3 (1:2:3:2:1 quintet, J_{CD} = 20 Hz, CD_2).

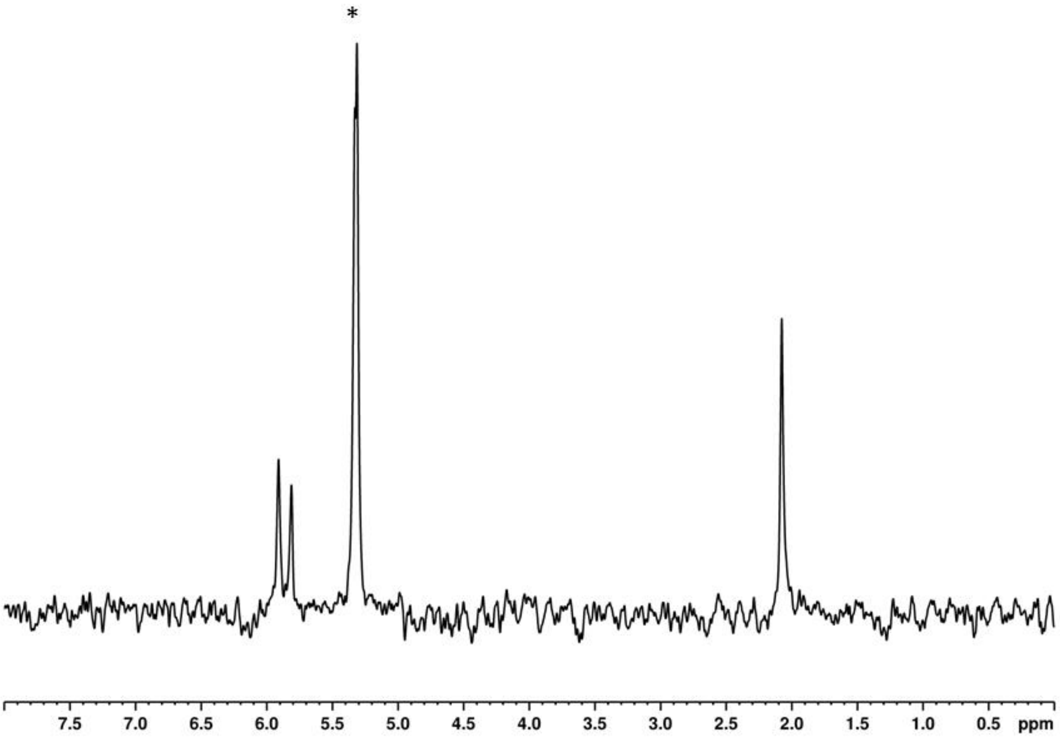

Figure S90: The solution ^2H NMR (CH_2Cl_2, 298 K, 61 MHz) spectrum of liberated alkene. The resonance marked * is due to $CHDCl_2$.

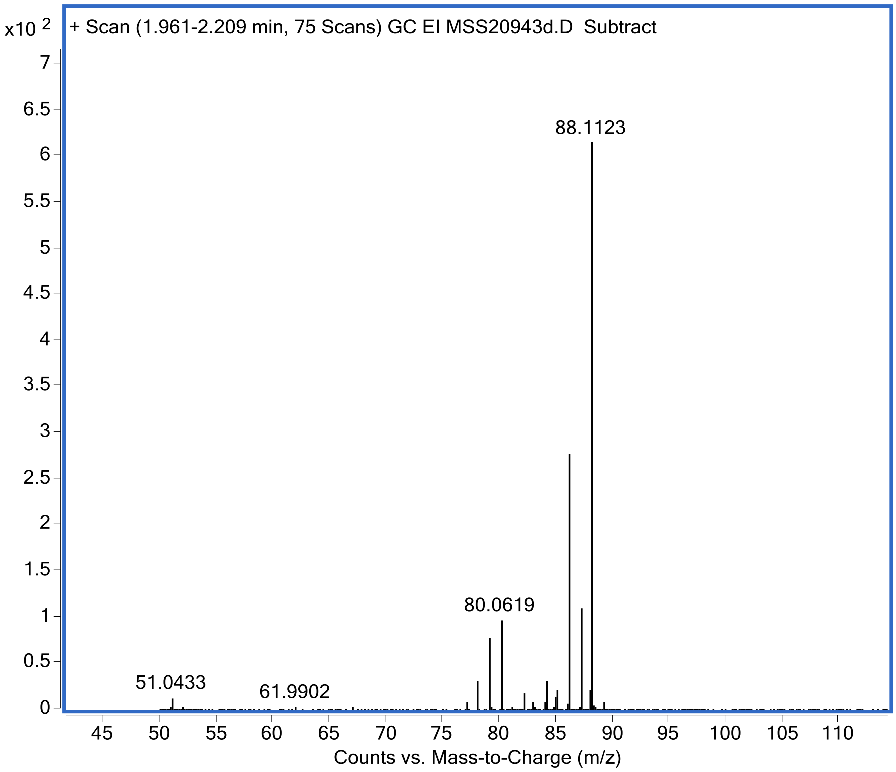

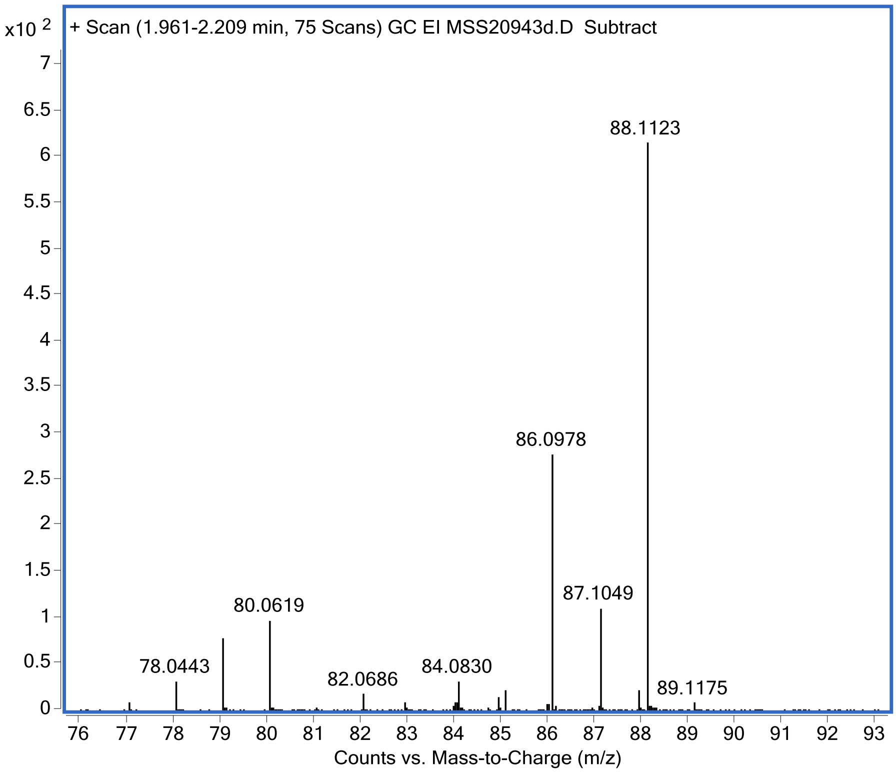

Figure S91: Mass spectrum of the isolated volatiles (top). Enlargement of m/z = 76 – 93 region (bottom). The signal at m/z = 88.1123 matches that of C_6D_8 (calc. 88.1123). The peak at m/z = 86.0978 represents that of C_6D_8-D (calc. 86.0987).

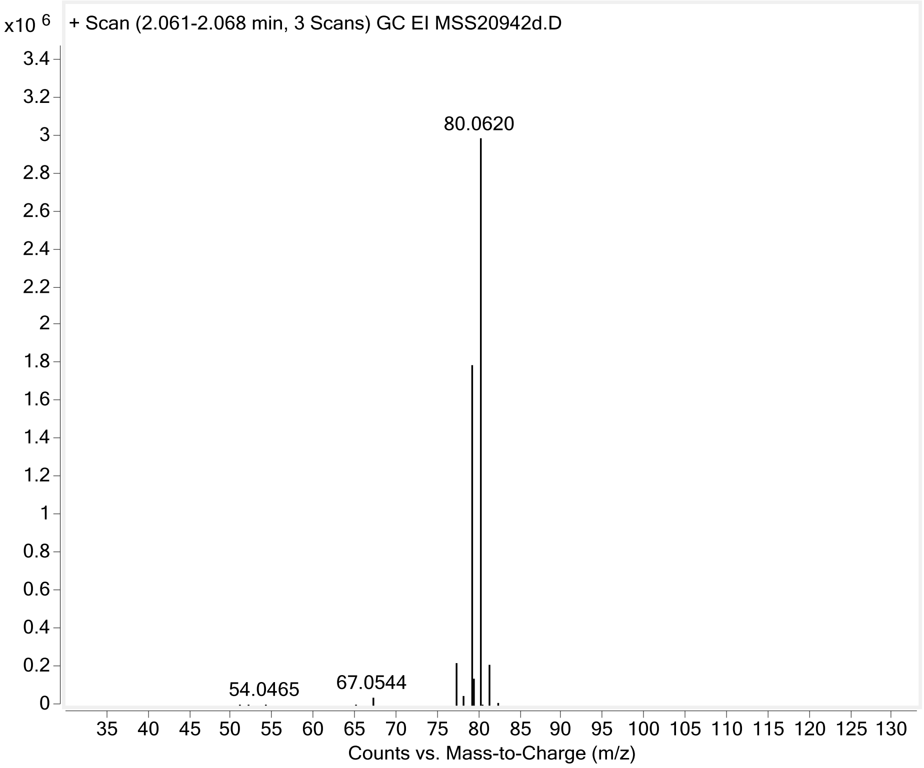

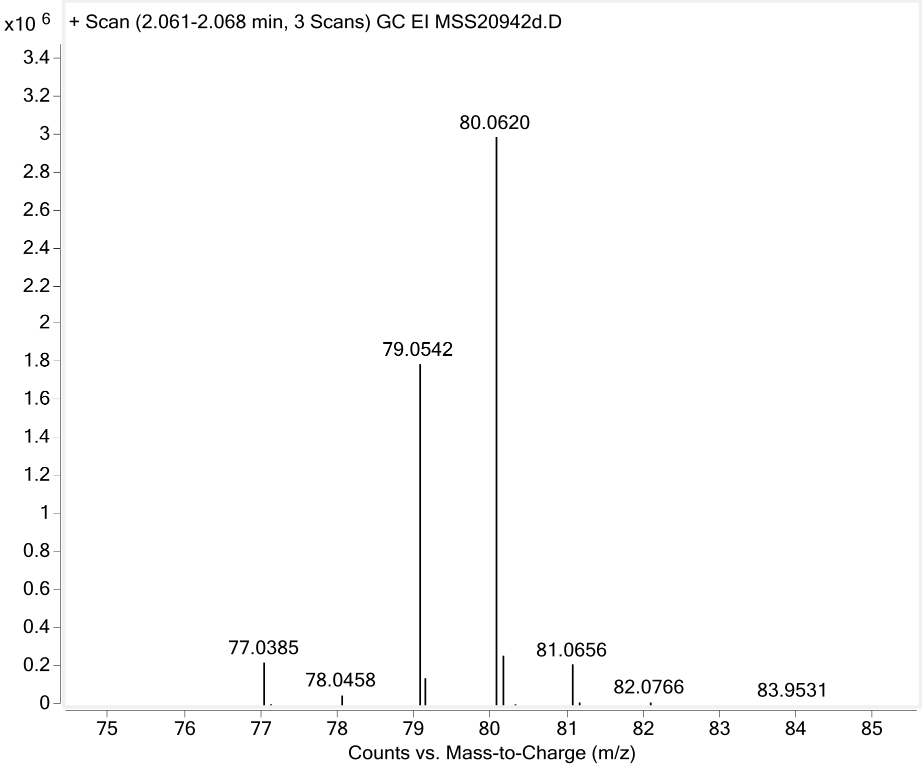

Figure S92: Mass spectrum of a commercially sourced sample of 1,3-cyclohexadiene (top). Enlargement of m/z = 75 – 85 region (bottom). The signal at m/z = 80.0620 matches that of $C_6H_8^+$ (calc. 80.0626). The peak at m/z = 79.0542 represents the $C_6H_7^+$ (calc. 79.0548).

S.5. Crystallographic and refinement data

S.5.1. Crystal structure determinations

Single crystal X-ray diffraction data for all samples were collected as follows: a typical crystal was mounted on a MiTeGen Micromounts using perfluoropolyether oil and cooled rapidly to the collection temperature in a stream of nitrogen gas using an Oxford Cryosystems Cryostream unit.[S11] The structures of **[1-C_4H_8][$BAr^F{}_4$]** (150 K), **[1-C_4H_{10}][$BAr^F{}_4$]** (100 K) & **[1-C_6H_{12}][$BAr^F{}_4$]** (150 K) were collected at the Oxford Chemical Crystallography Service from the University of Oxford, with an Agilent SuperNova diffractometer (Cu K_α radiation, λ = 1.54180 Å). **[1-C_6H_8][$BAr^F{}_4$]** (250 K) was collected at the National Crystallography Service, University of Southampton, Southampton, UK, using a Rigaku 007HF diffractometer equipped with Varimax confocal mirrors (Cu K_α radiation, 1.54184 Å), an AFC11 goniometer, and HyPix 6000 detector.

Raw frame data were reduced using CrysAlisPro.[S12] The structures were solved using SHELXT[S13] and refined using full-matrix least squares refinement on all F^2 data using the SHELXL-18[S14] using the interface OLEX2.[S15] All hydrogen atoms were placed in calculated positions (riding model). Disorder of the -CF_3 groups was treated by introducing a split site model and restraining geometries and displacement parameters.

S.5.2. Additional comments crystal structures and refinement data

[1-C_4H_{10}][$BAr^F{}_4$]:
In reply to A-Level Alert [PLAT971_ALERT_2_A]: The origin of this residual electron density relates to a positional disorder affecting a dicyclohexylphosphino group from the 1,2-Bis(dicyclohexylphosphino)ethane phosphine ligand from the asymmetric unit. This is too small contribution to be satisfactorily modelled. As such it was deemed better to retain this electron density with a low R-factor.

In reply to B-Level Alert 3 [PLAT910_ALERT_3_B]: The sequential single-crystal to single-crystal transformation caused a loss in data quality at high angles. Because of this data set was collected to satisfy a sine(theta_max)/wavelength 0.82 giving an acceptable R-factor.

In reply to B-Level Alerts 2 [PLAT971_ALERT_2_B], [PLAT971_ALERT_2_B] and [PLAT973_ALERT_2_B]: The origin of this residual electron density relates to a positional disorder affecting a dicyclohexylphosphino group from the 1,2-Bis(dicyclohexylphosphino)ethane phosphine ligand from the asymmetric unit. This is too small contribution to be satisfactorily modelled. As such it was deemed better to retain this electron density with a low R-factor.

[1-C_4H_8][$BAr^F{}_4$]-SC-SC:

In reply to A-Level Alert [PLAT029_ALERT_3_A]: The sequential two single-crystal to single-crystal transformations caused a loss in data quality. Because of this, this data set was collected to satisfy an acceptable atom connectivity model only.

In reply to B-Level Alert [THETM01_ALERT_3_B]: The sequential two single-crystal to single-crystal transformations caused a loss in data quality at high angles. Because of this, this data set was collected to satisfy a sine(theta_max)/wavelength of 0.56 giving a model for atom connectivity with an acceptable R-factor.

In reply to B-Level Alert [PLAT023_ALERT_3_B]: The sequential two single-crystal to single-crystal transformations caused a loss in data quality. Because of this, this data set was collected to satisfy an acceptable atom connectivity model only.

In reply to B-Level Alert [PLAT088_ALERT_3_B]: The sequential two single-crystal to single-crystal transformations caused a loss in data quality. Because of this, the data/parameter ratio is acceptable.

In reply to B-Level Alert [PLAT911_ALERT_3_B]: The sequential two single-crystal to single-crystal transformations caused a loss in data quality. Because of this, this data set was collected to satisfy an acceptable atom connectivity model only.

[1-C_6H_8][$BAr^F{}_4$]

Crystals of this material undergo a phase change upon slow cooling to 100 K. For this reason, the presented data was measured at 250 K.

[1-C_6H_{12}][BAr^F_4]

In reply to B-Level Alert [PLAT088_ALERT_3_B]: The single-crystal to single-crystal transformation caused a loss in data quality. Because of this, the data/parameter ratio is acceptable.

*In reply to B-Level Alert [PLAT971_ALERT_2_B and [PLAT972_ALERT_2_B]: T*he origin of this residual electron density relates to a positional disorder affecting the Rh metal centre. This is too small contribution to be satisfactorily modelled. As such it was deemed better to retain this electron density with a low R-factor.

In reply to CB-Level Alert [PLAT971_ALERT_2_C] and [PLAT972_ALERT_2_C]: The origin of this residual electron density relates to a positional disorder affecting the Rh metal centre. This is too small contribution to be satisfactorily modelled. As such it was deemed better to retain this electron density with a low R-factor.

	[1-C_4H_8][BAr^F_4]	**[1-C_4H_{10}][BAr^F_4]**	**[1-C_4H_8][BAr^F_4] ***	**[1-C_6H_8][BAr^F_4]**	**[1-C_6H_{12}][BAr^F_4]**
Chemical formula	$C_{62}H_{68}BF_{24}P_2Rh$	$C_{62}H_{70}BF_{24}P_2Rh$	$C_{62}H_{68}BF_{24}P_2Rh$	$C_{64}H_{68}BF_{24}P_2Rh$	$C_{64}H_{72}BF_{24}P_2Rh$
Formula weight	1444.82	1446.84	1444.82	1468.84	1472.87
Temperature (K)	150	100	150	250	150
Crystal system	triclinic	monoclinic	triclinic	monoclinic	monoclinic
Space group	P-1	$P2_1/n$	P-1	C2/c	C2/c
a (Å)	12.7477(3)	19.1238(3)	12.7582(16)	19.2893(2)	19.1736(8)
b (Å)	13.0092(3)	34.6204(5)	12.9595(15)	17.2828(1)	17.6512(8)
c (Å)	19.8574(4)	19.5735(3)	19.8097(8)	20.2622(1)	19.7601(12)
α (deg)	92.3462(17)	90	92.028(6)	90	90
β (deg)	90.9972(16)	90.624(2)	90.685(7)	91.1490(1)	91.086(5)
γ (deg)	96.6033(17)	90	96.2300(10)	90	90
V (Å^3)	3267.70(13)	12958.3(3)	3253.5(6)	6753.52(9)	6686.3(6)
Z	2	8	2	4	4
ρ(calcd) (g cm^{-3})	1.468	1.483	1.475	1.445	1.463
μ (mm^{-1})	3.530	3.561	3.545	3.426	3.461
Reflections collected	77320	160559	11700	32330	36704
Unique reflections	12411	24598	11700	6335	6351
Restraints / Parameters	791/1014	1706/1939	1171/1029	192/555	2524/806
R_{int}	0.0406	0.0943	0.0555	0.0349	0.0563
R_1 [$I > 2\sigma(I)$]	0.0511	0.0949	0.1095	0.0548	0.1031
wR_2 [all data]	0.1509	0.2543	0.2956	0.1709	0.2141
GooF	1.096	1.059	1.139	1.098	1.082
Residual electron density (e Å^{-3})	2.38/-1.12	3.42/-1.76	1.99/-1.41	0.97/-0.44	3.45/-2.31
CCDC no.	1916756	1916755	N / A	1916748	1916750

Table S1: Selected crystallographic and refinement data. * is from the dehydrogenation of **[1-C_4H_{10}][BAr^F_4]**, see section S.4.1.3.

S.5.3. Single Crystal X-ray Diffraction Images

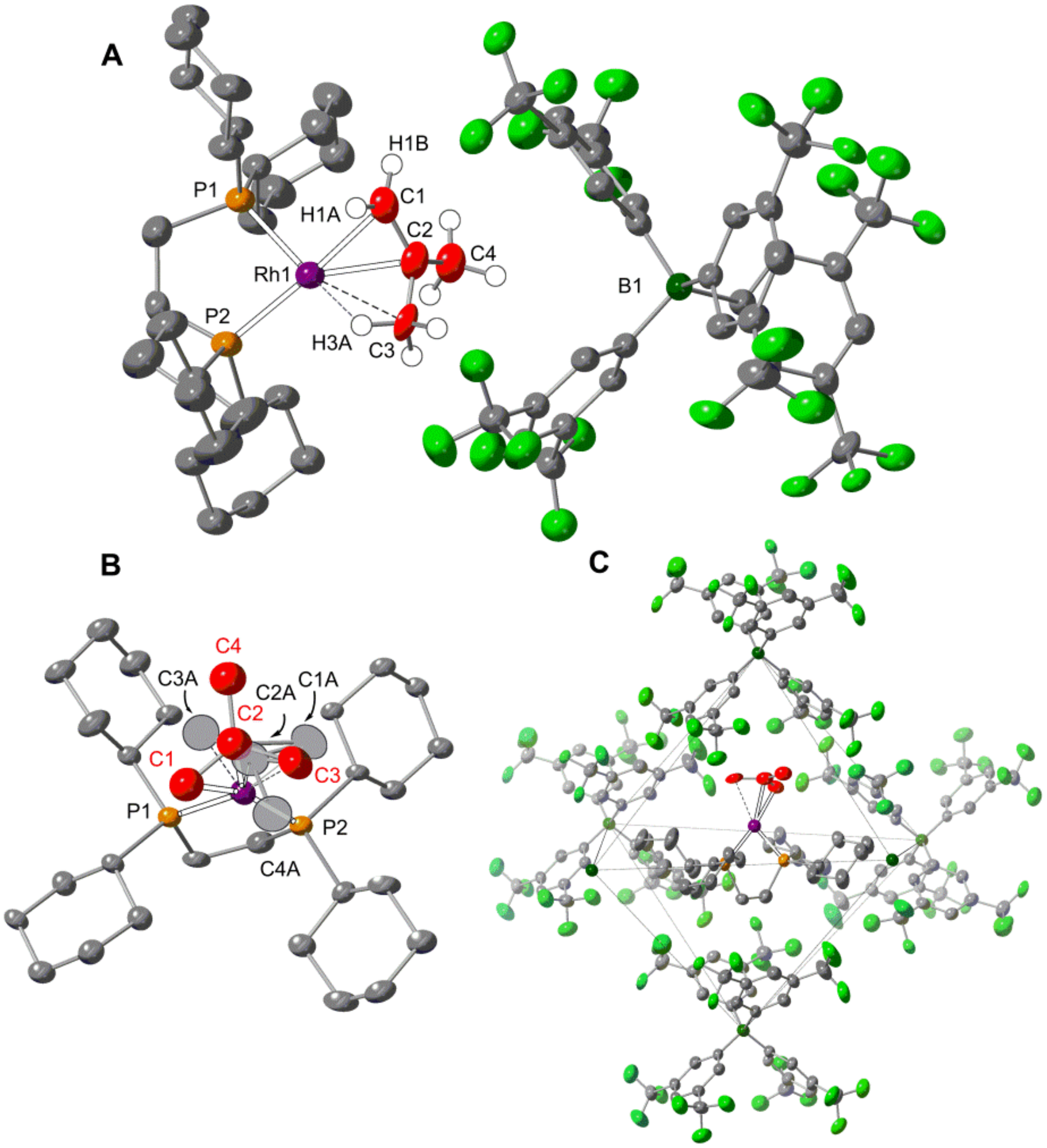

Figure S93: (A) Molecular structure of **[1-C_4H_8][$BAr^F{}_4$]**. **(B)** Cationic fragment of **[1-C_4H_8][$BAr^F{}_4$]** showing major disorder components, where the ratio of disorder components is 0.71: 0.29 for major: minor. **(C)** Structure displaying O_h anion network of the [$BAr^F{}_4$]$^-$ ion, with cationic fragment sat within the cavity; –($Ar^F{}_4$) removed from 2 boron atoms for clarity. Thermal ellipsoids set at 30 % and hydrogen from phosphine ligand and [$BAr^F{}_4$]$^-$ anion removed for clarity in all parts.

Selected bond lengths (Å): Rh1-P1 2.2238(9), Rh1-P2 2.2400(9), Rh1-C1 2.262(6), Rh1-C2 2.136(8), Rh1-C3 2.368(9), Rh1-H3A 1.848, C1-C2 1.320(12), C2-C3 1.474(13), C2-C4 1.513(13).

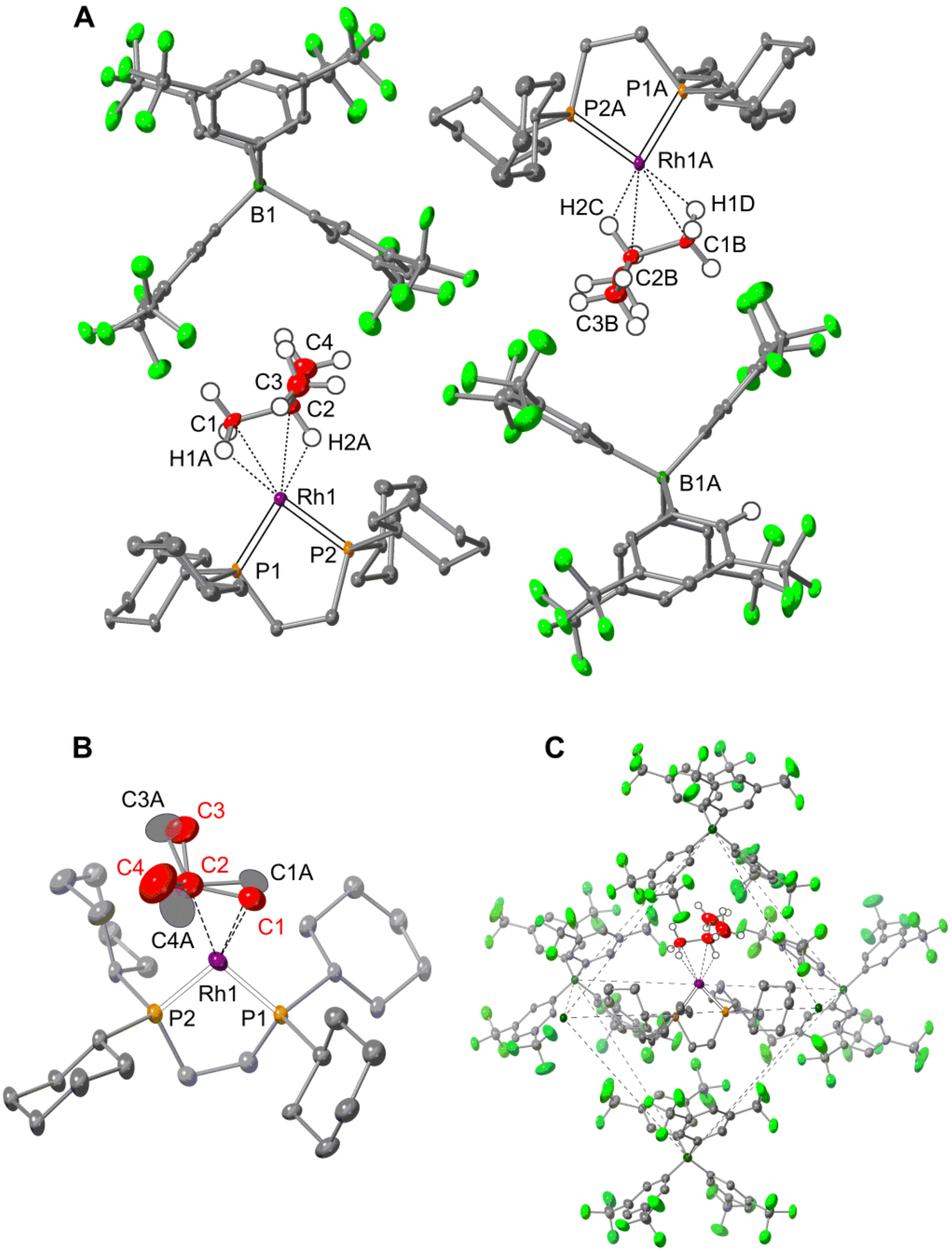

Figure S94: (A) Molecular structure of **[1-C$_4$H$_{10}$][BAr$^F{}_4$]**, showing only the major disorder components for both independent molecules in the asymmetric unit cell.

(B) Cationic fragment of the first molecule of **[1-C$_4$H$_{10}$][BAr$^F{}_4$]** in the asymmetric cell, showing both disorder components (0.67: 0.33 for major (CX) and minor (CXA). No disorder is present on C2, and is shared between the two disorder components. Not shown is the disorder in the second molecule in the asymmetric unit, however is visually indistinguishable from that shown in **(B)**. The disorder ratio for the second molecule is 0.56: 0.44 for major: minor.

(C) Structure displaying O$_h$ anion network of the [BAr$^F_4$]$^-$ ion, with cationic fragment sat within the cavity. –(Ar$^F_4$) removed from 2 boron atoms for clarity. Thermal ellipsoids set at 30 % and hydrogen from phosphine ligand and [BAr$^F_4$]$^-$ anion removed for clarity in all parts.

Selected bond lengths for the 1st molecule (Å): Rh1-P1 2.1830(14), Rh1-P2 2.1914(14), Rh1-C1 2.362(14), Rh1-H1A 1.920, Rh1-C2 2.442(7), Rh1-H2A 1.8055, C1-C2 1.551(13), C2-C3 1.528(13), C2-C4 1.516(13).

Selected bond lengths for the 2nd molecule (Å): Rh1A-P1A 2.1841(14), Rh1A-P2A 2.1887(15), Rh1A-C1B 2.390(14), Rh1A-H1D 1.980, Rh1A-C2A 2.438(8), Rh1A-H2C 1.7978, C1B-C2B 1.544(16), C2B-C3B 1.500(19).

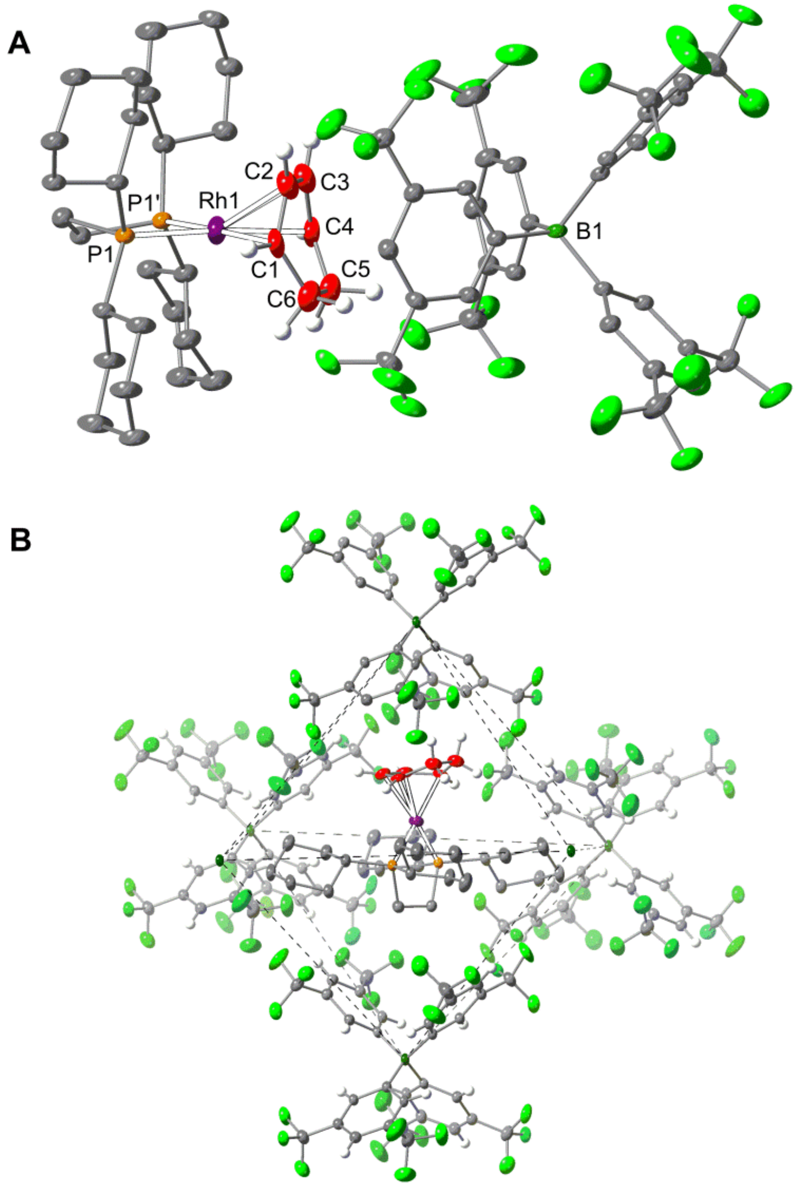

Figure S95: (A) Molecular structure of **[1-C_6H_8][BAr^F_4]** displaying major disorder component only. Operation used to generate symmetry related atoms (P1 & P1’) 1-x,y,½-z. **(B)** Structure displaying O_h anion network of the [BAr^F_4]$^-$ ion, with cationic fragment sat within the cavity. –(Ar^F_4) removed from 2 boron atoms for clarity. Thermal ellipsoids set at 30 % and hydrogens from phosphine ligand and [BAr^F_4]$^-$ anion removed for clarity in all parts.

Selected bond lengths (Å): Rh1-P1 2.2715(8), Rh1-P1’ 2.2715(8), Rh1-C1 2.20(2), Rh1-C2 2.270(9), Rh1-C3 2.284(9), Rh1-C4 2.277(10), C1-C2 1.37(3), C2-C3 1.499(18), C3-C4 1.35(3), C4-C5 1.50(3), C5-C6 1.397(19), C6-C1 1.57(3).

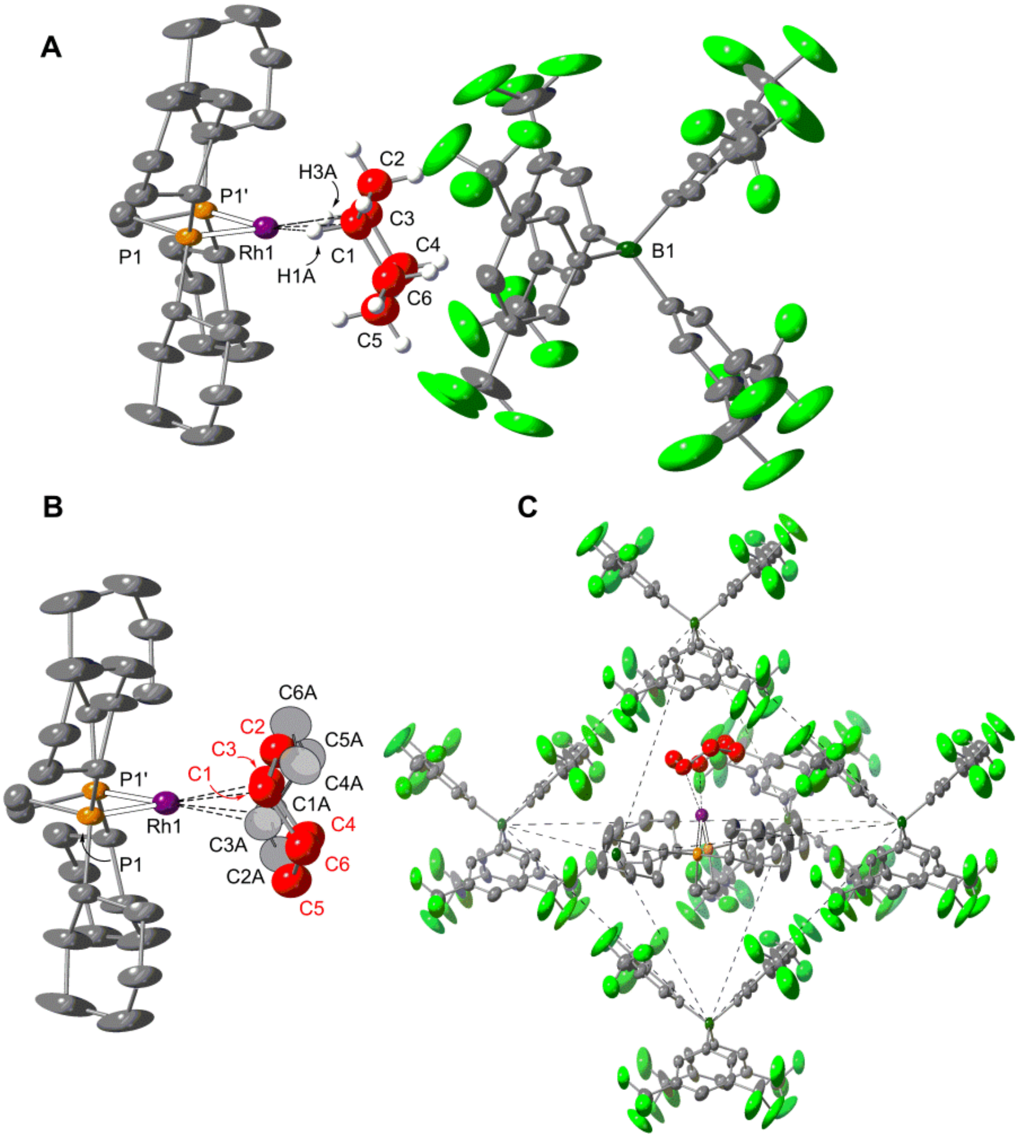

Figure S96: (A) Molecular structure of **$[1\text{-}C_6H_{12}][BAr^F{}_4]$**. **(B)** Cationic fragment of **$[1\text{-}C_6H_{12}][BAr^F{}_4]$** showing major disorder components (50%). Operation used to generate symmetry related atoms (P1 & P1') 1-x,y,½-z. **(B)** Structure displaying O_h anion network of the $[BAr^F{}_4]^-$ ion, with cationic fragment sat within the cavity. $-(Ar^F{}_4)$ removed from 1 boron atoms for clarity. Thermal ellipsoids set at 30 % and hydrogens from phosphine ligand and $[BAr^F{}_4]^-$ anion removed for clarity in all parts.

Selected bond lengths (Å): Rh1-P1 2.191(2), Rh1-P1' 2.191(2), Rh1-C1 2.62(2), Rh1-H1A 1.9065, Rh1-C3 2.53(2), Rh1-H3A 1.7777, C1-C2 1.529(15), C2-C3 1.531(15), C3-C4 1.517(15), C4-C5 1.516(16), C5-C6 1.510(15), C6-C1 1.510(15).

S.6. Computational Methods

S.6.1. Solid-State Calculations

All static Kohn-Sham DFT calculations were performed on periodic models of the studied rhodium complexes, employing the Gaussian Plane Wave (GPW) formalism as implemented in the QUICKSTEP[S16] module within the CP2K program suite (Version 5.0).[S17] Molecularly optimized basis sets of double-ζ quality plus polarization in their short-range variant (DZVP-MOLOPT-SR-GTH)[S18] were used on all atomic species. The interaction between the core electrons and the valence shell (Rh: 17, B: 3, C: 4, P: 5, F: 7, H: 1 electrons) was described by Goedecker-Teter-Hutter (GTH) pseudo potentials.[S19-21] The generalized gradient approximation (GGA) to the exchange-correlation functional according to Perdew-Burke-Ernzerhof (PBE)[S22] was used in combination with Grimme's D3-correction for dispersion interactions.[S23] The auxiliary plane wave basis set was truncated at a cutoff of 500 Ry. The maximum force convergence criterion was set to 10^{-4} Eh·Bohr^{-1}, whilst default values were used for the remaining criteria. The convergence criterion for the self-consistent field (SCF) accuracy was set to 10^{-7} Eh and 10^{-8} Eh for geometry optimizations and vibrational analysis, respectively.

The Brillouin zone was sampled using the Γ-point. Initial coordinates for **[1-C_6H_{12}][BAr$^F{}_4$]**, **[1-C_6H_8][BAr$^F{}_4$]**, **[1-C_4H_{10}][BAr$^F{}_4$]** and **[1-C_4H_8][BAr$^F{}_4$]** were obtained from the experimental crystallographic data, with the hydrogen positions normalised where possible with Mercury.[S50] Periodic boundary conditions (PBC) were applied throughout in combination with fixed unit cell parameters obtained from experiment. All geometries were first partially relaxed, keeping the heavy atoms (non-H, F) fixed, then fully relaxed without imposing any constraints, whilst keeping unit cell parameters constant in both cases. **[1-C_6H_{12}][BAr$^F{}_4$]** displays two crystallographically equivalent components. For **[1-C_4H_{10}][BAr$^F{}_4$]** two inequivalent disordered components are observed and all calculations were performed on the major component. Both independent cations were assessed in electronic structure and NMR calculations and gave similar results.

The structure of **[1-C_6H_{10}][BAr$^F{}_4$]** was constructed by removing appropriate hydrogen atoms from the experimental structure of **[1-C_6H_{12}][BAr$^F{}_4$]** under the constraint of retaining the crystal symmetry and fully optimising the remaining atomic positions. This generated two possible structures depending on which C–C bond was dehydrogenated and the more stable form was used in the main paper.

For reactivity studies different reaction pathways were initially explored using an isolated rhodium molecular cation model with the Gaussian suite of programs (see details below). Transition states located in this way provided the basis for transition state searches in the solid state, with pre-optimisations in the solid state run by fixing the key reacting atoms at one of the Rh-centres. A partial vibrational analysis was then used to identify the corresponding imaginary mode. This pre-optimized TS structure was then refined using the dimer method[S24] with the tighter convergence criteria detailed above. For challenging fluxional processes the climbing image nudged elastic band (CI-NEB) method,[S25] using 8 or 12 images, was used to obtain candidate transition states that were then optimised using the dimer method as above. All optimized stationary points were characterized by analysis of their numerical second derivatives with a displacement of 0.01 Bohr. Minima and transition states have no or exactly one imaginary eigenvalue, respectively. All transition states were further analysed using an "IRC-like" approach, whereby transition state geometries were displaced along the negative mode in both directions and then fully optimising the two resulting structures. Further details on this protocol have been reported elsewhere.[S26] A spurious imaginary frequency ($i = 6$ cm^{-1}) was found in one of the stationary points (**IX**), which appears to be due to numerical inaccuracies in the vibrational analysis, which is a familiar issue in these type of calculations.[S27-28]

Gibbs free energies for structures computed in the solid state were calculated using the TAMkin software toolkit.[S29]

All computed structures are available as a separate file of Cartesian coordinates.

S.6.2. Molecular Calculations

Molecular calculations employed the GAUSSIAN 09 (revision D.01) program package[S30] and employed the BP86 GGA functional.[S31-32] Stuttgart-Dresden (SDD)[S33] relativistic effective core potentials (ECP) in combination with the associated basis sets were utilized to describe Rh and P, with polarization functions added for P ($\zeta = 0.387$).[S34] The 6-31G(d,p) basis sets[S35-36] were used on remaining atoms.

Electronic structure analyses were performed on the geometries of the Rh cations extracted from the CP2K-optimised structures with the heavy atoms fixed at the experimental positions. An electron density file suitable for further analysis was generated from a single-point calculation.

The topology of the electron density was analysed by means of QTAIM (Quantum Theory of Atoms in Molecules),[S37] as implemented in the AIMALL package.[S38] Inner shell electrons on Rh and P modelled by ECPs were represented by core density functions (extended wavefunction format).

NBO calculations were performed using the NBO 6.0 program[S39], using the same geometries as for the QTAIM calculations above.

NCI calculations were performed using the NCIPLOT program[S40-41], using the nearest neighbour ion-pair molecular structures extracted from CP2K optimised geometries. The promolecular electron density was employed.

Orbital plots were created with Chemcraft[S42] with an outer contour value of 0.0625.

S.6.3. NMR Calculations

Isotropic ^{13}C and ^{1}H magnetic shielding constants (σ_{iso}) were generated using the GIPAW method[S43-44] as implemented in CASTEP 17.21.[S45] For **[1-C_6H_{12}][BAr$^F_4$]** three approaches were assessed: Model 1 based on the fully optimised geometry in the solid-state; Model 2 based on the experimental structure with only the positions of H and F atoms being optimised and; an ion-pair model based on the nearest neighbour ion-pair extracted form the fully optimised geometry used in Model 1. Use of the ion-pair model gave comparable results. For **[1-C_4H_{10}][BAr$^F_4$]** the size of the unit cell precluded calculations on the full unit cell and so the ion-pair model was adopted. The plane wave basis set was truncated at 80 Ry, while the Brillouin zone was sampled using a Monkhorst-Pack grid[S46] with a k-point spacing of 0.04 Å^{-1}. These settings were shown to yield converged NMR parameters on related systems.[S26] The single-point calculations were performed using the PBE GGA functional,[S22] using Ultra-soft pseudopotentials generated on-the-fly to represent the core electron shells. Scalar-relativistic effects were incorporated through the zeroth-order regular approximation (ZORA).[S47-48] The ultrafine SCF convergence threshold of 10^{-8} eV atom^{-1} was used throughout. Computed ^{13}C isotropic shielding constants were then converted into chemical shift values (δ) using the linear regression fit[S49] from the previously studied pentane system.[S26] As previously relative isotropic proton (^1H) chemical shifts were obtained by referencing computed shielding constants against those of the standard tetramethylsilane (TMS) according to $\delta iso(\ ^1H) = \sigma_{ref}(TMS) - \sigma_{iso}$, where $\sigma_{ref}(TMS)$ was calculated as δ 31.15 (cubic supercell with length 20 Å).[S26]

S.7. Computed Reactions Profiles

S.7.1. Dehydrogenation of the Isolated [1-C_6H_{12}]$^+$ Cation

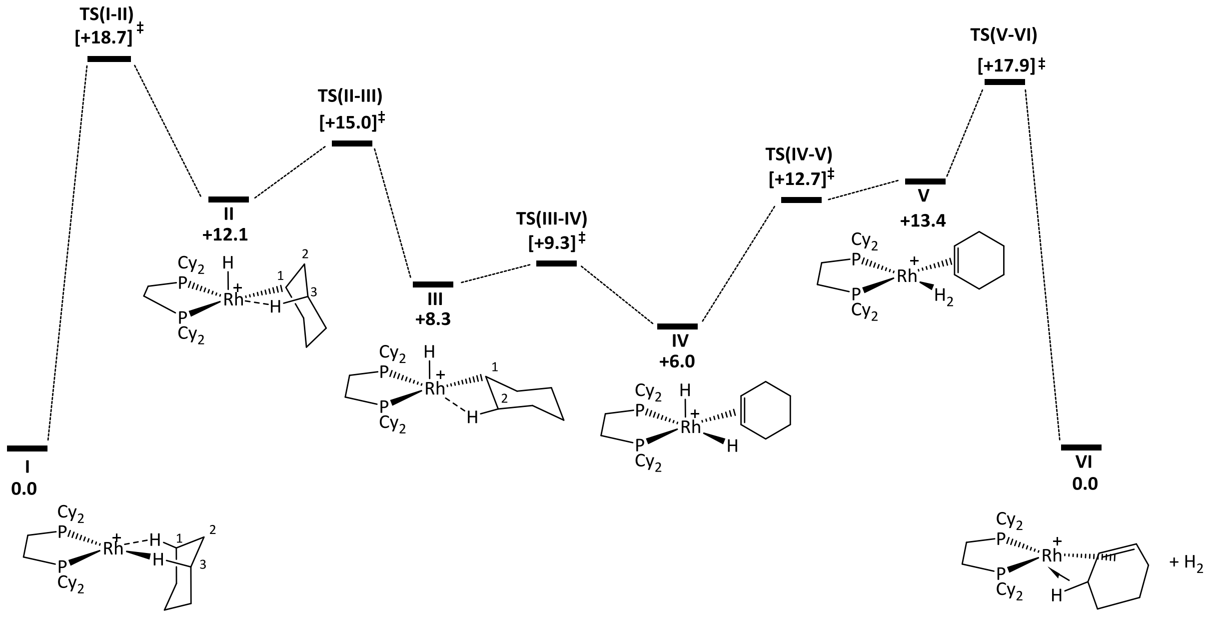

Figure S97: Computed free energy reaction profile (kcal/mol) for dehydrogenation of the isolated **[1-C_6H_{12}]$^+$** cation via initial oxidative cleavage of the C-H^1 bond.

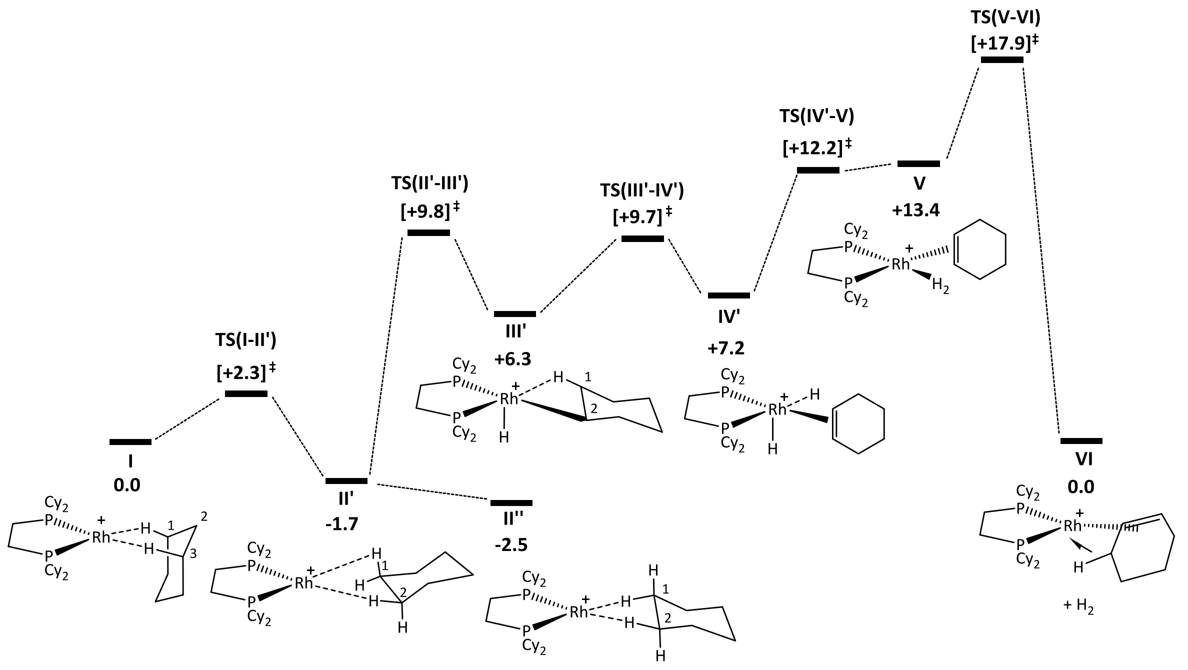

Figure S98: Computed free energy reaction profile (kcal/mol) for dehydrogenation of the isolated **[1-C_6H_{12}]$^+$** cation via an initial rearrangement to a 1,2 binding mode followed by oxidative cleavage of the C-H^2 bond.

Isolated Cation	**SCF Energy (a. u.)**	**Free Energy @ 298.15 K (a. u.)**
I	-1379.280683	-1378.505513
TS (I – II)	-1379.248161	-1378.475735
II	-1379.259755	-1378.486258
TS (II – III)	-1379.255972	-1378.481609
III	-1379.265112	-1378.492212
TS (III – IV)	-1379.260011	-1378.49068
IV	-1379.267128	-1378.495987
TS (IV – V)	-1379.254042	-1378.485205
V	-1379.255114	-1378.484236
TS (V – VI)	-1379.245969	-1378.477052
VI	-1379.258177	-1378.505514
TS (I – II')	-1379.27733	-1378.501771
II'	-1379.28219	-1378.508175
II''	-1379.283105	-1378.509544
TS (II' – III')	-1379.260945	-1378.489911
III'	-1379.266156	-1378.495414
TS (III' – IV')	-1379.259012	-1378.490066
IV'	-1379.264991	-1378.493974
TS (IV' – V)	-1379.254484	-1378.486136

Table S2: Computed energies of stationary points along the pathways shown in Figures S97 and S98.

S.7.2. Dehydrogenation of the Isolated $[1\text{-}C_6H_{10}]^+$ Cation

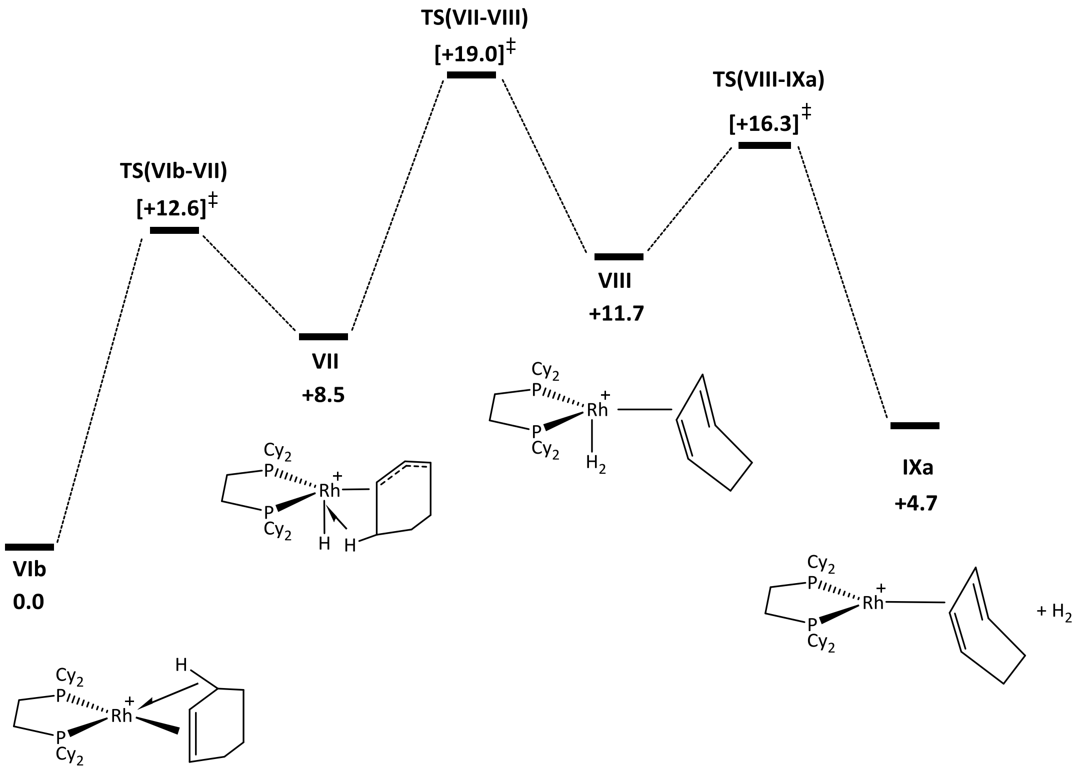

Figure S99: Computed free energy reaction profile (kcal/mol) for dehydrogenation of the isolated $[1\text{-}C_6H_{10}]^+$ cation via initial oxidative cleavage to form an exo-allyl hydride intermediate.

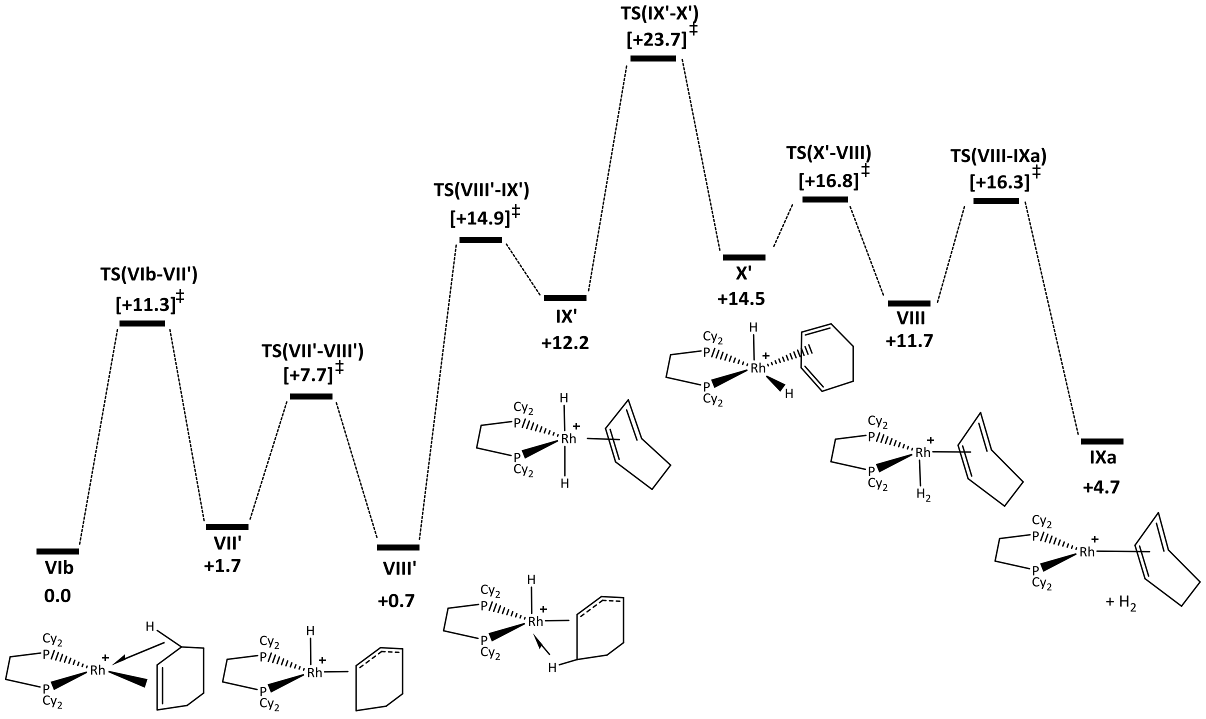

Figure S100: Computed free energy reaction profile (kcal/mol) for dehydrogenation of the isolated **[1-C$_6$H$_{10}$]$^+$** cation via initial oxidative cleavage of the agostic C-H bond to form an endo-allyl hydride intermediate.

Isolated Cation	**SCF Energy (a. u.)**	**Free Energy @ 298.16 K (a. u.)**
VIb	-1378.081611	-1377.327262
TS (VIb – VII)	-1378.0601	-1377.307252
VII	-1378.067685	-1377.313707
TS (VII – VIII)	-1378.047275	-1377.296996
VIII	-1378.058924	-1377.308609
TS (VIII – IXa)	-1378.048014	-1377.301305
IXa	-1378.055202	-1377.319806
TS (VIb – VII’)	-1378.061473	-1377.309208
VII’	-1378.077601	-1377.324588
TS (VII’ – VIII’)	-1378.068109	-1377.314998
VIII’	-1378.08005	-1377.326224
TS (VIII’ – IX’)	-1378.05293	-1377.303595
IX’	-1378.056535	-1377.307883
TS (IX’ – X’)	-1378.038878	-1377.289551
X’	-1378.055905	-1377.304155
TS (X’ – VIII)	-1378.0513	-1377.300499

Table S3: Computed energies of stationary points along the pathways shown in Figures S99 and S100.

S.7.3. Dehydrogenation of [1-C_6H_{12}][$BAr^F{}_4$] in the Solid-State

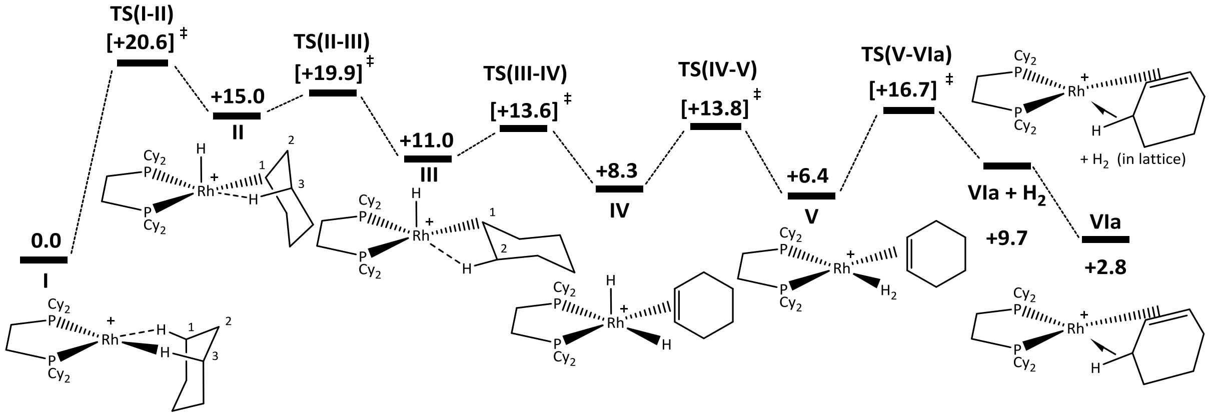

Figure S101: Computed free energy reaction profile (kcal/mol) for dehydrogenation of the **[1-C_6H_{12}][$BAr^F{}_4$]**, system via initial oxidative cleavage of the C-H^1 bond. Only the reacting Rh complex is shown with [$BAr^F{}_4$]$^-$ anions and spectator Rh cations omitted for clarity.

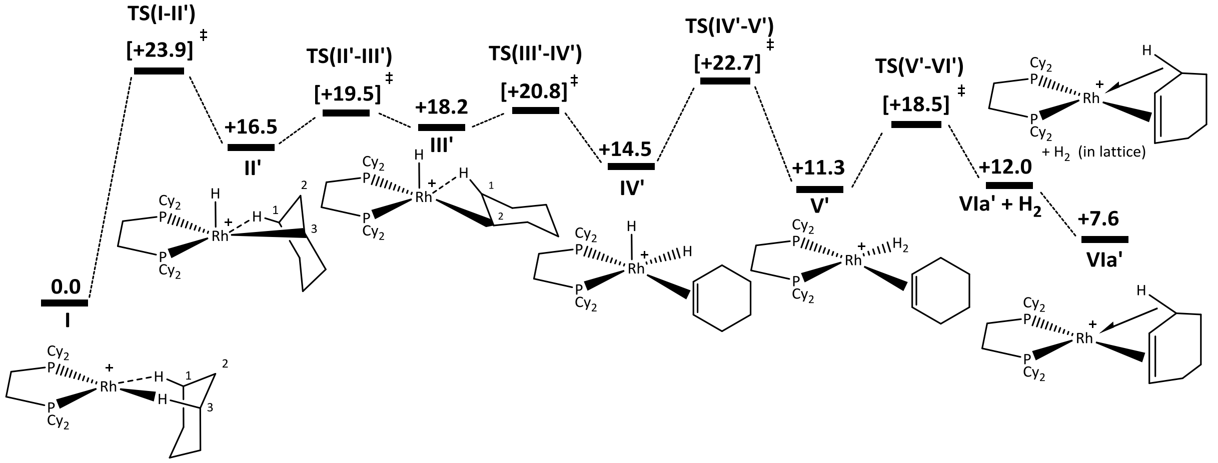

Figure S102: Computed free energy reaction profile (kcal/mol) for dehydrogenation of the **[1-C_6H_{12}][$BAr^F{}_4$]**, system via initial oxidative cleavage of the C-H^3 bond. Only the reacting Rh complex is shown with [$BAr^F{}_4$]$^-$ anions and spectator Rh cations omitted for clarity.

Solid State	**SCF Energy (a. u.)**	**SCF Energy Diff. (kcal / mol)**
I	-4462.088766	0.0
TS (I – II)	-4462.053131	22.3609
II	-4462.063259	16.0057
TS (II – III)	-4462.056574	20.2009
III	-4462.061968	16.8156
TS (III – IV)	-4462.055429	20.9190
IV	-4462.065180	14.8002
TS (IV – V)	-4462.053137	22.3571
V	-4462.065450	14.6306
TS (V – VIa)	-4462.044764	27.6116
VIa + H_2	-4462.056994	19.9371
VIa	-4460.891269	22.3211
TS (I – II')	-4462.048997	24.9551
II'	-4462.060729	17.5930
TS (II' – III')	-4462.056793	20.0633
III'	-4462.062665	16.3784
TS (III' – IV')	-4462.055583	20.8225
IV'	-4462.064813	15.0303
TS (IV' – V')	-4462.051139	23.6108
V')	-4462.064886	14.9847
TS (V' – VIa')	-4462.049781	24.4632
VIa' + H_2	-4462.056830	20.0397
VIa'	-4460.891062	22.4514

Table S4: Computed energies of stationary points along the pathways shown in Figures S101 and S102.

S.7.4. Dehydrogenation of $[1\text{-}C_6H_{10}][BAr^F_4]$ in the Solid-State

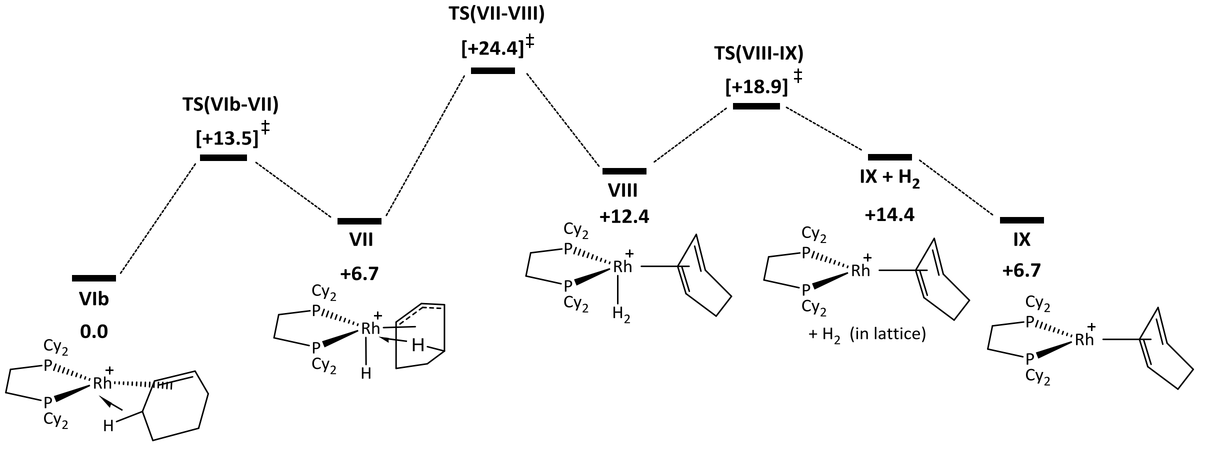

Figure S103: Computed free energy reaction profile (kcal/mol) for dehydrogenation of the **$[1\text{-}C_6H_{10}][BAr^F_4]$**, system via initial oxidative cleavage of the left agostic C-H bond, forming an exo-allyl hydride. Only the reacting Rh complex is shown with $[BAr^F_4]^-$ anions and spectator Rh cations omitted for clarity.

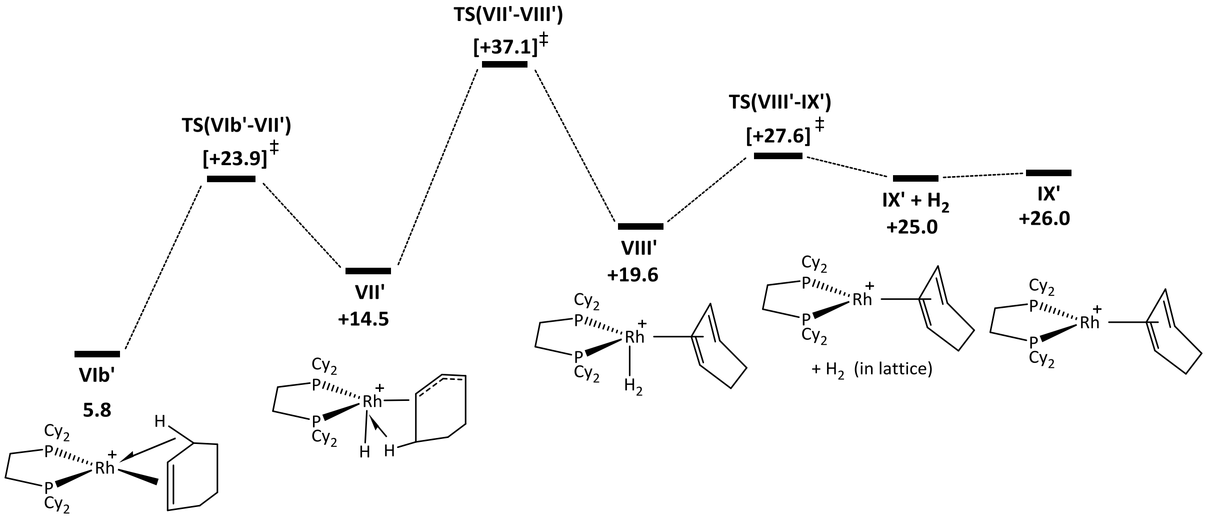

Figure S104: Computed SCF energy reaction profile (kcal/mol) for dehydrogenation of the **[1-C_6H_{10}][BAr^F_4]**, system via initial oxidative cleavage of the right agostic C-H bond, forming an endo-allyl hydride. Only the reacting Rh complex is shown with $[BAr^F_4]^-$ anions and spectator Rh cations omitted for clarity.

Solid State	**SCF Energy (a. u.)**	**SCF Energy Diff. (kcal / mol)**
VIb	-4457.310242	0.0
TS (VIb – VII)	-4457.281984	17.7317
VII	-4457.295942	8.9730
TS (VII – VIII)	-4457.262857	29.7343
VIII	-4457.284235	16.3195
TS (VIII – IX)	-4457.270651	24.8434
IX + H_2	-4457.275759	21.6380
IX	-4456.111506	23.0988
VIb’	-4457.300921	5.8487
TS (VIb’ – VII’)	-4457.272084	23.9444
VII’	-4457.287112	14.5142
TS (VII’ – VIII’)	-4457.251144	37.0842
VIII’	-4457.279026	19.5859
TS (VIII – IX’)	-4457.266255	27.6021
IX’ + H_2	-4457.270451	24.9687
IX’	-4456.106834	26.0306

Table S5: Computed energies of stationary points along the pathways shown in Figures S103 and S104.

S.7.5. Cyclohexane rearrangement processes of [1-C_6H_{12}][BAr^F_4] in the Solid State

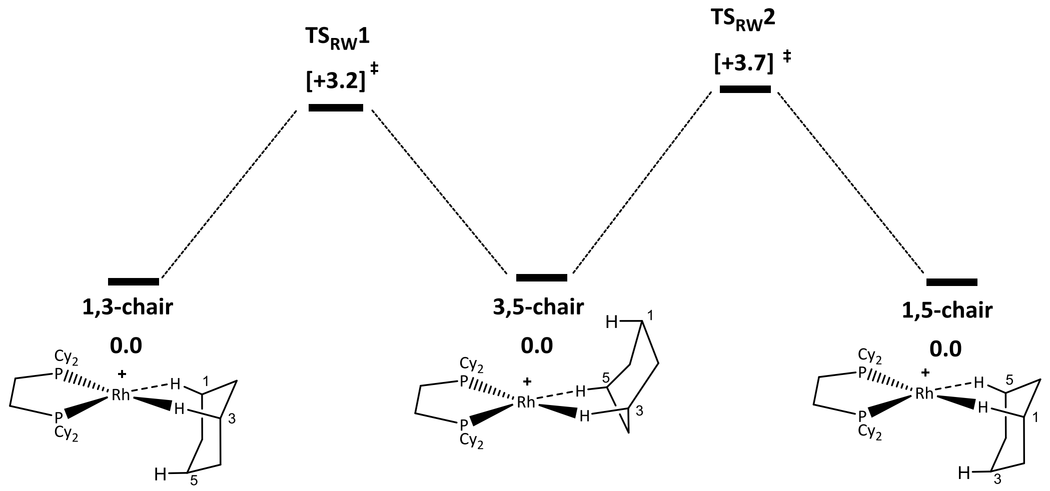

Figure S105: Computed free energy reaction profile (kcal/mol) for the 1,3,5 ring walk in **[1-C_6H_{12}][BAr^F_4]**. Only the reacting Rh complex is shown with [BAr^F_4]$^-$ anions and spectator Rh cations omitted for clarity.

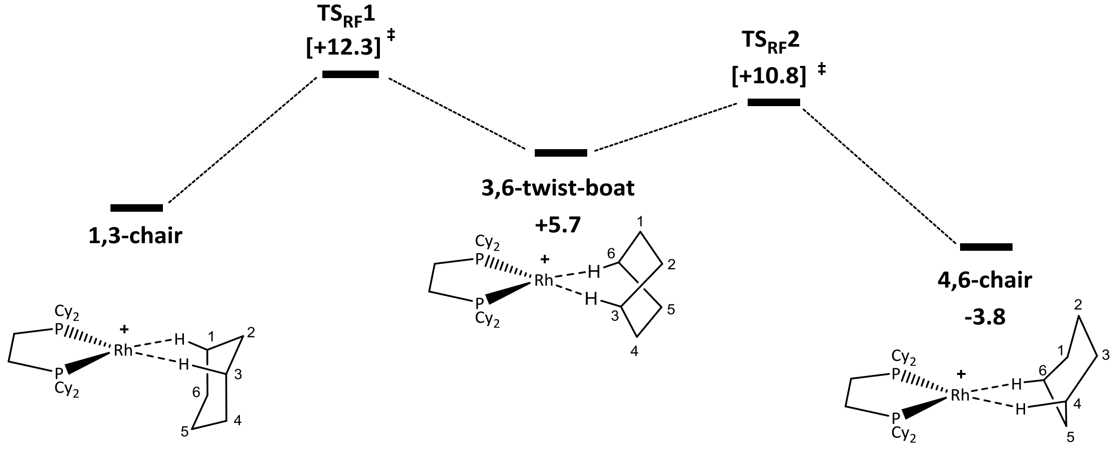

Figure S106: Computed free energy reaction profile (kcal/mol) for the ring flip of the **[1-C_6H_{12}][BAr^F_4]** system. Only the reacting Rh complex is shown with [BAr^F_4]$^-$ anions and spectator Rh cations omitted for clarity.

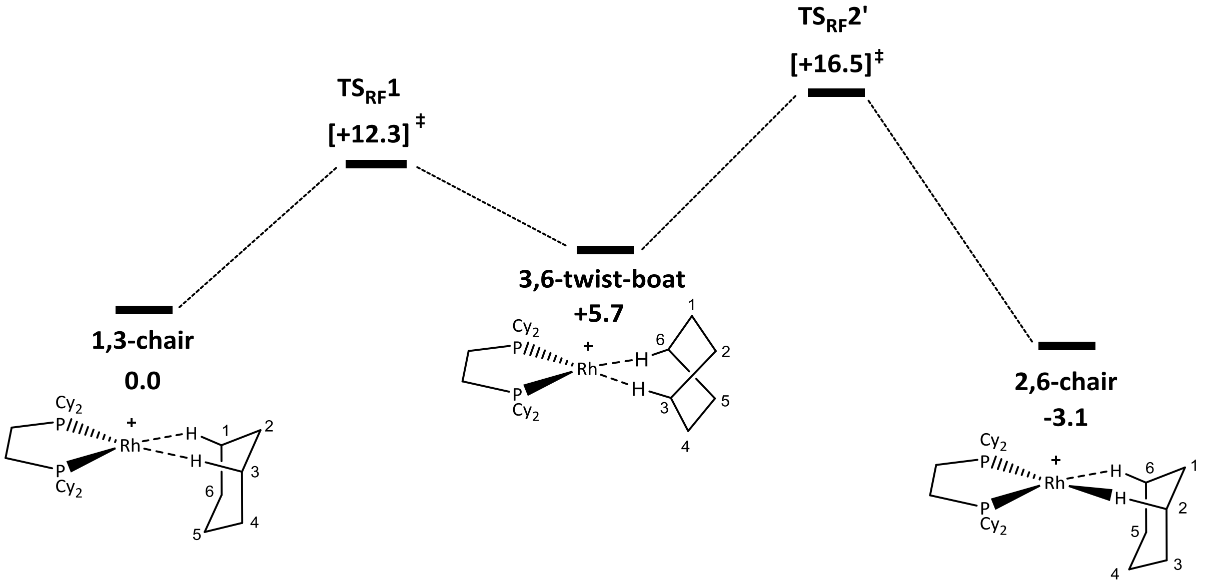

Figure S107: Computed free energy reaction profile (kcal/mol) for an alternative ring flip of the **[1-C_6H_{12}][BAr$^F{}_4$]** system. Only the reacting Rh complex is shown with [BAr$^F{}_4$]$^-$ anions and spectator Rh cations omitted for clarity.

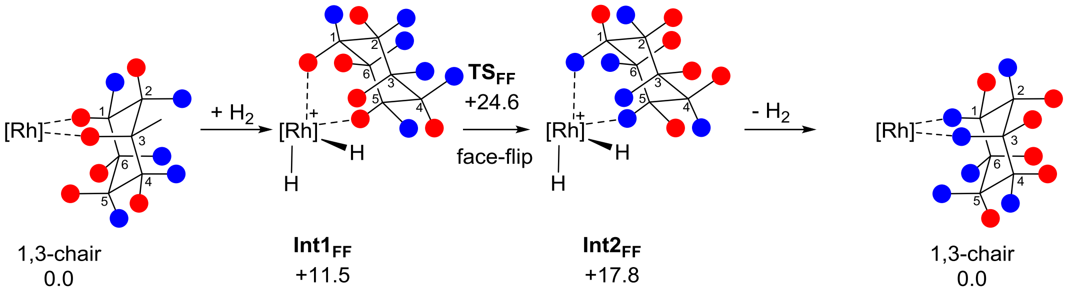

Figure S108: Computed free energies (kcal/mol) of key intermediates involved in the cyclohexane face flip in the **[1-C_6H_{12}][BAr$^F{}_4$]** system, highlighting the movement of the H atoms involved. Only the reacting Rh complex is shown with [BAr$^F{}_4$]$^-$ anions and spectator Rh cations omitted for clarity.

Solid State	**SCF Energy (a. u.)**	**SCF Energy Diff. (kcal / mol)**
1,3-chair	-4462.088766	0.0
TS$_{RW}$1	-4462.086084	1.6825
3,5-chair	-4462.088565	0.1261
TS$_{RW}$2	-4462.085353	2.1414
1,5-chair	-4462.088762	0.0022
TS$_{RF}$1	-4462.068397	12.7814
3,6-twist-boat	-4462.080250	5.3436
TS$_{RF}$2	-4462.067364	13.4299
4,6-chair	-4462.085361	2.1363
TS$_{RF}$2'	-4462.065488	14.6071
2,6-chair	-4462.087509	0.7886
Int1$_{FF}$	-4463.251501	-0.5076
TS1$_{FF}$	-4463.231182	12.2425
Int2$_{FF}$	-4463.242107	5.3869

Table S6: Computed energies of stationary points along the fluxional processes shown in Figures S105-S108.

S.8. Computed NMR Chemical Shifts

S.8.1. [1-C_4H_{10}][BAr$^F{}_4$]

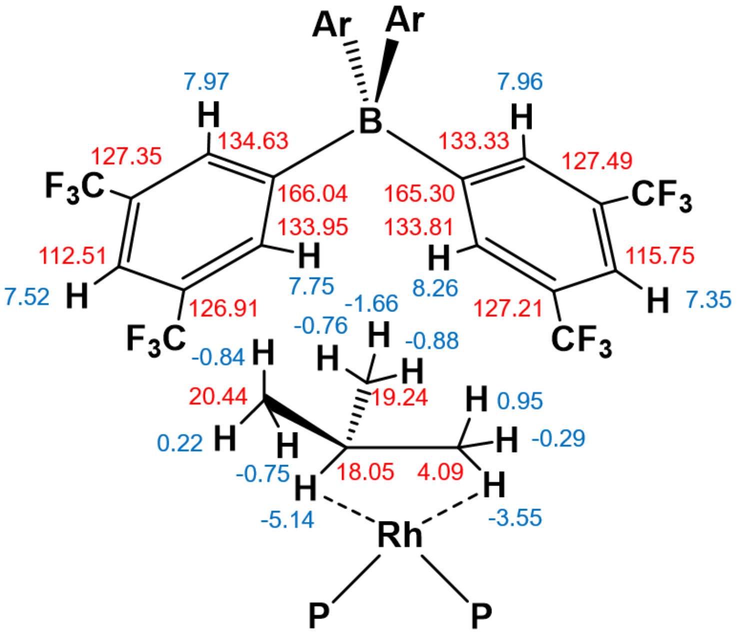

Figure S109: Computed NMR chemical shifts (ppm) for **[1-C_4H_{10}][BAr$^F{}_4$]** (cation 1). ^{1}H chemical shifts are shown in blue and ^{13}C shifts in red.

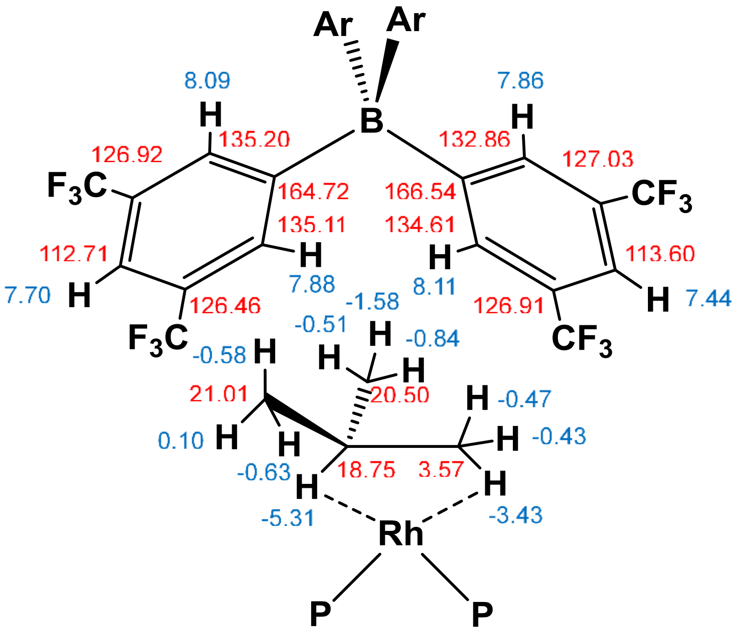

Figure S110: Computed NMR chemical shifts (ppm) for **[1-C_4H_{10}][BAr$^F{}_4$]** (cation 2). ^{1}H chemical shifts are shown in blue and ^{13}C shifts in red.

S.8.2. [1-C_6H_{12}][BAr^F_4]

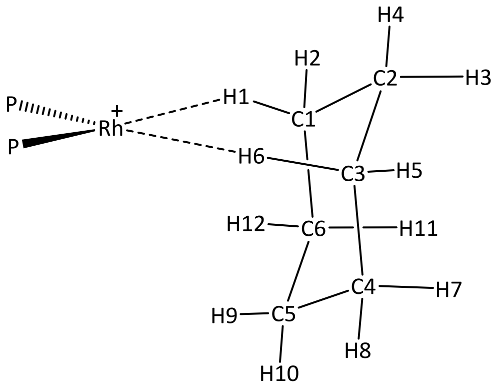

Figure S111: Labelling scheme employed.

		Model 1			**Model 2**			**Ion Pair**	
Nucleus	σ^{iso}	δ ^{1}**H**	**δ ^{13}C**	σ^{iso}	δ ^{1}**H**	**δ ^{13}C**	σ^{iso}	δ ^{1}**H**	**δ ^{13}C**
H1	37.1528	-6.00		36.1609	-5.01		37.6566	-6.51	
H2	30.0546	1.10		30.4775	0.67		30.5041	0.65	
H3	30.7537	0.40		31.0223	0.13		31.1643	-0.01	
H4	29.3258	1.82		28.8933	2.26		30.0916	1.06	
H5	29.7757	1.37		29.9983	1.15		30.3096	0.84	
H6	36.7497	-5.60		35.7647	-4.61		37.2708	-6.12	
H7	32.8162	-1.67		32.8452	-1.70		33.0983	-1.95	
H8	30.2027	0.95		30.0231	1.13		30.8968	0.25	
H9	30.7822	0.37		31.0827	0.07		31.4869	-0.34	
H10	29.4862	1.66		29.0109	2.14		30.2264	0.92	
H11	32.9866	-1.84		32.3977	-1.25		33.2908	-2.14	
H12	30.0397	1.11		29.5275	1.62		30.7145	0.44	
C1	148.0118		23.74	157.3883		15.60	147.6427		24.10
C2	149.5209		22.29	148.8721		23.89	151.8025		20.08
C3	149.3763		22.43	153.8161		19.08	148.929		22.86
C4	145.8353		25.85	144.1107		28.53	146.2955		25.40
C5	144.7839		26.86	144.4966		28.16	144.7953		26.85
C6	145.1803		26.48	143.0411		29.58	145.8146		25.87

Table S7: [1-C_6H_{12}][BAr^F_4] computed isotropic chemical shifts (σ^{iso}) and relative chemical shifts (ppm) using the labelling scheme shown in Figure S108.[a]

[a] Model 1 data are based on the fully optimised geometry of **[1-C_6H_{12}][BAr^F_4]** in the solid-state; Model 2: data are based on the experimental structure with only the positions of H and F atoms being optimised; ion-pair model based on the nearest neighbour ion-pair extracted from the fully optimised geometry in Model 1.

S.9. Electronic Structure Analyses

S.9.1. [1-C_4H_{10}][$BAr^F{}_4$]

Note: Analyses were performed for both crystallographically independent cations contained in the unit cell.

Distance (Å)	Fully Optimized	Heavy Atom Fixed[a]	Experiment
Rh – P2	2.200	2.183	2.183(1)
Rh – P3	2.207	2.191	2.191(1)
Rh – H34	1.923	1.933	1.920
Rh – H37	1.899	1.873	1.806
Rh – C4	2.361	2.363	2.363(14)
Rh – C5	2.480	2.442	2.442(7)
C4 – H34	1.150	1.148	0.981
C4 – H35	1.099	1.099	0.980
C4 – H36	1.096	1.094	0.980
C5 – H37	1.159	1.160	1.000
Bite Angle (°)	87.401	89.322	76.96

Table S8: Key bond distances (Å) for **1st Cation** from fully optimised and heavy atoms fixed geometries of **[1-C_4H_{10}][$BAr^F{}_4$]**, with experimental data for comparison.[S31]

[a] structure is based on the experimental structure with only the positions of H and F atoms being optimised.

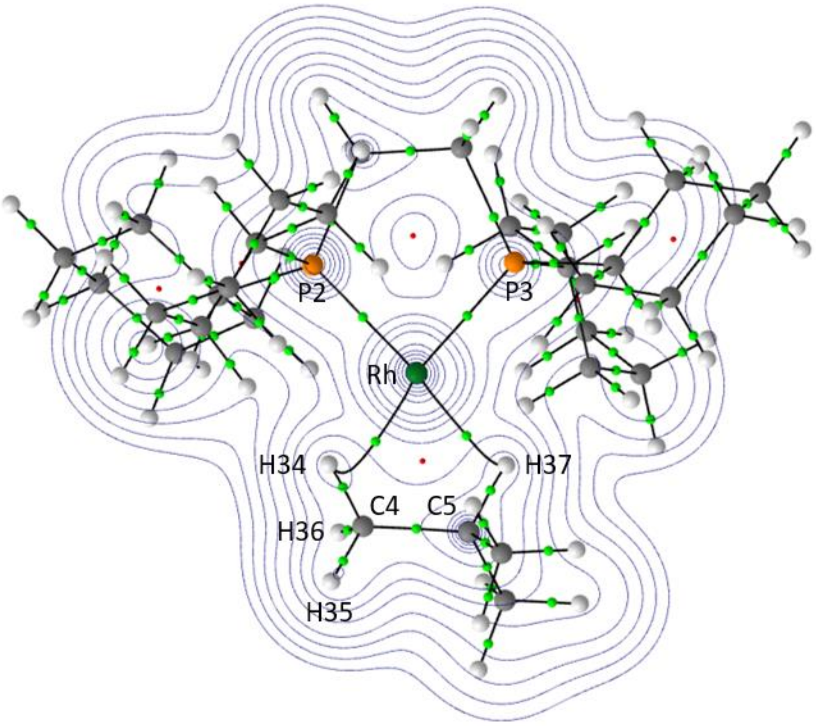

Figure S112: QTAIM molecular graph for 1st cation of **[1-C_4H_{10}][BAr$^F{}_4$]** in with density contours plotted in the Rh-H34-H37 plane.[S30] Bond critical points (BCPs) are indicated in green and ring critical points (RCPs) are indicated in red.

Bond	$\rho(r)$ /eÅ^{-3}	$\nabla^2 \rho(r)$ /eÅ^{-5}	**H** (r)
Rh – P2	0.124	0.066	-0.065
Rh – P3	0.123	0.068	-0.063
Rh – H34	0.056	0.247	-0.004
Rh – H37	0.060	0.241	-0.009
C4 – H34	0.236	-0.643	-0.209
C4 – H35	0.271	-0.911	-0.272
C4 – H36	0.277	-0.953	-0.280
C5– H37	0.232	-0.601	-0.200

Table S9: Key BCP metrics for the 1st cation of **[1-C_4H_{10}][BAr$^F{}_4$]**.

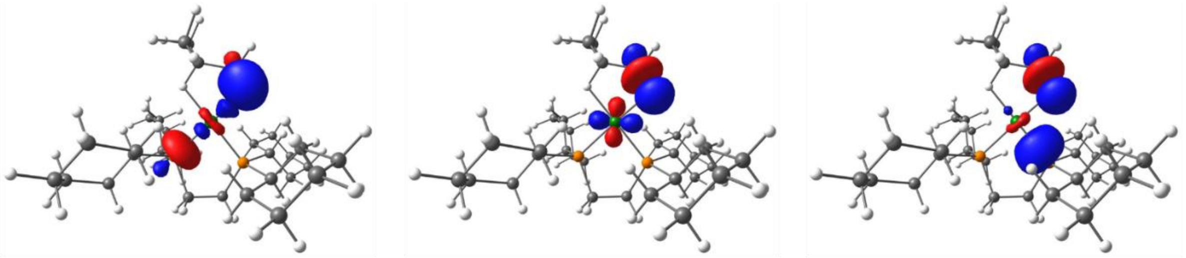

a) $\sigma_{C\text{-}H} \rightarrow \sigma^*_{Rh\text{-}P}$: (22.30 kcal mol^{-1}) b) $LP_{Rh} \rightarrow \sigma^*_{C\text{-}H}$: (3.80 kcal mol^{-1}) c) $\sigma_{Rh\text{-}P} \rightarrow \sigma^*_{C\text{-}H}$: (2.54 kcal mol^{-1})

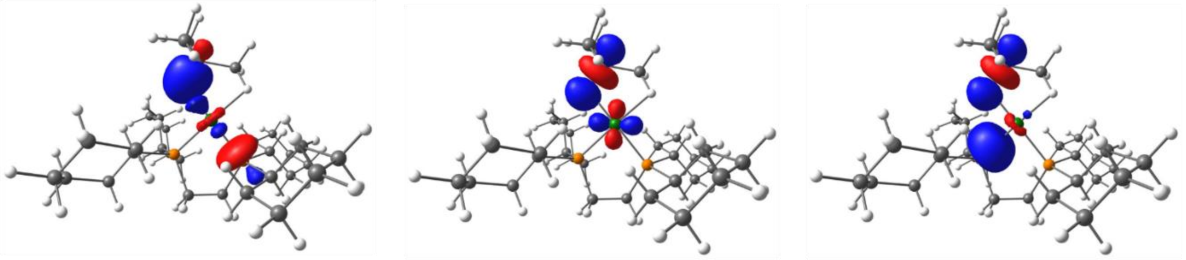

d) $\sigma_{C\text{-}H} \rightarrow \sigma^*_{Rh\text{-}P}$: (21.41 kcal mol^{-1}) e) $LP_{Rh} \rightarrow \sigma^*_{C\text{-}H}$: (3.40 kcal mol^{-1}) f) $\sigma_{Rh\text{-}P} \rightarrow \sigma^*_{C\text{-}H}$: (3.89 kcal mol^{-1})

Figure S113: NBO donor-acceptor pairs for the 1st cation of **[1-C_4H_{10}][$BAr^F{}_4$]** with NBO occupancies as indicated.

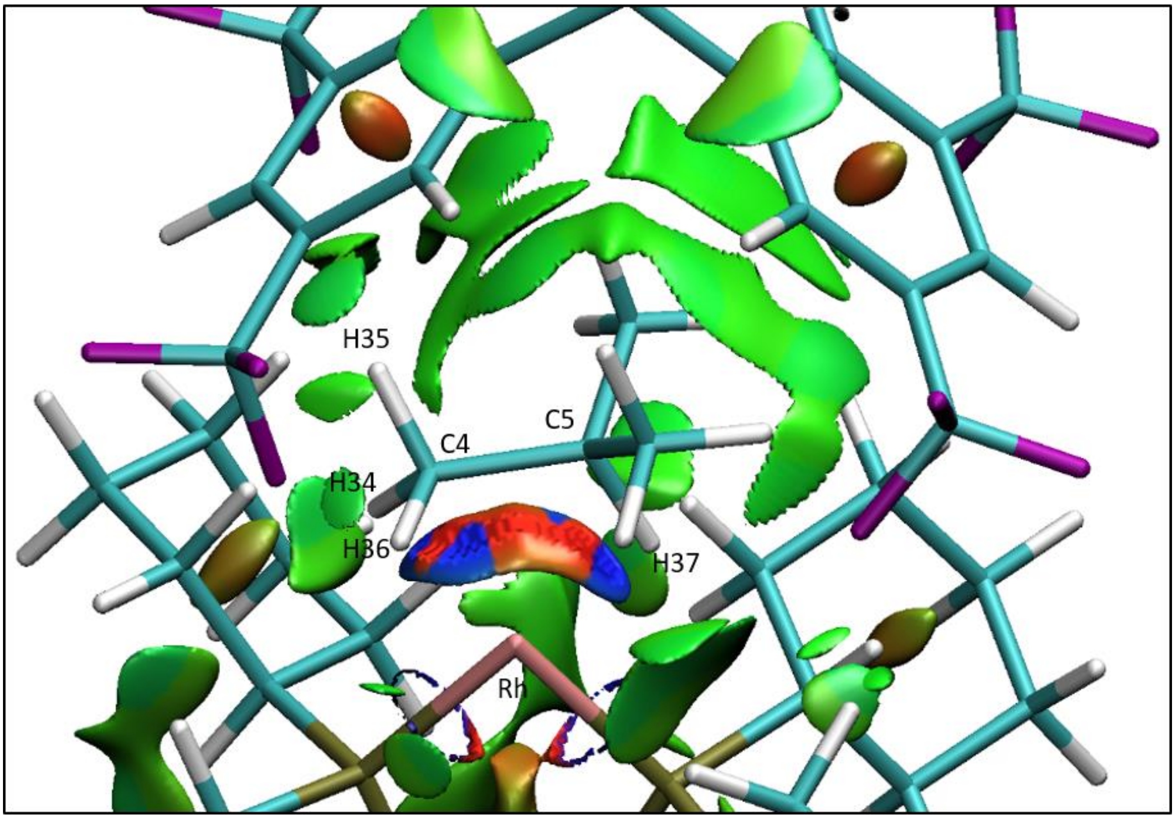

Figure S114: NCI plot of the 1st cation of **[1-C_4H_{10}][$BAr^F{}_4$]** ion-pair. Isosurfaces generated for s = 0.3 au and $-0.07 < \rho < 0.07$ au.

Distance (Å)	Fully Optimized	Heavy Atom Fixed[a]	Experiment
Rh – P2	2.203	2.184	2.184(1)
Rh – P3	2.206	2.189	2.189(1)
Rh – H34	1.934	1.955	1.981
Rh – H37	1.885	1.868	1.798
Rh – C4	2.383	2.390	2.390(14)
Rh – C5	2.480	2.438	2.438(8)
C4 – H34	1.147	1.145	1.098
C4 – H35	1.100	1.099	1.098
C4 – H36	1.096	1.094	1.098
C5 – H37	1.160	1.159	1.001
Bite Angle (°)	87.283	89.324	76.70

Table S10: Key bond distances (Å) for the **2nd cation** of **[1-C_4H_{10}][BAr^F_4]** from fully optimised and heavy atoms fixed geometries of the 1st cation of **[1-C_4H_{10}][BAr^F_4]**, with experimental data for comparison.[S31]

[a]structure is based on the experimental structure with only the positions of H and F atoms being optimised.

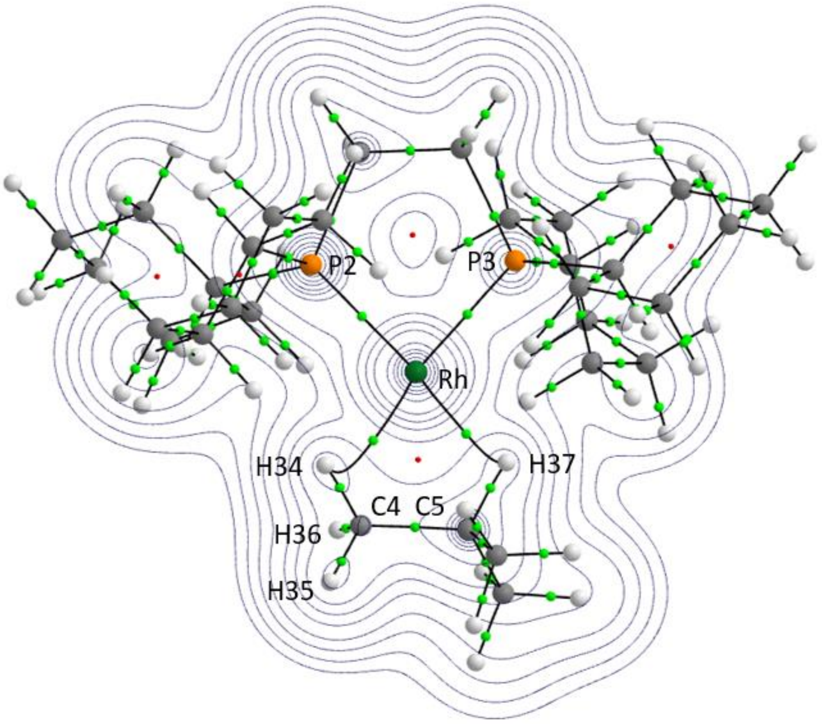

Figure S115: QTAIM molecular graph for the 2nd cation of **[1-C_4H_{10}][BAr^F_4]**, with density contours plotted in the Rh-H34-H37 plane.[S30] Bond critical points (BCPs) are indicated in green and ring critical points (RCPs) are indicated in red.

Bond	$\rho(r)$ /eÅ^{-3}	$\nabla^2 \rho(r)$ /eÅ^{-5}	H (r)
Rh – P2	0.124	0.070	-0.064
Rh – P3	0.124	0.061	-0.064
Rh – H34	0.053	0.235	-0.003
Rh – H37	0.061	0.245	-0.009
C4 – H34	0.239	-0.659	-0.213
C4 – H35	0.271	-0.919	-0.272
C4 – H36	0.277	-0.954	-0.281
C5– H37	0.232	-0.608	-0.201

Table S11: Key BCP metrics for the 2nd cation of **[1-C_4H_{10}][BAr$^F{}_4$]**.

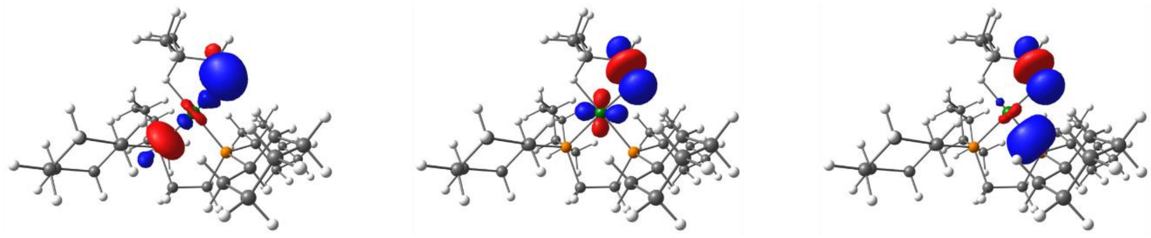

a) $\sigma_{C\text{-}H} \rightarrow \sigma^*_{Rh\text{-}P}$: (20.16 kcal mol^{-1}) b) $LP_{Rh} \rightarrow \sigma^*_{C\text{-}H}$: (3.13 kcal mol^{-1}) c) $\sigma_{Rh\text{-}P} \rightarrow \sigma^*_{C\text{-}H}$: (2.56 kcal mol^{-1})

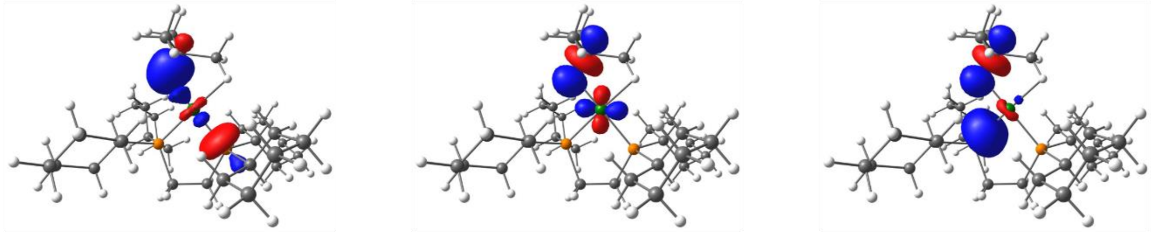

d) $\sigma_{C\text{-}H} \rightarrow \sigma^*_{Rh\text{-}P}$: (21.05 kcal mol^{-1}) e) $LP_{Rh} \rightarrow \sigma^*_{C\text{-}H}$: (3.57 kcal mol^{-1}) f) $\sigma_{Rh\text{-}P} \rightarrow \sigma^*_{C\text{-}H}$: (3.78 kcal mol^{-1})

Figure S116: NBO donor-acceptor pairs for the 2nd cation of **[1-C_4H_{10}][BAr$^F{}_4$]** with NBO occupancies as indicated.

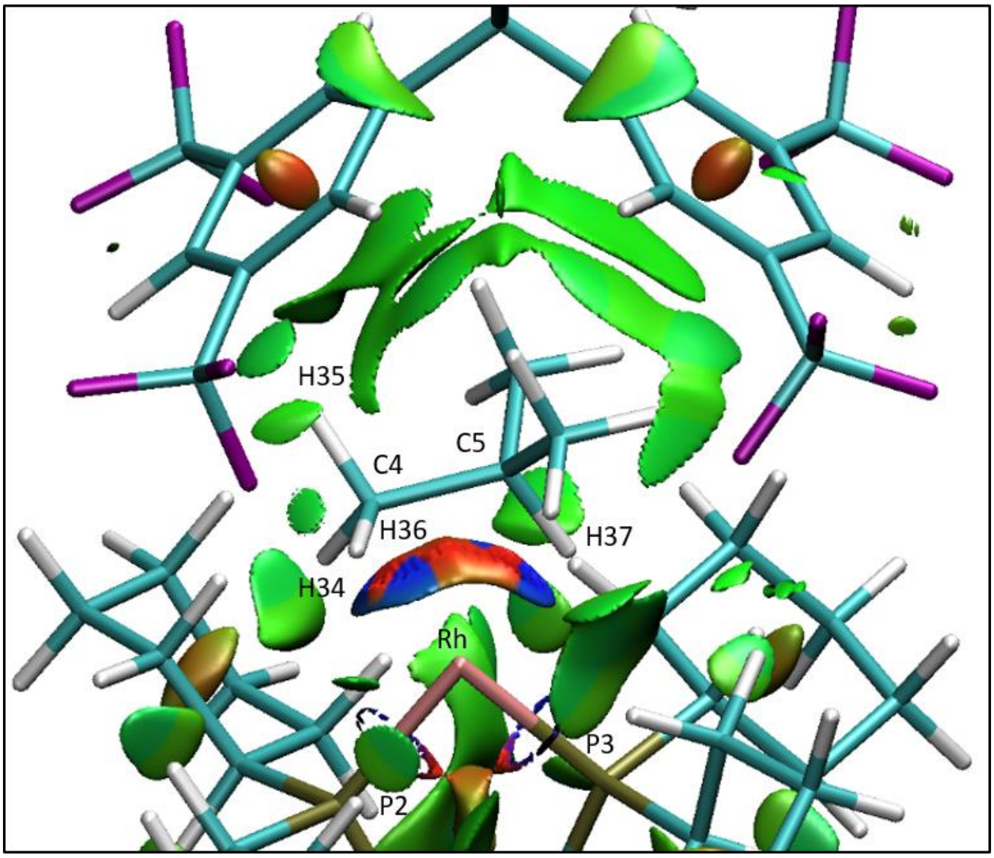

Figure S117: NCI plot for the 2nd cation of **[1-C_4H_{10}][BAr$^F{}_4$]** ion-pair. Isosurfaces generated for s = 0.3 au and -0.07 < ρ < 0.07 au.

S.9.2. $[1\text{-}C_6H_{12}][BAr^F_4]$

Distance (Å)	Fully Optimised	Heavy Atom Fixed[a]	Experiment
Rh – P1	2.201	2.192	2.192(2)
Rh – P2	2.195	2.192	2.192(2)
Rh – C1	2.679	2.530	2.530(2)
Rh – C3	2.681	2.642	2.642(2)
Rh – H11	1.928	1.852	1.777
Rh – H31	1.923	1.933	1.931
Rh – H51	2.677	2.668	2.721
C1 – H11	1.140	1.141	0.970
C1 – H12	1.101	1.100	0.970
C3 – H31	1.139	1.137	0.970
C3 – H32	1.100	1.099	0.971
C5 – H44	1.109	1.109	0.970
C5 – H45	1.098	1.094	0.970

Table S12: Key bond distances (Å) for fully optimised and heavy atoms fixed geometries, compared with experimental data.[S31]

[a] struture is based on the experimental structure with only the positions of H and F atoms being optimised.

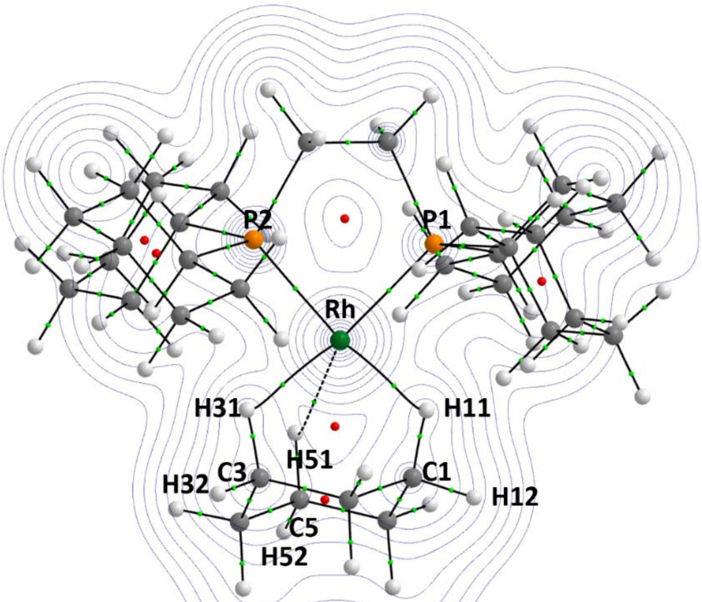

Figure S118: QTAIM molecular graph with density contours plotted in the Rh-H11-H31 plane. Bond critical points (BCPs) are indicated in green and ring critical points (RCPs) are indicated in red.

Bond	$\rho(r)$ **/eÅ^{-3}**	$\nabla^2 \rho(r)$ **/eÅ^{-5}**	**H** (r)
Rh – P1	0.123	0.065	-0.063
Rh – P2	0.123	0.070	-0.063
Rh – H11	0.061	0.226	-0.011
Rh – H31	0.050	0.181	-0.008
Rh – H51	0.015	0.041	0.000
C1 – H11	0.239	-0.648	-0.214
C1 – H12	0.274	-0.920	-0.274
C3 – H31	0.242	-0.671	-0.219
C3 – H32	0.274	-0.922	-0.274
C5 – H51	0.266	-0.853	-0.259
C5 – H52	0.276	-0.932	-0.279

Table S13. Key BCP metrics of **[1-C_6H_{12}][BAr^{F}_{4}]**

Donor	**Acceptor**	**E(2) (kcal / mol)**
Rh LP	σ* C1 – H11	4.26
σ Rh – P1	σ* C1 – H11	5.99
σ Rh – P2	σ* C1 – H11	1.63
σ C1 – H11	σ* Rh – P2	20.03
Rh LP	σ* C3 – H31	2.60
σ Rh – P1	σ* C3 – H31	1.76
σ Rh – P2	σ* C3 – H31	5.45
σ C3 – H31	σ* Rh – P1	15.13

Table S14: Key donor-acceptor interactions from the NBO second order perturbation analysis of **[1-C_6H_{12}][BAr^{F}_{4}]**.

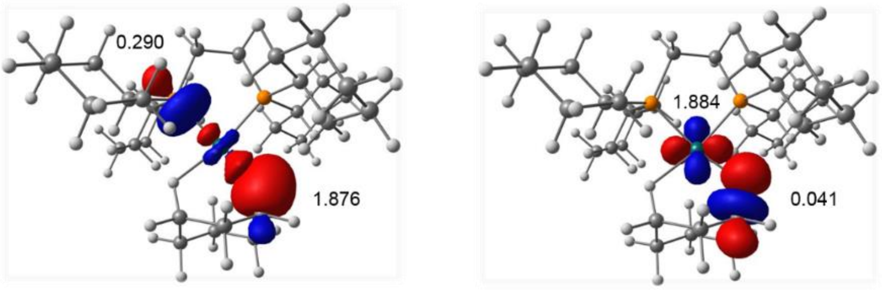

(a) $\sigma_{C1-H11} \rightarrow \sigma^*_{Rh\text{-}P2}$ (20.03 kcal/mol) (b) $Rh_{LP} \rightarrow \sigma^*_{C1-H11}$ (4.26 kcal/mol)

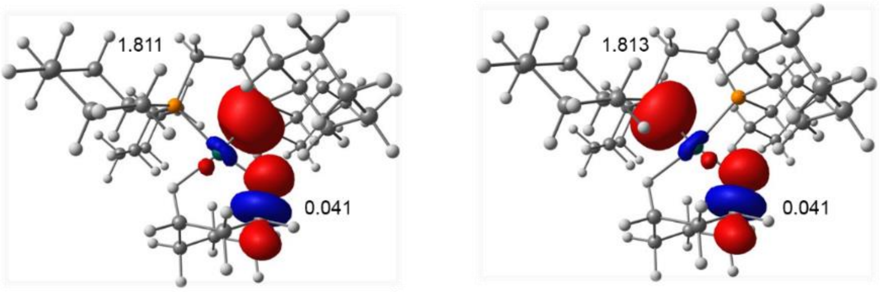

(c) $\sigma_{Rh-P1} \rightarrow \sigma^*_{C1-H11}$ (5.99 kcal/mol) (d) $\sigma_{Rh-P2} \rightarrow \sigma^*_{C1-H11}$ (1.63 kcal/mol)

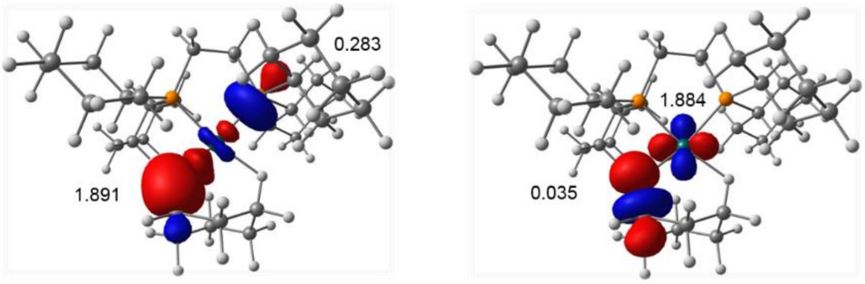

(e) $\sigma_{C3-H31} \rightarrow \sigma^*_{Rh\text{-}P1}$ (15.13 kcal/mol) (f) $Rh_{LP} \rightarrow \sigma^*_{C3-H31}$ (2.60 kcal/mol)

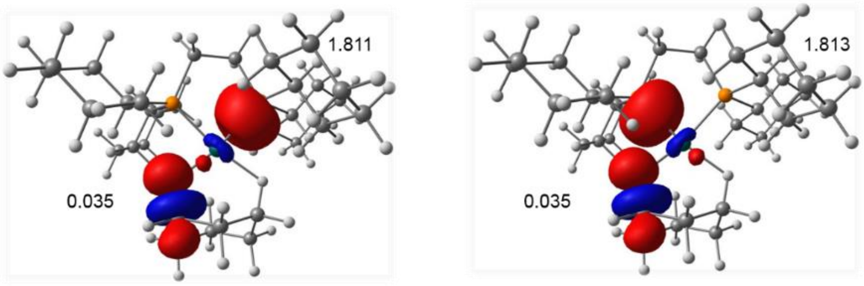

(g) $\sigma_{Rh-P1} \rightarrow \sigma^*_{C3-H31}$ (1.76 kcal/mol) (h) $\sigma_{Rh-P2} \rightarrow \sigma^*_{C3-H31}$ (5.45 kcal/mol)

Figure S119: NBO donor-acceptor pairs for **[1-C_6H_{12}][BAr^F_4]** with NBO occupancies as indicated.

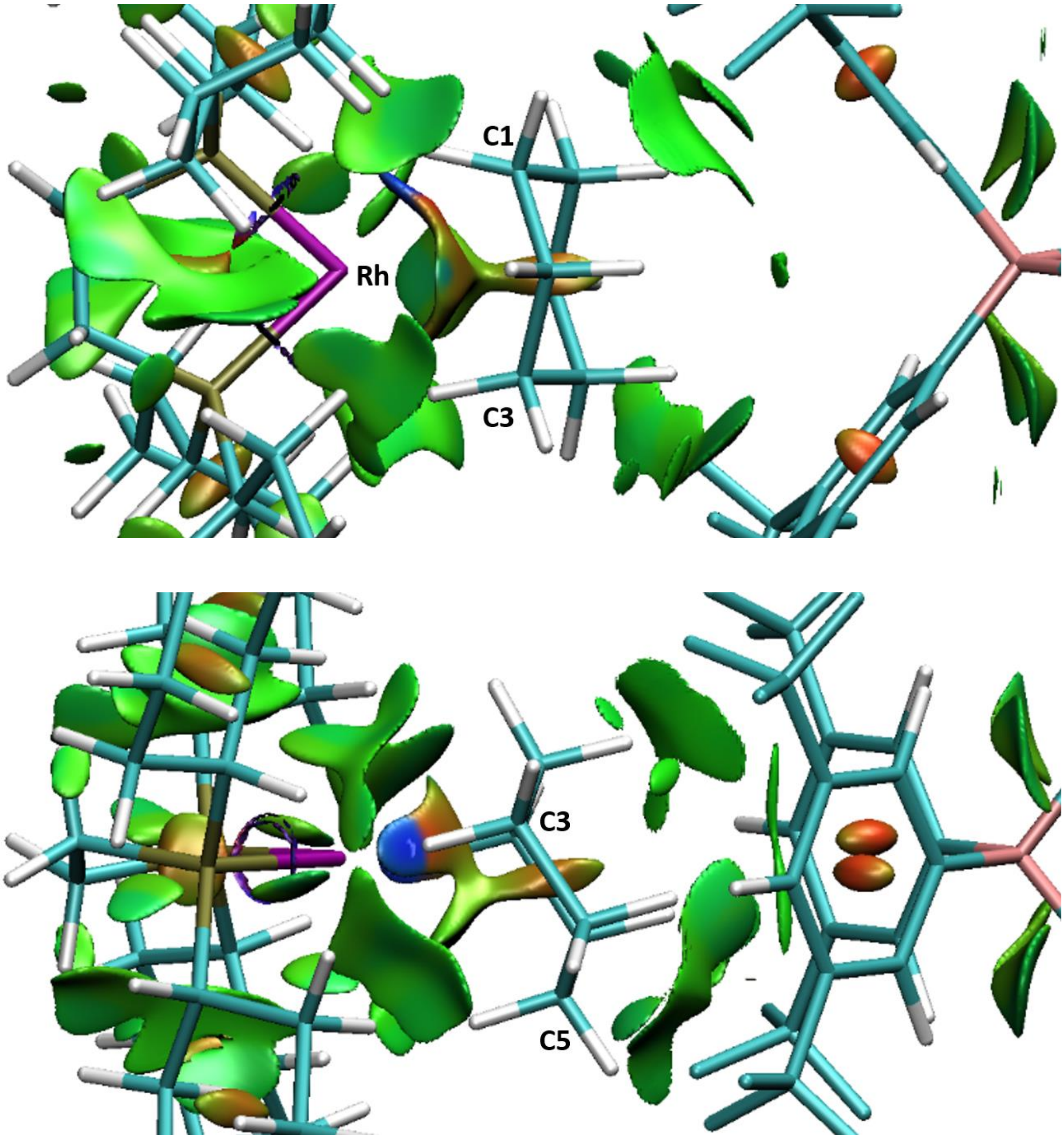

Figure S120: Two views of the NCI plots of the **$[1\text{-}C_6H_{12}][BAr^F_4]$** ion-pair. Isosurfaces generated for s = 0.3 au and -0.07 < ρ Isosurface

S.10. References

S1 Chadwick, F. M.; Rees, N. H.; Weller, A. S.; Krämer, T.; Iannuzzi, M.; Macgregor, S. A. A Rhodium-Pentane Sigma-Alkane Complex: Characterization in the Solid State by Experimental and Computational Techniques. *Angew. Chemie - Int. Ed.* **2016**, *55* (11), 3677.

S2 Pike, S. D.; Chadwick, F. M.; Rees, N. H.; Scott, M. P.; Weller, A. S.; Krämer, T.; Macgregor, S. A. Solid-State Synthesis and Characterization of σ-Alkane Complexes, [Rh(L2)(H2,H2-C7H12)][BArF4] (L2 = Bidentate Chelating Phosphine). *J. Am. Chem. Soc.* **2015**, *137* (2), 820.

S3 Earl, W. L.; Vanderhart, D. L. Measurement Of 13C Chemical Shifts in Solids. *J. Magn. Reson.* **1982**, *48* (1), 35.

S4 McKay, A. I.; Krämer, T.; Rees, N. H.; Thompson, A. L.; Christensen, K. E.; Macgregor, S. A.; Weller, A. S. Formation of a σ-Alkane Complex and a Molecular Rearrangement in the Solid-State: [Rh(Cyp 2 PCH 2 CH 2 PCyp 2)(η 2 :η 2 -C 7 H 12)][BArF4]. *Organometallics* **2017**, *36* (1), 22.

S5 Pike, S. D.; Krämer, T.; Rees, N. H.; Macgregor, S. A.; Weller, A. S. Stoichiometric and Catalytic Solid-Gas Reactivity of Rhodium Bis-Phosphine Complexes. *Organometallics* **2015**, *34* (8), 1487.

S6 Lubben, A. T.; Scott McIndoe, J.; Weller, A. S. Coupling an Electrospray Ionwization Mass Spectrometer with a Glovebox: A Straightforward, Powerful, and Convenient Combination for Analysis of Air-Sensitive Organometallics. *Organometallics* **2008**, *27* (13), 3303.

S7 Chadwick, F. M.; McKay, A. I.; Martinez-Martinez, A. J.; Rees, N. H.; Krämer, T.; Macgregor, S. A.; Weller, A. S. Solid-State Molecular Organometallic Chemistry. Single-Crystal to Single-Crystal Reactivity and Catalysis with Light Hydrocarbon Substrates. *Chem. Sci.* **2017**, *8* (9), 6014.

S8 Newsome, G. A.; Steinkamp, F. L.; Giordano, B. C. Isobutane Made Practical as a Reagent Gas for Chemical Ionization Mass Spectrometry. *J. Am. Soc. Mass Spectrom.* **2016**, *27* (11), 1789.

S9 Benedict, J. B.; Coppens, P. Kinetics of the Single-Crystal to Single-Crystal Two-Photon Photodimerization of α-Trans-Cinnamic Acid to α-Truxillic Acid. *J. Phys. Chem. A* **2009**, *113* (13), 3116.

S10 Hoops, S.; Sahle, S.; Gauges, R.; Lee, C.; Pahle, J.; Simus, N.; Singhal, M.; Xu, L.; Mendes, P.; Kummer, U. COPASI--a COmplex PAthway SImulator. *Bioinformatics* **2006**, *22* (24), 3067.

S11 Cosier, B. J.; Glazer, A. M. A Nitrogen-Gas-Stream Cryostat for General X-Ray Diffraction Studies. *J. Appl. Crystallogr.* **1986**, *19* (2), 105.

S12 *Oxford Diffraction Ltd.*; 2011.

S13 Sheldrick, G. M. A Short History of SHELX. *Acta Crystallogr. Sect. A Found. Crystallogr.* **2008**, *64* (1), 112.

S14 Sheldrick, G. M. SHELXT - Integrated Space-Group and Crystal-Structure Determination. *Acta Crystallogr. Sect. A Found. Crystallogr.* **2015**, *71* (1), 3.

S15 Dolomanov, O. V.; Bourhis, L. J.; Gildea, R. J.; Howard, J. A. K.; Puschmann, H. OLEX2: A Complete Structure Solution, Refinement and Analysis Program. *J. Appl. Crystallogr.* **2009**, *42* (2), 339.

S16 Van de Vondele, J.; Krack, M.; Mohamed, F.; Parrinello, M.; Chassaing, T.; Hutter, J.Comput. QUICKSTEP: Fast and accurate density functional calculations using a mixed Gaussian and plane waves approach. *Phys. Commun*. **2005**, *167*, 103.

S17 Hutter, J.; Iannuzzi, M.; Schiffmann, F.; VandeVondele. CP2K: atomistic simulations of condensed matter systems. J. *Wires Comput. Mol. Sci.* **2014**, *4*, 15.

S18 VandeVondele, J.; Hutter, J. Gaussian basis sets for accurate calculations on molecular systems in gas and condensed phases. *J. Chem. Phys.* **2007**, *127*, 114105.

S19 Hartwigsen, C.; Goedecker, S.; Hutter, J. Relativistic separable dual-space Gaussian pseudopotentials from H to Rn. *Phys. Rev. B* **1998**, *58*, 3641.

S20 Goedecker, S.; Teter, M.; Hutter, J.; Separable duel-space Gaussian pseudopotentials. J. Phys. Rev. B **1996**, *54*, 1703.

S21 Krack, M. Pseudopotentials for H to Kr optimized for gradient-corrected exchange-correlation functionals. *Theor. Chem. Acc.* **2005**, *114*, 145.

S22 Perdew, J. P.; Burke, K.; Ernzerhof, M. Generalized Gradient Approximation Made Simple. *Phys. Rev. Lett.* **1996**, *77*, 3865.

S23 Grimme, S.; Antony, J.; Ehrlich, S.; Krieg, H. A consistent and accurate ab initio parametrization of density functional dispersion correction (DFT-D) for the 94 elements H-Pu. *J. Chem. Phys.* **2010**, *132*, 154104.

S24 Henkelman, G.; Jonsson, H. A dimer method for finding saddle points on high dimensional potential surfaces using only first derivatives. *J. Chem. Phys*. **1999**, 111, 7010.

S25 Henkelman, G.; Uberuaga, B. P.; Jonsson, H. A climbing image nudged elastic band method for finding saddle points and minimum energy paths. *J. Chem. Phys*. **2000**, 113, 9901.

S26 Chadwick, F. M.; Krämer, T.; Gutmann, T.; Rees, N. H.; Thompson, A. L.; Edwards, A. J.; Buntkowsky, G.; Macgregor, S. A.; Weller, A. S. Selective C–H Activation at a Molecular Rhodium Sigma-Alkane Complex by Solid/Gas Single-Crystal to Single-Crystal H/D Exchange. *J. Am. Chem. Soc*. **2016**, 138, 13369.

S27 Brogaard, R. Y.; Weckhuysen, B. M.; Noerskov, J. K. Guest–host interactions of arenes in H-ZSM-5 and their impact on methanol-to-hydrocarbons deactivation processes. *J. Catal*. **2013**, 300, 235.

S28 Piccini, G.; Sauer, J. Quantum Chemical Free Energies: Structure Optimization and Vibrational Frequencies in Normal Modes. *J. Chem. Theory Comput*. **2013**, 9, 5038.

S29 Ghysels, A.; Verstraelen, T.; Hemelsoet, K.; Waroquier, M.; Van Speybroeck, V. TAMkin: A Versatile Package for Vibrational Analysis and Chemical Kinetics *J. Chem. Inf. Model.* **2010**, 50, 1736.

S30 Gaussian 09 (Revision D.01); Frisch, M. J.; Trucks, G. W.; Schlegel, H. B.; Scuseria, G. E.; Robb, M. A.; Cheeseman, J. R.; Scalmani, G.; Barone, V.; Mennucci, B.; Petersson, G. A.; Nakatsuji, H.; Caricato, M.; Li, X.; Hratchian, H. P.; Izmaylov, A. F.; Bloino, J.; Zheng, G.; Sonnenberg, J. L.; Hada, M.; Ehara, M.; Toyota, K.; Fukuda, R.; Hasegawa, J.; Ishida, M.; Nakajima, T.; Honda, Y.; Kitao, O.; Nakai, H.; Vreven, T.; J. A. Montgomery, J.; Peralta, J. E.; Ogliaro, F.; Bearpark, M.; Heyd, J. J.; Brothers, E.; Kudin, K. N.; Staroverov, V. N.; Keith, T.; Kobayashi, R.; Normand, J.; Raghavachari, K.; Rendell, A.; Burant, J. C.; Iyengar, S. S.; Tomasi, J.; Cossi, M.; Rega, N.; Millam, J. M.; Klene, M.; Knox, J. E.; Cross, J. B.; Bakken, V.; Adamo, C.; Jaramillo, J.; Gomperts, R.; Stratmann, R. E.; Yazyev, O.; Austin, A. J.; Cammi, R.; Pomelli, C.; Ochterski, J. W.; Martin, R. L.; Morokuma, K.; Zakrzewski, V. G.; Voth, G. A.; Salvador, P.; Dannenberg, J. J.; Dapprich, S.; Daniels, A. D.; Farkas, O.; Foresman, J. B.; Ortiz, J. V.; Cioslowski, J.; Fox, D. J.; Gaussian Inc., Wallingford, CT, 2013.

S31 Becke, A. D. Density-functional exchange-energy approximation with correct asymptotic behavior. *Phys. Rev. A* **1988**, *38*, 3098.

S32 Perdew, J. P. Density-functional approximation for the correlation energy of the inhomogeneous electron gas. *Phys. Rev. B* **1986**, *33*, 8822.

S33 Andrae, D.; Haussermann, U.; Dolg, M.; Stoll, H.; Preuss, H. Energy-adjusted *ab initio* pseudopotentials for the second and third row transition elements. *Theor. Chim. Acta* **1990**, *77*, 123.

S34 Hollwarth, A.; Bohme, M.; Dapprich, S.; Ehlers, A. W.; Gobbi, A.; Jonas, V.; Kohler, K. F.; Stegmann, R.; Veldkamp, A.; Frenking, G. A set of d-polarization functions for pseudo-potential basis sets of the main group elements Al・Bi and f-type polarization functions for Zn, Cd, Hg. *Chem. Phys. Lett.* **1993**, *208*, 237.

S35 Hehre, W. J.; Ditchfield, R.; Pople, J. A. Self—Consistent Molecular Orbital Methods. XII. Further Extensions of Gaussian—Type Basis Sets for Use in Molecular Orbital Studies of Organic Molecules. *J. Chem. Phys.* **1972**, *56*, 2257.

S36 Hariharan, P. C.; Pople, J. A. The influence of polarization functions on molecular orbital hydrogenation energies. *Theor. Chim. Acta* **1973**, *28*, 213.

S37 Bader, R. F. W. *Atoms in Molecules: A Quantum Theory*; Oxford University Press, 1990.

S38 AIMAll (Version 17.11.14), Todd A. Keith, TK Gristmill Software, Overland Park KS, USA, 2017 (aim.tkgristmill.com)

S39 NBO 6.0. E. D. Glendening, J. K. Badenhoop, A. E. Reed, J. E. Carpenter, J. A. Bohmann, C. M. Morales, C. R. Landis, and F. Weinhold (Theoretical Chemistry Institute, University of Wisconsin, Madison, WI, 2013); http://nbo6.chem.wisc.edu/

S40 Johnson E. R.; Keinan S.; Mori-Sanchez P.; Contreras-Garcia J.; Cohen A. J.; Yang W. Revealing Noncovalent Interactions. *J. Am. Chem. Soc.* **2010**, *132*, 6498.

S41 Contreras-Garcia J.; Johnson E. R.; Keinan S.; Chaudret R.; Piquemal J-P.; Beratan D. N.; Yang W. NCIPLOT: A Program for Plotting Noncovalent Interaction Regions. *J. Chem. Theory Comput*. 2011, **7**, 625.

S42 Chemcraft - graphical software for visualization of quantum chemistry computations. https://www.chemcraftprog.com

S43 Pickard, C. J.; Mauri, F. All-electron magnetic response with pseudopotentials: NMR chemical shifts. *Phys. Rev. B* **2001**, 63, 245101.

S44 Yates, J. R.; Pickard, C. J.; Mauri, F. Calculation of NMR chemical shifts for extended systems using ultrasoft pseudopotentials. *Phys. Rev. B* **2007**, 76, 024401.

S45 Clark, S. J.; Segall, M. D.; Pickard, C. J.; Hasnip, P. J.; Probert, M. J.; Refson, K.; Payne, M. C. First principles methods using CASTEP. *Z. Kristallogr*. **2005**, 220, 567.

S46 Monkhorst, H. J.; Pack, J. D. Special points for Brillouin-zone integrations. *Phys. Rev. B* **1976**, 13, 5188.

S47 van Lenthe, E.; Baerends, E. J.; Snijders, J. G. Relativistic regular two-component Hamiltonians. *J. Chem. Phys*. **1993**, 99, 4597.

S48 van Lenthe, E.; Baerends, E. J.; Snijders, J. G. Relativistic total energy using regular approximations. *J. Chem. Phys*. **1994**, 101, 9783.

S49 Lodewyk, M. W.; Siebert, M. R.; Tantillo, D. Computational Prediction of ^{1}H and ^{13}C Chemical Shifts: A Useful Tool for Natural Product, Mechanistic, and Synthetic Organic Chemistry. *J. Chem. Rev*. **2012**, 112, 1839.

S50 C. F.; Bruno, I. J.; Chisholm, J. A.; Edgington, P. R.; McCabe, P.; Pidcock, E.; Rodriguez-Monge, L.; Taylor, R.; van de Streek, J.; Wood, P. A. Mercury CSD 2.0 - new features for the visualization and investigation of crystal structures. *J. Appl. Cryst*., **2008**, *41*, 466.